ABSTRACT

Title of dissertation: A FUNDAMENTAL STUDY OF
                           BOUNDARY LAYER DIFFUSION
                           FLAMES
                           Ajay Vikram Singh, Doctor of Philosophy, 2015

Dissertation directed by: Professor Michael J. Gollner
                           Department of Fire Protection Engineering

Modeling the realistic burning behavior of condensed-phase fuels has remained out of reach, in part because of an inability to resolve complex interactions at the interface between gas-phase flames and condensed-phase fuels. This interaction is even more complex as scales increase, because realistic fires occur under fully turbulent conditions which have yet to be fully replicated or understood at the bench scale, where detailed measurements can be conducted. The current research explores the dynamic relationship between combustible condensed fuel surface and gas-phase flames in laminar boundary layers, representing the small scales in which materials are tested (where much of todays theoretical knowledge is also isolated) to realistic large-scale turbulent flames present in almost all unwanted fires, hybrid rocket motors and other similar combustion phenomena.

A thorough numerical and experimental investigation of laminar boundary-layer

diffusion flames established over the surface of a condensed fuel is presented. By extension of the Reynolds Analogy, it is hypothesized that the non-dimensional temperature gradient at the surface of a condensed fuel is related to the local mass-burning rate through some constant of proportionality. First, this proportionality is tested by using a validated numerical model for a steady flame established over a condensed fuel surface, under free and forced convective conditions. Second, the relationship is tested by conducting experiments in a free and forced convective environment using methanol and ethanol as liquid fuels and PMMA as a solid fuel, where a detailed temperature profile is mapped during steady burning using fine-wire thermocouples mounted to a precision two-axis traverse mechanism. The results from the present study suggests that there is indeed a unique correlation between the mass burning rates of liquid/solid fuels and the temperature gradients at the fuel surface. The correlating factor depends upon the Spalding mass transfer number and gas-phase thermo-physical properties and works in the prediction of both integrated as well as local variations of the mass burning rate as a function of non-dimensional temperature gradient. Convective and radiative heat feedback from the flames were also measured both in the pyrolysis and plume regions by using temperature gradients near the wall. Additional results from precise measurements of the thermal field are also presented.

A FUNDAMENTAL STUDY OF
BOUNDARY LAYER DIFFUSION FLAMES

by

Ajay Vikram Singh

Dissertation submitted to the Faculty of the Graduate School of the
University of Maryland, College Park in partial fulfillment
of the requirements for the degree of
Doctor of Philosophy
2015

Advisory Committee:
Assistant Professor Michael J. Gollner, Chair
Associate Professor Christopher Cadou
Associate Professor Peter Sunderland
Associate Professor Andre Marshall
Associate Professor Stanislav Stoliarov

Acknowledgments

I owe my gratitude to all the people who have made this thesis possible and because of whom my graduate experience has been one that I will cherish forever.

First and foremost I'd like to thank my advisor, Professor Michael J. Gollner for giving me an invaluable opportunity to work on challenging and extremely interesting projects over the past two and a half years. He has always made himself available for help and advice and there has never been an occasion when I've knocked on his door and he hasn't given me time. It has been a pleasure to work with and learn from such an extraordinary individual. Michael remains to be my best friend till date.

I would also like to thank Professor Elaine S. Oran for her immense support and help during the course of my Ph.D. I feel totally honored and privileged to work with and learn from such an extraordinary researcher, teacher, advisor and friend. Elaine and Michael continues to be my guiding star in times of hardship and de-motivation. In a nutshell, they both are absolutely "amazing and wonderful".

I would also like to thank Professor Arnaud Trouve for his help and support during the course of my Ph.D. Thanks are also due to his research group for wonderful discussions on wildland fire modeling.

Thanks are due to Professors Christopher Cadou, Peter Sunderland, Stanislav Stoliarov and Andre Marshall for serving on my thesis committee and for sparing

I owe my deepest thanks to my family - my father, my wife, my brother and my sister who have always stood by me and guided me through my career, and have pulled me through against impossible odds at times. Words cannot express the gratitude I owe them.

Last, but not least, I would like to thank my wife Gunjan Singh for standing beside me in times of hardship and motivating me to achieve goals that seemed a distant dream for me.

It is impossible to remember all, and I apologize to those I've inadvertently left out.

Lastly, thank you all and thank God!

Table of Contents

List of Figures

xi

xii

xv

List of Tables

Nomenclature

B	B-number (Spalding mass transfer number) (-)
c_p	Specific heat at constant pressure (J/kg-K)
D	Species diffusivity (m^2/s)
d	Diameter (m)
g	Gravitational acceleration (m/s^2)
Gr	Grashof number (-)
h	Convective heat transfer coefficient (W/m^2-K)
$h_g, \Delta H_g$	Effective heat of gasification or vaporization (J/kg)
ΔH_c	Heat of combustion per unit mass of oxygen (J/kg)
k	Thermal conductivity (W/m-K)
L	Length of the condensed fuel surface (m)
L_v, L_{eff}	Effective heat of vaporization (J/kg)
$\dot{m}_f''$	Mass-burning rate (mass flux) (kg/m^2-s)
Nu	Nusselt number (-)
Pr	Prandtl number (-)
$\dot{q}_{net}''$	Net heat flux (W/m^2)
$\dot{q}_{fl,c}''$	Convective heat flux (W/m^2)
$\dot{q}_{fl,r}''$	Radiative heat flux (W/m^2)
$\dot{q}_{s,rr}''$	Surface Re-radiation heat flux (W/m^2)
$\dot{q}_{s,i}''$	Incident heat flux (W/m^2)
$\dot{q}_{id,cond}''$	In-depth conduction into the solid (W/m^2)
$\dot{q}_{id,r}''$	In-depth radiation into the solid (W/m^2)
$\dot{q}_{hfg}''$	Total heat flux from heat flux gauge (W/m^2)
r	Surface reflectivity (-)
Re	Reynolds number (-)
Ri	Richardson number (-)
t	Time (s)
T	Temperature (K)
T^*	Non-dimensional temperature (-)
U_∞	Free-stream velocity (m/s)
v_s	Stefan mass transfer velocity (m/s)
x	Coordinate parallel to the condensed fuel surface (m)
y	Coordinate perpendicular to the condensed fuel surface (m)
x^*	Non-dimensional distance, x/L (-)
y^*	Non-dimensional distance, y/L (-)
y_f	Flame standoff distance (m)
Y_f	Fuel vapor mass fraction (-)
Y_{O_2}	Mass fraction of Oxygen (-)

Nomenclature

Greek Symbols

α	Thermal diffusivity (m^2/s)
δ	Surface regression of PMMA (m)
ε	Emissivity (-)
ν	Kinematic viscosity (m^2/s)
ρ	Density (kg/m^3)
τ_s	Shear stress at the surface (N/m^2)
υ_s	Oxygen-fuel mass stoichiometric ratio (-)

Subscripts

ad	Adiabatic
f	Film (mean properties)
fl	Flame
g	Gas
hfg	Heat flux gauge
id	In-depth
∞	Ambient
p	Pyrolysis
s	Surface
ig	Ignition
tc,b	Thermocouple junction or bead
w	Wall / Wire

Abbreviations

HFG	Heat Flux Gauge
LBL	Laminar Boundary Layer
PMMA	Poly Methyl Methacrylate

Chapter 1: Introduction

1. Problem Statement

Ascertaining conditions under which a fire will spread from a burning fuel element to an adjacent combustible is a problem of obvious practical importance. A rational approach to this fire spread problem should be based on a thorough knowledge of the burning characteristics of isolated fuel elements. The fuel mass-burning rate, which is roughly proportional to the heat-release rate (HRR) by an effective heat of combustion, is often cited as the most fundamental quantity in fire research [1]. In general, this burning rate is approximately taken as the mass-loss rate of the condensed-phase fuel, namely the evaporation rate of a liquid fuel or the pyrolysis rates of a solid fuel [2, 3].

The burning rate can be thought of as a measure of the flammability of a material and is a critical parameter in fire risk analysis and the design for fire suppression systems. The local mass loss (or burning) rate, $\dot{m}_f''$, of a vertical wall is an important variable in many fire-related problems, such as flame spread on a wall, fire growth and energy release rate in an enclosure fire, and the spread of smoke and hot gas plumes. For prediction of upward flame spread on a vertical wall, the flame height must be calculated, which depends on the total energy release rate; that, in turn, is

directly influenced by the local mass loss rate integrated over the entire pyrolyzing area of the wall. Knowledge of local mass burning rates provides increased experimental information on the burning of condensed fuels, enabling more insight into the mechanisms which affect small scale burning. While measurements of the average mass burning rates of a condensed fuel are readily available, local burning rate measurements are difficult to determine, even in small scale-scale experiments.

The work presented here has utilized simulations and experiments of steady laminar flames established over condensed fuel surfaces to verify that a relationship exists between the non-dimensional temperature gradient at the fuel surface and the local mass-burning rate. This relationship is essentially a further extension of the Chilton-Colburn extension [4] to the Reynolds Analogy [5] to relate heat, momentum and mass transfer. For laminar buoyant and forced-convective configurations, numerical and experimental results show that the relationship remains valid for both solid and liquid fuels. Further measurements provide local heat fluxes, burning rates and heat transfer correlations that should prove useful for the study of laminar burning fuels and future numerical validation, as the laminar wall fire is a canonical fire research problem.

1.1. Boundary Layer Diffusion Flames

Free and forced convection boundary layer diffusion flames have been widely studied because of their importance in wall fires, ceiling fires, and wind driven fires on flat surfaces such as walls, roofs and floors. Diffusion flames in turbulent boundary layers have also been studied because of their practical importance in other applications such as hybrid rocket engines. Bulkhead fires and spilled fuel fires on aircraft carrier decks are typical examples of boundary layer type fires. Boundary layer diffusion flames have also been investigated in connection with various applications such as ablative cooling, erosive burning of solid propellants, and surface combustion of liquid fuels. Boundary layer diffusion flames present a number of characteristics which permit fundamental studies on the mechanism of combustion of condensed phase fuels.

In boundary layer diffusion flames, heat transfer from the reaction zone to the unburnt material has been considered to take place mainly through the gas phase. At small scale the amount of heat transferred from the gas phase to the condensed phase depends on the temperature profile in the gas phase adjacent to the combustible surface, and is closely related to the behavior of gasified fuel, air and combustion products. Boundary layer combustion has been found to be controlled by the rate at which heat can be delivered to the fuel surface, rather than by the surface reaction

rates, therefore careful measurements of the temperature profile in the gas phase close to the surface are useful for investigation. Knowledge of local mass burning rates along with various components of flame heat flux also provides more insight into the mechanisms which affect boundary layer combustion processes. While measurements of the average burning rate of a condensed fuel are readily available, local burning rates are difficult to determine both in large and small scale experiments. Similarly, a considerable amount of effort has been made in the past to quantify the various components of flame heat flux to the condensed fuel surface, however they have been reported with high uncertainty.

The rate of flame propagation over any solid or liquid fuel surface, and its ultimate growth to a large fire primarily depends on the burning or mass-loss rate of the fuel. The burning rate in turn depends on external conditions, such as the free stream velocity (for burning of fuels in a forced convective environment) and the angular orientation of the combustible surface with respect to the normal gravity direction. In most problems related to flame propagation over fuel surfaces, it is necessary to have a means of estimating the rate of vaporization of the diffusing fuel vapor, also called the mass-burning rate. There is, therefore, a need to develop a convenient method of applying a well-substantiated correlation to permit predictions of the burning behavior of fuels, where there is no experimental data at the scale of interest.

1.2. Characteristics of Boundary Layer Diffusion Flames: The Emmons Problem

Pioneering work on the modeling of boundary layer flames includes the work of Emmons [6], where a solution for the burning rate of a diffusion flame established over a liquid fuel subjected to a forced flow parallel to the surface is derived. A schematic of the burning of a condensed fuel, subjected to a forced flow parallel to its surface is shown in Figure 1.1. All free-stream properties are denoted by the subscript ∞.
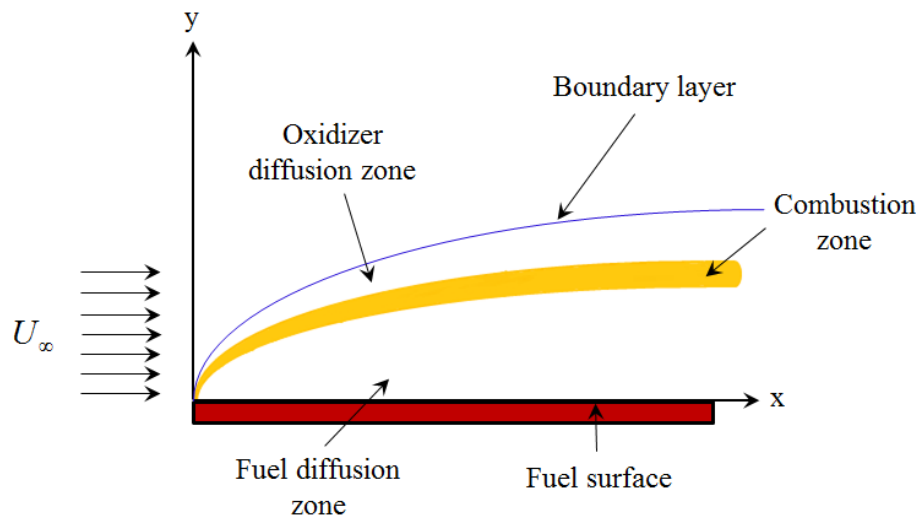
Figure 1.1: Combustion of a liquid fuel film in a boundary layer (Emmons problem).

As the liquid fuel evaporates it convects along the surface and diffuses away until it is mixed with oxygen and is sufficiently heated to burn. Thus, somewhere within

the boundary layer there is a reaction zone. Oxygen diffuses from the air toward the surface and again is largely consumed in the reaction zone. Simultaneously, heat convects away from the combustion zone toward both the air and the fuel surface. Heat transfer from the flame supports the continued evaporation of the fuel from the condensed fuel surface. The heat arriving at the fuel surface must therefore supply the latent heat required to evaporate the fuel and also any heat that conducts into the condensed fuel surface or is re-radiated away. It is to be noted that the combustion zone is assumed to exist within the boundary layer. Although the rate of combustion is controlled by heat and mass transfer processes, the existence of a combustion zone in the assumed position depends upon chemical effects as well.

According to this model the boundary layer comprises two zones, one above the flame where the temperature gradient and velocity gradient are opposed in direction, and one below the flame where the gradients are in the same direction. The zone below the flame is the effective boundary layer for heat transfer to the wall, while both zones together form the boundary layer for momentum transfer.

1.3. Types of Boundary Layer Diffusion Flames

Boundary layer diffusion flames can be steady or transient based on their burning characteristics.

1.3.1. Steady Boundary Layer Diffusion Flames

Boundary layer diffusion flames can be sustained over condensed fuel surfaces in a variety of free, forced and mixed convective conditions. The laminar boundary layer diffusion flame over a flat plate has been studied by a number of investigators. Forced convective conditions could involve the flow of oxidizer (in general, air) in different configurations with respect to the fuel surface. When the air flow is parallel to the fuel surface, the configuration is called cross-flow. Based on the velocity of the air flow, the effects of gravity will be important. Flow fields could be altered due to buoyancy (free convection) and this depends on the orientation of the fuel surface with respect to the normal gravity vector.

Figure 1.2 shows the schematic of a diffusion flame established over a horizontal liquid fuel pool in a forced-convective flow field. For the cross flow configuration, as shown in Fig. 1.2, the flow of air is parallel to the horizontal fuel surface. A laminar boundary layer type diffusion flame is formed over the fuel. For low cross-flow air velocities, the flame is anchored near the leading edge of the fuel surface as denoted in Fig. 1.2. As the air velocity is increased, the flame anchoring point continues to shift further downstream of the leading edge. At a certain critical air velocity, the flame blows off due to a reduced residence time.
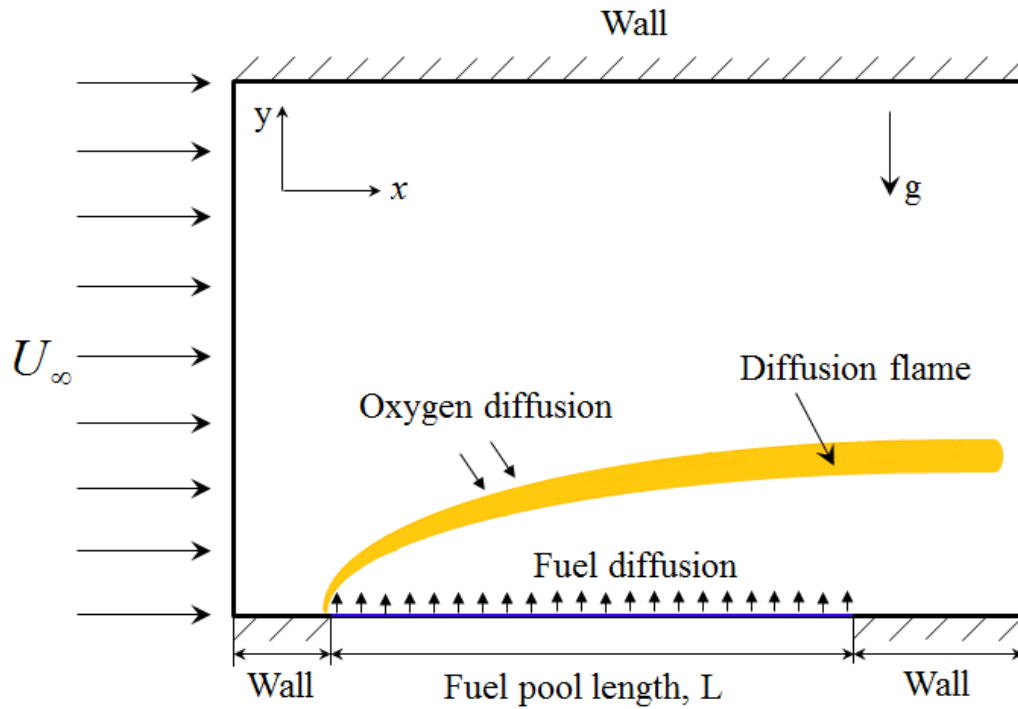
Figure 1.2: Schematic of a steady diffusion flame in a forced-convective environment.

Combustion in forced-convective boundary layer diffusion flames is controlled by convection and diffusion processes. Oxygen from the oxidizer stream is transported by forced convection as well as by mass diffusion towards the flame zone. Fuel vapor from the pool surface is transported towards the flame zone by diffusion. Heat transfer from the flame supports continued evaporation of the fuel from the condensed fuel surface.

A combustible liquid fuel film formed over porous surfaces, or wick type materials, can be oriented under various angular positions with respect to the gravity vector

8

under normal gravity conditions. A schematic of the steady burning of such thin liquid fuel surfaces in a free-convective environment is shown in Fig. 1.3 [7]. Figure 1.3 (a) shows that within the laminar burning regime, a free convective type boundary layer flame is established when the fuel surface is oriented vertically ($\theta = 0$ deg). The orientation angle is measured with respect to the vertical line. For a fuel surface burning in a ceiling configuration [Fig. 1.3 (b)], where the fuel film is upside-down, ($\theta = $ -90 deg), a sheet like flame structure is obtained that completely envelops the fuel surface and extends on either side of the leading and the trailing edge. In this case, hot combustion products rise upwards, forming a stagnation zone below the fuel surface [Fig. 1.3 (b)]. For fuel burning in a horizontal configuration, wherein the fuel surface is facing upwards (a pool fire like configuration), hot combustion products and fuel vapor are transported in the upward direction due to buoyancy driven flow, giving a buoyant plume like structure [Fig. 1.3 (c)].

For surface orientation in the intermediate ranges, the flame shape and burning rate depend on the flow field due to natural convection. In all these configurations, oxygen and fuel vapor are transported towards the flame by buoyancy induced convection as well as mass diffusion. The flame is sustained by continued evaporation of the fuel from the interface due to heat transfer from the flame. Significant differences in flame shapes, fuel burning rates and flame standoff distances exist among these

9
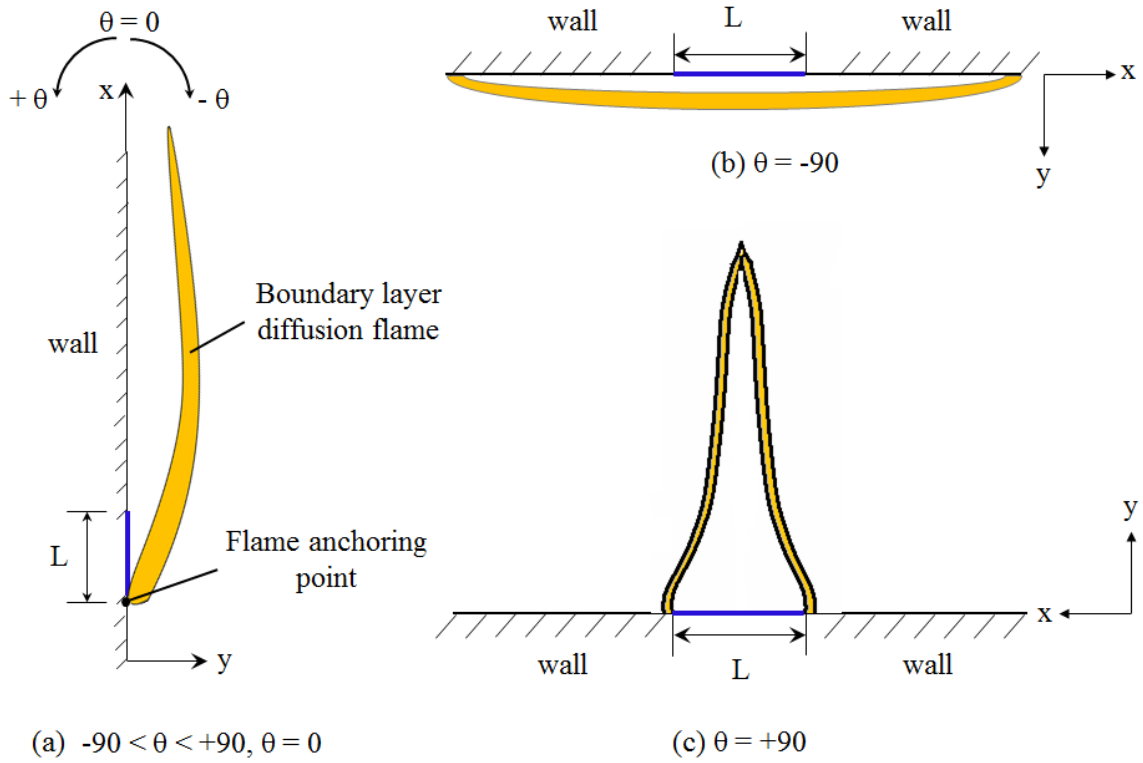
Figure 1.3: Schematic of steady diffusion flames in a free-convective environment [7].
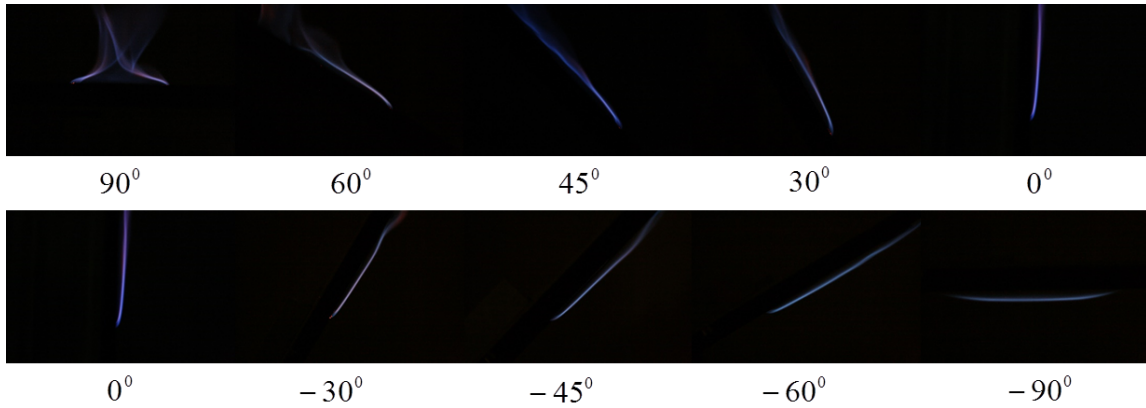
Figure 1.4: Side-view flame photographs for steady boundary-layer diffusion flames in a free-convective environment stabilized at various angular orientations for a 8×8 cm methanol fuel wick.

configurations due to the differences in fluid dynamics involved. Figure 1.4 shows the side-view flame photographs for steady boundary-layer diffusion flames stabilized at various angular orientations in a free-convective environment for a 8×8 cm methanol fuel wick.

1.3.2. Transient Boundary Layer Diffusion Flames

As mentioned earlier, transient flame propagation over a liquid or solid fuel surface mainly depends on the fuel properties, ambient conditions and the strength and direction of the convective flow field. Based on the convective flow field, the flame propagation can be classified as either concurrent flame propagation or opposed flame propagation, depending on the direction of flame propagation with respect to that of the oxidizer flow. In concurrent flame spread, oxidizer flows in the same direction as that of the propagating flame and in opposed flame spread oxidizer flow is opposite to that of the flame propagation direction. Figure 1.5 illustrates several modes of flame spread on a solid surface [8].

In a wind-aided (or concurrent) flame spread scenario, the pyrolysis front, x_p moves in the direction of the induced buoyant or pressure-driven ambient flow speed, U_∞. At $x = x_p$, T_s (surface temperature) is equal to the ignition temperature T_{ig}. In general, $T_s(x)$ is the upstream or downstream surface temperature of the virgin material and δ_f is the flame extension over the new material to ignite. A wind-

11

directed flame on the floor will be different than one on the ceiling. In the floor case, the larger the fire becomes, the more its buoyant force grows and tries to make the flame become vertical despite the wind. This phenomenon will be profoundly different in a channel than on an open floor. In the ceiling case, the gravity vector helps to hold the flame to the ceiling, and even tries to suppress some of its turbulence.
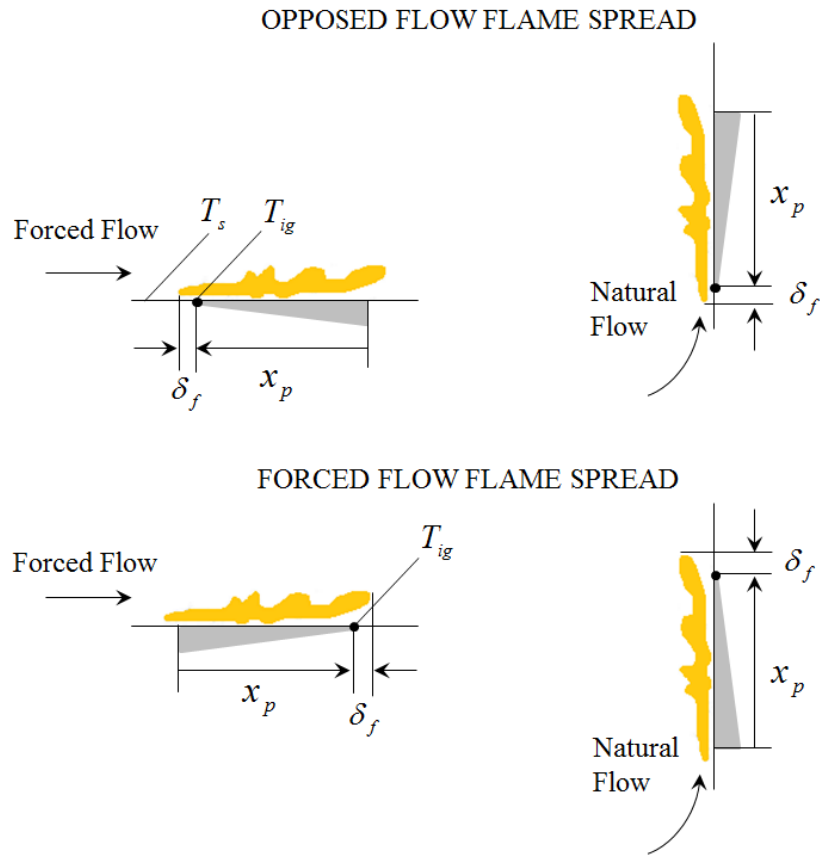
Figure 1.5: Several modes of flame spread on a solid surface.

When the ambient flow is directed into the advancing flame, we call this case

12

counter-current or opposed flow flame spread. The flow can be both natural and artificially forced. Opposed flow spread is much slower than wind-aided spread and tends to be steady. Even in quiescent air, $U_\infty = 0$, it will still appear to an observer an opposed flow flame is approaching as the flame entrains air counter to this propagation direction. Under zero gravity conditions, where blowing air is common for cooling and ventilation, opposed flow spread may play a significant role in spacecraft (microgravity) fires. Thus, transient boundary layer diffusion flames over a liquid or solid fuel are of importance and have been investigated in the past to examine the mechanisms of flame spread over surfaces.

1.4. Theoretical Formulation for the Local Mass Burning Rate

The method proposed here has its basis in the work of Chilton-Colburn [4] and Silver [5] whose extension to the Reynolds analogy establishes a relationship between mass, momentum, and heat transfer in a boundary layer over a solid or liquid fuel surface and is given by

$$\frac{\tau_s}{u_\infty \nu^{2/3}} \equiv \frac{h}{c_p \alpha^{2/3}} \equiv \frac{\dot{m}''}{D^{2/3} ln(1+B)}, \tag{1}$$

where ν is the kinematic viscosity or momentum diffusivity, α represents the thermal diffusivity, and D is the species diffusivity. Equation (1) implies that the shear stress at the surface τ_s is related to the heat transfer h and mass transfer from combustion,

13

$\dot{m}_f''$. The terms, U_∞, h and c_p are the free-stream velocity, convective heat-transfer coefficient, and the specific heat of the gas, respectively. The term B that appears in Eq. (1) is a non-dimensional proportionality constant that relates the rate of mass transfer (e.g., vaporization, combustion) to the rate of heat transfer and shear stress, and is essentially the driving force for mass transfer, and was first referred to as the transfer number by Spalding [9]. This dimensionless parameter is quite simply a ratio that compares a summation of the various impetuses (eg. heat of combustion) for burning to a summation of the various resistances (e.g. heat of vaporization) to the process. Originally a purely thermodynamic quantity, its definition can be extended to encompass effects of different heat-transfer processes. The B-number is defined by Torero et al. [10] as,

$$B = \frac{(1-\chi)(\Delta H_c Y_{O_2,\infty})/v_s - c_{p,\infty}(T_p - T_\infty)}{\Delta H_g + Q}. \tag{2}$$

where χ is the fraction of the total energy released by the flame that is radiated to the environment and is a function of the emissivity of the flame. ΔH_g denotes the heat of gasification of the condensed fuel and ΔH_c represents the heat of combustion per unit mass of oxygen. Here v_s denotes the oxygen-fuel mass stoichiometric ratio, $Y_{O_2,\infty}$ is the mass fraction of oxygen in ambient air, $c_{p,\infty}$ represents the specific heat of air at an ambient temperature of T_∞, and T_p equals the pyrolysis temperature of the fuel.

14

The parameter Q in Eq. (2) represents the normalized non-convective heat transfer at the surface, given by

$$Q = \frac{\dot{q}_{s,c}'' + \dot{q}_{s,r}'' - \dot{q}_{fl,r}''}{\dot{m}_f''},$$

(3)

where $\dot{m}_f''$ is the mass burning rate per unit area, $\dot{q}_{s,c}''$ represents the rate of conduction of energy into the solid per unit area, $\dot{q}_{s,r}''$ represents the rate of surface re-radiation of energy per unit area, and $\dot{q}_{fl,r}''$ denotes the radiative energy feedback from the flame to the surface per unit area. Thus, a large B-number basically implies a highly exothermic fuel relative to the heat required for gasification. The existing B-numbers have deficiencies for some fires because they do not involve external radiation and/or they assume the flame is transparent to thermal radiation. Recently, Jiang et al. [11] extended the concept of the B-number using a one-dimensional steady state diffusion flame model. An analytical expression of the B-number was derived which applies to semi-transparent flames with external radiation. In order to examine its physical significance, new parameters were defined and illustrated, such as the mass transfer equivalent absorption coefficient, specific radiant heat feedback and radiation factor, that demonstrate interactions of heat and mass transfer and radiative absorption and emission within inhomogeneous flames. Following this work, there is now potentially a method to fundamentally include radiation, which enhances the utility of the B-number, making it one of the most simple and effective means of expressing the

flammability of a condensed-phase fuel.

The logarithmic function of B in Eq. (1) is due to the stagnant film hypothesis and more exact functions of B than $\ln(1+B)$ can be derived in particular cases by solving the conservation equations with appropriate physical processes and boundary conditions. For example, Emmons [6] used the relationship between the shear stress at the fuel surface and the mass-burning rate [the first and third term in Eq. (1)] to analyze the film combustion of a flat fuel surface in a forced convective flow field. Following Chilton-Colburns relationship [4], Emmons [6] hypothesized that the shear stress at the surface of a combusting fuel must be proportional to the mass-burning rate. Emmons mathematically showed that if such a proportionality exists, the constant of proportionality is the B-number. In other words,

$$\dot{m}_f^{''} = B\frac{\tau_s}{U_\infty},\tag{4}$$

where, $\tau_s = \mu(\partial u/\partial y + \partial v/\partial x)_{y=0}$. If the value of B is known, Eq. (4) allows for the prediction of the mass burning rate when the gas-phase shear stress at the surface is known. This approach provides a conceptual convenience for modeling a phenomenon like fuel pyrolysis, since there is no need to explicitly account for the interaction between the gas and liquid phases. This relationship will be shown to work for non-deforming, non-charring fuels as well, as long as more complicated chemical-kinetic effects are neglected.

16

Based on Chilton-Colburns equation, a relationship between mass and heat transfer also exists. This relationship originates from the fact that processes in which material is transferred by diffusion are closely related to heat transfer, since the latter can be considered merely as the diffusion of hot molecules into a region of cold ones and a corresponding diffusion of cold molecules in the reverse direction. Since the mechanism is so similar, it would be expected that a relationship could be obtained for diffusional processes entirely analogous to that for heat transfer. The convective heat transfer coefficient at the surface of a flat fuel can then be expressed as,

$$h = \frac{k_w \left(\partial T / \partial y \right)_{y=0}}{T_{fl,ad} - T_{w,p}} = + \frac{k_w}{L} \left(\frac{\partial T^*}{\partial y^*} \right)_{y^*=0}, \tag{5}$$

where $T^* = (T - T_{w,p}/T_{fl,ad} - T_{w,p})$ represents the non-dimensional temperature, $T_{w,p}$ and $T_{fl,ad}$ represent the wall (taken as the pyrolysis temperature of the given fuel) and adiabatic flame temperature, respectively for a given fuel, L is a length scale representing the length of the region that is pyrolyzing or vaporizing and $y^* = (y/L)$ denotes the non-dimensional normal direction with reference to the surface that is issuing fuel vapor. This non-dimensional temperature gradient is therefore analogous to the Nusselt number. The definition of the non-dimensional temperature was chosen so that the boundary layer equations can be properly normalized. Also, defining T^* in the manner outlined above helps in making the relationship universally applicable over a wide range of fuels and geometry [12].

17

Using the first and second term in Eq. (1) and substituting for shear stress at the surface, τ_s, and convective heat transfer coefficient, h, one can derive the following expressions,

$$\frac{\dot{m}_f''}{B\nu^{2/3}} = \frac{k_w}{Lc_p\alpha^{2/3}}\left(\frac{\partial T^*}{\partial y^*}\right)_{y^*=0}, \tag{6}$$

$$\dot{m}_f'' = \frac{Bk_w}{c_pL}\left(\frac{\nu}{\alpha}\right)^{2/3}\left(\frac{\partial T^*}{\partial y^*}\right)_{y^*=0}, \tag{7}$$

which can be represented as,

$$\dot{m}_f'' = \frac{Bk_w}{c_pL}(\mathrm{Pr})^{2/3}\left(\frac{\partial T^*}{\partial y^*}\right)_{y^*=0}. \tag{8}$$

Eq. (8) represents the complete expression for the mass burning rate in terms of non-dimensional temperature gradients. Using Eq. (8), and the assumption of a unity Prandtl number near the fuel surface, one can obtain the following relationship between the mass-burning rate and the temperature gradient,

$$\dot{m}_f'' = \frac{C}{L}\left(\frac{\partial T^*}{\partial y^*}\right)_{y^*=0} = \frac{Bk_w}{c_pL}\left(\frac{\partial T^*}{\partial y^*}\right)_{y^*=0}, \tag{9}$$

where the proportionality constant C appearing in Eqn. (9) equals (Bk_w/c_p), where k_w is the thermal conductivity of the gas phase evaluated at the wall temperature and c_p is the mean specific heat measured at the adiabatic flame temperature of the given fuel. The term B that appears in Eq. (9) is a non-dimensional proportional-ity constant (defined earlier as the B-number) that relates the rate of mass transfer

18

(e.g., vaporization, combustion) to the rate of heat transfer, and is essentially the driving force for mass transfer. The Prandtl number, Pr, is assumed to be equal to unity, which also helps in selecting the transport properties at appropriate temperatures, shown later. The burning rate correlation proposed in Eq. (9) is based on a convective scheme. Radiation is neglected in formulating the above expression.

Conceptually, Eq. (9) states that the proportionality between the velocity gradient at the surface (momentum transfer) and the fuel vaporization rate in a chemically reacting boundary layer will extend to the temperature gradient as well. A similar analysis can be performed to demonstrate the proportionality between the fuel species and mass transfer using the assumption of a constant Schmidt number. For fire science, the utility of Eq. (9) is evident as it allows estimation of the local mass-burning rate by measurement of the temperature profiles along the fuel surface.

The burning rate correlation proposed in Eq. (9) has been tested and validated in this work for steady laminar boundary layer diffusion flames, established under both free and forced convective conditions, by using a validated numerical model and a dedicated experimental setup for such flames. First, this proportionality was tested by using a validated numerical model for a steady flame established over a condensed fuel surface, under free and forced convective conditions. Second, the relationship was tested by conducting experiments in a free and forced convective environment

using methanol and ethanol as liquid fuels and PMMA as a solid fuel.

The work presented here has also utilized experimental data of steady laminar flames established over vertical and horizontal condensed fuel surfaces in free and forced convective environments to separate the convective and radiative components of heat feedback to condensed fuel surfaces. Accurately determining the convective and radiative components of flame heat flux is important for the study of laminar burning fuels and future numerical validation. Although this study only approaches laminar wall fires, smaller in scale than realistic unwanted fires, the laminar wall fire is a canonical fire research problem and serves as an important first step for future development of the techniques and numerical models of fire spread. Detailed high resolution temperature measurements were taken both in the pyrolysis and plume regions of boundary layer diffusion flames using both liquid and solid fuels. Temperature profiles were measured by using fine-wire thermocouples and time-averaged fuel consumption rates were measured using a load cell. The convective heat feedback to the wall was then determined by utilizing the detailed temperature measurements near the wall. Total flame heat fluxes were also measured in the plume region of a free convective boundary layer diffusion flame using a standard water-cooled heat flux gauge. By comparing both of these measurements with local mass-loss data from our new technique, which utilizes local temperature gradients near the fuel surface

[13], convective, radiative and net heat flux components were extracted locally for this canonical fire research problem. This study therefore seeks to improve the accuracy and predictive capability of theoretical and numerical models while providing an experimental data set for local burning rates and various components of incident flame heat flux to the condensed fuel surface.

1.5. Organization of the Thesis

There are seven chapters in this thesis which are organized as follows:

The present chapter provides an overview of the features of boundary layer diffusion flames established over condensed fuel surfaces. The characteristics of boundary layer diffusion flames along with the problem statement is discussed. The effects of various parameters such as fuel type, convective conditions, angular orientation and fuel properties on the flame spread and burning processes are also briefly described.

In the second chapter, a comprehensive literature review on steady and transient flame spread processes under various environmental conditions is provided. The review includes theoretical studies, experimental as well as numerical investigations on flames established over condensed fuel surfaces.

The third chapter describes the experimental facility and set-up used for obtaining the experimental results along with detailed error and uncertainty analysis. Experimental set-ups for both free and forced flow experiments is also discussed along

with requisite hardware and instrumentation.

The fourth chapter describes the numerical models used for predicting steady burning over liquid fuel surfaces. A detailed discussion on all relevant boundary conditions, combustion chemistry, radiation sub-model, grid system, discretization procedure, solution methodology and the convergence criteria used to obtain the numerical solutions is discussed in this chapter. Detailed discussions on the flame structure, velocity profiles and mass burning rates are provided. Results for steady burning of a methanol film under natural convective conditions are also discussed in this chapter. Based on the numerical results, the theoretical correlation given in Eq. (9) is also tested and validated for steady laminar boundary layer diffusion flames.

The fifth chapter discusses the results from free convection boundary layer diffusion flames. Thermal and mass burning rate characteristics for free convection boundary layer diffusion flames is discussed along with local heat flux distribution in the pyrolysis and plume zone for Methanol, Ethanol and PMMA flames. Based on the experimental investigation, the theoretical correlation proposed earlier has been used for the estimation of local mass burning rates and flame heat fluxes over a laminar boundary layer diffusion flame. Convective and radiative heat feedback from the flames are also discussed both in the pyrolysis and plume regions by using temperature gradients near the wall.

The sixth chapter discusses the results from forced convection boundary layer diffusion flames. Effects of freestream conditions on local mass burning rates and heat flux profiles are discussed. The theoretical correlation proposed in Eq.(9) is also validated for different freestream conditions.

In the concluding chapter, the major conclusions from the present research work are highlighted. The limitations of the present theoretical model are discussed along with suggestions for further improvements in future work.

Chapter 2: Literature Survey

2. Literature Survey

Diffusion flames in laminar boundary layers have been widely studied mainly because of the importance of this problem in the study of fires, solid propellant burning and other applications of practical importance. This type of diffusion flame also presents a number of characteristics which permit fundamental studies on the mechanism of combustion for liquid fuels. In particular, mathematical modeling of these flames appear to be reasonably simple; temperature and velocity fields can be considered to be monodimensional in terms of the boundary layer coordinate; the length across the flame over which diffusion of species and chemical reactions occur can be sufficiently large to allow a precise spatial resolution of the flame; these flames are very stable and their characteristics can be kept constant for long times.

Over the years, a large body of literature involving theoretical, experimental and numerical studies has been published for steady burning as well as transient flame spread phenomena over the surfaces of condensed (solid and liquid) fuels. The literature survey presented in this chapter is broadly categorized into characteristics of steady flames and transient flame propagation over condensed fuel surfaces.

2.1. Study of Steady Flames over Condensed Fuel Surfaces

The physical nature of steady, laminar diffusion flames sustained over condensed fuel surfaces have been investigated by a number of researchers in the past. Burke and Schumann [14] were one of the earliest researchers to present a theoretical analysis of a general diffusion flame from homogeneous reactants. They solved for the flame zone in concentric duct burners with a gaseous fuel flowing in the core and air flowing in the annular regions. An infinite-rate chemical reaction approach to eliminate the highly non-linear reaction-rate terms from the energy and species conservation equations was employed. Spalding [15] addressed the problem of fuel pyrolysis due to energy transfer from the combustion zone. The modern era of studies on diffusion flames with application to fire safety began with the pioneering work on mathematical modeling of a steady flame subjected to forced air flow parallel to its surface which was carried out by Emmons [6]. A similarity solution of the classical reacting boundary layer problem under a zero-gravity environment was reported. In his analysis, Emmons established the foundation for theoretical modeling of boundary layer flames in many configurations. Using the boundary layer and flame sheet approximations he obtained explicit formulas for the mass burning rate in terms of the gas flow parameters and fuel properties. In the Emmons model, the primary modes of heat transfer considered were convection and conduction, neglecting radiation. Due

to the simplicity of the closed-form equation, Emmons classical solution was used widely and provided a starting point for both steady and flame propagation studies carried out subsequently by Kosdon et al. [16], Kim et al. [17], Pagni and Shih [2] and Annamalai and Sibulkin [18].

Kosdon et al. [16] investigated burning of vertical α-cellulose cylinders. A similarity theory for the natural-convection boundary layer adjacent to a vertical flat plate was developed for conditions of large temperature variations, wall mass transfer and boundary-layer combustion. The theory was then used to calculate the stand-off distance of the envelope flame that surrounded α-cellulose cylinders. Experimental measurements of the flame stand-off distance supported the similarity hypothesis used in the theory and were found to be in good agreement with the theoretical calculation. Kim et al. [17] examined physical processes that influence the burning characteristics of vertical, inclined and horizontal cylindrical fuel surfaces under a laminar regime. They developed a Pohlhausen solution applicable to the burning of vertically oriented surfaces, which was an improvement over the solution proposed earlier by Spalding [15]. The main conclusion drawn from these studies was that laminar burning rates are controlled by fuel, geometrical and chemical parameters. These studies showed that the geometric or fluid-mechanical effects were governed by the Grashof number, while the chemical effects were primarily controlled by the

mass-transfer number, B. In addition, it was found that the thermo-physical properties such as viscosity, thermal conductivity and specific heat, also play an important role in influencing the burning rates. Much later, Pagni [19] presented a review of various aspects of classical diffusion flames relevant to fire safety. He explored among others, problems involving forced, free, mixed, and stagnation point combusting boundary layers. In these analyses the flames were assumed to be steady and laminar, having infinite chemical reaction rates. Radiation effects were also neglected. Several research studies reported the usage of boundary layer assumptions to describe fire related parameters such as flame length [2], flame spread rate [18], and flame standoff distance [10]. Extensive reviews on the application of Emmons' model to predict laminar flame propagation on liquid and solid fuel surfaces are also found in the works of Sirignano [20] and Williams [21].

Pagni and Shih [2] proposed the concept of excess pyrolysate for the estimation of flame length over solid fuel surfaces. The basic concept was that the fuel burnt per unit area at the flame location is less than the gaseous fuel liberated per unit area [22]. Therefore, this excess fuel could be burnt in the excess flame region. A numerical analysis of this problem in free and forced convection environment was then presented [2]. Extending this work, theoretical analysis of upward burning over finite slabs and rods and in semi-infinite fuel beds was reported by Sibulkin and Kim [23].

A solution for the flame spread velocity as a function of heat flux to the fuel surface was provided for various fuel configurations. Approximate expressions were reported for the rate of fuel burning due to convective heat transfer. Later, Annamalai and Sibulkin [18] presented a theoretical analysis of flame spread over combustible solid surfaces for laminar, buoyant, forced convective as well as stagnation flow conditions using the concept of excess pyrolysate to obtain results for heat fluxes to the burnt and unburnt regions, which contributed to the flame spread rate. It was shown that the heat transfer from the plume to the virgin fuel surface played a key role in promoting rapid flame spread. Continuing their study, these authors investigated theoretically the effect of "excess fuel" on flame height and spread velocity. The flame height and heat flux results were combined to obtain a theoretical expression for the laminar flame spread over thermally thick solids.

Experimental studies followed analytical work, investigating various aspects of non-spreading, steady, boundary layer type diffusion flames. The structure of diffusion flames formed over horizontal fuel surfaces has been studied analytically and experimentally by a number of authors [24, 25]. One of the earliest experimental investigations on the aerodynamic structure and stability of diffusion flames stabilized over a fuel surface was reported by Hirano and co-authors [26, 27], where gaseous fuels were injected uniformly through a porous flat plate into a parallel air

stream. These experiments showed that the aerodynamic structure of the boundary layer is significantly different in the presence of a diffusion flame when compared to the boundary layer without a flame. Both velocity as well as temperature profiles were obtained at various locations along the plate surface for the above mentioned gaseous fuels. It was elucidated that pressure distortion on the air stream side of the flame zone is responsible for a velocity overshoot within the boundary layer. In their subsequent experimental studies, Hirano and Kinoshita [28] measured gas velocities and temperature profiles across a diffusion flame established over a liquid fuel surface with a free air stream parallel to the plate. Later, Andreussi and Petarca [29] carried out experiments similar to those by Hirano and Kinoshita [28] using ethyl alcohol as a fuel. Both authors studied the structure of the diffusion flame formed over a liquid surface with a parallel oxidizer flow experimentally, analytically or both. Later, Andreussi and co-authors [30] developed a theoretical model based on a Shvab-Zeldovich formulation of the problem. In a subsequent study, Andreotti and co-authors [31] completed the analysis of boundary layer diffusion flames with measurements of velocity profiles, fuel-burning rates and temperature profiles over a wide range of conditions for various liquid fuels. Gas velocity and temperature profiles were measured by Hirano and Kinoshita [28] whereas Andreussi and co-authors [30] measured the temperature, velocity and species concentration profiles across the

boundary layer diffusion flame. However, neither study measured the local temperature gradients at the surface of a condensed fuel and no attempt was made to measure the local fuel consumption rate. The role of buoyancy on chemically reacting boundary layer flows over a horizontal flat plate was later studied by Lavid and Berlad [32], Ahmad and Faeth [33] and Ahmad [34]. Ahmad [34] conducted a detailed investigation of fire induced plumes on upright surfaces in both laminar and turbulent regimes. For laminar plumes, an integral analysis was used to predict the mass burning rates and heat flux to the walls, whereas for turbulent plumes, more emphasis was given to the experimental results.

Many theoretical and experimental studies have been performed to understand the structure of a boundary layer diffusion flames over flat plates. One of the most characteristic features of the boundary layer diffusion flame is a velocity overshoot that occurs near the flame zone. In the formulation of the burning plate problem it is usually assumed that the pressure is constant across the boundary layer as well as in the flow direction, with negligible gravity effects. Under these assumptions, calculated velocity profiles are monotonic functions of distance from the wall. These, however contradict measurements by Hirano and co-workers [26, 27], which clearly indicate an overshoot of the velocity profile close to the flame zone.

Hirano et al. showed in their experimental studies that a favorable pressure

gradient, due to the local release of chemical energy in the flame zone created a positive local acceleration resulting in a velocity overshoot which could be observed, even far downstream. In a turbulent boundary layer diffusion flame, Ueda et al. [35] similarly observed a velocity overshoot in their experimental study. Through their theoretical analysis on the effect of buoyancy in a chemically reacting boundary layer flow, Lavid and Berlad [32] concluded that the buoyancy-induced body force acts to produce a streamwise pressure gradient in the fluid adjacent to the plate surface, responsible for the velocity overshoot near the flame zone. Ramachandra and Raghunandan [36] later suggested that the confined nature of flow was also responsible for inducing a favorable pressure gradient and consequent acceleration of the flow. Meanwhile, an experimental study by Andreotti et al. [31] showed that the velocity overshoot could only be observed for the case of a lower free stream velocity, not higher free stream velocities. Ha et al. [37] later studied the effect of burner geometry on separation of the flame at the leading edge at high freestream velocities (> 1 m/s). They found that in flow without separation, a positive local acceleration created distortion and an overshoot of velocity in the boundary layer. In the flow affected by separation, however, the effect of chemical heat release in the flame zone suppressed the tendency for flow separation. Therefore, lower mass fluxes of fuel (resulting in decreased rates of heat release) were not able to overcome the influence

31

of flow separation and a velocity overshoot region was not observed. For cases with increased mass fluxes of fuel, a favorable pressure gradient was formed such that a positive local acceleration resulted in a velocity overshoot downstream.

The effect of buoyancy on extinction limits and the flame shape of a laminar diffusion flame established over a horizontal flat plate has been reported by Torero et al. [38]. In their experiments, ethane was injected through a sintered bronze plate under microgravity conditions with a free stream velocity below 0.2 m/s.

Of all the experiments reported in literature, the experiments of Hirano and Kinnoshita [28], and Andreussi and Petarca [29] conform closest with the Emmons model. With the exception of the presence of normal gravity, all other conditions were the same. The results from these two experimental studies were shown to be qualitatively similar to the Emmons solution by both Andreussi [30] and Andreotti et al. [31].

Several experimental investigations on forced convection boundary layer flames over PMMA plates have also been reported. The practical motivation for studying combustion of PMMA rather than liquid or gaseous fuels ranges from interests in hybrid-rocket propulsion to problems of fire prevention. Because it is readily available, relatively uniform, well defined in composition, and is combustible under easily established laboratory conditions, PMMA has been studied more thoroughly

32

than any other polymer, from the viewpoint of its processes of degradation and combustion. Also, PMMA burns relatively clean and does not form char making it easier to model for research purposes. Krishnamurthy and Williams [39] investigated forced convective boundary layer flames over a PMMA plate. In this study, the entire PMMA surface was ignited at once so that a steady flame could be obtained. Regression rates were reported for different concentrations of oxygen in the bulk flow. It was shown that a square root relationship existed between the measured regression rate of the PMMA surface and the distance from the leading edge of the flame. Among the investigations carried out later, the work of Mekki et al. [40], Zhou and Fernandez-Pello [41], Agrawal and Atreya [42] and Agrawal [43] are notable. Mekki et al. [40] conducted experiments on wind-aided flame spread underneath a PMMA plate, which was fixed to the ceiling of a rectangular channel. They found that the total species production rate increased linearly with the length of the pyrolysis zone, contrary to the square root relationship predicted by the Emmons theory. Agrawal and Atreya [42] generalized Emmons solution by combining it with a one-dimensional theory for the transient heat up and pyrolysis of a PMMA plate. Agrawal and Atreya [42] showed qualitative agreement between their theory and the measurements of Mekki et al [40].

Zhou and Fernandez-Pello [41] conducted experiments on concurrent flame spread

over a long PMMA plate fixed to the floor of a rectangular channel. Local regression rate distributions were reported for experiments carried out both with and without externally imposed grid-generated turbulence on the bulk flow. The dimensionless regression rates were found to be proportional to $Re^{1/2}$ for laminar flow, in qualitative agreement with Emmons solution at large distances from the leading edge. Similar experiments were reported by Agrawal [43], where concurrent flame spread beneath a horizontal PMMA plate fixed to the ceiling of a rectangular channel was considered. The theory proposed by Agrawal and Atreya [42] for unsteady heat conduction into the solid was used along with the experimental regression rates, to arrive at the surface heat flux. Experiments on laminar flame propagation on a flat solid fuel (PMMA) surface in a predominantly forced flow environment under microgravity have also been reported by Vietoris et al. [44]. Ananth et al. [45] reported experimental as well as numerical results for burning rates of PMMA plates, over which a non-spreading boundary layer flame under forced convection was formed. Comparison of numerical and experimental burning rates with the classical Emmons solution were presented. The temperature profiles across the diffusion flame were shown to be in good agreement with the experimental data for the entire length of the PMMA plate. Later, using the same experimental setup used by Ananth et al. [45], Ndubizu et al. [46] investigated transient burning of PMMA surfaces under

34

forced convective conditions. Time- averaged regression rates and gas-phase temperatures were measured in tests conducted at various burn times. The results showed that the surface regression-rate was transient and that it decreased significantly in the leading section and increased slowly downstream. It was shown that the local burning rate was dependent on the location on the surface, convective flow conditions as well as the burning time of the sample.

Theoretical investigation of burning vertically-oriented solid surfaces can be found in the works of Kosdon et al. [16], Kim et al. [17], Pagni and Shih [2], Annamalai and Sibulkin [18]. Theoretical and experimental studies on flame spread on vertically oriented PMMA slabs have also been reported by Rangwala et al. [47, 48].

Similar to the experimental studies discussed above, there are several numerical studies reported in literature. Ramachandra and Raghunandan [49] performed a numerical analysis of the aerodynamic structure of a two-dimensional laminar boundary diffusion flame over a porous flat plate in a confined flow. The governing equations of aerothermochemistry with the appropriate boundary conditions were solved using the Patankar-Spalding method. Their analysis predicted flame shapes, profiles of temperature, concentrations of various species and the density of the mixture across the boundary layer. In addition, they predicted the pressure gradient in the flow direction arising from the confinement of the flow and the subsequent velocity over-

shoot near the flame surface. Chen and Tien [50] were the first to numerically study flame stabilization and blow-off of a laminar diffusion flame established on a vertically oriented solid fuel surface under forced convective conditions. The flame structure of the envelope and the open-tip flames were reported. The model involved solution of steady, two dimensional Navier-Stokes momentum, energy and species equations with a one-step overall chemical reaction and second-order finite rate Arrhenius kinetics. Radiation heat transfer was neglected in their analysis. Non-dimensional parameters were identified and the effect of Damkohler number on the stability of the diffusion flame in a forced convective flow field was discussed. For large Damkohler numbers, envelope flames were found to exist where the computed fuel evaporation rate, the flame stand-off distance and the velocity profiles showed certain similitude. However, for low Damkohler numbers, a transition to an open tip flame was found to take place where the flame became stabilized on the sides of the fuel plate.

Kodama et al. [51] studied the process of extinction and stabilization of a diffusion flame over a flat combustible surface in a mixed convective, oxidizing, gas flow parallel to the fuel surface. The authors solved the elliptic set of Navier-Stokes equations, including finite rate chemical kinetics, to establish flame stability criteria around the leading edge of the fuel surface as a function of velocity and oxygen concentration of the oxidizer flow. Their interfacial boundary conditions were sim-

ilar to those employed by Chen and Tien [50]. Two representative fuels, n-heptane (liquid) and PMMA (solid) were used. They also neglected the effect of radiation heat transfer. Rouvreau et al. [52] developed a two-dimensional numerical model to study a configuration similar to the experimental setup employed by Torero et al. [38]. The majority of these numerical models assumed negligible thermal radiation transfer and employed averaged values of thermo-physical properties in their models. In addition, the main focus of these studies has been to determine a stability criterion, namely, a convective condition up to which a stable flame would be anchored around the leading edge of the flat plate.

More recently, Raghavan et al. [53] investigated the range of Reynolds number where the classical Emmons solution is valid by carrying out parametric studies for unconfined flames, neglecting the effect of gravity. Their numerical model included global single-step finite rate chemistry without dissociation of product species, and an optically thin radiation sub-model. Their study showed that the Emmons solution is valid in a range of Reynolds number where the flame anchors near the leading edge of a methanol pool and the combustion is confined around the hydrodynamic and thermal boundary layers. Emmons' solution was found to deviate for low flow velocities. Ali et al. [54] later performed a numerical study of a steady laminar diffusion flame over a methanol pool surface, under the influence of forced air flow parallel

37

to the pool surface. The model involved the solution of transient, two-dimensional mass, momentum, species and energy conservation equations to predict flame characteristics. An optically thin radiation model was incorporated to account for thermal radiation losses by absorbing species in a non-luminous flame. The influence of free-stream air velocity on fuel mass burning rate, flame stand-off distance, temperature and flow fields were reported. The authors also performed numerical calculations for the combined effects of angular orientation and surface temperature on flame heat transfer characteristics in the overfire region [55]. Their study showed that irrespective of the orientation angle, the lower the wall temperature, the higher will be the local heat flux parameter at any location on the wall.

2.2. Transient Flame Propagation over Condensed Fuel Surfaces

Many fire-spread situations involve a succession of several basic burning processes. First, heat from the hot flame is transferred to the unburned fuel bed (see Fig. 2.1) [56]. When an unburned fuel-surface element becomes sufficiently hot, additional heat vaporizes it. The resulting gaseous fuel reacts upon coming into contact with the oxygen supplied by the air flowing into the flame zone. Some of the released chemical energy is transferred to the unburned fuel bed, thus completing the energy

cycle necessary to maintain the fire-spread process. For the flame to spread, enough heat must be transferred from the flame to the unburnt material ahead of the flame to pyrolyse the solid. The rate of flame spread is therefore determined by the ability of the flame to transfer the necessary heat to pyrolyse the solid and ignite the combustible mixture ahead of it. Each of the above processes takes place by a variety of physical mechanisms depending upon the particular fire-spread configuration being considered.
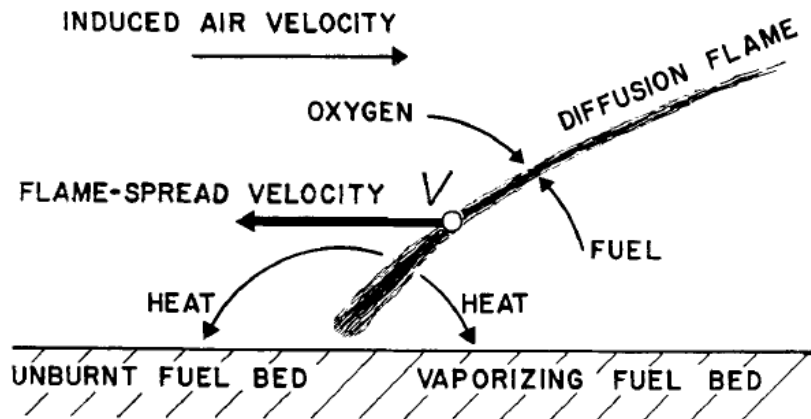
Figure 2.1: Physical description of a flame spreading over a stationary fuel bed [56].

The heat transfer from the flame to the unburnt combustible ahead is strongly dependent on the shape of the flame, which in turn is dependent on the characteristics of the ambient gas flow. When the ambient flow, either naturally induced or forced, opposes the direction of spread, the flow keeps the flame close to the surface downstream of the pyrolysis front, deterring heat transfer ahead of the flame. This

type of spread is commonly known as opposed flow flame spread and is generally slow. In natural convection, it occurs in downward or horizontal flame spread. If the ambient flow is in the direction of spread, the flame is pushed forward ahead of the pyrolysis region, which favors the transfer of heat from the flame to the unburnt material, and results in a spread process that is generally fast. This mode of spread is known as concurrent or wind-aided flame spread, and occurs during the upward spread of flames in natural convection or in forced flows moving in the direction of flame propagation.

This section presents a variety of configurations in which a flame can propagate over a condensed fuel surface.

2.2.1. Effect of Convective Conditions

2.2.1.1 Concurrent flow flame spread

In the concurrent mode of flame spread, the flame covers the solid element during the heating and pyrolysis processes, and when the pyrolysed fuel leaves the surface, it is rapidly ignited by the flame. Thus, in this case, the ignition process can be viewed as a strong piloted ignition or one with an ambient gas at very high temperatures, and that is consequently controlled by the solid's heating and pyrolysis.

A detailed theoretical analysis for concurrent modes of flame propagation over

solid fuels was presented by Fernandez-Pello and Mao [57]. Laminar boundary layer and flame sheet approximations were used. A similarity solution was adopted for the gas and solid phases. Since the gas-phase transport processes are much faster than that of the solid phase, the problem was assumed to be quasi-steady and was described using the steady state reacting boundary- layer equations. The main observations were: (1) the faster the growth of the boundary layer, the slower the flame spread rate would be, (2) if the boundary layer thickness is constant, then the spread rate will increase exponentially with time, (3) for forced-flow conditions, the spread rate will remain constant, (4) for free-convective conditions, the spread rate will increase with time and (5) for mixed convective conditions, the spread rate will decelerate with time. The length of heated region downstream the pyrolysis zone and the thickness of boundary layer (proportional to the flame stand-off distance) were identified as the main contributors to the spread rate and were used to explain the observed behavior for each configuration.

Suzuki and Hirano [58], based on their detailed experimental investigations, explained the mechanism of flame propagation over methanol pool surfaces in super flash (liquid temperature higher than its flash point) and near flash regimes, under concurrent as well as opposed flow conditions. These experiments brought to light the following observations on concurrent flame spread. First, the flame spread veloc-

ity remains constant until the free-stream velocity is less than the spread velocity. Second, once the free stream velocity exceeds the flame propagation velocity, the flame propagates almost at the same velocity as the free stream. Finally, the behavior of hot gas just ahead of the leading edge of the flame and heat transfer from this gas to the pool is the key phenomena affecting the spread rate.

Flame spread in natural convection is particularly important in the fire safety field because most fires are driven by free or mixed convection flows. For this reason, a large number of flame spread investigations have been conducted in natural convection configurations. Upward flame spread is perhaps the most important mode of flame spread in fire safety because it is often present during the development of a fire and is rapid and hazardous. Considerable work has been conducted in this area in the past, among which notable are the reviews of Fernandez-Pello and Hirano [59] and Fernandez-Pello [60]. This type of flame spread is basically the same as concurrent forced flow flame spread except that, since the flow is naturally induced by the flame, the flow parameters are from natural convection. In this case, natural convection heat transfer will be dominant initially, but as the flame progresses and the size of the flame increases, the flame will become turbulent and radiative heat transfer will start to become dominant. As the flame becomes more turbulent and radiation dominated, the flame spread rate is found to increasingly accelerate, in

quantitative agreement with experimental measurements [61, 62, 63]. Experimental observations of Annamalai and Sibulkin [18] suggest that the spread rate is also acceleratory under laminar flow conditions. This is because the increase in the flame stand-off distance at increasing heights, which would decrease flame spread rates is sufficiently counteracted by increasing flame lengths (Mao and Fernandez-Pello [57]), whose increased heating rate cause acceleratory flame spread.

2.2.1.2 Opposed flow flame spread

One of the first numerical studies to examine the influence of forced opposed air flow conditions on flame spread over n-propanol pools was presented by Schiller and Sirignano [64]. The mathematical formulation was similar to the earlier numerical model by Schiller et al. [65]. Parametric studies were presented with respect to free stream air velocity, fuel temperature and inclusion of gravity induced flow. Differences in flame propagation at normal as well as zero gravity conditions were discussed in detail. Similar numerical studies were also reported later by Kim et al. [66] on axisymmetric flame propagation over propanol pools in quiescent (no flow) conditions under both normal and zero gravity. Experimental studies on flame spread across n-butanol with very low-speed opposed or concurrent airflow in normal and microgravity environment have been reported by Ross and Miller [67]. The differences in

flame spread behavior under these conditions were brought out clearly. These findings corroborated the computational observations of Schiller et al. [65] and Schiller and Sirignano [64] for the opposed flow configuration. Kim and Sirignano (2003) extended the earlier study of Schiller and Sirignano [64] to investigate the influence of initial fuel temperature and pool depth on flame spread characteristics. Parametric studies were conducted with respect to different opposed free stream velocities, pool depths, gravity effects and initial pool temperatures. Based on this, the regions of uniform and pulsating flame spread were mapped. A more comprehensive, three-dimensional numerical model was developed by Cai et al. [68], which employed a second order time accurate numerical scheme and an adaptive grid that significantly improved the computational efficiency and accuracy. This model was used to investigate the flame spread process in a wind tunnel with a closed top, simulating the experimental study by Ross and Miller [67]. This study considered a specific pool dimension and an opposed air flow velocity. Continuing with this study, Cai et al. [68] extended the investigations on the effects of above-mentioned parameters in detail.

A numerical model for opposed flame spread on a thermally thin fuel was employed by Borgeson and T'ien [69] to study the effect of initial bulk fuel temperature on the extinction limit. This study provided insight into the mechanisms of flame

extinction. A qualitative comparison of the flame spread rates and extinction with experimental data was reported. In the case of opposed flame propagation over solid fuel surfaces, the rate of flame spread is controlled by heat transfer to the unburnt fuel as well as by the rate of gas-phase chemical reaction. This was discussed in detail by Fernandez-Pello et al. [57]. The gas-phase velocity field influences both of these processes. Many studies consider the velocity profile to be specified, thus eliminating the need to solve the momentum equations. The uniform velocity profile is the most common one that is used in such studies, as reported by de Ris [56], Frey and T'ien [70], Wichman et al. [71] and Di Blasi et al. [72]. Other velocity profiles, such as a constant velocity gradient (Wichman et al. [71]) and parabolic (di Blasi et al., [72, 73]), have also been used. Subsequent studies conducted by di Blasi et al. [74] to elucidate the effect of gas-phase velocity profiles on the opposed flame spread over thick solid fuel surface considered both Oseen as well as Hagen-Poiseuilli profiles. It was shown that the spread rates obtained by assuming these profiles were in qualitative agreement with experimental results. The importance of selecting the appropriate velocity profile in the gas-phase was shown to be important in case of opposed flame propagation on solid fuel surfaces.

A two-dimensional numerical model was developed by Kumar et al. [75] for investigation of opposed as well as concurrent flame spread over thin solids. A

comparison between the two modes was brought out in detail. It was found that the spread rate in concurrent mode increases linearly with free stream velocity, whereas for opposed flame propagation, the variation is non-monotonic and a peak spread rate occurs at an intermediate free stream velocity. This model was employed to elucidate the effect of entrance length and explain the non-burnout phenomena (some solid fuel in the downstream region being left unconsumed) in opposed flame spread. Later, Kumar and Kumar [76] investigated the effect of burning onto the side edges of a thin strip of solid on the spread rate. Numerical studies were performed with and without considering the burning of the side edge to elucidate the differences involved. Inhibition of side burning under various gravity levels was also discussed by these authors.

Numerous experimental studies have also appeared in literature on the opposed/downward flame spread over thin fuel surfaces. Notable among these, are the works of Frey and T'ien [70], Hirano and Saito [77] and Olson [78]. In these experimental studies, the edges of the sample specimen are prevented from burning by chemical treatment or by using a metallic strip, so as to achieve a flat pyrolysis front. Creeden and Sibulkin [79] performed experiments on PMMA plates with one edge inhibited from burning and compared their results with those obtained from a similar experimental configuration in which both edges were inhibited. Three-dimensional numerical sim-

46

ulations as well as experimental results for small specimens were reported by Mell and Kashiwagi [80] and Mell et al. [81].

2.2.2. Effect of Surface Orientation

There have been several studies on flame spread and burning rates on horizontal and vertical surfaces, but very few studies seem to have considered steady burning and flame spread on inclined surfaces. One of the earliest studies on inclined surfaces was conducted by Hirano et al. (1974), who postulated flame spread mechanisms on inclined solid fuel sheets. Other notable works carried out earlier include the work of Sibulkin et al. [82] and Pello and Williams [83]. Results from the above studies confirmed that the flame spread rate increases when a vertical induced-flow component exists. Kashiwagi and Newman [84] reported experimental measurements on downward flame spread over thin cellulose sheets (1 mm thick) in a gravity opposed flame spread configuration. Their investigation also considered the effect of external radiation on the flame spread rates on an inclined specimen. Analytical expressions for flame spread rates were developed. Much later, flame spread experiments on PMMA slabs were reported by Ito and Kashiwagi [85], who elucidated the effect of heat transfer as a function of angular orientation using holographic interferometry to measure the temperature gradients within the PMMA slabs. This technique, though novel and elegant, restricted the slab width used for the experiments to about 25

mm. Further, only positive orientation angles of 10°, 30° and 90° were considered.

Later, Drysdale [86] reported preliminary experimental results on the burning of 0.18 mm thick computer cards, representing thin fuels, and 6 mm thick PMMA plaques, representative of thermally thick samples. Orientation angles in the range from 0° to +90° were considered. The difference in flame spread mechanisms over thick and thin fuel beds were elucidated. For thin fuels, the flame propagates on both sides and the rate of spread was shown to increase monotonically as the orientation angle was increased from 0° (horizontal) to 30°. However, for thick PMMA slabs, the rate of spread was governed by heat transport to the unheated portion and remained fairly constant for small inclination angles, up to approximately 20° in their experiments. With further increases in inclination, a more or less monotonic increase was observed with angle.

Quintiere [87] also investigated the effect of angular orientation on flame spread over a thin fuel surface. His experiments were conducted on two materials; the first was representative of aircraft thermal-acoustical films and the second was a paper towel (napkin). These were tested for upward and downward flame propagation over the entire orientation angles ranging from -90° $\leq \theta \leq$ +90°. A theoretical analysis was also presented, where heat transfer to the material ahead of the pyrolysis front and the ignition of this portion were considered as important processes that control

flame spread. In the theoretical work, to elucidate forward heating in a gravity-assisted configuration, results from the work of Ahmed [34] were extensively used. For gravity opposed conditions, the works of Kashiwagi [84] and de Ris [56] were referenced. Analytical relations were presented for flame length and correlations were proposed for burning rates in terms of the pyrolysis length of the solid fuel and surface orientation for laminar as well as turbulent burning.

Ali et al. [54] studied laminar diffusion flames established over a condensed fuel surface, inclined at several angular orientations. Based on the numerical results, a theoretical correlation was proposed to predict the mass burning rate as a function of fuel surface orientation. Later, the same authors [55] carried out numerical analysis of flame heating on arbitrarily oriented condensed fuel surfaces. They concluded that irrespective of the orientation angle, the lower the wall temperature, the higher the local heat flux parameter will be at any location on the wall. Later, Gollner et al. [88] used a thermally thick slab of PMMA to study the effects of inclination angle on upward flame spread. By performing experiments on 10 cm wide by 20 cm tall fuel samples, the authors reported that the maximum flame-spread rate configuration did not correspond to the maximum fuel mass-loss rate configuration, the former being close to a vertical-wall configuration and the latter to a horizontal pool-like orientation. Zhang et al. [89] also studied burning on flat plates at various angular

orientations with respect to gravity. It was observed that the onset of unsteady flow and transition to turbulence commenced at Grashof numbers of $10^6 - 10^7$, which increased with decreasing angle (towards underside burning). The average burning rate per unit area was also calculated for various angular orientations with respect to gravity.

2.3. Heat Flux Measurements for Laminar and Turbulent Boundary Layer Flames

Experimental studies have also been performed to evaluate the contribution of one or more surface energy flux components to the burning rate. Ahmad [34] and Ahmad and Faeth [33] studied the heat transfer characteristics and structure of laminar and turbulent fire-induced plumes along upright surfaces. In the case of a laminar fire plume, a numerical solution of the boundary layer equations was formulated for an upright burning surface under natural convection conditions. The wall heat flux and the flame shapes were measured for laminar wall fires using a variety of liquid fuel-soaked wicks. Predicted wall heat fluxes and flame shapes were in good agreement with measurements. In the case of a turbulent fire plume, formed by tripping the flow at the base of a burning fuel, measurements were made of burning rates, radiative and convective heat fluxes to the wall, and profiles of temperatures, concentrations

and mean velocities. An integral model was developed for the turbulent pyrolysis and the overfire combustion region. Burning rates and heat fluxes predicted by the integral model agreed with the measurements reasonably well. It was found that for both the laminar and turbulent fire plume the radiative contribution to the wall heat flux was at most 10-20% of the wall heat flux, owing to the small size of samples tested.

In their pioneering work, Orloff et al. [90] performed a detailed heat transfer analysis using 1.57 m high, 0.41 m wide, and 4.5 cm thick vertical slabs of transparent PMMA. They measured the burning rate and total outward radiation (flame plus surface re-radiation) at different heights along the slab, attributing the significant increase of the steady burning rate with height to increasing flame radiation. Reradiant heat loss from the fuel surface with height was deduced from that measured at midheight by means of a thermopile radiometer, relating the MLR to the surface temperature by a zeroth-order Arrhenius expression and a unit surface emissivity. Despite the large sample size, the Arrhenius correction induced only small variations of reradiant heat flux, no more than $\pm 7\%$. The convective heat flux was inferred from the steady surface energy balance equation for an infinitely thick slab and subsequently the total flame heat flux. A slight decrease of the convective flux with height was observed. Orloff et al. [3] later conducted a similar study on larger

samples, 3.56 m high, 0.914 m wide, and 6.4 cm thick. Unlike previously, the convective heat flux was assumed to be constant and equal to that measured in previous study [90] at midheight, which allowed the calculation of the radiant heat feedback. The findings reinforced the conclusions drawn from the earlier study [90]: for large-scale vertical surfaces, flame radiation is the dominant mode of energy transfer to the fuel surface and therefore dominates the local burning rates, and these rates increase with height. Quinterie et al. [91] measured the inward flame heat flux above the burning sections of six materials, including PMMA. Combustion was sustained with the assistance of varying external radiation, which led to some variations in the flame heat flux. Kulkarni and Kim [92] later estimated heat conduction into the solid from temperature measurements in the interiors of vertical, fully burning slabs of clear and black PMMA. They observed substantial unsteadiness in the early stage of combustion. Afterward, when conduction heat loss into the interior reached a plateau, the thermally thick slab assumption was found to be in good agreement with experimental results.

Kulkarni et al. [92] and Brehob and Kulkarni [93] measured the total heat feedback from the flame for clear and black vertically oriented 120 cm high and 30 cm wide PMMA walls with external radiation. On a larger scale, Wu and Tewarson [94] conducted experiments on 5 m high, 0.6 m wide and 2.54 cm thick vertical PMMA

samples. For such large samples, they measured total heat fluxes from the flame to the slab surface of up to 40 kW/m^2. Beaulieu and Dembsey [95] quantified the effect of enhanced ambient oxygen concentration on the flame heat flux for 9 cm high black PMMA slabs. Both vertical and horizontal configurations were studied. For the vertical configuration, a total flame heat flux of 33±3 kW/m^2 in the pyrolysis zone at an ambient oxygen concentration was reported.

Tsai and Wan [96] developed specific experiments to determine the influence of sidewalls on the width effect of wall fires during the flame spread process and, particularly, on the total and radiative heat fluxes from the flame. 6 and 20 mm thick clear PMMA samples were used, with a height of 1 m and widths from 10-90 cm. They found that width effects were slight in terms of the total heat flux distribution and that radiant heat fluxes measured were lower than those reported in previous studies. They estimated the total heat flux to be in the range of 23.5 to 30.2 kW/m^2 using 100 cm high and 2 cm thick slabs of clear PMMA with widths ranging from 10-70 cm. Tsai later [97] conducted similar experiments with and without sidewalls for 1 m tall and 9 mm thick clear PMMA samples, with widths ranging from 10-70 cm. He determined the total heat flux from the flame to the surface and confirmed that the heat flux to the fuel did not vary much with the fuel width.

More recently, Gollner et al. [88] studied the effects of the inclination angle of

a fuel surface on the upward flame spread on 10 cm wide, 20 cm high, and 1.27 cm thick sheets of PMMA. Total heat fluxes were measured using an array of 11 thin-skin calorimeters mounted above the centerline of the sample. A more recent work by Pizzo and co-authors [98], in which they studied both the steady and transient burning of thick clear PMMA slabs, suggest total heat flux from the flame to be in the range of 30.9-23.4 kW/m^2 as the sample height increases from 2.5 to 20 cm. The values reported for total heat flux seem to be in relatively good agreement with the values obtained in our study.

The analysis of reported literature data shows the difficulty of determining and differentiating the heat flux components at the surface of burning slabs of PMMA. Moreover, a wide scattering of data is observed, which can be attributed to a number of reasons, such as heat flux scalability, variability in PMMA composition and thus in thermophysical properties, achievement of steady state conditions and heat flux gauge technology and implementation. One of the main objectives of the present study is to estimate the various components of flame heat flux by using a new methodology that is based on the estimation of the local mass burning rates and temperature gradients at the fuel surface.

2.4. Motivation

From the above literature review, numerous gaps in current knowledge can be found which motivate the present work.

Several experimental studies have reported gas-phase velocity and temperature profiles of diffusion flames established over liquid fuels. However, from these experiments, little information is available on the local and average burning rates under forced and natural convective conditions. A number of studies have also reported temperature profiles in the boundary layer of a diffusion flame for both liquid and solid fuels. However, no attempt has been made to measure the local mass burning rate and the non-dimensional temperature gradient at the surface.

The analysis of reported literature data shows the difficulty of determining local heat transfer, combustion and friction coefficients at the condensed fuel surface, which are important for understanding the physics and the underlying mechanisms that drive a particular fire and its spread. Differentiating the heat flux components at the surface of condensed fuel surfaces is also observed to be similarly challenging. Moreover, a wide scattering of data is observed, which can be attributed to a number of reasons, such as heat flux scalability, variability in the composition of the condensed fuel surface and thus in thermophysical properties, achievement of steady state conditions and heat flux gauge technology and implementation.

The above summary points out several directions for further research. The present study aims to carry out research which will begin to address these gaps.

Chapter 3: Experimental Facility and Instrumentation

3. Experimental Facility and Instrumentation

In order to study free and forced convection boundary-layer diffusion flames two different experimental setups were designed and constructed. In addition to relevant components of the apparatus, this chapter will discuss the overall experimental procedure and the evaluation of measured quantities. This chapter will also discuss the uncertainties associated with measurements.

3.1. Experimental Setup for Free Convection Flames

An experimental setup was constructed to enable simultaneous measurements of average mass-loss rates and local temperature profiles in a boundary-layer diffusion flame established over a condensed fuel surface. Two U-shaped aluminum brackets were connected to an aluminum sheet and mounted vertically atop a load cell. A sheet of ceramic fiber insulation board 1.27 cm thick, with a section 12.7 cm from the base of the sheet cut out for holding the fuel sample, was mounted atop the aluminum sheet. The front surface of the insulation wall was coated with a black radiation absorbing paint having an absorbptivity of approximately 98%.

Figure 3.1: Schematic diagram of the experimental setup in a vertical configuration. The black dots above the wick represent the holes drilled for wall heat flux measurements by a water-cooled heat flux gauge.

The liquid fuel wick was an 8 cm × 8 cm × 1.27 cm thick sheet of porous noncombustible material (Alkaline earth silicate wool). In order to eliminate leakage of the liquid fuel from the sides, sodium silicate was applied to all interfaces of the wick except the top face. Burning was limited to the front surface of the wick by shielding the remaining sides with aluminum foil. During testing, the wick was soaked with liquid fuel up to its point of saturation so that it gave a stable boundary-layer diffusion flame for the longest time duration possible (enough to take precise

58

temperature measurements). The fuel wick was soaked with approximately 90 ml of liquid fuel for each test. In case of a solid fuel, an 8 cm × 8 cm × 1.27 cm thick sheet of PMMA was used. Figure 3.1 shows a schematic diagram of the experimental setup for studying free-convection diffusion flames in a vertical configuration. Figure 3.2 shows the picture of a clear cast PMMA slab (measuring 8 cm × 8 cm × 1.27 cm).
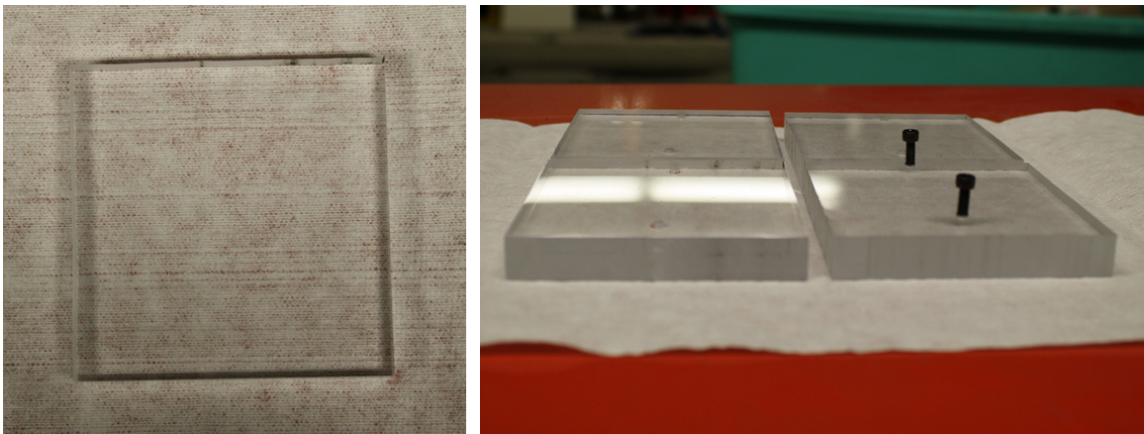
Figure 3.2: Photograph of a clear cast PMMA slab used for free-convection experiments.

3.2. Experimental Setup for Forced Convection Flames

In order to carry out forced flow experiments, a laboratory-scale wind tunnel was designed and developed at the UMD Fire Lab. The design for the laboratory-scale wind tunnel was accomplished in Catia and ANSA and detailed numerical simulations were carried out in Fluent in order to characterize the flow field inside

the wind tunnel. The wind tunnel has a $100 \times 75 \times 100$ cm plenum at one end into which an Ebm papst (G3G250-MW72-01) variable speed blower pressurizes the air. This pressure buildup in the plenum drives the flow of the air through the wind tunnel; hence, the effects of the blower on the flow are minimized. A 30.48 cm converging section connects the plenum to the 122 cm straight section, which has a 30.48×30.48 cm cross-section. A set of fine screens are placed at the entrance and exit of the converging section and a combination of turbulence reduction screens and 5 cm thick honeycomb with 0.3 cm diameter holes, is inserted 110 cm upstream from the tunnel exit to smooth the flow. The flow velocity in the wind tunnel is selected by adjusting the speed of the blower with the help of a pulse-width-modulation (PWM) controller. Figure 3.3 shows the laboratory scale wind tunnel in the UMD Fire Lab along with numerical simulation results (using Fluent) for the flow-field inside the wind tunnel. Figure 3.4 shows various components of the laboratory-scale wind tunnel with dimensions.

Figure 3.5 shows the schematic of the experimental set-up, the key components of which include the wind tunnel, the fuel wick holder, and thermocouples mounted on a set of Velmex X-Y unislides. The fuel soaked wick or solid fuel was positioned outside the wind tunnel, at the center of the tunnel exit. This makes it easier for the thermocouples to be moved freely in and out of the flame to measure gas-phase

temperatures. The sample holder sits on a load cell and consists of two U-shaped aluminum brackets that were connected to an aluminum sheet (measuring 30.48 × 60.96 cm and 1.5 mm thick) and mounted vertically atop a load cell. A sheet of ceramic fiber insulation board 1.27 cm thick, with a section 2 cm from the base of the sheet cut out for holding the fuel sample, was mounted atop the aluminum sheet.
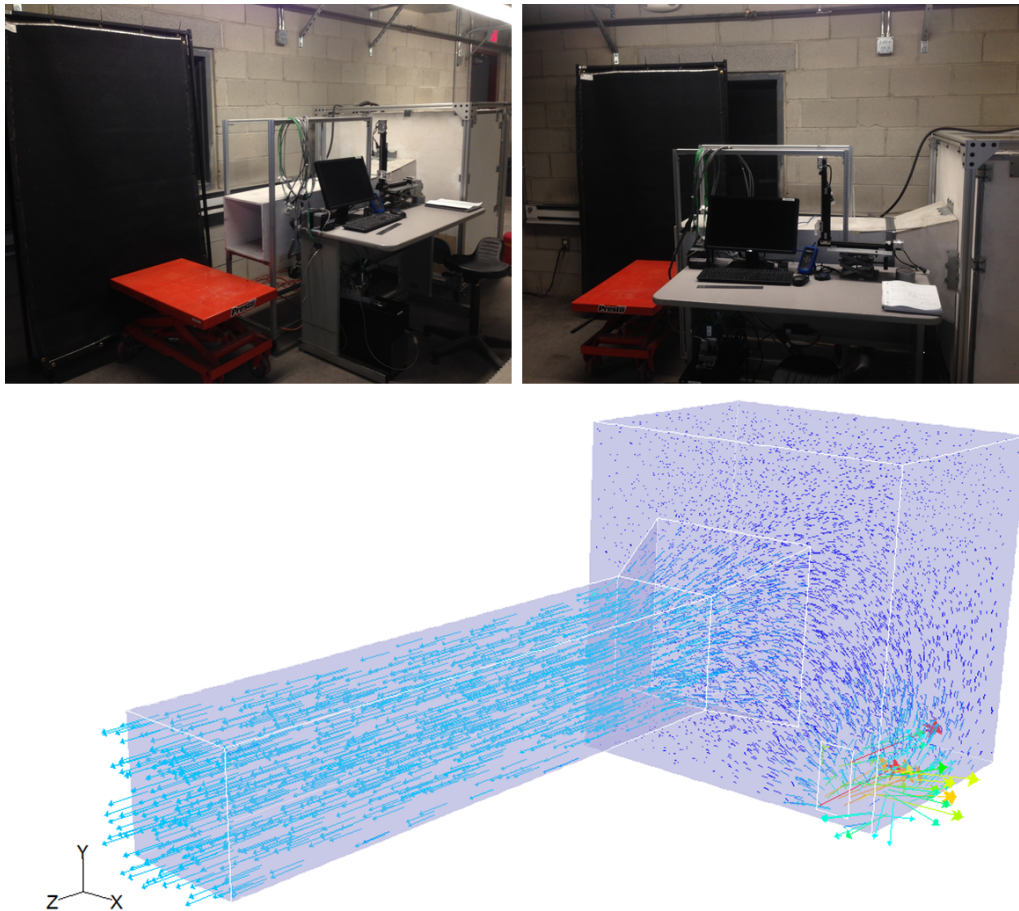
Figure 3.3: Laboratory-scale wind tunnel at the UMD Fire Lab (top) along with Fluent simulation results depicting the flow-field inside the wind tunnel (bottom).
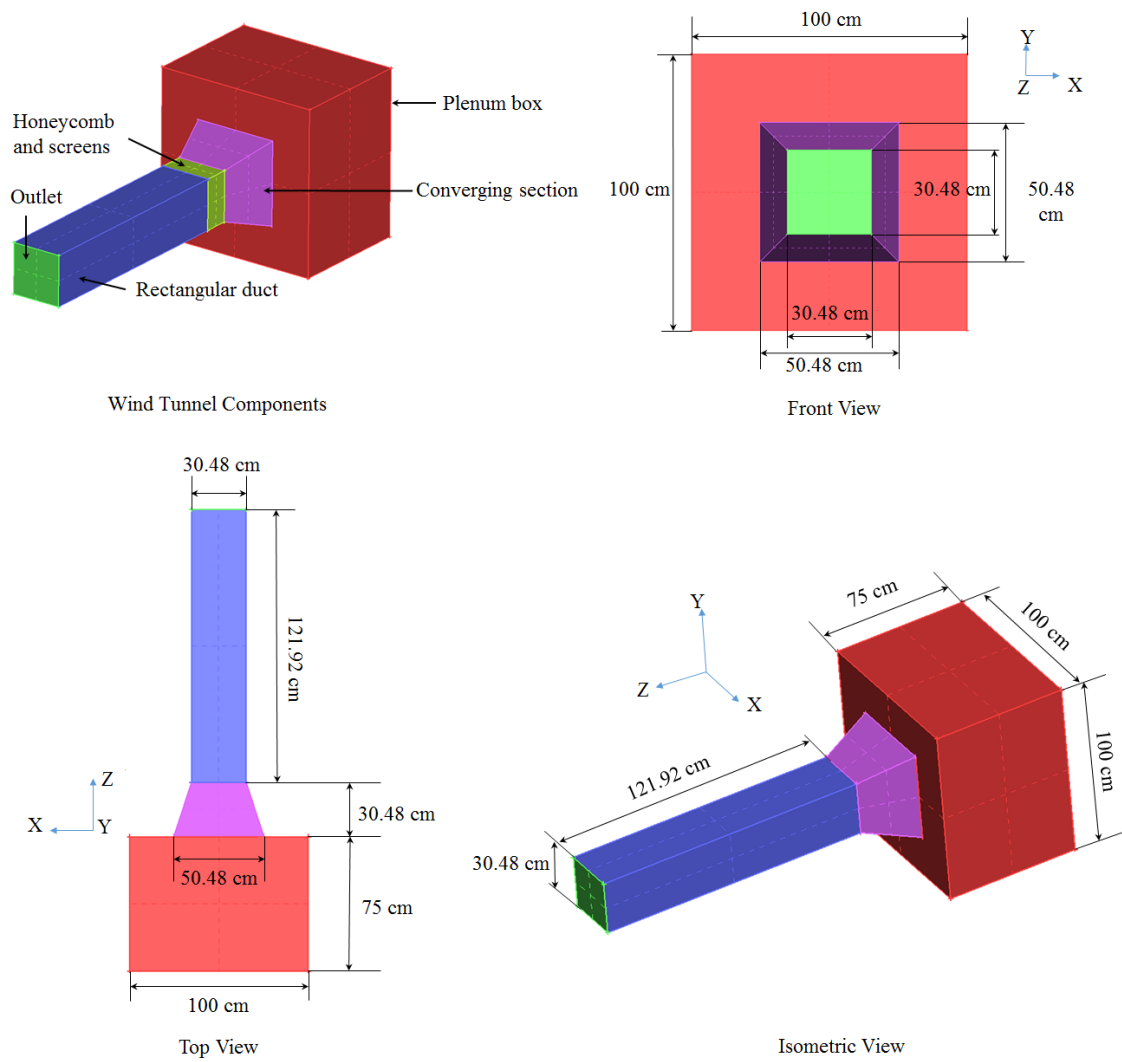
Figure 3.4: Schematic diagram of the laboratory-scale wind tunnel along with critical dimensions in cm.

A thin metal lip measuring 40.64×10 cm was attached just before the leading section of the condensed fuel surface to reduce the flow separation and bluff body effects of the sample holder and to prevent transition of the laminar boundary layer

due to surface roughness of the upstream insulation board. According to Ha et al. [37], by attaching an extension plate at the leading edge of the fuel surface, the separation of flow may be prevented and an ordinary boundary layer diffusion flame can be established. In the flow without an extension plate, the interaction between flow separation and the diffusion flame was found to exist [37]. Therefore, our condensed fuel surface starts 10 cm away from the exit of the wind tunnel. At the measurement location, the holder is positioned with its leading edge against the wind tunnel exit at the center of the channel. As the metal sheet lip is wider (40.64 cm) than the the width of the tunnel (30.48 cm), the exiting air jet is divided into two and the top half forms a boundary layer over the sample.

The front surface of the insulation wall was coated with a black radiation absorbing paint having an absorbptivity of approximately 98% (according to manufacturer's specifications). The liquid fuel wick was a 10 cm × 10 cm × 1.27 cm thick sheet of porous noncombustible material (Alkaline earth silicate wool). In order to eliminate leakage of the liquid fuel from the sides, sodium silicate was applied to all interfaces of the wick except the top face. Burning was limited to the front surface of the wick by shielding the remaining sides with aluminum foil. During testing, the wick was soaked with liquid fuel up to its point of saturation so that it gave a stable boundary-layer diffusion flame for the longest time duration possible (enough to take precise

temperature measurements). The fuel wick was soaked with approximately 120 ml of liquid fuel for each test. In case of a solid fuel, an 10 cm $\times$ 10 cm $\times$ 1.27 cm thick sheet of clear cast PMMA was used.
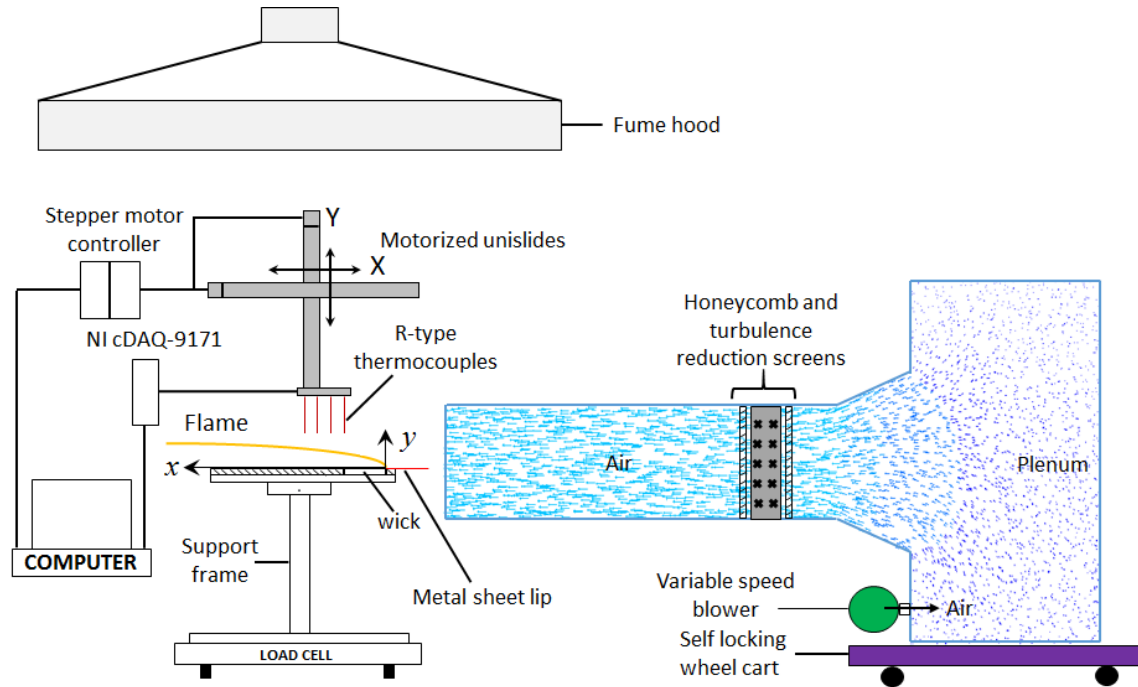
Figure 3.5: Schematic of the experimental setup used to measure mass-loss rates and temperature profiles over a forced-convection boundary layer diffusion flame.

Generally, in forced-flow boundary layer flame experiments, the fuel sample is placed inside a wind tunnel. In this work, we placed the condensed fuel surface at the exit of the wind tunnel in the center of the air stream. This arrangement provided easy access to the boundary layer flame and condensed fuel surface for temperature and flow field characterization, without affecting the free-stream flow

near the sample.

3.3. Instrumentation and Software

A detailed description of the instrumentation and software used for data acquisition and analysis is given in the following section.

3.3.1. Mass balance

Table 1: MS32001L Precision mass balance specifications.

Product Details	MS32001L Mass Balance
Maximum capacity	32200 g
Readability	0.1 g
Calibration	Automatic internal adjustment (FACT)
Repeatability (sd)	0.1 g
Linearity	0.3 g
Sensitivity temperature drift (10-30 ^{o}C)	5 ppm/^{o}C
Stabilization time	2 s
Size of weighing pan	351×245 mm
Power requirement	100-240 VAC/0.3 A

A Mettler Toledo precision mass balance (Model MS 32001L) was used to measure the mass-loss rate of the condensed fuel surface. The given load cell has a maximum capacity of 32.2 kg with a resolution of 0.1 g. More information about the mass balance is given in Table 1.

3.3.2. Traverse mechanism

An X-Y computer-controlled traverse system was used to obtain accurate positioning and incremental movement of the temperature and velocity probe. For temperature measurements micro-thermocouples were mounted to a set of of computer-controlled Velmex X-Y unislides. For free-convection flames, the positioning system in the Y direction was utilized to move the probe horizontally across the flame thickness (see Figure 3.1). The positioning system in the X direction was utilized to move the probe vertically along the flame length. Velmex X-Y unislides were equipped with stepper motors that could move the probe to a target position with a maximum spatial resolution of 1.5 μm. In forced-convection flames, the X-positioning system was used to move the probe horizontally along the flame length while the Y-positioning system was used to move the probe vertically across the flame thickness (see Figure 3.5).

The stepper motors were controlled by a Velmex VXM-2 programmable stepper motor controller. The stepper motor controller could either be operated as stand

alone via the jog buttons on the front panel or run interactively from the computer through a custom developed National Instruments LabVIEW program to set the control variables of the stepper motors such as: moving direction, motor speed, motor position, zeroing motor position and the capability to switch between stand-alone or interactive controller operation. The LabVIEW program sends commands in the format of ASCII characters to the controller through an RS-232 interface and displays the indexing feedback from the controller. A detailed grid scanning algorithm was written in LabVIEW that sends a series of commands to the controller and moves the requisite probes in a grid fashion automatically. This allows the probe to grid scan the various locations in a boundary-layer flame with ease and high accuracy.

3.3.3. Digital Camera

Both Canon (Canon EOS) and Nikon (Nikon D7000) digital SLR cameras were used for taking the side and top-view images of the boundary-layer diffusion flames. The images were then processed in Matlab to obtain an averaged image followed by processing in ImageJ to obtain flame edges. The built-in edge detection algorithm in ImageJ was employed for flame edge detection. The images were scaled and the flame stand-off distance was then measured at each stream-wise location by measuring the distance of the center of the flame zone from the condensed fuel surface.

3.3.4. Thermocouples

Thermocouples are widely used for the measurement of gas temperatures in flames and combustion environments. In this study, precise temperature measurements were carried out using R-type Pt/Pt-13% Rh micro thermocouples (spot welded) of 50 μm (0.002 in) and 75 μm (0.003 in) wire diameter with a bead of approximately 100 μm and 150 μm in diameter respectively (according to manufacturer's specifications). In practice, most thermocouples have diameters in the range 1.5 $d_w < d_b < 2.5$ d_w (in our case $d_b \sim 2d_w$). The high melting point of a type-R thermocouple (2040 K) made it a suitable probe for the range of temperatures in this study. The small size of the probe also provides high resolution, minimal disturbance of the flame, a low response time and reduction in the radiation losses from the thermocouple bead. The micro thermocouple wires were housed in a single 1.1 mm diameter twin bore ceramic cylinder, while a smaller length of thermocouple wire was left exposed ($\sim$ 10 mm). The exposed wire was shaped into a flat semi-circular form, which reduces probe-induced perturbations. Figure 3.6 shows a schematic of the given thermocouple single support design. Both 50 μm and 75 μm wire-diameter thermocouples were used over the same sample in order to ensure accurate radiation corrections by reading the difference between these two at the same location and applying the correlation of Collis and Williams [99] as discussed later.
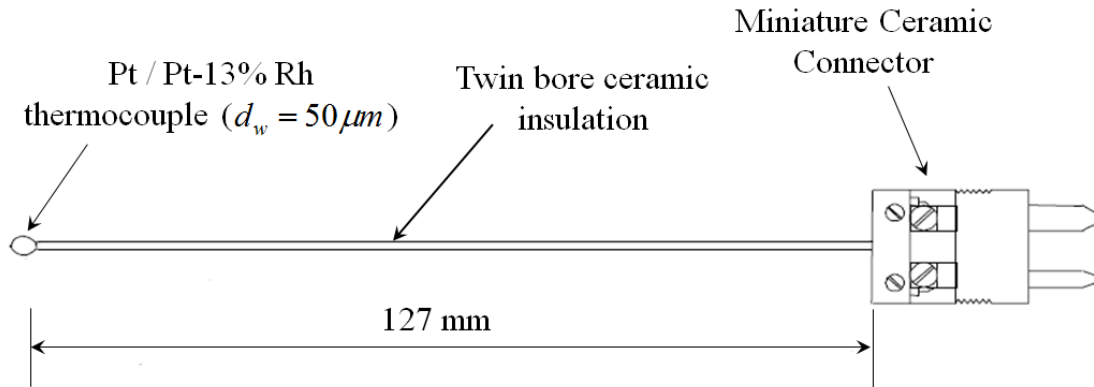
Figure 3.6: Schematic of thermocouple single support design.

3.3.5. Heat Flux Gauge

A Medtherm water cooled total heat flux gauge (Gardon gauge, model 64-10-20) was used to measure the wall heat flux in the overfire region for methanol, ethanol and PMMA wall flames in a vertical configuration. Gardon gauges absorb heat in a thin metallic circular foil and transfer the heat radially (parallel to the absorbing surface) to the heat sink welded around the periphery of the foil. The emf output is generated by a single differential thermocouple between the foil center temperature and foil edge temperature. The front face of the heat flux gauge was coated with a black absorbing paint having an absorbtivity of 0.92. The water cooled heat flux gauge was calibrated against a known incident heat flux by Medtherm Corporation. The full scale output level for the given heat flux gauge was estimated to be 8.30 mV at 100 kW/m^2. The responsivity of the given device was then estimated to be 0.083

mV per kW/m² or in other words, 12.05 kW/m² per mV.

Table 2 lists the details for the heat flux gauge employed in the present study. A typical calibration curve for the given heat flux gauge is shown in Figure 3.7. An inset picture shows the typical heat flux gauge employed in the present study. Total uncertainty for a single heat flux sample acquired with a total heat flux gauge under typical experimental conditions including calibrator uncertainty, was found to be less than ±3% with a 95% confidence interval.
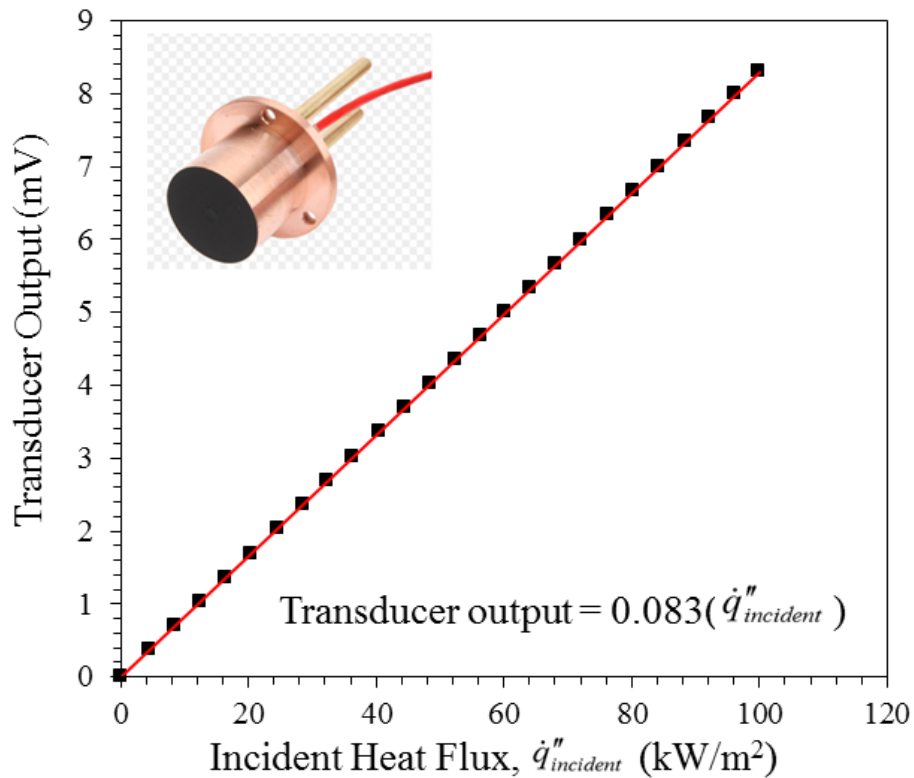
Figure 3.7: Calibration curve for Medtherm total heat flux gauge. The picture-inset shows the total heat flux gauge employed for the present study.

Table 2: Medtherm water cooled heat flux gauge 64-10-20 specifications.

Product Details	64-10-20 Gardon Gauge
Output signal	Linear output, 10 mV nominal at full range
Maximum non-linearity	± 2% of full range
Repeatability	±0.5%
Sensor absorptance	0.92
Time constant (typical)	Less than 250 ms

3.3.6. Hot Wire Anemometer

Hot wire anemometry is the most common method used to measure instantaneous fluid velocity. The technique depends on the convective heat loss to the surrounding fluid from an electrically heated sensing element or probe. If only the fluid velocity varies, then the heat loss can be interpreted as a measure of that variable. Hot wire anemometry enjoys its popularity because the technique involves the use of very small probes that offer very high spatial resolution and excellent frequency response characteristics. The basic principles of the technique are relatively straightforward and the probes are difficult to damage if reasonable care is taken. Most sensors are operated in the constant temperature mode. Hot-wire anemometers have been

used for many years in the study of laminar, transitional and turbulent boundary layer flows and much of our current understanding of the physics of boundary layer transition has come solely from hot-wire measurements.

In order to characterize the incoming flow field at the wind tunnel outlet, a Dantec Dynamics MiniCTA Anemometer system (54T42) was used. A typical MiniCTA system is shown in Figure 3.8.
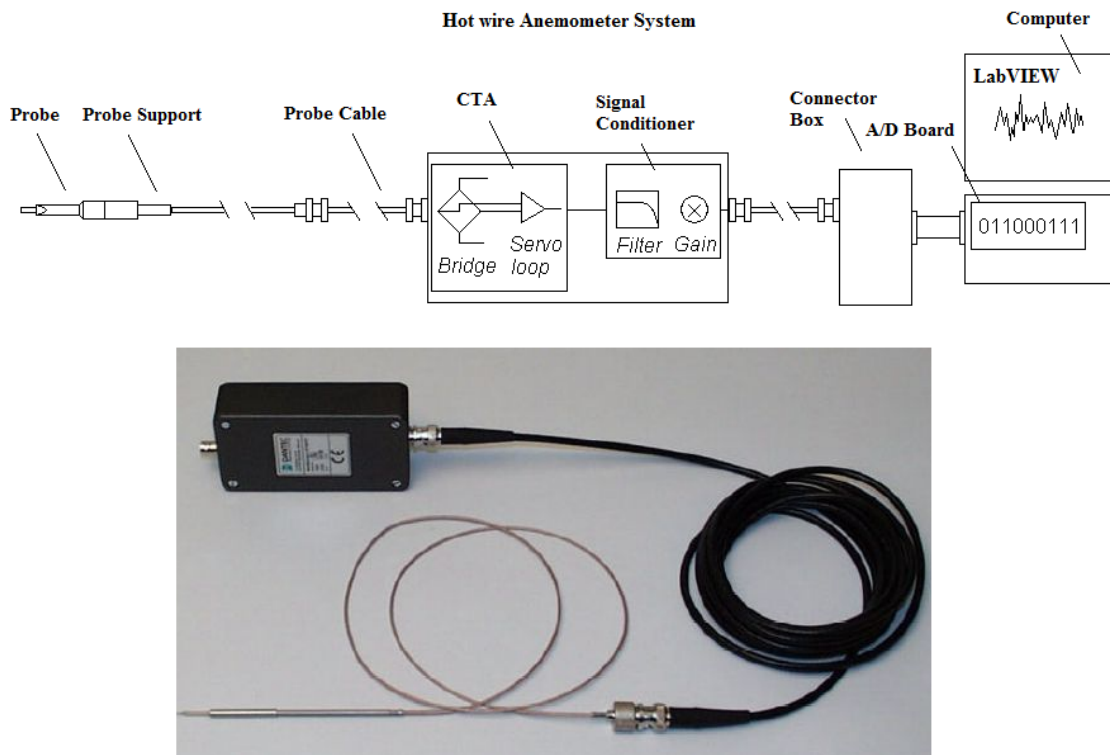
Figure 3.8: (top) Diagram illustrating a CTA measuring chain. (bottom) A typical hot wire anemometer system.

3.3.6.1 Temperature correction of CTA voltages

If the overheat ratio has not been adjusted prior to the data acquisition, the Constant Temperature Anemometer (CTA) output voltage must be corrected for possible temperature variations before conversion. The fluid temperature therefore needs to be acquired along with the CTA signal. The corrected CTA voltage is then represented as

$$E_{corr} = \left(\frac{T_w - T_0}{T_w - T_a}\right)^{0.5} E_a,$$ (10)

where E_a is the acquired voltage, T_w is the sensor hot temperature, T_0 is the ambient reference temperature related to the last overheat set-up before calibration and T_a is the ambient temperature during acquisition. T_w in the above expression is given as

$$T_w = \frac{a}{\alpha_0} + T_0,$$ (11)

where α_0 is the sensor temperature coefficient of resistance at T_0 and a is the overheating ratio,

$$a = \frac{R_w - R_0}{R_0},$$ (12)

where R_w is the sensor resistance at operating temperature T_w and R_0 is its resistance at ambient (reference) temperature T_0.

3.3.6.2 Calibration Rig

A hot wire calibration establishes a relationship between the CTA output and the flow velocity. It is performed by exposing the probe to a set of known velocities, U, and then records the voltages, E. A curve fit through the points (E, U) represents the transfer function to be used when converting data records from voltages into velocities. Calibration may either be carried out in a dedicated probe calibrator, which normally is a free jet, or in a wind tunnel.

In our case, the hot wire probe was calibrated in a free jet-style calibration rig against a calibrated Omega handheld hot wire anemometer as the velocity reference. Figure 3.9 shows the photograph of the calibration rig that was used to calibrate the Dantec Dynamics hot wire probe. The calibration rig consists of a tube of 1 inch (2.54 cm) diameter through which air is allowed to flow at a given flow rate. An Alicat brand mass flow controller was used to alter the air flow rate through the given tube. The velocity flow field at the outlet was then measured at a given location with the help of an Omega hot wire probe for different flow rates of air. The Dantec Dynamics hot wire anemometer was then calibrated against the Omega hot wire probe by recording the voltage signals at different flow rates at the same location. Temperatures were recorded during calibration and the CTA output voltage was corrected for possible temperature variations before conversion.
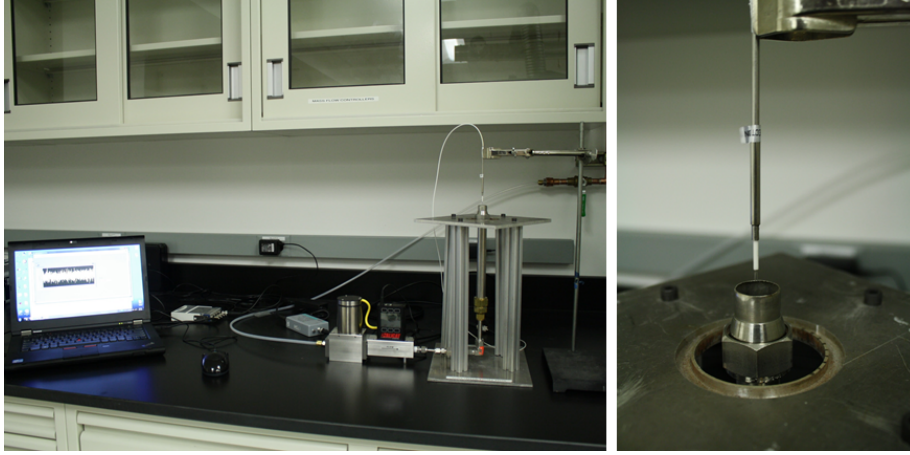
Figure 3.9: Photograph of the hot wire calibration rig.

The hot wire responds according to King's Law,

$$E^2 = A + BU^n, \tag{13}$$

where E is the voltage across the wire, U is the velocity of the flow normal to the wire and A, B and n are constants. Plotting E^2 as a function of U^n in double logarithmic scale (n=0.45 is a good starting value for hot wire probes) and creating a linear trend line gives the calibration constants A and B in the above function. n should be varied repeatedly until the curve fit errors are acceptable. Similarly, polynomial fits can be used to create trend lines and can be represented as

$$U = C_0 + C_1 E + C_2 E^2 + C_3 E^3 + C_4 E^4. \tag{14}$$

This polynomial fit is normally recommended, as it makes very good fits with linearisation errors often less than 1%. Typical calibration curves for our hot wire
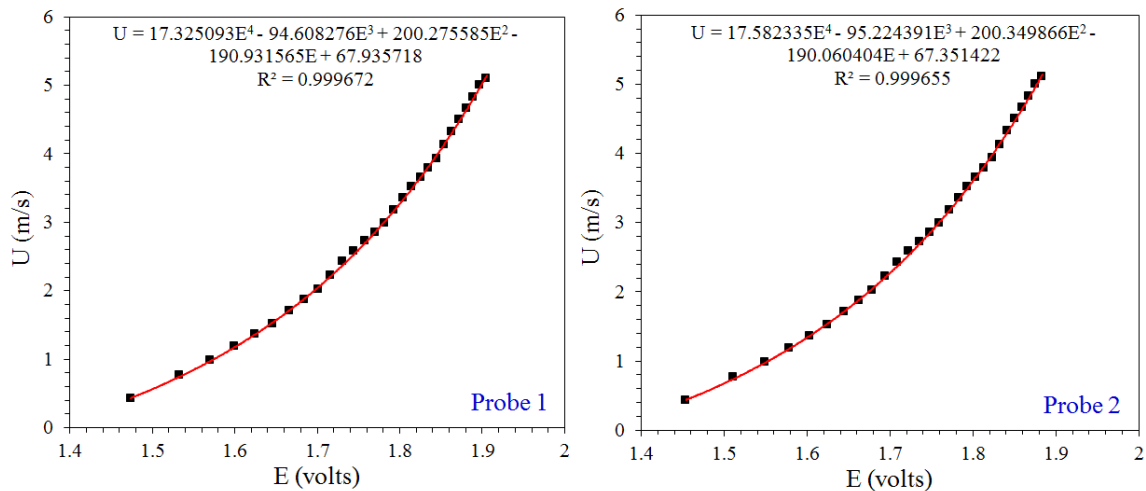
Figure 3.10: Calibration curves for the Dantec Dynamics Mini CTA hot wire probes.
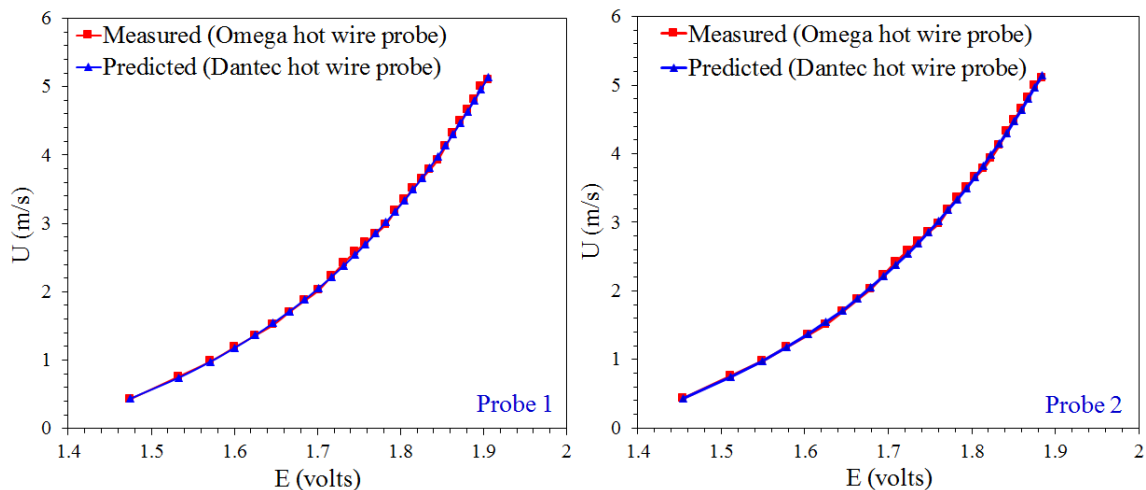
Figure 3.11: Dantec Dynamics Mini CTA hot wire probe predictions for velocity using the polynomial trend lines in Figure 3.10 compared to the calibration data.

probes are given in Figure 3.10. The CTA voltage data, E at each point was acquired with a sampling rate of 50,000 samples/s for a total duration of 10 s. Three indepen-

dent tests were performed at a given flow rate for a given location. The repeatability of these measurements was within 0.8% of the mean. Similarly, 3 independent tests were performed with an Omega hot wire probe to measure the velocity, U at a given location for a given flow rate. The repeatability of these measurements was within 0.7 % of the mean. Figure 3.11 shows a comparison of the velocity predicted by the Dantec Dynamics hot wire probe by using the polynomial trend line of 4th order in Figure 3.10 compared to the calibration data (from the Omega hot wire probe).

3.3.7. Data Acquisition Hardware and Software

A National Instruments CompactDAQ USB chassis was used in conjunction with a NI C-series I/O modules for custom analog input and output. The NI cDAQ-9178 is an 8-slot NI CompactDAQ USB chassis designed for small, portable, mixed-measurement test systems. The NI cDAQ-9178 chassis comes with a built-in signal conditioner to condition the voltage signals acquired through various input modules. Voltage signals from thermocouples were acquired, conditioned and digitized through a National Instruments NI 9214, which is a 24-bit high density 16-channel thermocouple input module and can be used up to 0.02°C measurement sensitivity. The NI 9214 has a built-in cold-junction compensation (CJC) circuit to eliminate errors caused by the physical connection of the sensor to the instrumentation. The NI 9214 has cold junction compensation sensors for J, K, T, E, N, B, R, and S types

thermocouples. The NI 9214 also has a built-in signal conditioner and comes with a channel-earth ground isolation for higher measurement sensitivity. In addition to the CJC, the NI 9214 features an extra, internal-only channel known as the auto-zero channel. By measuring the auto-zero channel at the beginning of each channel scan, offset errors can be further eliminated to provide a more accurate temperature measurement. The NI 9214 is capable of sampling at a rate of 1088 samples/s.

NI cDAQ-9178   **NI 9214 c-module**   **NI 9239 c-module**
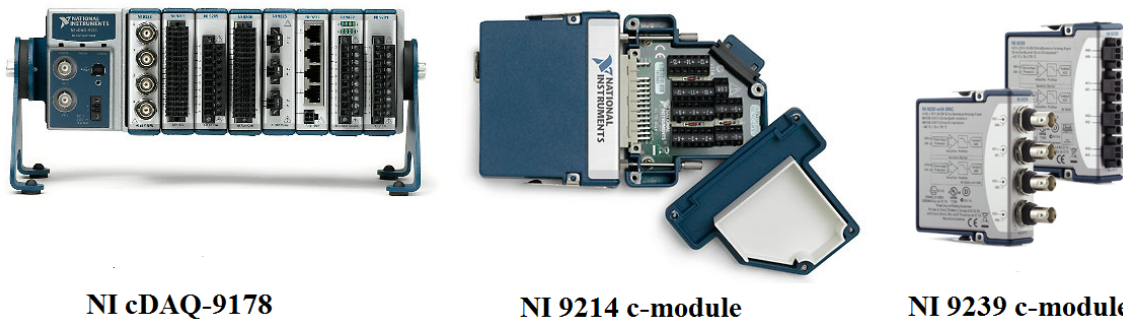
Figure 3.12: A front view of the NI-cDAQ 9178 along with the NI 9214 and NI 9239 C-series modules.

Voltage signals from the hot wire probe were acquired, conditioned and digitized through a National Instruments NI 9239, which is a 4-channel, 24-bit C Series analog input module and comes with a channel-to-channel isolation and built-in signal conditioner. The NI 9239 consists of 4 simultaneous analog input channels and is capable of acquiring signals at a sampling rate of 50 kS/s/channel. Figure 3.12 shows a front view of the NI-cDAQ 9178 along with the NI 9214 and NI 9239 C-series mod-

ules. Table 3 shows a summary of the specifications for both the NI 9214 and NI 9239 C-series modules.

Table 3: Specification summary for the NI data acquisition devices used in this study.

Product Details	NI 9214	NI 9239
Measurement Type	Temperature Thermocouple	Voltage
Form Factor	CompactDAQ, CompactRIO	CompactDAQ, CompactRIO
Isolation Type	Ch-Earth Ground Isolation	Ch-Ch Isolation
Differential Channels	16	4
Analog Input Resolution	24 bits	24 bits
Maximum Voltage Range Range Accuracy	-78.125 mV to 78.125 mV $25\mu V$	-10 to +10 V 0.019 V
Simultaneous Sampling	No	Yes
Signal Conditioning	Cold-junction compensation Open thermocouple	Anti-aliasing filter

LabVIEW software was used for continuous temperature and velocity data acquisition. A detailed script in LabVIEW was written that acquired and analyzed

voltage signals received by different modules. The script also provided statistical temperature and velocity data such as mean, minimum, maximum, and standard deviations. Temperature and velocity fluctuations were automatically calculated by the LabVIEW script and were subsequently written to a measurement file.

3.4. Measurement Methodology

3.4.1. Mass Loss Rate Measurements

The fuel burning rate was measured by monitoring the mass loss of the burning wick over a timed interval. A Mettler Toledo precision mass balance was used, which had a maximum capacity of 32.2 kg and a resolution of 0.1 g, to measure the mass-loss rate of the condensed fuel surface. The mass loss of the condensed fuel wick or PMMA sample during the experiment was recorded at a frequency of 1 Hz. Following ignition, the burning rate (indicated by the rate of mass loss) remained constant for most of the test time. However, as the wick dried up, the burning rate decreased. For burning slabs of PMMA, after a fairly steady burning regime, the rate of mass loss would increase as in-depth conduction heated the fuel. The burning rate measurements were made in the early stages of the burning process when the average burning rate is constant and governed by the rate of fuel evaporation, rather than diffusion through the fuel wick. The average mass-loss rate of the condensed
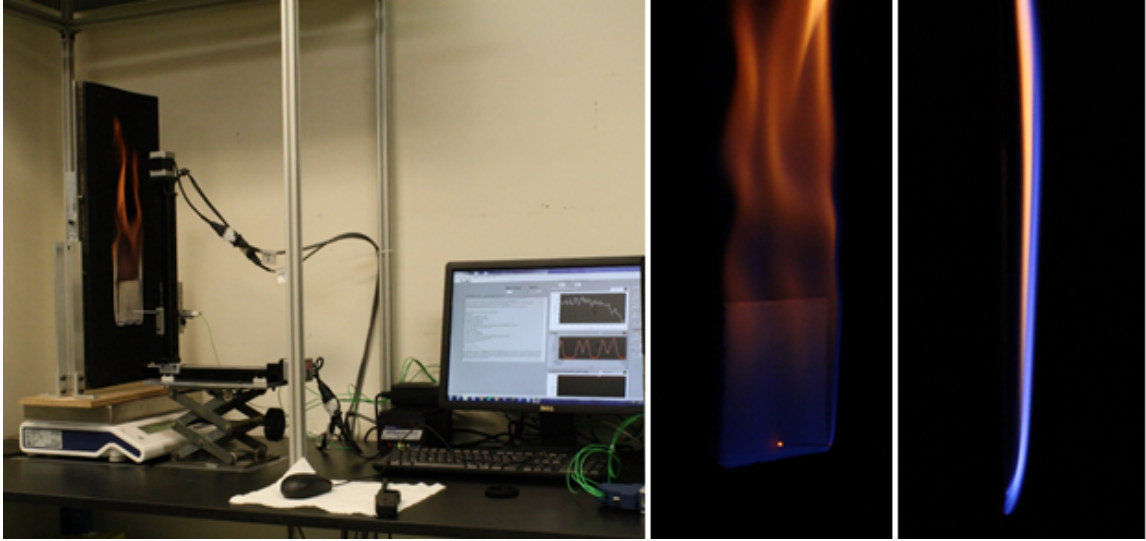
Figure 3.13: (left) Photograph of the experimental setup used to measure mass-loss rates and temperature profiles over a vertical, free-convection boundary layer diffusion flame. (right) Front and side-view photograph of a vertical ethanol diffusion flame.

fuel surface was determined by measuring the slope of the linear mass-loss versus time curve during steady burning. The burning rate measurements presented are averages of six tests at a given condition. The repeatability of these measurements was within 2% of the mean for both free and forced flow experiments. Figure 3.13 shows the photograph of the experimental set-up used to measure mass-loss rates and temperature profiles over a vertical, free-convection boundary layer diffusion flame. Figure 3.13 also shows the front and side-view photographs of a vertical ethanol diffusion flame. The bright yellow spot in the front-view photograph represents the micro-thermocouple probe inside the flame zone.

81

3.4.2. Measurements of Flame Standoff Distance

The flame stand-off distance measurements were made by two different methods: non-intrusive (visual) and intrusive (recorded by a thermocouple). The intrusive flame standoff distance here is taken as the distance measured in a normal direction from the condensed fuel surface to the point where the peak temperature was recorded. The visual non-intrusive flame standoff distance is defined as the flame stand-off distance measured through direct flame photographs, the procedure for which is defined below.

Measurements of the flame stand-off distances were recorded by digital photographs, where the distance from the condensed-fuel surface to the center of the blue flame zone was measured and taken as the position of the flame for methanol and ethanol wall-bounded flames. In case of a methanol, ethanol and PMMA wall flame in free and forced convective environment, more weightage was given to the experimental results obtained by the intrusive technique using thermocouples. The flames were photographed in a darkened room with a side-view digital camera (Canon EOS). Before a sample was ignited, the camera was calibrated by taking a picture of a sheet of graph paper that was aligned along the vertical axis of the fuel surface. Four calibration images were taken. An average pixel/mm count was then obtained from the four images taken. This value of pixels/mm was later used during the post-
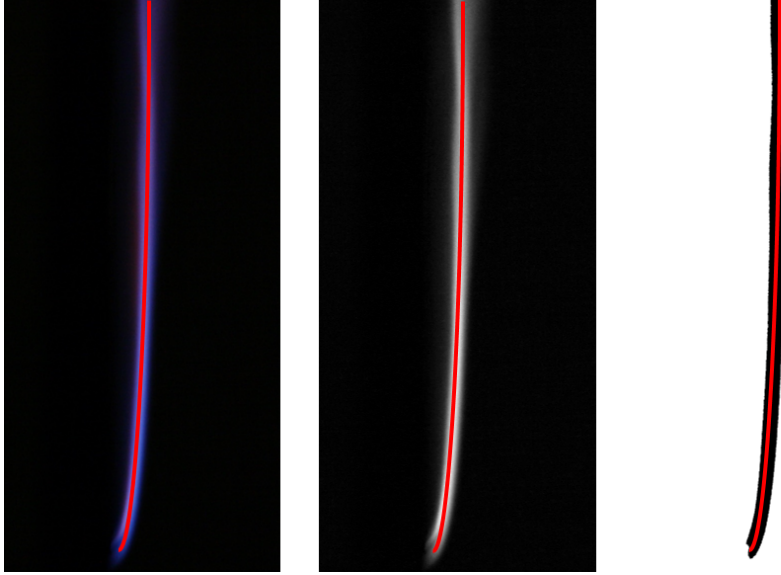
Figure 3.14: Photograph of a free-convection methanol diffusion flame in color, grayscale and binary mode. The red marker represents the center of the blue flame zone.

processing of the images while calculating the standoff distance. The field of view was chosen to reduce errors in the standoff distance measurement to less than 5%. A field of view at the center of the fuel specimen covering an area of 20 cm × 14 cm was imaged for calculating the flame stand-off distance in the pyrolysis zone for free-convection flames. For forced-convection flames, a field of view at the center of the fuel specimen covering an area of 16 cm × 8 cm was imaged for calculating the flame stand-off distance in the pyrolysis zone. The digital images were averaged in Matlab and flame stand-off distances were measured by using ImageJ software. In a particular test, 200 images were averaged during the steady burning regime time

83

to obtain an averaged image. The flame standoff measurements were carried out independently for 3 repeated tests at a given flow condition. The results were then averaged to give an averaged flame standoff distance profile. The repeatability of these measurements was within 2% of the mean. Figure 3.14 shows a larger picture of the flame with a marker representing the center of the blue flame zone.

3.4.3. Temperature Measurements

3.4.3.1 Measurement Methodology

Precise temperature measurements were carried out using R-type Pt/Pt-13% Rh micro thermocouples (spot welded) of 50 μm (0.002 in) and 75 μm (0.003 in) wire diameter. Both 50 μm and 75 μm wire-diameter thermocouples were used over the same sample in order to ensure accurate radiation corrections by reading the difference between these two at the same location and applying the correlation of Collis and Williams [99]. For the 50 μm wire-diameter thermocouple, a typical radiation correction at 1700 K was found to be approximately +83 K for free convection flames. Since the thermocouples cross regions of high temperature gradients, the measurements are expected to include conduction errors, however they have been estimated to be small here ($< 1\%$) since the heat-transfer area (the cross section of the thermocouple) is very small, therefore no corrections were made in the data for

conduction errors. More details on neglecting a conduction correction for the given thermocouple can be found in the subsequent sections.

Often Silicon dioxide (SiO_2) or yttrium oxide (Y_2O_3) coatings are used to prevent exothermic reactions on the possibly catalytic platinum surface of the thermocouple. Such reactions can lead to erroneously high temperatures. The use of these coatings in our experiment was discouraged by several factors. SiO_2 coatings in a reducing atmosphere can lead to the formation of a silicon solid solution in the Pt and Pt-13% Rh legs of the thermocouple. This would shift the Fermi energy levels of the two components of the junction and decalibrate the potential difference output [100]. In addition, above 1800 K the (SiO_2) melts and flows into beads. As a practical constraint, yttrium oxide coatings are avoided for their toxic nature. An additional consideration is that most catalytic reactions involve radical recombination [101]. This makes coating of platinum thermocouples important for premixed flames, but much less important in diffusion flame thermometry. With diffusion flames, radicals exist only in the very narrow flame zone, where gas phase reactions are very rapid [102]. Also, the addition of a SiO_2 or Y_2O_3 layer would increase the radiation correction and significantly complicate the energy balance on the bead.

The previously-described micro-thermocouples were mounted to a set of computer-controlled Velmex X-Y unislides such that they can be moved precisely up and down

85

along the flame length or left and right across the flame thickness with a maximum spatial resolution of 1.5 μm (for free-convection flames). Voltage signals from the thermocouples were acquired, conditioned and digitized through a National Instruments NI 9214, which is a 24-bit high density 16-channel thermocouple input module which can be used with up to 0.02°C measurement sensitivity. The LabVIEW software was used for synchronized motor control and continuous temperature data acquisition. During free and forced-convection experimental tests, the data acquisition system acquired temperatures at a maximum sampling rate of 100 and 500 samples per second, respectively, providing 100 and 500 samples to average per spatial point, respectively. The dwell time at each point was 1 s for the pyrolysis region and 10 s for the plume or overfire region. Due to higher fluctuations in the plume, temperature data at a given point was acquired for a longer duration of time in order to average over the temperature fluctuations in the plume. Reported temperatures are averages of at least 5 tests at a given condition in the pyrolysis and plume region for both free and forced-convection flames. Because the temperature gradients are very steep within a boundary-layer diffusion flame, very fine movements were necessary. Through numerical testing, it was determined at least 22-36 measurements at 0.5 mm intervals should be made across the methanol free-convection flame in order to fully resolve the thermal boundary layer. Measurements were taken at 0.25 mm

spacings near the condensed fuel surface and then subsequently incrementing the spatial distance to 0.5 mm. The thermal boundary layer thickness for a methanol free-convection flame is approximately 18 mm at the trailing edge of the sample surface.

In the case of a PMMA slab, steady burning samples were ignited by a standard blowtorch, which was passed over the surface for approximately 50 s until the entire surface was uniformly ignited. Thus, a boundary-layer flame was established over the entire surface and every point on the surface was exposed to the flame for the entire duration of the test. Experimental time was started immediately after uniform ignition. Unlike liquid wicks, as the PMMA sample burns its surface regresses with time, therefore it was necessary to complete the temperature mapping while the surface remained relatively flat, measured to be within approximately 150 s following uniform ignition. 5-point temperature measurements from the molten layer into the gas-phase at 0.25 intervals were recorded at 12 x-locations within 150 s of ignition. PMMA samples were also burned for different time intervals to assess errors from surface regression and to calculate the local mass-burning rates for comparison. The sample was allowed to burn for a known time interval before the flame was extinguished. Since the PMMA surface regresses with time, it becomes difficult to measure the molten layer temperature at the PMMA surface. However, it

becomes imperative and essential to measure the molten layer temperature in order to compute temperature gradients accurately. Therefore, measurements with one thermocouple (50 μm) at various stream-wise locations was made by carefully moving the thermocouple down through the flame until it penetrated the molten layer. Molten layer temperatures were measured at various stream-wise locations along the condensed fuel surface for both free and forced convection flames.

3.4.3.2 Radiation Correction for the Thermocouple

The temperature measurements reported in this study have been corrected for thermocouple radiation. Flame temperature measurements across the width of the fuel sample showed no significant variation, except near the edges. Therefore, thermocouples at the center of the flame were used to produce a map of temperatures in the boundary layer by moving it across the flame (y-direction) and along the length of the flame (x-direction). Two thermocouples (50 μm and 75 μm wire-diameter) were traversed along the same path at the center of the flame for accurate radiation corrections. All temperature measurements reported in this work are an average of at least five independent tests conducted under the same conditions. In the most general case, an energy balance on the thermocouple junction takes the following form,

$$\dot{Q}_{cat} + \dot{Q}_{conv} + \dot{Q}_{rad} + \dot{Q}_{cond} = m_{tc}c_p\frac{dT_{tc}}{dt}, \tag{15}$$

with heat transfer associated with surface-induced catalytic reactions, convection between the gases and the thermocouple, radiant heat transfer between the thermocouple and its surroundings, conduction along the thermocouple wires, and transient heating or cooling of the thermocouple incorporated in Eq. (15). The thermocouple junction properties that characterize the transient term in the above expression include the mass of the thermocouple junction, m_{tc} and the specific heat c_p. For transient measurements, the convection and thermal inertia terms are both important, in addition to radiation. Neglecting the conduction error and errors due to catalytic effects, Eq. (15) reduces to the following form for transient measurements,

$$(T_g - T_{tc}) = \frac{m_{tc}c_p}{hA_{tc}}\frac{dT_{tc}}{dt} + \frac{\varepsilon_{tc}\sigma}{h}\left(T_{tc}^4 - T_{surr}^4\right) \tag{16}$$

and

$$(T_g - T_{tc}) = \tau\frac{dT_{tc}}{dt} + \frac{\varepsilon_{tc}\sigma}{h}\left(T_{tc}^4 - T_{surr}^4\right), \tag{17}$$

where τ is the characteristic response time or time constant of the thermocouple. Eqs. (16) and (17) show that the time constant of the thermocouple is not only related to the physical properties of the thermocouple (i.e. the mass of the thermocouple junction, m_{tc}, the specific heat, c_p, and the surface area of the junction, A_{tc}) but also depends on the heat transfer coefficient of the flow, h. There is a substantial

89

literature devoted to the measurement of the time constant for the thermocouple [103, 104, 105, 106, 107, 108].

For steady state measurements, as in our case, Eq.(15) reduces to a convective-radiative heat balance (neglecting the conduction error and errors due to catalytic effects), given by

$$h\left(T_g - T_{tc}\right) = \varepsilon_{tc}\sigma\left(T_{tc}^4 - T_{surr}^4\right) \tag{18}$$

and

$$\left(T_g - T_{tc}\right) = \frac{\varepsilon_{tc}d_w\sigma}{kNu}\left(T_{tc}^4 - T_{surr}^4\right), \tag{19}$$

where T_g is the real gas temperature, T_{tc} is the thermocouple junction (or bead) temperature, T_{surr} is the temperature of the surroundings, ε_{tc} is the emissivity of the thermocouple junction, σ is the Stefan-Boltzmann constant and h is the convective heat transfer coefficient of the flow over the thermocouple junction defined as $h = k\,\mathrm{Nu}/d_w$. k is the thermal conductivity of the gas, Nu is the Nusselt number, and d_w is the thermocouple wire diameter. The choice of the Nusselt number correlation is of paramount importance in calculating a radiation correction to the measured thermocouple temperature because, as shown in Eq. (19), the radiation correction is inversely proportional to the Nusselt number. This choice is complicated, however, due to the existence of multiple "appropriate" Nusselt number correlations and the difficulty in estimating properties of the gas mixture surrounding the thermocouple,

90

particularly thermal conductivity. The bulk of the evidence in the literature, however, clearly indicates that a cylindrical Nusselt number correlation is most appropriate for describing the convective heat transfer to nearly all practical thermocouples [109], preferably that of Collis and Williams [99]. A commonly-used expression from Collis and Williams can be written as [99]

$$
\mathrm{Nu}\left(\frac{T_m}{T_g}\right)^{-0.17} = 0.24 + 0.56 \mathrm{Re}_{d_w}^{0.45} = 0.24 + 0.56\left(\frac{U d_w}{\nu}\right)^{0.45}, \tag{20}
$$

which was obtained for $0.02 < \mathrm{Re} < 44$, with the Reynolds number evaluated at the so-called film temperature, T_m the mean of the thermocouple and free-stream temperatures, i.e. $0.5\left(T_g + T_{tc}\right)$. Here, Re is the Reynolds number defined as indicated for the local gas flow velocity, U and kinematic viscosity, ν. Substituting Eq. (20) into Eq. (19) and neglecting the small temperature dependence in Eq. (20), we have a system of two equations with two unknowns (namely T_g and U),

$$
T_g - T_{tc_1} = \frac{\varepsilon_{tc_1} d_{w_1} \sigma}{k\left[0.24 + 0.56\left(U d_{w_1}/\nu\right)^{0.45}\right]}\left(T_{tc_1}^4 - T_{surr}^4\right) \tag{21}
$$

and

$$
T_g - T_{tc_2} = \frac{\varepsilon_{tc_2} d_{w_2} \sigma}{k\left[0.24 + 0.56\left(U d_{w_2}/\nu\right)^{0.45}\right]}\left(T_{tc_2}^4 - T_{surr}^4\right), \tag{22}
$$

which demonstrates that the difference between a thermocouple reading and the actual gas temperature (i.e. the error in gas temperature measurement) increases for

larger-diameter thermocouples, while it is reduced by increasing the gas flow velocity over the junction. In solving the above equations [Eqs. (21) and (22)], iteration is required since the gas conductivity and kinematic viscosity are a function of the gas temperature. Initially the gas temperature is taken to be the bead temperature for the purpose of evaluating the thermal conductivity and kinematic viscosity; then, the approximate value of the gas temperature is used to re-evaluate the thermal conductivity and viscosity.

The emissivity of the bead (ε_{tc}) can also be found as a function of its temperature. In an analysis outlined by Jakob [110], Maxwells wave equations can be solved to yield the complex indices of refraction for a metal as a function of its electrical resistivity. In the limit of low resistivity and assuming a large index of refraction, which is true for most metals, Jakob [110] gives the hemispherical total emissivity of platinum (Pt) as

$$\epsilon = 0.751 \left(r_e T \right)^{1/2} - 0.396 \left(r_e T \right), 0 < r_e T < 0.2, \tag{23}$$

where, for platinum, $r_e = r_{e,273} T / 273$, with T in K and $r_{e,273} = 11 \times 10^{-6}$ Ωcm [111]. Therefore, the platinum emissivity becomes,

$$\epsilon = 1.507 \times 10^{-4} T - 1.596 \times 10^{-8} T^2 \tag{24}$$

for $0 < T < 2230$ K. This equation is also confirmed by comparison with experimental data [112]. It was shown [112] that for temperatures where radiation is important,

predicted and observed emissivities agree to within 1%. Figure 3.15 shows the total

emissivity of platinum vs. temperature based on Jakob's theoretical prediction [110].

The emissivity of the thermocouple bead or junction can therefore be evaluated by

using the above expression in Eq. (24). Note that iteration is not needed for the

evaluation of the platinum emissivity, since this property is a function of the junction

or bead temperature, which is known.
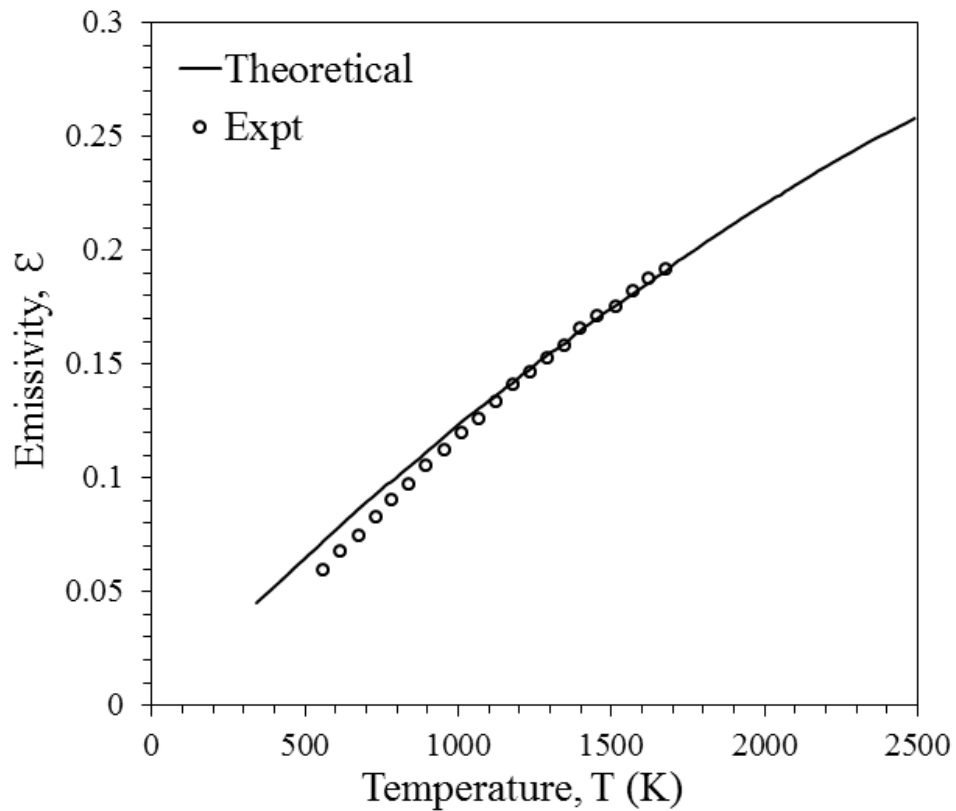
Figure 3.15: Total emissivity of platinum vs temperature based on Jakob's theoretical calculation
and experimental data from the Honeywell Research Center [111].

The actual gas temperature can then be evaluated by solving Eqs. (21) and (22). During experiments, the two thermocouples were traversed exactly to the same measurement points and data was sampled to account for the radiation correction in the temperature measurements. A typical raw and compensated temperature measurement is shown in Figure 3.16 for a methanol free-convection diffusion flame at two different streamwise locations along the condensed fuel surface.
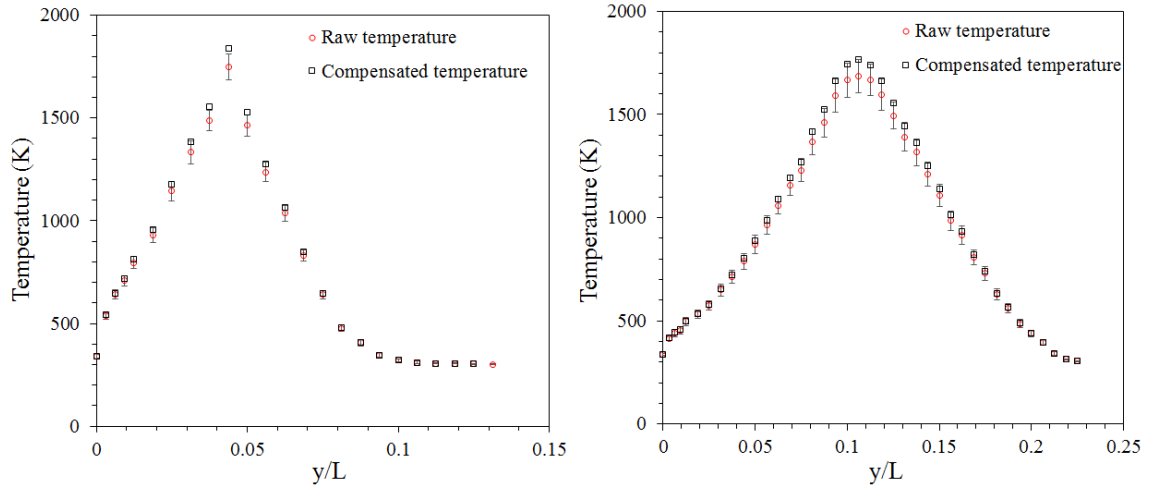
Figure 3.16: Raw and compensated temperature measurements for a free-convection methanol diffusion flame at two different streamwise locations along the condensed fuel surface, (left) x/L=0.05 and (right) x/L=1.

3.4.3.3 Conduction Correction for the Thermocouple

Rapid thermal conduction along thermocouple wires can result in significant heat losses from the thermocouple wire and junction to the larger, cooler lead wires or

94

support (cooler on account of increased radiation and conductive losses through the thermocouple support structure). However, this mechanism of heat loss from the thermocouple is usually avoidable through the use of sufficiently long and thin thermocouple wires on both sides of the junction. According to Bradley and co-authors [113] the conduction heat loss is assumed to be negligible if $l > 200d_w$, where l is the length of the fine wire. However, a more detailed analysis by Petit and co-authors [114] reveals that a better criterion is to use wires of length l such that $l/l_c > 10$, in which l_c is the characteristic length defined as,

$$l_c = \sqrt{\frac{k_w d_w}{4h_{conv}}}. \tag{25}$$

This criterion accounts for both the characteristics of the flow and of the sensor. Values obtained from applying Petit's criterion to the thermocouples used in this study with an exposed wire of 10 mm length and wire diameter of 50 μm at different locations in and out of the flame, were found to be in the range of 12-17 for the l/l_c ratio which is above the recommended value of 10. Overall, the conduction error is therefore considered negligible in this study.

3.4.4. Heat Flux Measurements

The heat flux to the wall in the overfire region was measured using a total heat flux gauge. Holes were drilled into the insulation board at several locations in the overfire

region to allow for placement of a water-cooled Medtherm total heat flux gauge (model 64-10-20). For measurements with the heat flux gauge, the data acquisition system acquired samples at a rate of 1000 Hz for a total time duration of 500 s. The data was then processed and averaged over the time duration of steady burning of liquid and solid fuels. Reported heat fluxes are averages of at least 3 tests in a given condition. In all tests, total flame heat flux was measured at 14 locations downstream of the condensed fuel surface. Temperature measurements were also carried out in the plume region at several locations downstream of the pyrolysis region. Temperature measurements were carried out at 7 stream-wise locations (at every other measurement location), downstream of the pyrolysis zone. Detailed temperature profiles in the combusting and thermal plume ensured calculation of convective heat fluxes with high accuracy as described later.

3.4.5. Ambient Flow Field Velocity Measurements

The wind tunnel was fully characterized for different blower speeds including velocity profiles and turbulence intensity levels measured at the wind tunnel outlet using a Dantec Dynamics hot wire anemometer. The free-stream velocity, U_∞, was then calculated by integrating the obtained velocity profile at the center of the tunnel outlet. The velocity data at each point was acquired at a sampling rate of 50,000 samples/s for a total duration of 10 s. The repeatability of these measurements was

within 2% of the mean. The velocity profile across the tunnel outlet were found to be relatively uniform near the center. The turbulence intensity in the region of interest (at the center of the tunnel outlet) was found to be less than 2%. Figure 3.17 (a) shows the velocity profiles obtained at the wind tunnel outlet for 4 different blower speeds.

To ensure that the flow is well defined at the location of the flame, we chose the dimensions of the sample to be small enough such that the condensed fuel surface would be within the potential flow core of the exit jet. It has been shown that velocity profiles in both x and y directions do not change significantly within the potential core of a jet [115, 116]. Experimental measurements from Sforza and co-authors [117] show that for an air jet at the exit of a square channel, with Reynolds number Re_d between 2.6 and 8.8 $\times$ 10^4, the potential flow core length is about $5d$ downstream of the exit, where d is the height of the channel. In the current work, $d = 30.48$ cm and hence our sample is within $1d$ (20 cm from the tunnel exit). Our Re_d is between 1.5 $\times$ 10^4 and 3.9 $\times$ 10^4; therefore, the flame would be within the potential flow core of the jet. To further confirm that the velocity profiles would not change significantly within the space where the flame would exist, the velocity profiles were also measured above the non-burning sample. Figure 3.17 (b) shows the variation of inlet velocity within the potential core of the exit jet with the streamwise distance x

97
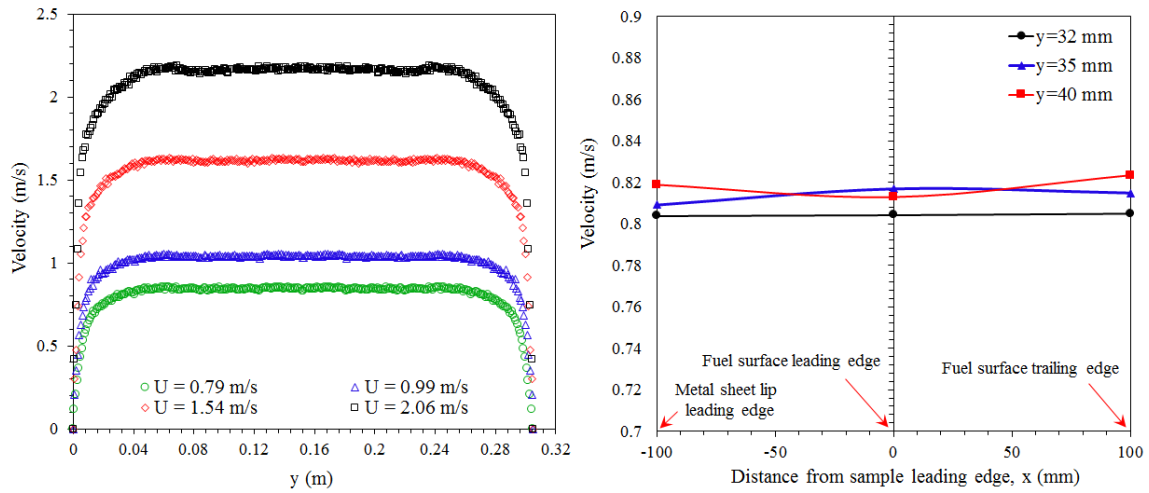
Figure 3.17: (a) (left) Velocity profiles at wind tunnel outlet for different blower speeds giving an average free-stream velocity of U_∞=0.79, 0.99, 1.54 and 2.06 m/s (b) (right) Streamwise variation of air velocity beyond the tunnel exit.

from the leading edge of the sample holder surface. Figure 3.17 (b) shows results for heights of 32, 35 and 40 mm above the sample surface at three distinct streamwise locations. The thermal boundary layer thickness at the trailing edge of the sample is approximately 30 mm for U_∞=0.79 m/s. Considering Pr⩽1, velocity boundary layer thickness at the trailing edge of the sample will be approximately ⩽30 mm for U_∞=0.79 m/s. Figure 3.17 (b) shows that the velocity profiles have not changed significantly within the core space where the flame is located.

3.5. Measurement Uncertainty

Current standards refer to the ISO uncertainty model which combines uncertainty contributions $u(y_i)$ from each individual input variable x_i into a total uncertainty, $U(tot)$, at a given confidence level. The output variable is defined as $y_i = f(x_i)$. The relative standard uncertainty $u(y_i)$ is a function of the standard deviation of the input variance

$$u(y_i) = \frac{1}{y_i} \frac{\partial y_i}{\partial x_i} \left(\frac{\triangle x_i}{k_i} \right), \tag{26}$$

where $S = \partial y_i / \partial x_i$ is the sensitivity factor and k_i is the coverage factor related to the distribution of the input variance (Gaussian, rectangular, etc.). As most engineering applications are assumed to have a Gaussian error distribution, the 95% confidence interval normally required is achieved by multiplying the standard uncertainty with the coverage factor $k = 2$. The total relative expanded uncertainty then becomes

$$U(tot) = 2\sqrt{\sum u(y_i)^2}. \tag{27}$$

3.5.1. Uncertainty in Mass Loss Rate Measurements

The mass loss rate measurements were carried out on a Mettler Toledo precision mass balance. The important factors considered in estimating the measurement uncertainty include readability, repeatability, linearity, temperature effects and uncertainty from the balance calibration report. The standard uncertainty contributed

by each factor listed above is given in the Table 4 below.

Table 4: Uncertainty Table for Mass Measurements

Factors	Value	Distribution	Standard uncertainty (u), g
Readability	0.1 g	Rectangular	$\frac{\frac{0.1}{2}}{\sqrt{3}} = \frac{0.05}{\sqrt{3}} = 0.0289$
Repeatability	0.1 g	Normal	0.1
Linearity	0.3 g	Rectangular	$\frac{\frac{0.3}{2}}{\sqrt{3}} = \frac{0.15}{\sqrt{3}} = 0.1040$
Temperature coefficient	5 ppm/deg C (5×10^{-6} g/g/deg C)	Rectangular	$\frac{5 \times 10^{-6} \times 5 \times 4800}{\sqrt{3}}$ $= 0.0832$
Uncertainty from balance calibration report ($u(balcal)$, coverage factor k=2)	0.0131 g	Normal	$\frac{0.0131}{k} = \frac{0.0131}{2} = 0.0066$
Subtotal of individual u values	$\sum u_n$		0.3227
Subtotal of squared u values	$\sum (u_n)^2$		0.0286

Considering all factors noted above as uncorrelated for a single weighing event,

the combined standard uncertainty can be expressed mathematically as,

$$u_c = \sqrt{u(read)^2 + u(repeat)^2 + u(linear)^2 + u(temp)^2 + u(balcal)^2}, \qquad (28)$$

where u is the standard uncertainty and u_c is combined standard uncertainty. There-fore, the combined standard uncertainty is,

$$u_c = \sqrt{0.0289^2 + 0.1^2 + 0.1040^2 + 0.0832^2 + 0.0066^2} = 0.1691\,\text{g} \qquad (29)$$

The total relative expanded uncertainty is expressed mathematically as,

$$U = ku_c, \qquad (30)$$

where k is the coverage factor. Using a coverage factor $k = 2$ (confidence level of approximately 95% and assuming the net mass follows a normal distribution), the expanded uncertainty is calculated as 0.3384 g. Thus, the total expanded uncertainty in measuring the mass by the given balance is approximately $\pm$ 0.34 g with a 95% confidence level. In our study, we are more interested in the mass loss rate of the burning sample. The mass loss of the burning sample can be determined without the necessity of a correction because the uncertainty in the final mass and initial mass cancel each other out.

3.5.2. Uncertainty in Temperature Measurements

Reported temperatures are averages of at least five tests in a given condition and the maximum standard deviation was $< 3.2\%$ of the mean for the pyrolysis region

and $< 6\%$ of the mean for the plume region (for the samples acquired in a particular test). The repeatability of these measurements was found to be within 5% and 8% of the mean for the pyrolysis and plume regions respectively. The inherent uncertainty in temperatures measured by the thermocouple (T_{tc}) are taken to be 0.25% of the measured value based on manufacturers specifications. The accuracy of the Nusselt number correlation used to calculate the radiation loss from the thermocouple bead was reported to be within 5% [99] and the uncertainty in k due to different species is assumed to be 3%. The error in the thermocouple emissivity used (ε_{tc}) is also small,$< \pm 3\%$ except that ε_{tc} is linear with T_{tc} so any error in T_{tc} increases the uncertainty in ε_{tc}. The Platinum emissivity was calculated using Jakobs theoretical correlation, confirmed by experimental data [27-28] which reported the Pt emissivity uncertainty $< \pm 3\%$ when using the calculation. The uncertainty in gas temperature is then calculated from a quadratic sum of the uncertainties:

$$dT_g = \left[\left(\frac{\partial T_g}{\partial T_{tc}} dT_{tc} \right)^2 + \left(\frac{\partial T_g}{\partial \varepsilon_{tc}} d\varepsilon_{tc} \right)^2 + \left(\frac{\partial T_g}{\partial k} dk \right)^2 + \left(\frac{\partial T_g}{\partial Nu} dNu \right)^2 \right]^{1/2}. \quad (31)$$

The maximum uncertainty in gas temperatures encountered in the flame zone is then found to be within ± 7 K. The total relative maximum expanded uncertainty in gas temperatures encountered in the flame zone is then found to be within ± 14 K with a 95% confidence interval.

102

3.5.3. Uncertainty in Heat Flux Measurements

The uncertainty of the results obtained with the heat flux gauge mainly arise from the calibrator itself. The heat flux gauge in our case was calibrated by the Medtherm Corporation. The total relative expanded uncertainty for the heat flux gauge was reported to be less than $\pm 3\%$ of responsivity with a 95% confidence level. Thus, the total uncertainty in heat flux measurements was found to be less than 3% with a 95% confidence interval.

3.5.4. Uncertainty in Velocity Measurements

The uncertainty of the results obtained with the CTA anemometer is a combination of the uncertainties of the individually acquired voltages converted into velocity and the uncertainty of the statistical analysis of the velocity series.

3.5.4.1 Drift, noise, repeatability and frequency response

Commercially available anemometers have low drift, low noise and good repeatability so that these factors do not add significantly to the uncertainty in comparison with other error sources.

3.5.4.2 Calibration equipment

The calibration, whether it is performed with a dedicated calibrator or with a pitot-static tube as reference, constitutes a major source of uncertainty. The error is *stochastic* with a normal distribution and the relative standard uncertainty can be expressed as,

$$U(U_{cal}) = \frac{1}{100}STDV(U_{calibrator}(\%)).$$ (32)

The calibrator uncertainty is often given as a relative standard uncertainty, a_{cal}, in percent plus a constant contribution b_{cal} in m/s given as,

$$STDV(U_{calibrator}) = \pm a(\%) + b_{cal}(m/s).$$ (33)

The $STDV(U_{calibrator}(\%))$ in our case, with an Omega hot wire probe as a dedicated calibrator, was found to be within 1%.

3.5.4.3 Linearisation

The linearisation uncertainty is related to curve fitting errors. It is stochastic with a normal distribution and its relative standard uncertainty can be calculated from,

$$U(U_{lin}) = \frac{1}{100}STDV(\Delta U_{lin}(\%))$$ (34)

where $STDV(\Delta U_{lin}(\%))$ is the standard deviation of the curve fitting errors in the calibration points in %. A typical curve fitting error in the calibration points in %

was found to be of the order of 0.5%.

3.5.4.4 A/D board resolution

The resolution uncertainty is stochastic with a square distribution and its relative standard uncertainty can be expressed as,

$$U(U_{res}) = \frac{1}{\sqrt{3}} \frac{1}{U} \frac{E_{AD}}{2^n} \left(\frac{\partial U}{\partial E} \right) \tag{35}$$

where E_{AD} is the A/D board input range, n is its resolution in bits, U is the velocity and $\partial U / \partial E$ is the slope (sensitivity factor) of the inverse calibration curve, $U = f(E)$.

3.5.4.5 Probe positioning

The positioning uncertainty relates to the alignment of the probe in the experimental set-up after calibration. The uncertainty is stochastic with a square distribution and its relative standard uncertainty can be expressed as

$$U(U_{pos}) = \frac{1}{\sqrt{3}} (1 - \cos\theta). \tag{36}$$

Normally a probe can be positioned with an uncertainty of $\Delta\theta = 1^o$.

3.5.4.6 Temperature variations

Temperature variations from calibration to experiment or during an experiment introduce systematic errors. If not corrected, a change in temperature changes the

sensor overheat temperature and contributes as a stochastic uncertainty with rectangular distribution. The relative standard uncertainty is,

$$U(U_{temp}) = \frac{1}{\sqrt{3}} \frac{1}{U} \frac{1}{T_w - T_0} \left(\frac{AU^{-0.5}}{b} + 1 \right)^{0.5}, \tag{37}$$

where T_w is the sensor temperature, T_0 the ambient reference temperature, and ΔT is the difference between the ambient reference temperature and the temperature during the measurement. This estimate is based on the power law calibration function,

$$E^2 = (T_w - T_0).(A + B.(U_{cal})^{0.5}) = (T_w - T_0)(A + B_1(\rho U)^{0.5}). \tag{38}$$

Since the velocity U_{cal} actually represents the mass flux, ρU, variations in density, ρ, with temperature will add to the uncertainty, if not accounted for. In gases, this gives following relative standard uncertainty,

$$U(U_{\rho,T}) = \frac{1}{\sqrt{3}} \Delta \rho_{,T} = \frac{1}{\sqrt{3}} \frac{\Delta T}{273}. \tag{39}$$

3.5.4.7 Ambient pressure variations

Ambient pressure changes also influence the density and hence the calculated velocity. These contribute as a stochastic uncertainty with a rectangular distribution following a relative standard uncertainty,

$$U(U_{\rho,P}) = \frac{1}{\sqrt{3}} \left(\frac{P_0}{P_0 + \Delta P} \right), \tag{40}$$

where P_0 is the ambient pressure.

3.5.4.8   Gas composition, humidity

Under normal conditions changes in gas composition are mainly caused by changes in humidity. The uncertainty is stochastic with a rectangular distribution having a relative standard contribution of

$$U(U_{hum}) = \frac{1}{\sqrt{3}} \frac{1}{U} \left(\frac{\partial U}{\partial P_{wv}} \right) \Delta P_{wv}. \tag{41}$$

The influence of gas composition and humidity on the heat transfer is very small, $\partial U / \partial P_{wv} \simeq 0.01U$ per 1 kPa change in water vapor pressure, P_{wv}.

3.5.4.9   Total uncertainty in a velocity measurement

Considering the relative standard uncertainty contributions from the factors above, uncertainty in a velocity measurement was calculated. The relative standard uncertainty due to probe positioning, humidity and A/D board resolution was found to be negligible. The relative standard uncertainty due to calibrator, linearisation, temperature variations, density variations and ambient pressure variations was calculated to be 0.01, 0.005, 0.008, 0.002 and 0.006 respectively. A total relative expanded uncertainty was then calculated to be 0.030 with a coverage factor of 2 ($k = 2$). From the above calculation, it appears that the voltage from a CTA with a wire probe can be acquired and converted into a velocity sample with an uncertainty of approximately 1% with a 95% confidence level with reference to the calibration and

neglecting the uncertainty of the calibrator itself. When the uncertainty of calibrator is included, the uncertainty of a velocity sample increases to typically 3%. The major contributions come from the calibrator, temperature variations in the flow and the linearisation (curve fitting). Thus, the total uncertainty in velocity measurements was found to be less than 3% with a 95% confidence interval.

Chapter 4: Numerical Simulations

4. Numerical Simulations

Laminar flame propagation over a horizontal fuel surface has been studied by numerous researchers in the past, for example Chen and Tien [50], Kodama et al. [51], Wang et al. [118], Rouvreau et al. [52] and V. Raghavan et al. [53]. The majority of numerical models used have assumed negligible thermal radiation and averaged thermo-physical properties to model gas-phase combustion. In addition, the main focus of many of these studies has been to determine a stability criterion for combustion, by considering various fuel injection velocity and free-stream air velocity combinations. Raghavan et al. [53] used a two-dimensional numerical model to investigate the validity of Emmons assumption by employing an optically thin radiation model. However, the authors used a single-step global reaction to model the combustion phase.

In the present study, CFD simulations were carried out for steady burning of a methanol/ethanol pool in a forced and free convective environment by using detailed reaction mechanisms for methanol-air and ethanol-air oxidation. This chapter describes the numerical models used for predicting steady burning over liquid fuel surfaces. A detailed discussion on all relevant boundary conditions, combus-

tion chemistry, radiation sub-model, grid system, discretization procedure, solution methodology and the convergence criteria used to obtain the numerical solutions is discussed in this chapter. Detailed discussions on the flame structure, velocity profiles and mass burning rates are provided. Results for steady burning of a methanol and ethanol film under natural convective conditions are also discussed in this chapter. Based on the numerical results, the theoretical correlation given in Eq. (9) is tested and validated for steady laminar boundary layer diffusion flames.

4.1. Steady Burning of a Methanol and Ethanol Pool in a Forced Convective Environment

The present numerical study is conducted as a means to understand the characteristics of a boundary-layer diffusion flame established over a horizontal methanol pool that is subjected to forced air flow under atmospheric and normal gravity conditions. Hirano and Kinoshita [28] have reported experimental studies on a diffusion flame stabilized in the free-stream of air over a liquid fuel. The gas velocity and temperature profiles across the laminar boundary layer with a diffusion flame established over methanol or ethanol were measured with the free stream of air parallel to the liquid-fuel surface. The experiments were conducted in a rectangular combustion chamber of 3 cm $\times$ 9.8 cm cross-section and 13.5 cm long. Air was supplied

from a blower and was allowed to flow parallel to the liquid-fuel surface. A water cooled fuel vessel of 2.6 cm wide, 8.0 cm long and 1.0 cm deep was mounted flush with the lower wall of the combustion chamber. Methanol or ethanol were supplied from another vessel fed by gravity. A Pt / Pt-13% rhodium thermocouple having a wire diameter of 0.0025 cm was used to measure the temperature profiles across the boundary layer and the temperature was corrected for thermometric errors due to radiation. Figure 4.1 shows the experimental setup of Hirano and Kinoshita. Numerical simulations described in this chapter were carried out in Ansys Fluent to simulate the experiments of Hirano and Kinoshita [28].
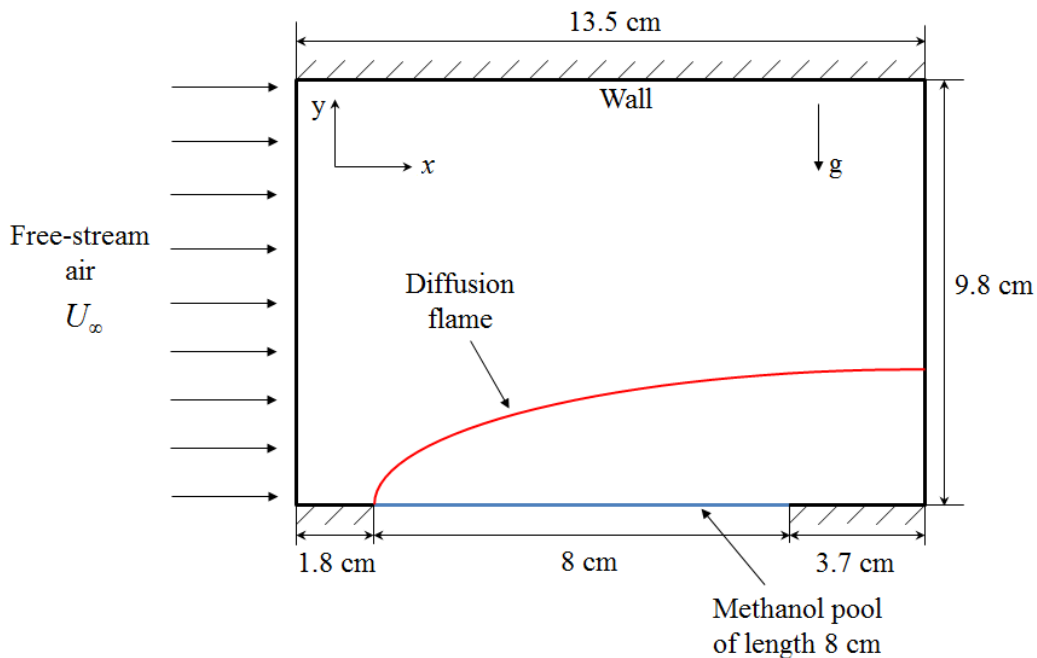
Figure 4.1: Schematic of Hirano and Kinoshita's [27] experimental configuration.

4.1.1. Numerical Model

In the present study, 2D transient numerical simulations of laminar diffusion flames established over a methanol or ethanol pool under a forced convective environment are carried out using commercial CFD software, Ansys Fluent. The salient features of the numerical model include temperature and concentration dependent thermo-physical properties such as density, specific heat, thermal conductivity and viscosity, multi-component species diffusion, multi-step chemical kinetics mechanism, and a detailed Discrete Ordinates radiation model. The governing equations involving conservation of species, mass, momentum and energy in Cartesian coordinates, are described in Appendix B. A Finite Volume Method (FVM) based discretization approach and SIMPLE algorithm for pressure velocity coupling are employed for solving the governing transport equations. A second order upwind scheme has been employed in convective terms. A laminar species transport model is used along with finite rate chemistry. Full multi-component diffusion along with a diffusion energy source is used to model the species diffusion. A skeletal mechanism for methanol-air diffusion flames has been obtained from Chen et. al. [119]. The skeletal mechanism of methanol oxidation consists of 30 reactions steps and 17 species. Similarly, to simulate the ethanol pool, a reduced reaction mechanism for ethanol oxidation was employed from Vaz et al. [120]. The reduced mechanism of ethanol oxidation

consists of 18 elementary reactions and 15 species. The effect of normal gravity has been taken into account in the given model. The flow induced due to density differences (naturally convective flow) is achieved by adding buoyancy source terms in the momentum equations. Variable thermo-physical properties in the gas phase are calculated as follows. Density (ρ) is calculated using the ideal gas equation of state and mixture molecular weight. Viscosity (μ) and thermal conductivity (k) are evaluated as a function of temperature and molecular weight using kinetic theory. In order to evaluate the specific heat of each species, piece-wise polynomials in temperature have been employed from CHEMKIN thermodynamic database. Mass diffusivity for any species diffusing into the mixture has been calculated using a multi-component diffusion approach. The effect of gravity-driven flow is considered in the given case. The governing equations for mass, momentum, species and energy conservation in the gas-phase are given in Appendix B. Grid sizes are chosen after a careful grid independence study. It has been found that for this problem, a grid of approximately 550 $\times$ 400 cells in x and y directions provides a good balance between solution accuracy and computational economy. The given numerical model was validated against the experimental data of Hirano and Kinoshita [28].

4.1.2. Numerical Domain and Boundary Conditions

The boundary conditions for the given CFD model are described in this section. More details on the initial and boundary conditions can be found in Appendix B. Figure 4.2 shows the computational domain along with relevant boundary conditions in order to simulate steady burning of methanol pool in a forced-convective environment. The leftmost boundary in Figure 4.2 has been modeled as an air inlet boundary. At the air inlet, a uniform velocity of air is given as the boundary condition with an oxygen mass fraction of 0.23 and a constant temperature of 300 K. At the exit boundary, the flow with the products of combustion leaves to the atmosphere. Due to the buoyancy driven flow, an incoming flow can also occur at this boundary for a few cells. Therefore, a pressure outlet condition, which drives the flow with respect to the local pressure gradient, has been chosen at this boundary. The pressure outlet boundary conditions require the specification of a static gauge pressure at the outlet boundary. All other flow quantities are extrapolated from the interior. For reversible flow from the exit, proper back flow conditions such as ambient temperature and chemical species mass fractions (0.23 for oxygen and 0.77 for nitrogen) are specified. The top and bottom walls have been modeled as zero thickness walls with a no slip condition for the velocities at the wall and an adiabatic condition for the temperature. For species, its first derivative is set to zero at the

wall. The adiabatic condition used at the lower wall may have some deviations from

Wall $u=0, v=0, \dfrac{\partial T}{\partial y}=0, \dfrac{\partial Y_i}{\partial y}=0$

Velocity inlet

Pressure outlet

$u=U_\infty, v=0, T=T_\infty$

$Y_{O_2}=0.23, Y_{N_2}=0.77$

y

x

g

Diffusion
flame

$\left(\dot{m}/V\right)=k\left(\partial T/\partial y\right)_s/L_{eff}\,\Delta y$

Interface boundary
condition

Wall

Wall

Fuel pool length, L

x/L=0

x/L=1.6875
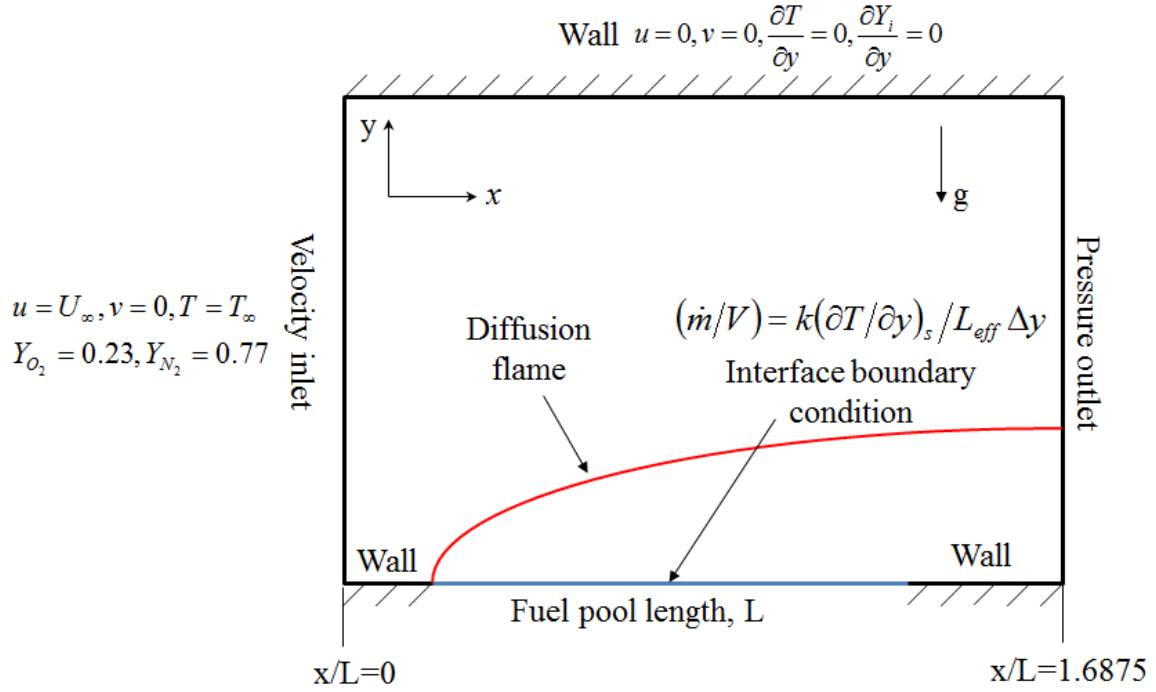
Figure 4.2: CFD model to simulate steady burning of methanol pool in a forced convective environment.

the actual boundary condition existing in the experimental setup [28]. Hirano and

Kinoshita did not describe the conditions prevailing at the combustor walls for their

experiments [28]. The boundary condition at the methanol pool interface was spec-

ified as a liquid-gas interface with no slip boundary condition for tangential velocity

(x-direction velocity) and no liquid-phase heating effects at the film/pool surface.

Ignition of the fuel vapor is achieved by bringing high temperature air into the sys-

tem for a short duration of time. More details on the initial and boundary conditions along with solution procedure are given in Appendix B.

Interface boundary conditions at the liquid-gas interface are defined in Appendix B and are very similar to the one employed by Raghavan et al. [53]. A user-defined function is used to create a mass source at the interface that is based on an energy balance at the surface of the fuel film. This allows for the liquid film to be maintained at the interface at all times. The moving boundary layer effects due to the regression of liquid pool surface are therefore minimized in the numerical simulations by creating a mass source at the interface. The energy balance across the liquid-gas interface is modeled by assuming that heat feedback from the flame to the liquid fuel surface is equal to the energy needed to vaporize the fuel. In order to create a mass source at the interface, radiation from the flame and energy loss into the liquid pool were assumed to be negligible since conductive (or convective) heat transfer was found to be the dominant mode of heat transfer in such flames. The user-defined function was $\dot{m}/V = k(\partial T/\partial y)_s/L_{eff}\Delta y$, where k is the thermal conductivity of the gas, $(\partial T/\partial y)_s$ is the temperature gradient at the film surface, $\dot{m}/V$ the burning rate per unit volume (computational cell volume), L_{eff} the effective latent heat of vaporization of the liquid fuel and Δy the height of the row of fluid cells. This allows for the liquid film to be maintained at the interface at all times.

Local mass burning rate at each streamwise location is calculated from the expression, $\rho_s v_s$, where ρ_s represents the gas phase density of the pool surface and v_s represents the Stefan mass transfer velocity (normal velocity component at the liquid surface). More details on calculating the Stefan mass transfer velocity (v_s) are given in Appendix B.

4.1.3. Numerical Simulation Results for Forced-convective Boundary-layer Diffusion Flames

4.1.3.1 Average Mass Burning Rate and Flame Stand-off Distance

Liquid fuel combustion is dominated by the evaporation or the mass transfer rate, governed by Fick's law of diffusion. Thus, the normal gradient of fuel vapor mass fraction and the binary mass diffusivity of fuel vapor into the mixture, will determine the evaporation rate. In addition, the heat transfer from the flame to the fuel surface will also govern the mass burning rate.

The mass-transfer rate of any fuel is the value of the normal gradient of fuel vapor mass fraction at the fuel interface. Spalding [121] showed that the gradient of fuel vapor mass fraction is related to the temperature gradient, which is further related to the shear stress at the fuel surface. Thus, mass, heat and momentum transfers are intrinsically coupled. The value of the average mass burning rate is calculated

using the following equation, $\overline{\dot{m}_f''} = (\frac{1}{L}) \int_0^L \rho_s v_s dx$, where L represents the length of the condensed fuel surface, ρ_s represents the gas phase density of the pool surface and v_s represents the Stefan mass transfer velocity (normal velocity component at the liquid surface).
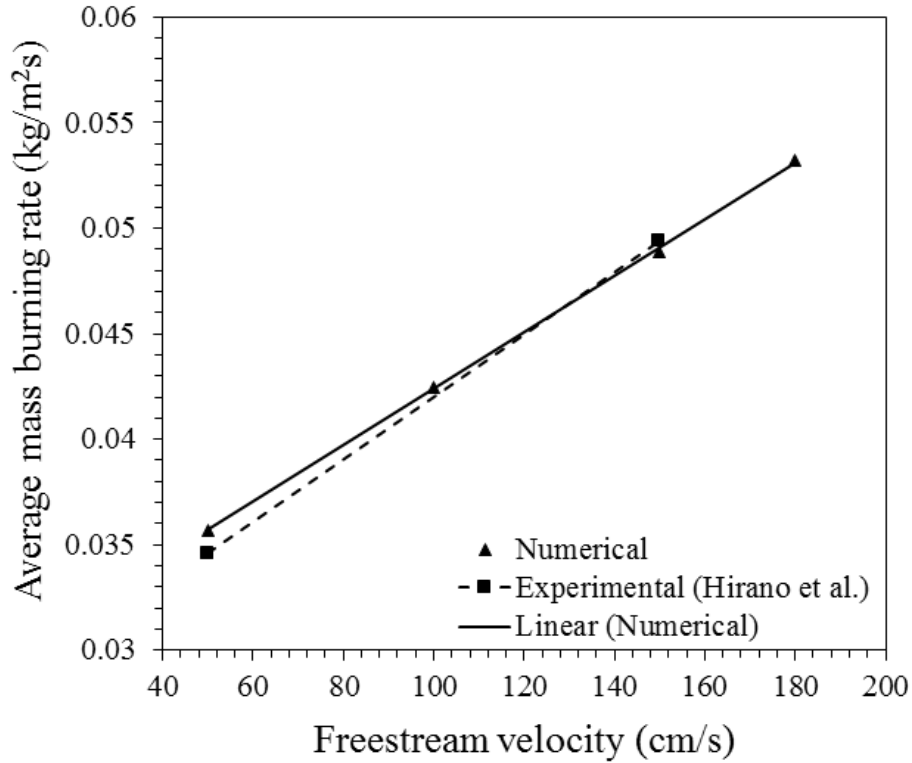
Figure 4.3: Variation of average mass burning rate per unit area with freestream velocity for a methanol boundary-layer diffusion flame. Experimental results from Hirano and Kinoshita are also plotted for validation and reference [27].

Figure 4.3 shows the variation of average mass burning rate per unit area with

118

freestream velocity. Also, plotted are the experimental results of Hirano and Ki-noshita [28] for comparison and numerical validation. It is seen that the average mass burning rate increases monotonically with increase in air velocity.

Flame standoff distance is taken as the distance measured from the pool surface to the center of the flame zone where peak temperature is recorded. Figure 4.4 shows the variation of non-dimensional flame standoff distance $(y_f^* = y_f/L)$ at several locations along the pool surface for methanol and ethanol boundary-layer diffusion flames established under different freestream velocities. Figure 4.4 shows a reduction in the non-dimensional flame standoff distance (y_f/L) with freestream velocity. At a given x-location, the flame standoff distance reduces as the freestream velocity increases due to decrease in the overall boundary layer thickness at higher freestream velocities. Due to a reduction in the flame standoff distance, increased heat transfer to the fuel surface is possible, which also supports the increased burning rate of fuel. Even though the flame standoff distance reduces with increasing freestream velocity, its variation becomes negligible after a certain value of freestream velocity, here greater than 1.8 m/s. This is primarily due to the combined effect of increased air flow and the subsequent increase in the fuel burning rate. In other words, after a certain value of freestream velocity, an increase in fuel burning rate with U_∞ results in a convection dominant (negligible diffusive-mode) fuel and oxidizer transport. Thus, an almost

constant flame zone prevails and the flame standoff distance does not change.

Furthermore, for a given freestream velocity, the flame standoff distance increases as we move downstream from the leading edge towards the trailing edge of the fuel surface. It can be clearly seen that at low freestream velocities (0.5-1.0 m/s), the overall flame shape changes from convex to concave, since the flame is pushed upwards by buoyancy induced flow, thereby giving a larger standoff distance near the domain exit. Similarly, for higher freestream velocities greater than approximately 1.0 m/s, since inertial effects dominate, the overall flame shape is closer to a typical boundary layer shape.
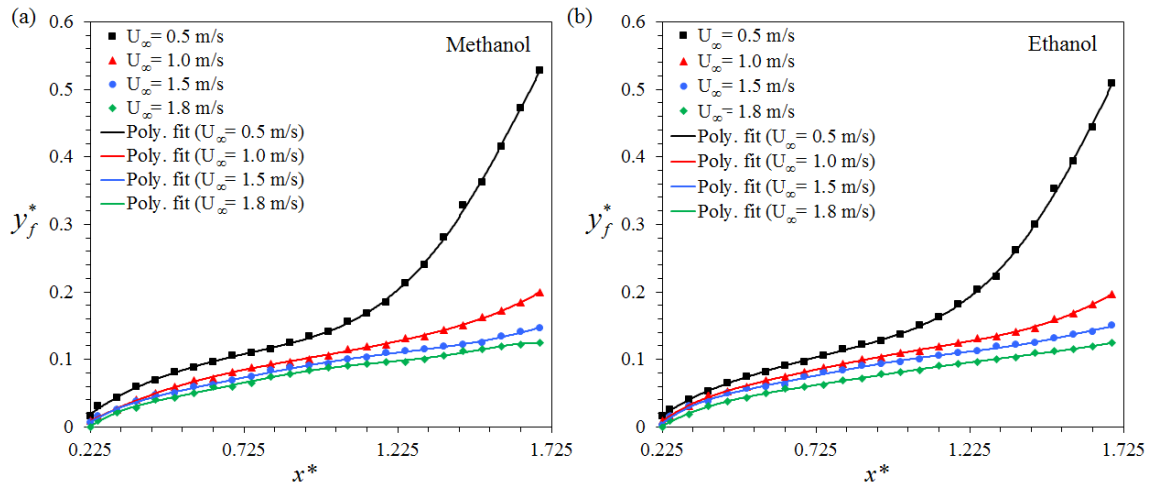
Figure 4.4: The flame stand-off distance at different locations along the pool surface for (a) (left) methanol and (b) (right) ethanol boundary-layer diffusion flames established under different freestream velocities.

4.1.3.2   Temperature and Flow Field

The structure of the flame in terms of temperature and velocity contours in the x and y-direction is presented in this section. Figure 4.5 shows the temperature contours for methanol and ethanol boundary-layer diffusion flames stabilized at different freestream velocities indicating the high temperature reaction zone.
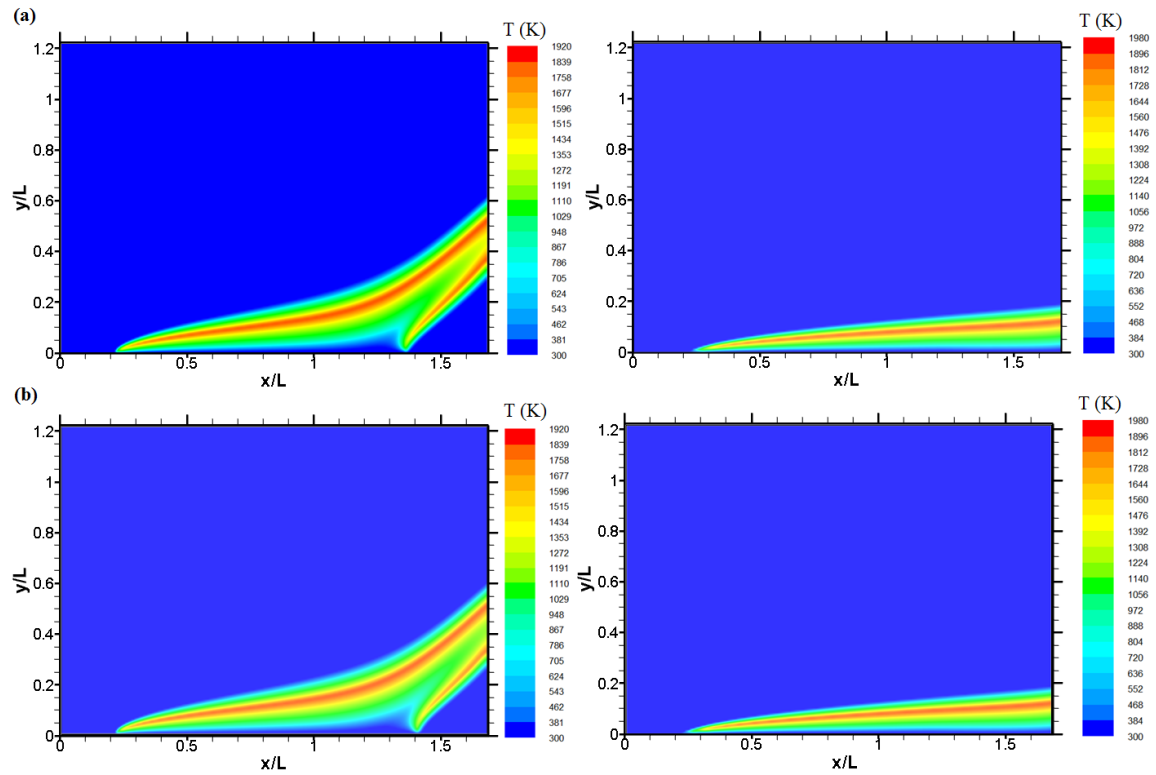
Figure 4.5: Temperature contours at various streamwise locations x along the fuel surface for (a) (top) methanol and (b) (bottom) ethanol boundary-layer diffusion flames stabilized at $U_\infty = 0.5$ (left) and 1.8 (right) m/s.

It is evident that for a given U_∞ and at a given x-location, the temperature increases in the y-direction to a maximum value in the flame zone and then decreases to ambient temperature at some y-location on the freestream side.

Figure 4.6 show the velocity magnitude contours for a methanol boundary-layer diffusion flame stabilized at different freestream velocities. Figures 4.5 and 4.6 show that for a low freestream air velocity (0.5 m/s), the flame has a first anchoring point just before the leading edge of the pool (x/L slightly less than 0.225) and a second anchoring point downstream of the trailing edge ($x/L > 1.225$). It is clear that due to buoyancy, a re-circulatory flow is induced near the domain exit due to which a second flame anchoring point exists near $x/L = 1.4$. Also, the flame is lifted upwards near the domain exit due to buoyancy and its shape changes from convex to concave. For this case, the buoyancy induced flow could create an air entrainment from the exit, thereby pushing the flame up. This creates a typical stretch in the flame in that region.

It has been observed that for air velocities less than 1.0 m/s, the second flame anchoring point occurs at x-locations well within the computational domain length of 13.5 cm ($x/L = 1.6875$), due to buoyancy induced flow from the domain exit. However, as the freestream air velocity increases, the second flame anchoring location shifts further downstream. At even higher velocities (greater than approximately
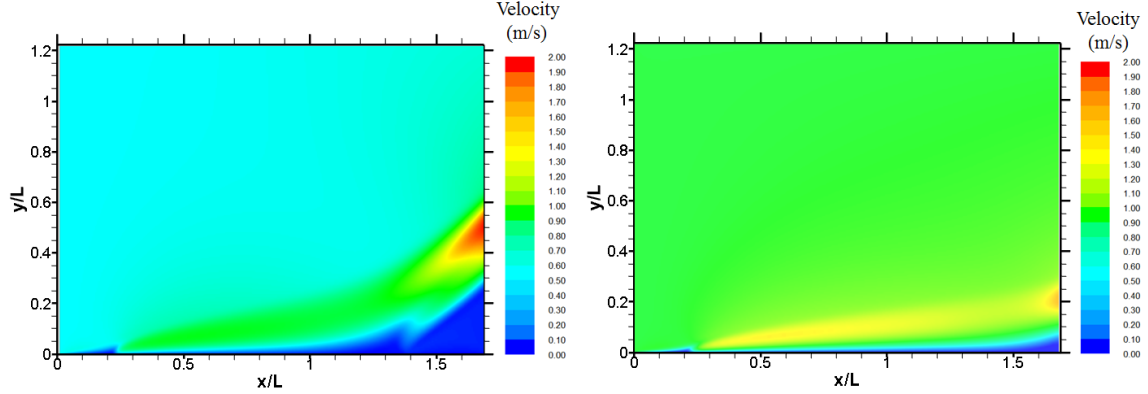
Figure 4.6: Velocity magnitude contours across the boundary layer at various streamwise locations x along the methanol fuel surface for $U_\infty = 0.5$ (left) and 1.0 (right) m/s.

1.0 m/s), the flame no longer anchors downstream of the trailing edge, within the computational domain. For instance, at a higher velocity of 1.8 m/s, the flame does not have a second anchoring point, as shown in the temperature contours in Figure 4.5. Similar observations were also made in the subsequent experimental studies described in Chapter 6.

It can be noted from Figure 4.5 that the effect of increasing air velocity is small on the location of the upstream anchoring point of the flame. Furthermore, when the air velocity is increased beyond 2.0 m/s, the flame moves away from the leading edge and sustains as a lifted flame. Similar observations were reported in the experiments of Hirano and Kinoshita as well [28]. However, in the present study only the stable flames anchored near the leading edge of the pool have been considered.

4.1.3.3   Thermal and aerodynamic structure of the flame

The temperature profiles at several streamwise x-locations, for freestream velocity cases of 0.5 m/s and 1.8 m/s, are shown in Figures 4.7 (a) and (b). It is evident that for a given freestream velocity at a given x-location, the temperature increases in the y-direction to a maximum at the flame zone and then decreases to ambient temperature at some y-location on the freestream side. This trend is observed at all the x-locations upstream of the second flame anchoring point. For locations downstream of the second flame anchoring point, as observed in Figure 4.5, a profile with two temperature peaks is obtained. For instance, since a second flame anchoring point prevails for $U_\infty = 0.5$ m/s, a two-peak temperature profile is observed at x/L = 1.5 as shown in Figure 4.7 (a). Two-peak temperature profiles are expected for air velocities lower than 1.0 m/s, where a second flame anchoring point is present. For a given value of freestream velocity, the temperature gradient at the fuel surface, $(\partial T/\partial y)_{y=0}$, is found to decrease significantly along the streamwise direction. This can be attributed to an increase in the flame standoff distance from the pool surface. It is also observed from Figures 4.7 (a) and (b) that, as x/L increases, the peak flame temperature increases until x/L reaches a value around 0.35. Beyond this location, the peak flame temperature decreases gradually. The observed trend is independent of the freestream velocity and is consistent with the results reported in the literature

[28].

It is also observed that as U_∞ increases, the peak flame temperature at a given x/L location also increases slightly. This is due to an increase in the mass burning rate when air velocity is increased. This results in higher heat release rates and hence temperature. The temperature gradient at the fuel surface,$(\partial T/\partial y)_{y=0}$, is also found to increase at a given x/L location, with the increase in freestream air velocity, which is due to the reduction of the flame standoff distance at higher velocities.
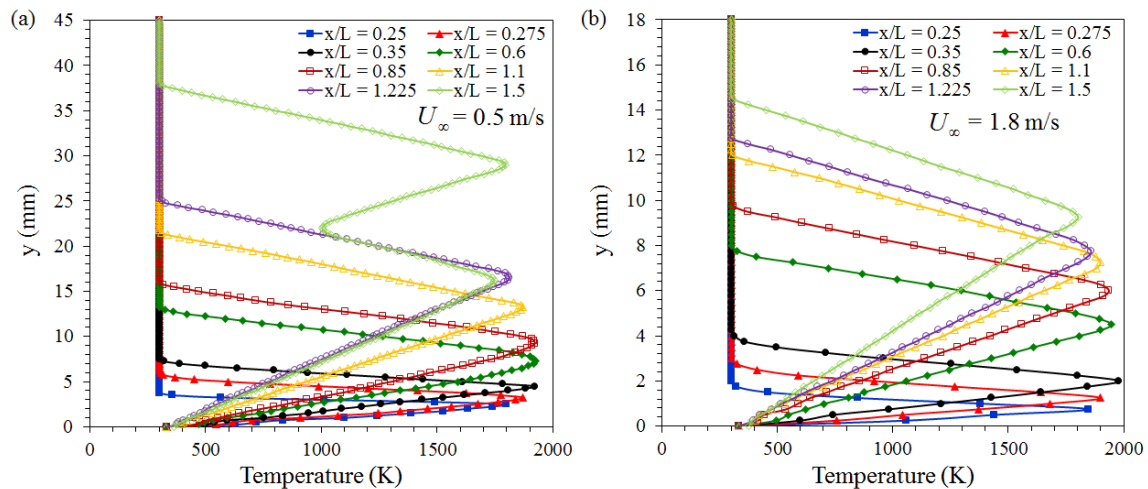
Figure 4.7: Temperature profiles at various streamwise locations for a methanol boundary-layer diffusion flame stabilized at U_∞ = (a) 0.5 m/s (b) 1.8 m/s.

An interesting feature of the velocity profiles within a reacting boundary layer is the occurrence of a velocity overshoot beyond the freestream velocity value at locations around the flame zone. The gas mixture is accelerated around the flame

zone because of local pressure gradient generated by the local temperature gradient and distortion of the streamline due to chemical reaction [27]. This shows that species diffusion is enhanced around the flame reaction zone. This is consistent with previous measurements reported in the literature [28, 27].
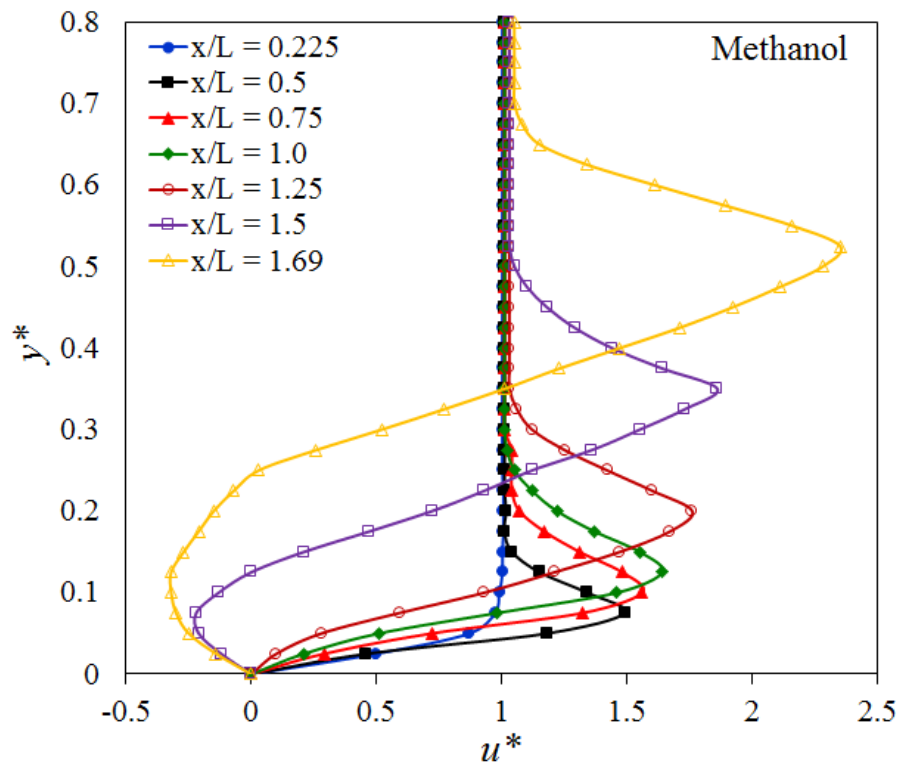
Figure 4.8: Variation of non-dimensional u-velocity profile at several streamwise locations for U_∞ = 0.5 m/s.

Figure 4.8 shows the non-dimensional u-velocity profiles, i.e., the variation of $u^* = u/U_\infty$ along the cross-stream direction, at various streamwise x-locations along

the pool length for a freestream velocity of 0.5 m/s. At any x-location, the u-velocity increases along the cross-stream direction to a maximum near the flame zone and then decreases to a value close to the freestream velocity and remain almost constant thereafter. As one moves downstream of the leading edge, the value of peak velocity increases and the y-location of the peak velocity increases. For a given freestream velocity, the velocity gradient at the fuel surface, $(\partial u/\partial y)_{y=0}$, is found to decrease along the pool surface which is due to an increase in the flame standoff distance.

Thus, both temperature and velocity gradients at the fuel surface follow a similar trend and thus the mass burning rate and shear stress at the fuel surface are intrinsically coupled. Emmons, in deriving his classical solution, showed that the rate of fuel evaporation and hence the rate of burning in the boundary layer is related to the shear stress at the surface [6]. Thus, the combustion rate in the boundary layer on a flat plate or a fuel surface is simply related to the velocity gradient at the surface. It can also be observed from Figure 4.8 that, beyond the trailing edge, the velocity profiles could be significantly different. The reason for this is that for this low velocity case (0.5 m/s), a buoyancy-induced recirculation zone having negative u-velocity is present downstream of the second flame anchoring point.

Non-dimensional velocity profiles at two streamwise locations, one within the pool length and the other at the domain exit, are shown in Figures 4.9 (a) and (b),

respectively. It is clear from Figure 4.9 that, at any x-location, as the freestream velocity increases, the velocity gradient at the fuel surface also increases as seen in the case of temperature profiles. This is mainly due to the reduction in the flame standoff distance at higher freestream velocities. It is also observed that the velocity overshoot at any x-location is higher at lower freestream velocity. This is because of the fact that at higher velocities, the inertial forces are able to overcome the enhanced species diffusion (dominated by convective transport), whereas at lower velocities the species diffusion velocity could become larger than the bulk velocity (dominated by diffusive transport).
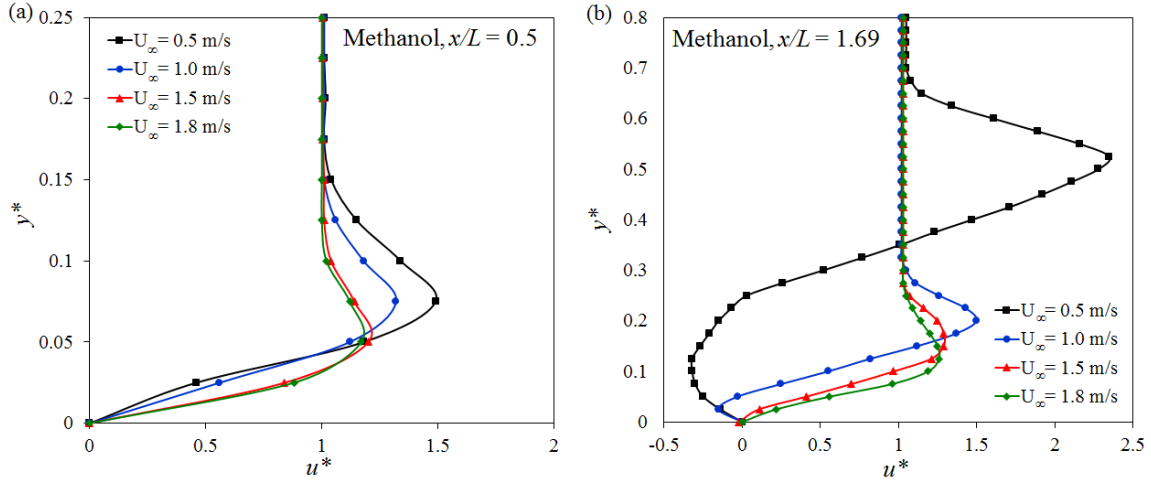
Figure 4.9: Non-dimensional u-velocity profiles for different freestream velocities at $x/L =$ (a) 0.5 and (b) 1.69.

Figure 4.9 (b) shows negative velocity profiles for the cases in which there is a sec-

ond flame anchoring point (U_∞ up to 1.0 m/s), which indicates the existence of a recirculation zone at lower freestream velocities. For higher freestream velocities, the velocity profiles become almost the same indicating that the flow-field and flame zone do not get affected beyond a particular freestream velocity due to convection-dominated reactant transport.

4.1.3.4 Local Mass burning rate and fuel vapor mass fraction gradient

At a given x-location, as U_∞ increases, the fuel vapor mass fraction gradient at the surface, $(\partial Y_f/\partial y)_{y=0}$, also increases due to increased transport of oxygen near the surface. Figure 4.10 shows an increase in the mass fraction gradient of fuel vapor at the fuel surface with an increase in freestream velocity at a given streamwise location.
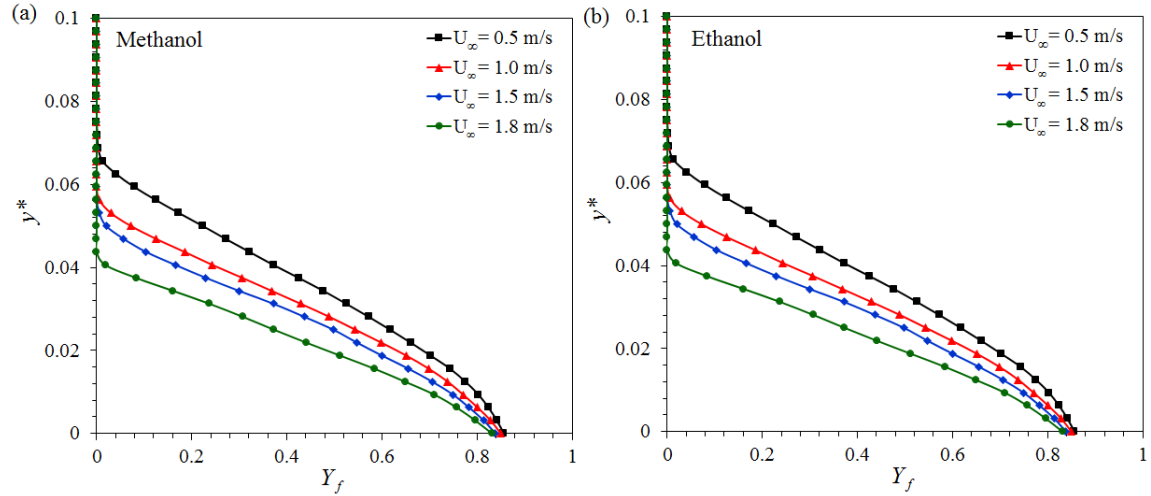
Figure 4.10: Profile of fuel vapor mass fraction at $x/L = 0.5$ for (a) (left) methanol and (b) (right) ethanol boundary-layer diffusion flames stabilized under different freestream velocities.

Due to an increase in $(\partial Y_f/\partial y)_{y=0}$, the fuel evaporation rate increases in accordance with Fick's law of diffusion. Therefore, at higher freestream velocities, the fuel vapor is required to travel a shorter distance before mixing with oxygen to produce a flammable mixture. Consequently, as freestream velocity increases, the flame standoff distance decreases.
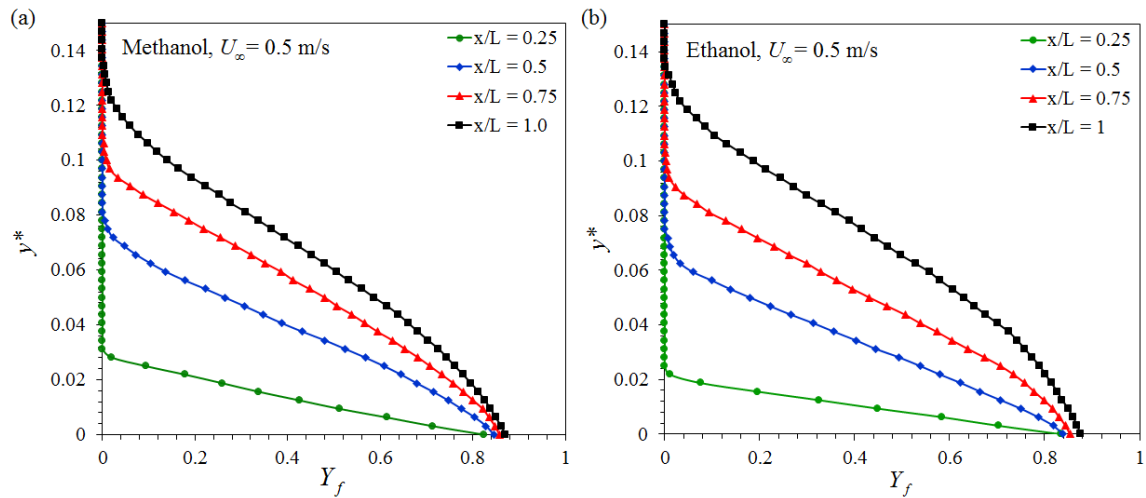
Figure 4.11: Profile of fuel vapor mass fraction at different x-locations for (a) (left) methanol and (b) (right) ethanol boundary-layer diffusion flames stabilized at $U_\infty = 0.5$ m/s.

For a given freestream velocity, the gradient of fuel vapor mass fraction at the fuel surface, $(\partial Y_f/\partial y)_{y=0}$, decreases along the streamwise direction x from the leading edge of the pool. Figure 4.11 shows fuel vapor mass fraction profiles at various streamwise locations for $U_\infty = 0.5$ m/s. Since the flame standoff increases with increase in the x-location from the leading edge, there is a consequent decrease of

heat transfer to the fuel surface at locations away from the leading edge. Also, there is a decreased transport of oxygen towards the fuel surface at locations away from the leading edge. This is due to unavailability of fresh oxygen at locations away from the leading edge (due to diffusion of combustion products). Therefore, due to reduction in heat and mass transfer to and from the pool surface, the mass burning rate decreases along the pool length.

Figure 4.12 shows the variation of local mass burning rate along the pool length for methanol and ethanol boundary layer diffusion flames stabilized at different freestream velocities.
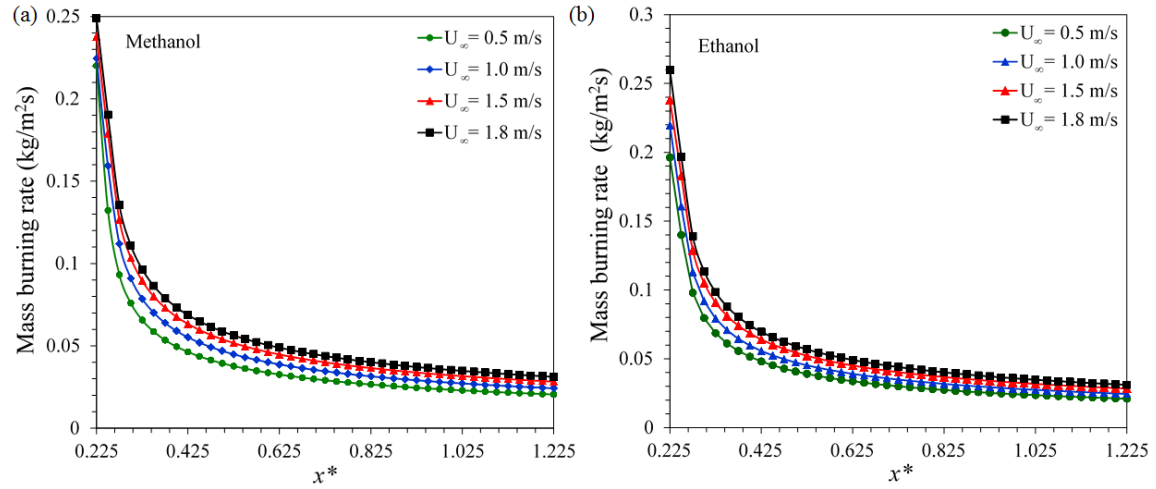
Figure 4.12: Variation of local mass burning rate along the pool length for (a) (left) methanol and (b) (right) ethanol boundary-layer diffusion flames.

Due to the availability of fresh oxidizer, higher convective heat feedback, higher

131

temperature gradients and lower standoff distances near the leading edge, the local burning rate is highest here and subsequently decreases as we move downstream towards the trailing edge. Also, the local mass-burning rates for a methanol and ethanol boundary layer diffusion flame is almost proportional to $x^{-0.5}$, confirming the power-law relationship for laminar forced-convective burning on a horizontal surface [6].

4.2. Steady Burning of a Methanol and Ethanol Film in a Free Convective Environment

Earlier, a numerical study of laminar diffusion flames established over a condensed fuel, inclined at several angular orientations with respect to the vertical axis, under atmospheric pressure and normal gravity environment was presented by Ali et al. [7]. Later, authors [55] carried out numerical analysis of flame heating on arbitrarily oriented condensed fuel surfaces.

In the present study, similar numerical investigations were carried out for a naturally convective laminar boundary-layer type flame with an attempt to look closely at the mass-burning rate correlation using Ansys Fluent. A schematic of quasi-steady burning of a vertical methanol and ethanol fuel surface of length L, under normal gravity conditions, is shown in Figure 4.13. The vertical axis (x-axis), in line with the

normal gravity direction, is parallel to the film surface. The simulations were carried out for a vertically-oriented fuel surface. For this case, the x-axis will be parallel to fuel surface, $x/L=0$ represents the fuel leading edge and $x/L = 1$ represents the fuel trailing edge, with the y-axis perpendicular to the fuel surface. The fuel length (L) is taken as 80 mm in the present study.

The salient features of the numerical model include temperature and concentration dependent thermo-physical properties such as density, specific heat, thermal conductivity and viscosity, multi-component species diffusion, multi-step chemical kinetics mechanism, and a detailed Discrete Ordinates radiation model, similar to the model described in Section 4.1.1. The effect of gravity-driven flow is specifically considered in the given case. Grid sizes are chosen after a careful grid independence study. It has been found that for this problem, a grid of 800×200 cells in x- and y-directions provide a good balance between solution accuracy and computational economy.

4.2.1. Numerical Domain and Boundary Conditions

The initial flow field within the computational domain is assumed to be quiescent $(u = v = 0)$ and only air $(Y_{O_2} = 0.23$ and $Y_{N_2} = 0.77)$ is present at an ambient temperature of 300 K. The typical boundary conditions are also illustrated in Figure 4.13. Liquid fuel combustion is dominated by the mass-transfer process, especially

for volatile fuels such as alcohols and gasoline. Methanol has a high volatility as well as a low boiling point (337 K). Accordingly, even at an ambient temperature of 300 K, a sufficient amount of vapor is present on top of the methanol pool. The boundary conditions at the fuel film surface are assumed to be of a liquid-gas interface type are described in Appendix B .

The leftmost boundary has been modeled as zero thickness walls with a no-slip condition for the velocities and an adiabatic condition for the temperature. At the walls, normal gradients of the temperature and the mass fractions of all species are set to zero, in addition to no-slip conditions for velocities. At the top, bottom and rightmost boundaries, a pressure-specified boundary condition has been imposed. At pressure-specified boundaries, atmospheric pressure is assumed to prevail. The normal gradient of all other variables are set to zero. The density variations with temperature and composition of the mixture are accounted for using equation of state and ideal-gas mixing rule. The flow induced due to density differences (natural convective flow) is achieved by adding buoyancy source terms in the momentum equations. A time step of 1×10^{-5} s is used for the computations. All other flow quantities are extrapolated from the interior. For reversible flow from the exit, proper back-flow conditions such as the ambient temperature and chemical species mass factions (0.23 for oxygen and 0.77 for nitrogen) are provided.
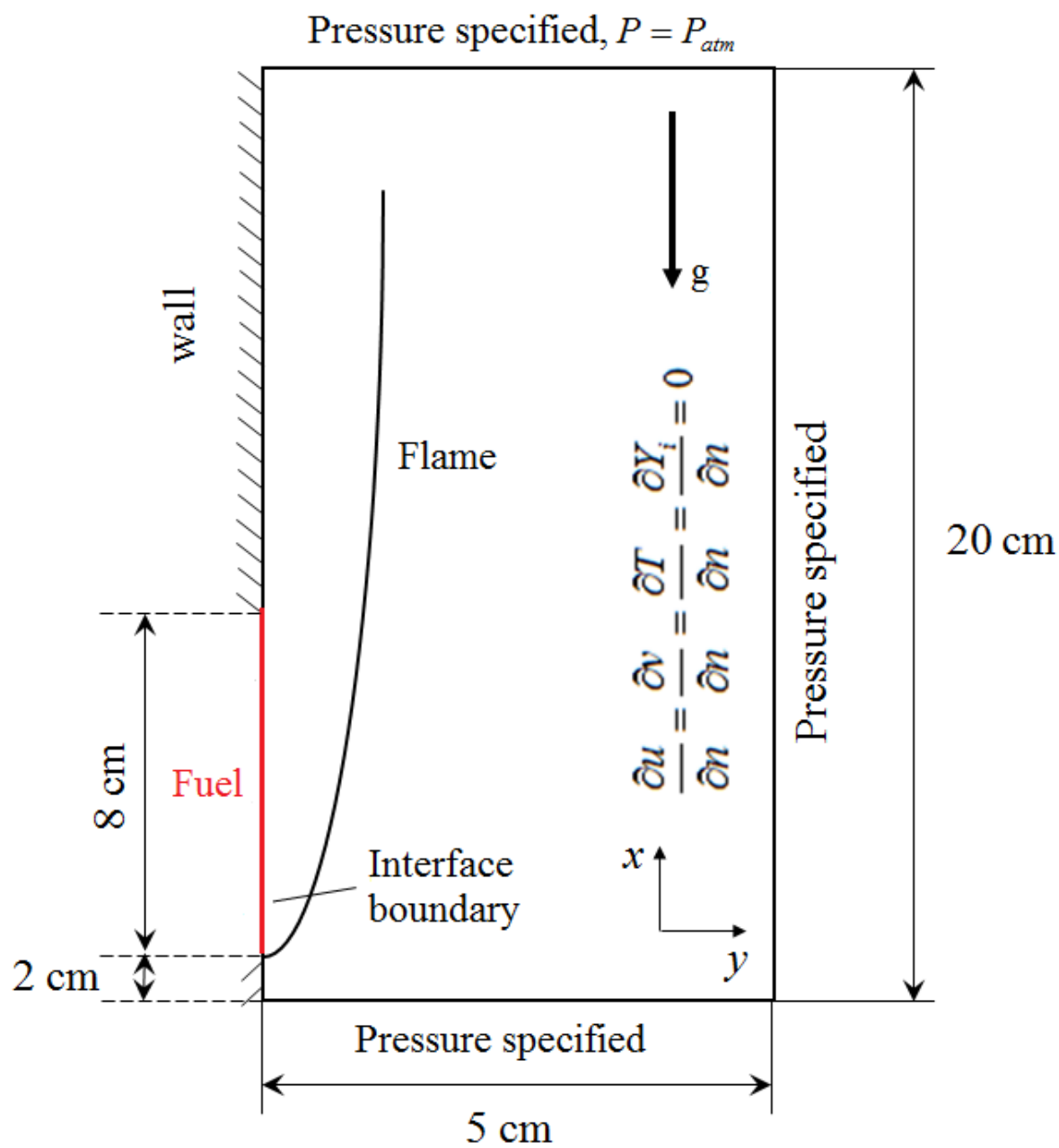
Figure 4.13: Computational domain and boundary conditions used to model a buoyancy-enhanced vertical diffusion flame.

4.2.2. Numerical Simulation Results for Free-convection Boundary-layer Diffusion Flames

4.2.2.1 Temperature and Flow Field

Figure 4.14 show the temperature and velocity contours for a vertically-oriented methanol boundary layer diffusion flame. The maximum flame temperature is predicted to be around 1920 K for this case. For the vertical case, the flame is anchored at a location ahead of the leading edge, at x/L = -0.03 which seems to be in good agreement with the experimental results obtained in this study (described in Chapter 5). The flame anchoring point is taken as the location of the maximum temperature on the solid surface measured from leading edge of the fuel surface. The velocity contour plot for the given case shows that the flow does not diverge away from the plate surface but remains almost parallel to the surface.

It is evident from Figure 4.14 that for the vertically-oriented flame, the temperature increases in the perpendicular direction to a maximum value and then decreases to an ambient temperature at some location away from the fuel surface. Similarly, the tangential velocity profile also increases in the normal direction from a zero value at the surface to a maximum value around the flame zone and then decreases further away tending to a zero value. In this case, the maximum velocity occurs near the

trailing edge of the fuel surface, due to the acceleration of hot gases around that region. The hot combustion products are accelerated further in the combusting plume region, giving rise to higher velocities.
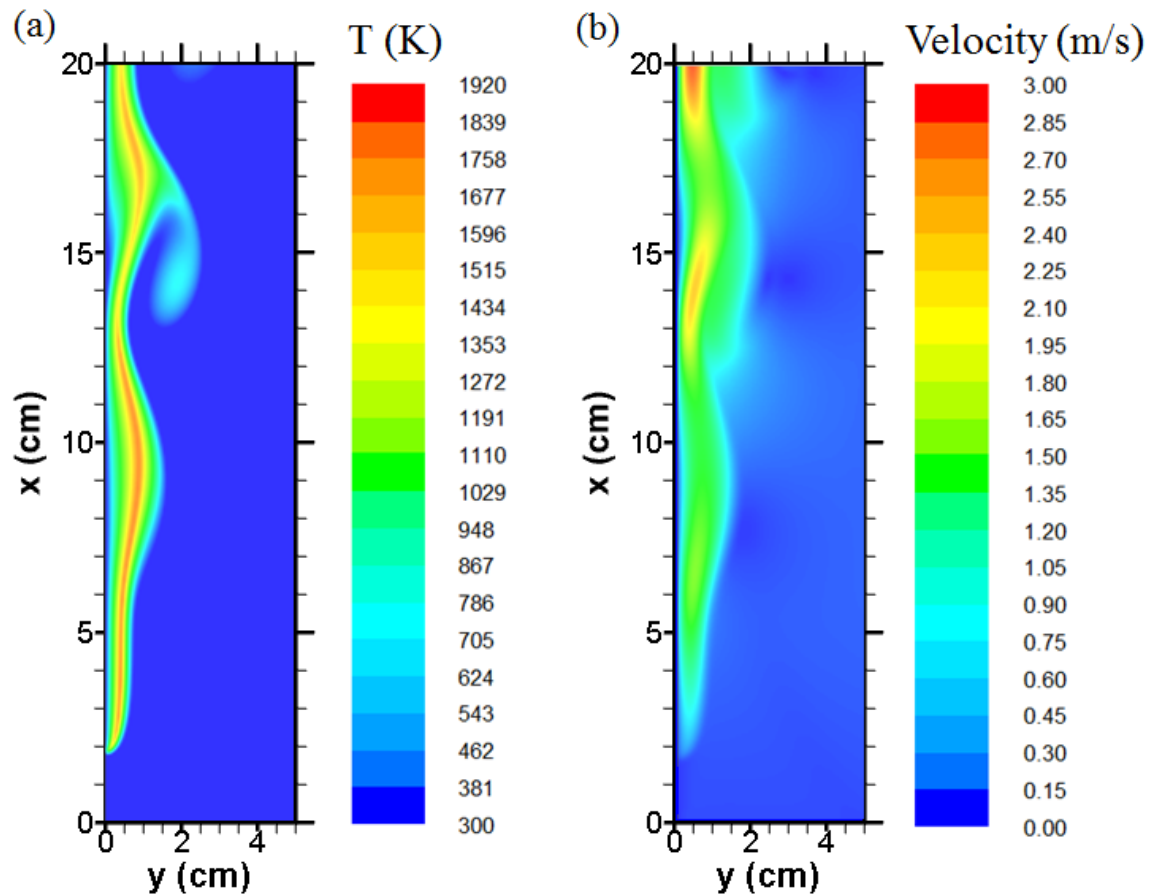
Figure 4.14: Temperature and velocity magnitude contours for a free-convection methanol boundary-layer diffusion flame after 75000 time steps. A quasi-steady state is attained approximately after 90000 time steps.

Figures 4.15 (a) shows the variation of flame standoff distance at several streamwise

locations along the fuel surface for a vertically-oriented methanol boundary-layer diffusion flame. Experimental flame standoff distance results (described in Chapter 5) are also plotted for comparison. When the gradient of fuel vapor mass fraction at the fuel surface $(\partial Y_f/\partial y)_{y=0}$ is large, the fuel vapor travels a short distance before mixing with the oxidizer. This results in a lower flame stand-off distance. Heat transfer to the fuel surface is enhanced when there is a reduction in the flame stand-off distance near the anchoring point. The flame stand-off distance is lower near the leading edge and it increases further downstream up to the trailing edge. This leads to enhanced heat transfer to the fuel surface at leading edge and hence higher evaporation rates of the fuel at this location. Accordingly, the local burning rate becomes highest at this location. The flame stand-off distance is higher for the regions near the trailing edge and hence heat transfer at these locations is lower. Due to lower rates of heat transfer at these locations, the local mass-burning rates are lower at these locations. It is evident from Figure 4.15 (a) that for the vertical case, the flame is anchored at a location slightly upstream of the leading edge. In experiments, the flame anchoring location for a methanol flame was found to be at 2.63 mm (upstream) from the leading edge of the fuel surface. Numerical results show a close agreement with experimental results and predict the flame anchoring location to be at 2.41 mm (upstream) from the leading edge of the fuel surface.

Figure 4.15 (b) presents the temperature profile at several streamwsie locations along the fuel surface for a vertically-oriented methanol diffusion flame. The temperature gradients in a direction normal to the fuel surface suggest that they are highest near the leading edge of the fuel surface and decrease further downstream towards the trailing edge. This results in higher convective heat transfer rates to the fuel surface near the leading edge and consequently higher burning rates at such locations. For the methanol flame, the highest peak temperature is approximately 1914 K, which occurs about 20 mm from the leading edge. Thereafter, the value of the peak temperature decreases slowly.
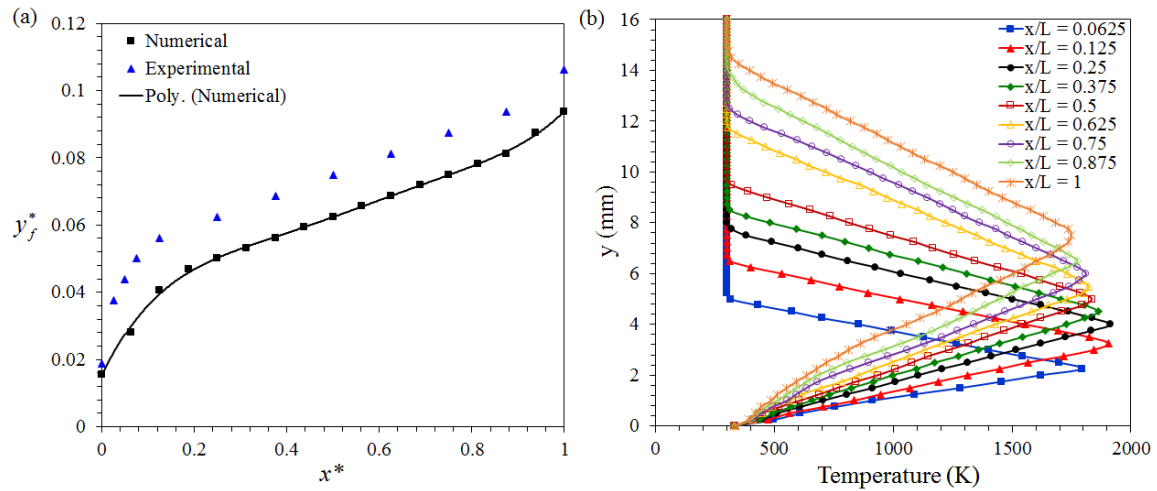
Figure 4.15: Variation of time-averaged (a) flame standoff distance and (b) temperature profiles at several streamwise locations along the fuel surface for a vertically-oriented methanol boundary-layer diffusion flame.

4.2.2.2 Local Mass Burning Rate

Figure 4.16 shows the variation of local mass burning rates along the length of the fuel surface for a vertically-oriented methanol and ethanol boundary layer diffusion flames. Theoretical results from Kim et al. [17] and experimental results obtained in this work are also plotted in Figure 4.16 for numerical validation and comparison.
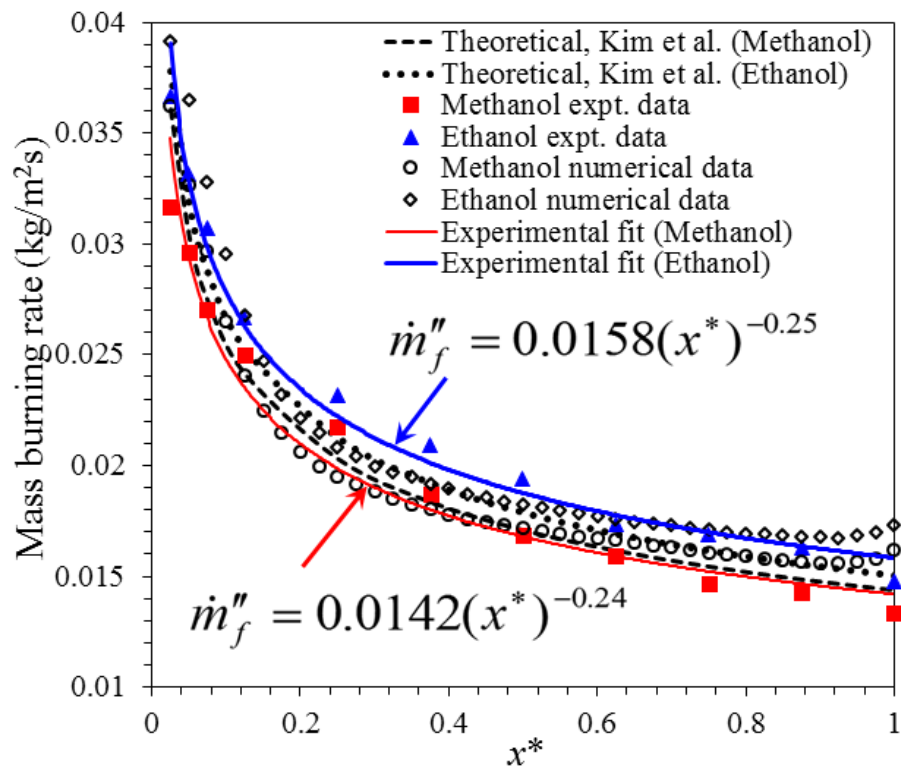
Figure 4.16: Variation of the local mass burning rate for a methanol and ethanol boundary-layer diffusion flame in a free-convective environment. The numerical results are also compared against the theoretical results of Kim et al. [16] and experimental results obtained in this work.

Close agreement of the theoretical, experimental and numerical results suggest that numerical simulations are capable of predicting local mass burning rates in such steady laminar flames. Since the experimental local mass burning rate was obtained by using the theoretical correlation in Eq. (9) (described in Chapter 5), the given plot also verifies and validates the use of theoretical correlation outlined in Eq. (9) as a useful methodology for estimating the local mass burning rates in such flames. The local mass burning rate was found to be highest near the leading edge and lowest near the trailing edge. The local mass burning rate decreases with streamwise direction x as we move downstream of the leading edge towards the trailing edge. Since the supply of fresh oxygen decreases with the distance x from the leading edge, it also plays a pivotal role in decreasing the local mass burning rate along the length of the fuel surface. It is observed that near the trailing edge of the fuel surface, the local mass burning rate increases slightly due to diffusion of oxidizer from the domain exit as shown in Figure 4.16 (for numerical computations).

4.3. Correlation Verification

The resulting temperature field from numerical simulations was used to compare the local temperature gradient to the local mass-burning rate, shown in Figure 4.17 for methanol under different forced and free-convective (vertical fuel) environments. When the local non-dimensional temperature gradient at the fuel surface,

$(\partial T^*/\partial y^*)_{y^*=0}$, was plotted against the corresponding local mass burning rate $(\dot{m}_f'')$ along the fuel surface, it results in a linear correlation irrespective of the flow conditions, similar to that proposed by Eq. (9).
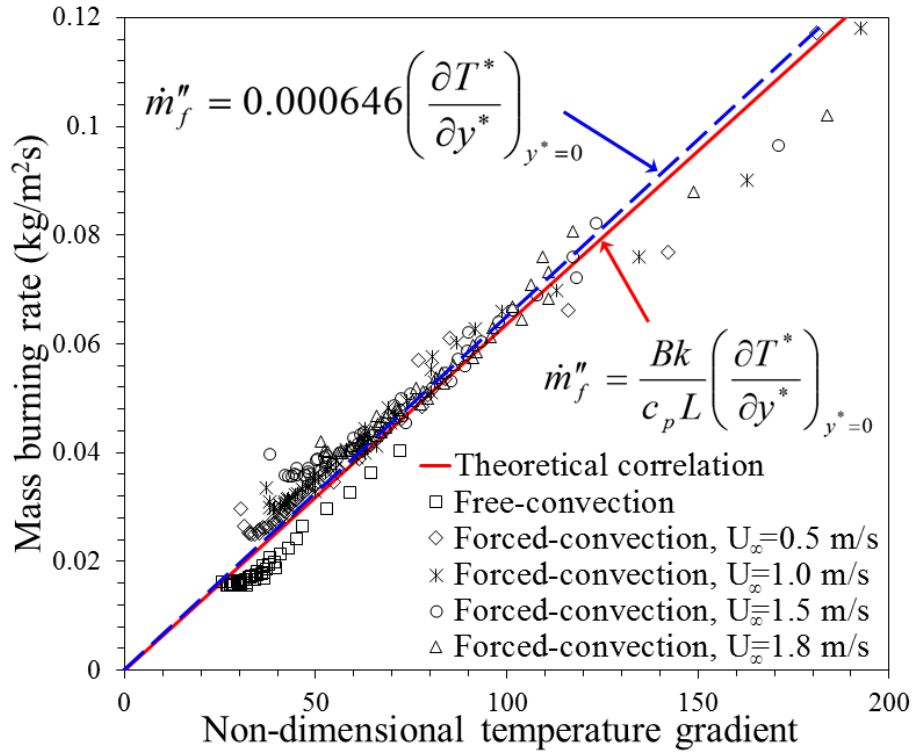
Figure 4.17: The local mass-burning rate per unit area vs. the non-dimensional temperature gradient at the fuel surface for numerical simulations of methanol flames under forced-convective and naturally-convective environments, with free-stream velocities U_∞ (m/s) over a fuel surface of length 8 cm. The dashed straight line indicates the linear fit through numerical data points indicated by symbols whereas solid straight line indicates the theoretical fit.

The slope of the linear curve was found to be equal to 0.646 g/m²s which is nearly

142

equal to Bk_w/c_pL for methanol, 0.627 g/m²s, using appropriate average values of B = 2.5 [8], k = 0.028 W/m-K [122], c_p = 1394.5 J/kgK [122] and L = 0.08 m. Here, k is the thermal conductivity of air evaluated at the pyrolysis wall temperature and c_p is the specific heat of the air evaluated at the adiabatic flame temperature of methanol T_{ad} = 2150 K, following the methodology by Kim, de Ris and Kroesser [17] where the mean specific heat was evaluated at the adiabatic flame temperature of the given fuel (outlined in Chapter 5).

4.4. Closure

A thorough numerical investigation of laminar boundary-layer diffusion flames established over the surface of a condensed fuel is presented. Two-dimensional transient numerical simulations of laminar diffusion flames established over a methanol and ethanol pool under both a forced convective and a vertically-oriented free-convective environment were carried out using commercial CFD software, Fluent 6.3. The results from the present study show that there is a unique correlation [Eq. (9)] between the local mass-burning rate and the local temperature gradient at a condensed fuel surface. The correlating factor depends upon the Spalding transfer number and gas-phase thermo-physical properties and works in the prediction of both integrated as well as local variations of mass burning rate. Numerical results closely support the given theoretical correlation. The correlation exists and holds good under both free

and forced (or mixed) convective environments. Methanol and Ethanol has been used as test fuels in this study. The study can be extended by using several types of liquid and solid fuels and the existence of the correlation in the case of a turbulent flame can be investigated in a future work.

Chapter 5: Free Convection Boundary Layer Diffusion Flames

This chapter discusses the experimental results obtained for free convection boundary layer diffusion flames (vertical wall fires). An experimental set-up was constructed to measure the burning rates and wall heat fluxes in a vertical wall fire. Local mass burning rates, local temperature gradients, flame stand-off distances, local wall heat fluxes, local convective heat transfer coefficients and profiles of mean temperatures were measured for methanol, ethanol and PMMA wall flames (for a 8×8 cm condensed fuel surface). Regression rates and regression profiles for a PMMA surface were also measured at different burn-out times.

Thermal and mass burning rate characteristics for a vertical wall fire is discussed in this chapter along with local heat flux distribution in the pyrolysis and plume zone for both liquid and solid fuels. Based on the experimental investigation, the theoretical correlation proposed earlier has been used for the estimation of local mass burning rates and flame heat fluxes over free convection laminar boundary layer diffusion flames. Convective and radiative heat feedback from such flames are also discussed. Additionally, a total heat flux gauge was used in the plume together with high spatial resolution temperature measurements to deconvolute the convective and radiative components of total flame heat flux incident on the heat flux gauge.

5. Free Convection Boundary Layer Diffusion Flames

5.1. Gas-phase temperatures

Using the experimental apparatus described in Chapter 3, measurements were taken for average mass-burning rates and local temperature profiles along condensed fuel surfaces. Figure 5.1 and 5.2 shows the temperature profiles at several streamwise locations along the condensed fuel surface for a methanol, ethanol and PMMA boundary layer diffusion flame (vertical wall fire). Under a free-convection environment, the temperature increases in the perpendicular direction to a maximum value and then decreases to an ambient temperature at some location away from the surface. Observation of the temperature gradients normal to the fuel surface suggests that they are highest near the leading edge and decrease further downstream. The peak temperatures at the flame front show a similar trend, reaching a maximum of 1915 K and 1888 K for the methanol and ethanol flames, respectively, $\sim$10 mm downstream of the leading edge. At the trailing edge of the sample, the peak temperature drops by about 151 K and 173 K for methanol and ethanol wall flames, respectively. This temperature decrease is primarily due to convective heat losses. The temperature of the condensed fuel surface also decreases with x, however this change was very slight. The temperature of the condensed fuel surface was found to
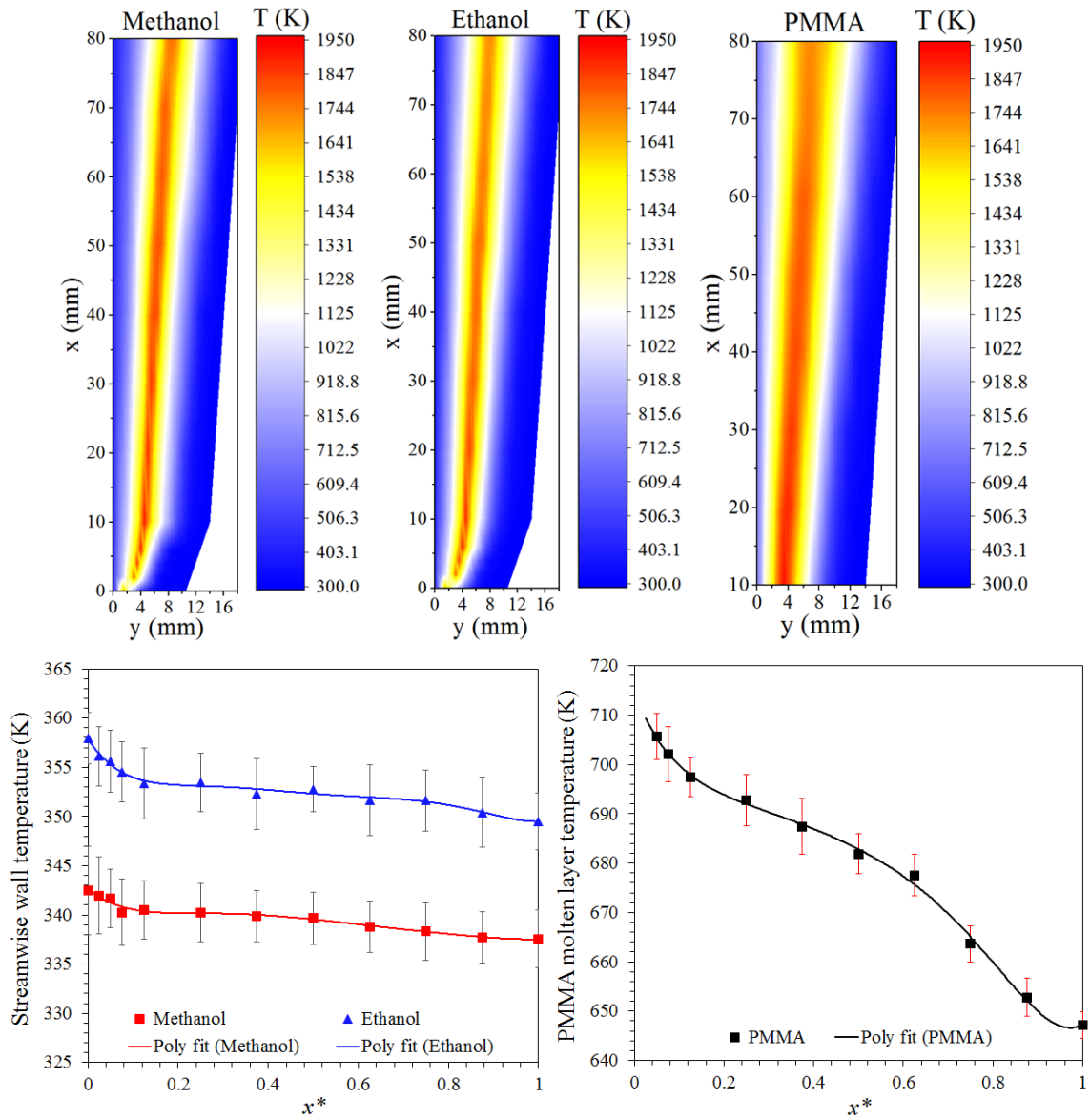
Figure 5.1: (left)Temperature profiles at several locations along the fuel surface of length 8 cm for a methanol, ethanol and PMMA boundary layer diffusion flame (wall fire). (right) Variation of the surface temperature for methanol and ethanol condensed fuel surface (left) Variation of the PMMA molten layer temperature along the length of fuel surface.

be approximately near the boiling points of the fuels studied here.

Figure 5.1 and 5.2 also shows the temperature profiles at several stream-wise locations for a PMMA slab in a vertical orientation. The maximum peak temperature for PMMA is about 1923 K, which occurs about ~ 10 mm from the leading edge. Thereafter, the value of the peak temperature decreases slowly, signaling the end of heat-release region. It dropped by about 198 K close to the sample trailing edge. Molten layer temperatures at various stream-wise locations were also measured for a PMMA slab, shown in Figure 5.1 as a function of x. The temperature of the molten layer decreased slowly with x, moving downstream of the leading edge. The average temperature of the molten layer was found to be 677 K. The convective heat feedback to the surface was also found to decrease with x. In the current tests, the convective heat flux has been estimated to be several times higher at the leading edge than in the trailing section, 26.1 kW/m^2 at $x = 10$ mm and 14.0 kW/m^2 at $x = 80$ mm for a methanol flame and 32.4 kW/m^2 at $x = 10$ mm and 15.0 kW/m^2 at $x = 80$ mm for a PMMA flame. The convective heat flux was evaluated here by measuring temperature gradients at the condensed fuel surface and using the expression $k_w \left(\partial T / \partial y \right)_{y=0}$. Thus, both the heat feedback and the measured pyrolysis temperature decreased with x, but the pyrolysis temperature decreased more slowly. This is consistent with the results of Vovelle et al. [122], who reported that the

148
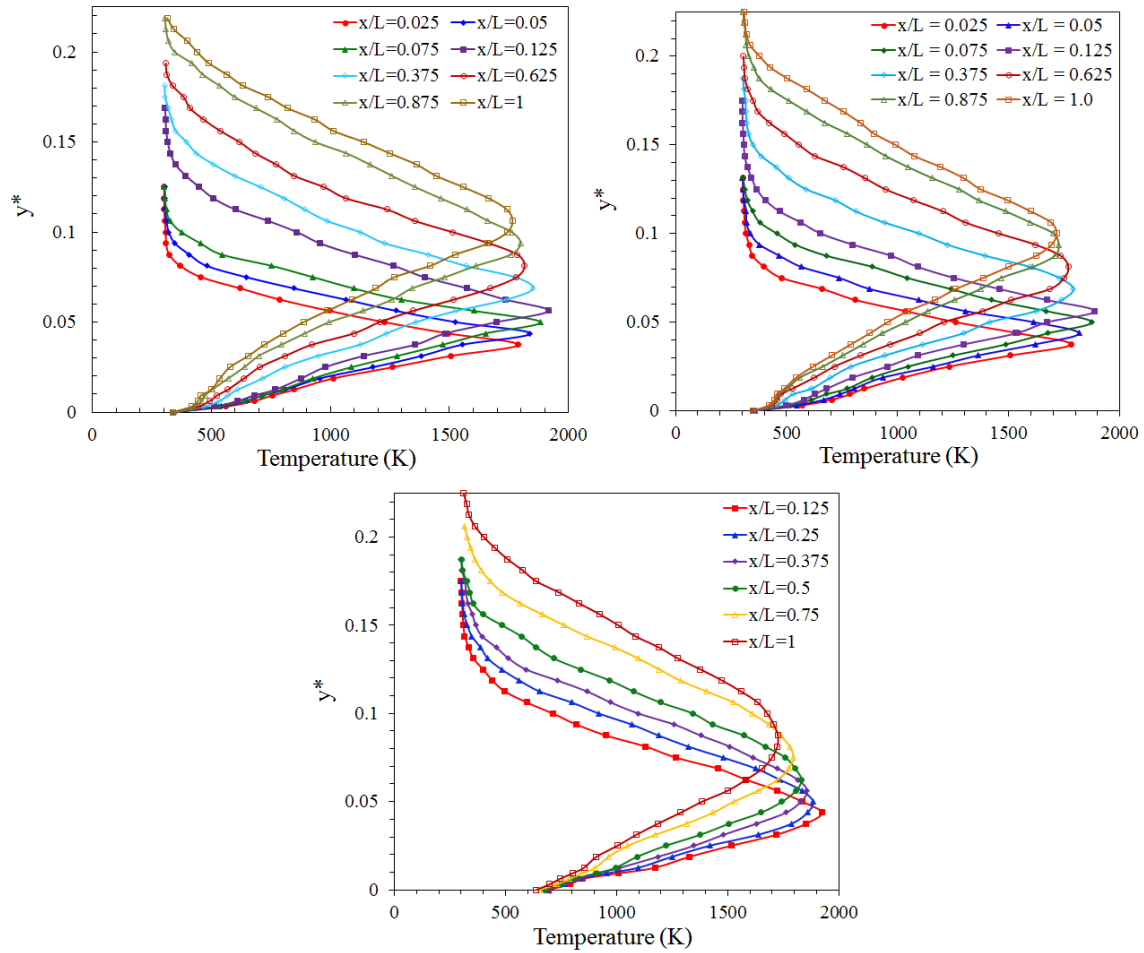
Figure 5.2: (top) Temperature profiles at several streamwise locations along the fuel surface for a methanol and ethanol boundary-layer diffusion flame. (right) Temperature profiles at several streamwise locations along the fuel surface for a PMMA7890- boundary layer diffusion flame.

pyrolysis temperature (in the case of PMMA) increases slightly with the increasing heat flux to the surface. Also, the wall temperature decreases more rapidly with x for PMMA when compared to methanol and ethanol fuel surface temperatures

149

shown in Figure 5.1. The local mass-loss rate from the fuel, driven by convective heat fluxes to the surface in these small, laminar flames, should similarly decrease with x. A comparison of the shapes of the temperature profiles at various x locations reveal that the temperature gradients decrease with x from the leading edge. This is consistent with known characteristics of boundary-layer diffusion flames, in that convective heat feedback decreases with x. The flame usually becomes thicker when moving downstream of the leading edge and the flame stand-off distance increases with increasing x. It follows, therefore, that the local mass burning-rate should also decrease with x, discussed later.

5.2. Flame stand-off distance

Figure 5.3 shows the side-view image of a PMMA wall flame in a free-convective environment, depicting flame stand-off distance in such flames. The non-dimensional flame stand-off distance, $y_f^* = (y_f/L)$, at different locations along the fuel surface are plotted in Figure 5.4 for methanol, ethanol and PMMA boundary-layer diffusion flames. The experimental flame stand-off distance is taken as the distance measured in the normal direction from the fuel surface to the point where the highest temperature was recorded. The flame stand-off distance, measured through side-view photographs, are also plotted against the experimental results. Reasonably close agreement of the flame stand-off distance measured by both methods confirms the

accuracy of measurements. The flame stand-off distance is lower near the leading edge and it increases further downstream up to the trailing edge. This leads to enhanced heat transfer to the fuel surface at the leading edge and hence higher evaporation rates of the fuel at this location. Accordingly, the local burning rate is highest at this location. The flame stand-off distance is higher for the regions near the trailing edge and hence heat transfer at these locations is lower.
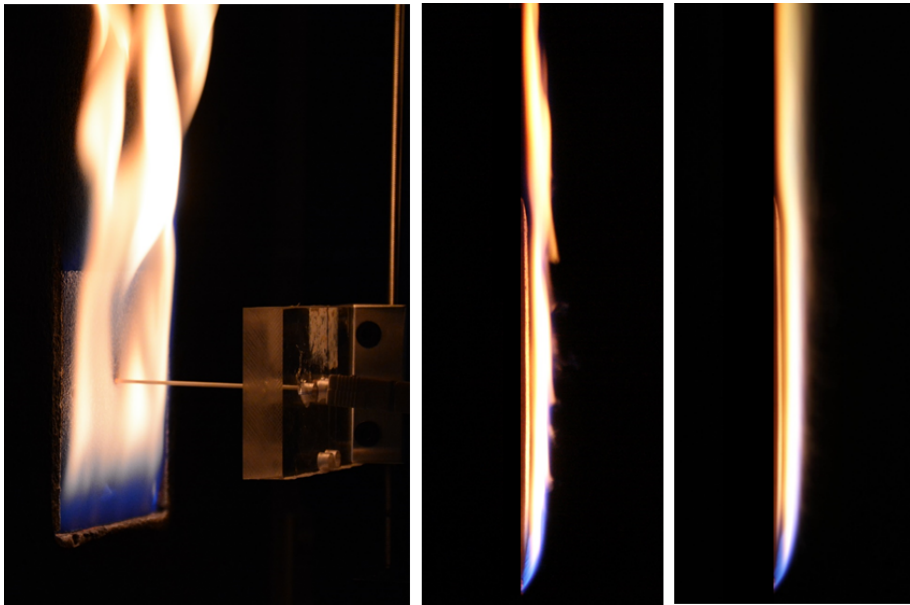
Figure 5.3: (left) Burning of a PMMA plate in a free-convective environment. (right) Instantaneous and averaged side-view image of a PMMA flame depicting flame stand-off distance.

Due to lower heat transfer rates at these locations, the local mass-burning rates are found to be lower at these locations. Also, the non-dimensional flame stand-off distance in both the methanol and ethanol cases is almost proportional to $x^{0.25}$,

151
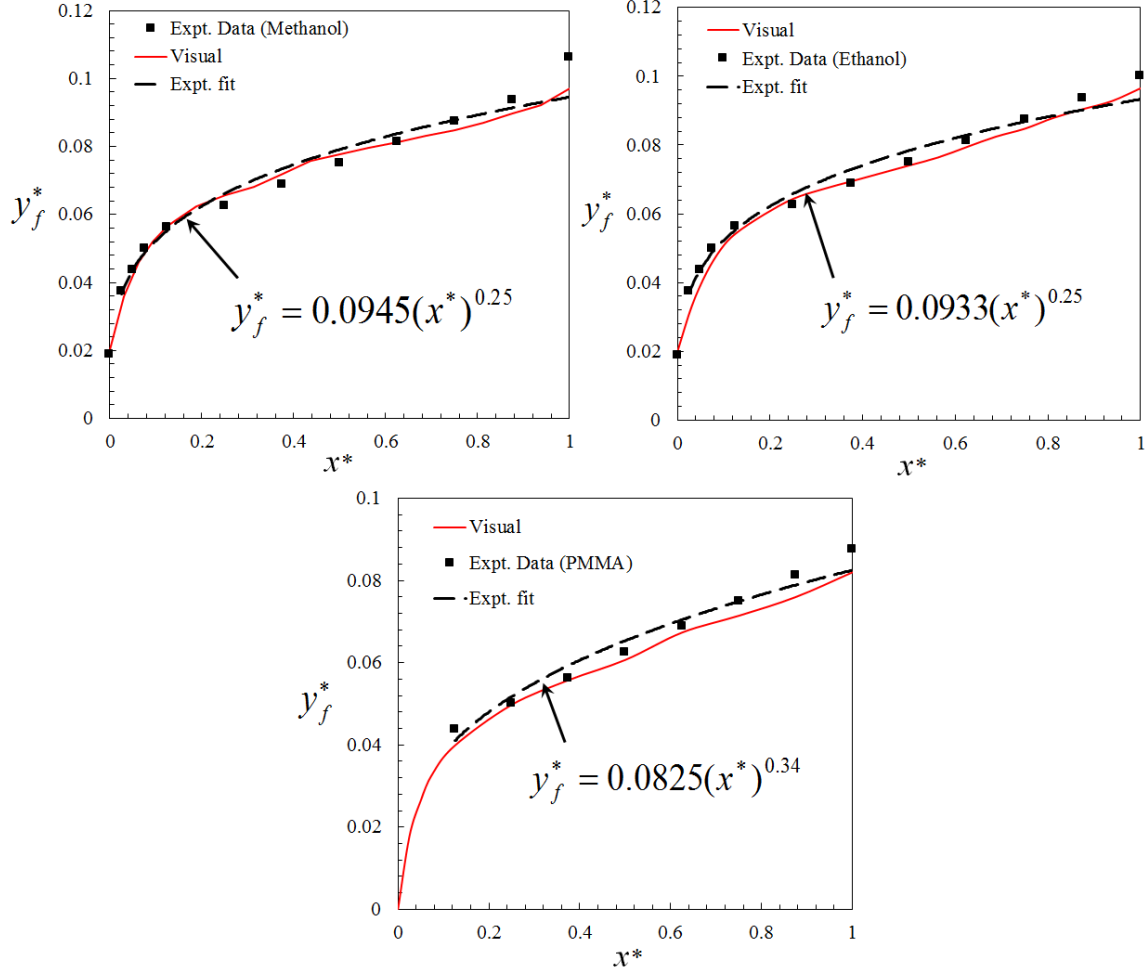
Figure 5.4: Non-dimensional flame stand-off distance for a boundary-layer diffusion flame established over a (top-left) methanol, (top-right) ethanol and (bottom) PMMA condensed fuel surface.

confirming the similarity theory for a natural-convection boundary layer adjacent to a vertical flat plate [6, 7]. However, for PMMA the non-dimensional flame stand-off distance does not follow the boundary layer similarity theory and was found to be proportional to $x^{0.34}$. It will later be shown that the PMMA local pyrolysis rate does

not follow the similarity theory either.

5.3. PMMA regression and local pyrolysis rate

The PMMA sample is allowed to burn for a known time interval before the flame is extinguished. After the sample cools, the sample is cut along the center-line and its thickness along the center-line is measured at various x locations. The results presented in this section are the average of three independent tests performed under the same atmospheric conditions. PMMA thermal expansion does not cause any significant variation in the results as they are measured after the sample cools, therefore, the measured thickness was not corrected for thermal expansion. Figure 5.5 (a) shows the regression profile of the PMMA surface at different burn-out times. Significant regression was observed in the leading section when compared with regression at locations downstream. This was found to be consistent with the non-uniform rate of heat feedback from the boundary-layer flame to the PMMA surface. At higher burn-out times ($t > 250$ s), the sample surface receded significantly below the level of the original surface. This resulted in the formation of a valley or step in the leading section as shown in Figure 5.5 (a). Figure 5.5 (a) also demonstrates that the valley deepens and the position of the deepest point moves slightly downstream with time.

The sample regression rate at each location was obtained as the difference in thickness (before and after the test) divided by the test duration. It is to be noted

that the regression rate calculated by this method is a time-averaged regression rate and may therefore be different from the more desirable instantaneous regression rate. The test duration time here also does not include the time taken for uniform ignition of the sample which is ~ 50 s. The regression rate calculated in Figure 5.5 (b) can similarly be calculated by including the time taken for uniform ignition (as one might believe that PMMA pyrolyzes during uniform ignition as well), in which case 50 s should be added to the test duration time. However, neglecting the time taken for uniform ignition results in more accuracy when calculating the average mass burning rates from regression rate profiles. Figure 5.5 (b) presents the time-averaged regression rate at various stream-wise locations. It is observed that the burned thickness is much larger upstream than downstream and similarly larger in the 850 second duration test than in 150 s test. Therefore, the error in burning rate measurement should be highest downstream at short times. Figure 5.5 (b) shows that the regression rate peaks near the leading edge and thereafter decreases sharply with x as we move downstream of the leading edge (neglecting the data at x=80 mm due to edge effects), consistent with the way heat feedback varies with x. The rate of decrease with x is slower at longer burn times. The rate also decreases sharply from the peak towards $x = 0$, especially at burn times of 550 s and 850 s. A sudden increase in the regression rate was observed at the trailing edge (x= 80

154

mm) which is primarily due to edge effects. It was observed that the surface was still flat near the trailing edge for a burn-out time of 250 s and becomes increasingly curved for longer burn times. This non-uniform regression leads to the formation of a valley that deepens with time, which affects the local burning rate. Figure 5.5 (b) also shows that the surface regression rate decreased with time in the leading 4 mm of the sample. Also, the peak regression rate decreased from ~ 0.03263 to ~ 0.00964 mm/s (a factor of 3.38) between the 100 s and 850 s tests. The x-position of the peak regression rate was observed to shift slightly downstream with time. It is clearly seen from Figures 5.5 (a) and (b) that uneven surface regression and the creation of a valley led to the transient surface regression rate in the leading section, supporting the observations made by Ndubizu et al. [46]. The heat feedback to the sample surface decreases significantly in the mid-section of the sample and therefore the degree of surface regression is small. The local burning or pyrolysis rate is time dependent and this can be clearly seen in Figure 5.5 (b). Closely observing the regression rate profiles for $50 \leq x \leq 70$ mm (neglecting the data at $x= 80$ mm due to edge effects), it is observed that the regression rate for tests at higher burn-out times is distinctly the largest at each x location, and a closer look at the data reveals an increasing trend. This observation is similar to the observations made by Ndubizu et al. [46]. The regression rate definitely increases with time in the trailing section

155
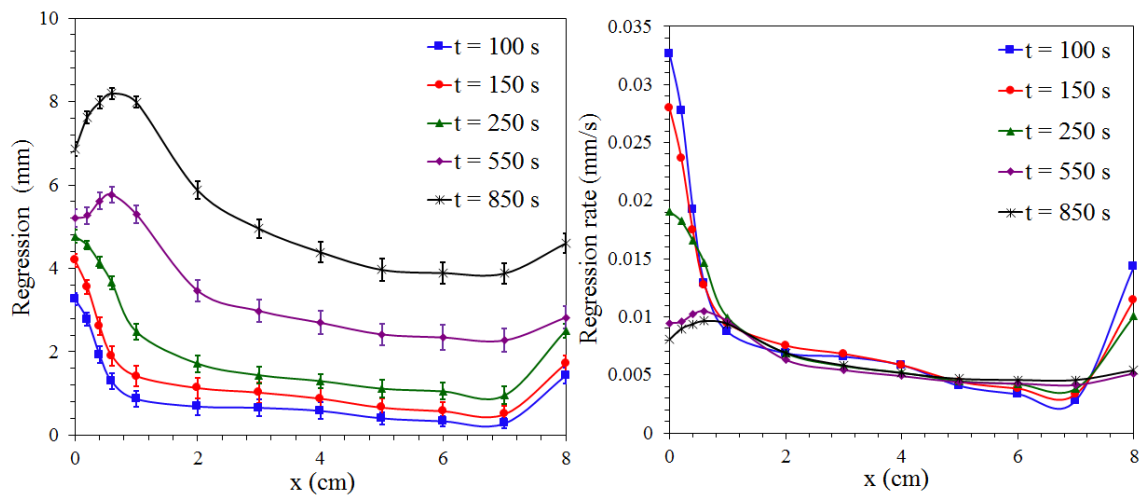
Figure 5.5: (a) (left) Regression profiles of the PMMA surface at different burn-out times (b) (right) PMMA surface regression rates at various stream-wise locations in tests lasting 100, 150, 250, 550 and 850 seconds.

Figure 5.6: Regression photographs of the PMMA surface at different burn-out times (LE: Leading edge, TE: Trailing edge).

and this is probably due to increased heat feedback with time and slow in-depth heat conduction in this section, where the heat feedback rate is small relative to that in the leading section. Figure 5.6 shows the regression photographs of the PMMA surface at different burn-out times. The given figure clearly shows the formation of valley in the leading section of the sample at higher burn-out times.

5.4. Non-dimensional Temperature Gradients and the Local Mass Burning Rate

Figure 5.7 shows the variation of the normal non-dimensional temperature gradient along the fuel surface extracted from experimental temperature data of methanol, ethanol and PMMA. The normal non-dimensional temperature gradients at the fuel surface, $(\partial T^*/\partial y^*)\mid_{y^*=0}$ were calculated from the slope at $y^* = 0$ of a third order polynomial fit to the non-dimensional temperature distribution near the fuel surface. The temperature gradient normal to the fuel surface was found to be highest at the leading edge and lowest at the trailing edge (x = 80 mm). The local mass-burning rate should follow a similar trend, as is revealed by the calculated rates in Figure 5.8.

Averaging the non-dimensional temperature gradient for the entire fuel surface from data in Figure 5.7, the average mass-burning rate is estimated to be 18.0 g/m^{2}s,

20.2 g/m²s and 9.8 g/m²s for methanol, ethanol and PMMA respectively, using Eq. (9). Appropriate average values of transport properties were used to calculate the constant C in Eq. (9) and are given in Table 6. It is to be noted that we evaluated the transport properties following the work of Kim et al. [17] where they evaluated the value of k at the wall and the value of c_p at the adiabatic flame temperature of the given fuel. The assumption of a unity Prandtl number in deriving Eqn. (9) also supports such selection of transport properties, as evaluation of the transport properties at the wall, namely μ_w and k_w, and evaluation of the specific heat at the adiabatic flame temperature of the given fuel results in a unity Prandtl number. Choosing the transport properties as outlined above works well in estimating the average mass burning rates for both liquid and solid fuels. The mass-burning rate evaluated though the load cell data was found to be 16.7 g/m²s, 17.6 g/m²s and 8.9 g/m²s for methanol, ethanol and PMMA respectively. The error in the estimation of the average mass-burning rate was therefore found to be +7.8%, +14.8% and +10.1% for methanol, ethanol and PMMA respectively. Factors causing the theoretical relationship from Eqn. (9) to over-estimate the average mass burning rate might include assumptions of a unity Lewis and Prandtl numbers, a lack of radiation effects and uncertainties associated with the calculation of transport properties.

Recall that the temperature measurements for liquid fuels were taken in a steady

burning regime, determined by global mass-loss data, however for PMMA the measurements were carried out within the first 150 s (after the surface is uniformly ignited, while the surface was still relatively flat), therefore the mass-loss rate reported is an average for this 150 s region.
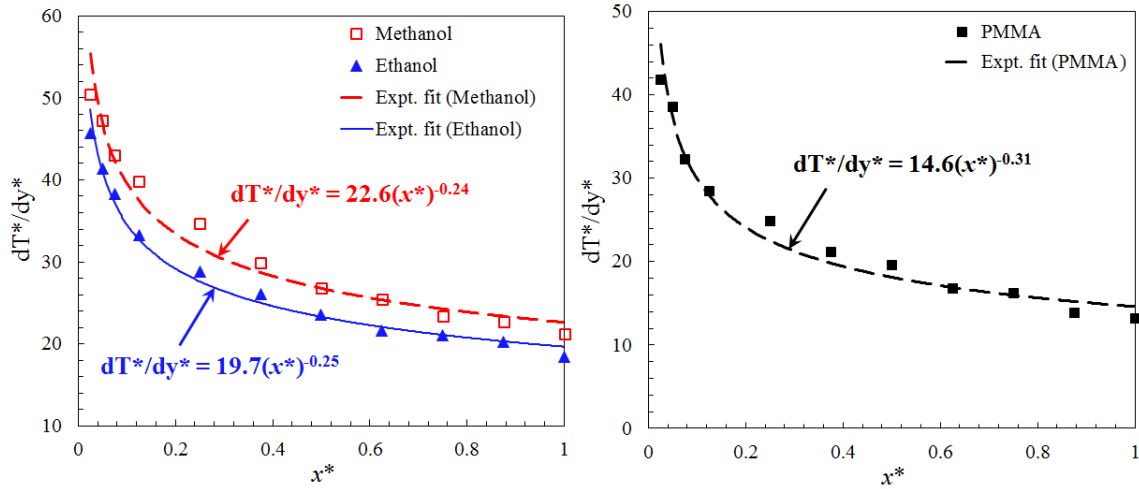
Figure 5.7: Variation of the non-dimensional temperature gradient at the methanol/ethanol condensed fuel surface (left) and PMMA surface (right) along its length.

In the PMMA case, even though solid fuel burning does not yet reach a steady state, the gas-phase reaches a steady state soon after uniform ignition. At the leading edge of the solid, where heat feedback is high, a local gas-phase steady state is achieved soon after ignition, before a significant valley is formed. In that period, approximately all the heat feedback is used to gasify the solid. Later, a valley is formed and the surface regression rate decreases with time in the leading section

(outlined in Section 5.3). This suggests that the heat reaching the surface in this section is no longer steady at times later. The same observations were made by Ndubizu et al. [46] when they burnt PMMA slabs in forced convective environments.

Table 6: Physical properties

Properties	Methanol	Ethanol	PMMA
Mass transfer number, B	2.5 [8]	3.1 [8]	1.3 [46]
Thermal conductivity, k_w (W/m-K) evaluated at the pyrolyzing wall temperature	0.028 [123]	0.029 [123]	0.050 [123]
Specific heat, c_p (J/kg-K) evaluated at the adiabatic flame temperature	1394.5 [123]	1417 [123]	1658.5 [123]
$T_{w,p}$ (K)	337 [8]	351 [8]	668 [89]
$T_{fl,ad}$ (K)	2150 [123]	2195 [123]	2494 [123]
Length of the condensed fuel surface (m)	0.08	0.08	0.08

Ndubizu and co-authors also observed that a more efficient mixing of oxygen and fuel was obtained near the leading edge of the sample at earlier stages of burning while the sample was still flat. However, as the test progressed and the valley formed

and deepened, it resulted in a richer fuel mixture in the leading section of the sample. They speculated that because of the valley, the combustion products in the valley were not swept away as readily as was the case when the surface was flat. They suggested that the oxygen mass fraction within the valley would decrease as the valley deepens. This would result in a drop in the flame temperature and, consequently, a drop in total heat feedback to the surface. They also found that the temperature gradients close to the PMMA surface decreased with time. The same observations were made in this study. After ignition, it was visually observed that the flame near the leading edge was bluish while the leading section of the sample was still flat. This is an indication that a more efficient mixing of oxygen and fuel was obtained in this region of the flame at this stage. However, as the test progressed and the valley formed and deepened, the length of this blue portion shrank, suggesting that the moving boundary layer effects resulted in a richer fuel mixture in this section confirming the observations of Ndubizu et al. [46]. Similarly, temperature gradients normal to the PMMA surface were found to decrease with time as the valley formed and deepened. No change in the temperature gradients was observed during the initial stages of burning while the surface was relatively flat. This strongly suggests that the heat feedback to the curved sample surface decreased with time as the valley deepens. Therefore, it becomes essential to accomplish steady mass loss rate

161

and temperature measurements during initial stages of burning while the surface is relatively flat. It is to be noted that for PMMA, both the temperature and mass loss rate measurements were carried out within the first 150 s (after the surface is uniformly ignited, while the surface was still relatively flat).

Figure 5.8 shows the variation of the local mass-burning rate for vertically-oriented methanol and ethanol flames, using the theoretical correlation from Eq. (9) and the non-dimensional temperature gradients at the condensed fuel surface. Due to the availability of fresh oxidizer, higher convective heat feedback, higher temperature gradients and lower stand-off distances near the leading edge, the local burning rate is highest here and subsequently decreases as we move downstream towards the trailing edge. The burning rate decreases, due to the lack of fresh oxidizer, lower convective heat feedback, lower temperature gradients and higher flame stand-off distances as we move downstream. Also, the local mass-burning rate for both methanol and ethanol is almost proportional to $x^{-0.25}$, confirming the power-law relationship for laminar natural convective burning on a vertical surface [16, 17]. The local mass-burning rate evaluated by using Eq. (9) was also compared against the theoretical mass-burning rate given by Kim, de Ris and Kroesser [17]. For laminar natural convection burning, the mass-burning rate on a vertical surface was found to be [17],

$$\dot{m}''_f = 3 \left[\frac{\rho_w^2 \mu_w^2 L_v g \cos \phi}{4 \bar{c}_p T_\infty x} \right]^{1/4} [-f(0)], \tag{42}$$

where ρ_w represents the density of the gas phase at the wall, μ_w dynamic viscosity at the wall, L_v the effective heat of vaporization, g acceleration due to gravity, ϕ the angle from vertical, $\bar{c}_p$ the mean specific heat for free convection, T_∞ the ambient temperature and x the coordinate parallel to the fuel surface. The transport properties were evaluated at the wall temperature, T_w . $[-f(0)]$ was numerically calculated for various liquid fuels elsewhere [17]. The close agreement in the theoretical and experimental local mass burning rates obtained by using the theoretical formulation in Eq. (42) and Eq. (9) suggest that the proposed correlation works well in estimating the local mass burning rates for the liquid fuels.

Unlike liquid fuels, for PMMA the local mass-burning rate can be approximated a posteriori by measuring the local surface regression over fixed intervals of time [124]. Once steady burning has been established the pyrolysis mass flow rate for PMMA is computed at each x location along the central symmetry axis using the first-order approximation given by Pizzo et al. [124],

$$\dot{m}''(x,t) = \rho_s \frac{d\delta}{dt} \approx \rho_s \frac{\delta(x, t + \Delta t) - \delta(x, t)}{\Delta t}. \tag{43}$$

Using a PMMA density (ρ_s) of 1190 kg/m^3 and measuring regression from samples

burned for fixed 50 s time intervals after ignition the local mass-burning rate over time can be assessed. A smaller time step would be desirable; however errors in measuring regression profiles become too apparent when the time step is less than 50 s. The regression data between burnout times of 100 and 150 s were used to evaluate the local mass-burning rate in Figure 5.8 for PMMA. Both the regression-measured and Eqn. (9) calculated mass-burning rates follow a power law decay in x with exponent -0.35 and -0.31, respectively. The same power law relationship for local mass-burning rates was observed by Pizzo et al. [124] for vertical PMMA slabs of length 2.5 to 20 cm. The departure from the $x^{-0.25}$ dependence predicted by the LBL theory could be due to a combination of the following reasons (1) the variations of flame and surface temperatures with x preclude the self-similar solution of boundary layer, and (2) radiative heat feedback to the solid does not follow the boundary layer scaling rule as discussed later. Jiang et al. [125] also observed that the downstream flame, in the case of PMMA, deviated from the self-similar boundary layer scaling relation. They observed that the variation in flame stand-off distance and the fuel vapor blowing rate with x does not follow the $x^{-0.25}$ dependence, as implied by the self-similar solution of the boundary layer. The close agreement, however, in estimating the local mass-burning rates by both the regression data and temperature gradients by using Eqn. (9) suggest that the proposed theoretical correlation works well for both

liquid and non-charring solid fuels, as the experimental mass burning rate was not

used in any way to obtain the theoretical mass-burning rate.
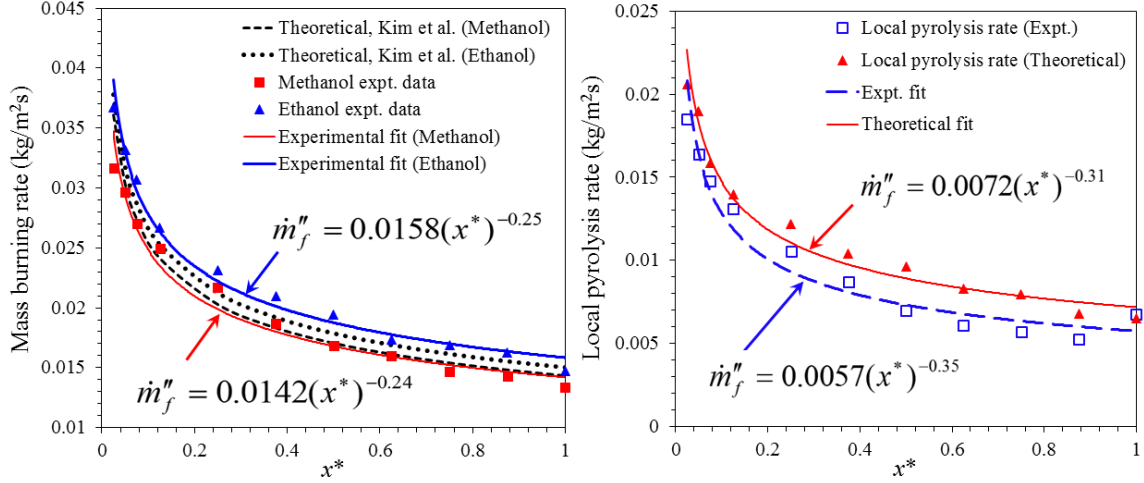
Figure 5.8: Variation of the local mass burning rates at the methanol/ethanol condensed fuel surface (left) and PMMA surface (right) along its length.

5.5. Wall Heat Fluxes in the Pyrolysis Zone

Utilizing gas-phase temperature measurements and local mass-burning rates, heat

fluxes were evaluated in the pyrolysis zone at various stream-wise locations along the

condensed fuel surface. Reasonable approximations were made to simplify the heat

balance analysis. The fuel surface was assumed to be opaque with an emissivity and

aborptivity of unity. The surface radiative heat loss was given with respect to T_∞.

The energy balance at the condensed fuel surface $(y = 0)$ for steady burning of liquid

fuels becomes

$$\dot{m}_f'' L_v = \dot{q}_{fl,c}'' + \dot{q}_{fl,r}'' - \dot{q}_{s,rr}'' \tag{44}$$

and

$$\dot{m}_f'' L_v = k_w \left(\frac{\partial T}{\partial y} \right)_{y=0} + \dot{q}_{fl,r}'' - \sigma \left(T_w^4 - T_\infty^4 \right), \tag{45}$$

where $\dot{q}_{fl,c}''$, $\dot{q}_{fl,r}''$, $\dot{q}_{s,rr}''$ and L_v represents the convective heat flux, radiative heat flux, re-radiation heat flux from the surface and effective heat of vaporization or gasification, respectively. Here, the convective heat flux is measured by using the expression $k_w \left(\partial T / \partial y \right)_{y=0}$. The flame imparts heat feedback to the condensed fuel surface primarily in two modes: convective and radiative. For steady burning, the convective heat flux from the flame is equal to $k_w \left(\partial T / \partial y \right)_{y=0}$ at the condensed fuel surface. Therefore, the convective heat flux from the flame is equal to the conductive heat flux at the fuel surface for steady burning.

For a transparent polymer, here clear cast PMMA, the local mass-loss rate due to pyrolysis, $\dot{m}_f''$, can be related to heat fluxes through an energy balance equation at the surface of the burning material as,

$$\dot{m}_f'' h_g = \dot{q}_{fl,c}'' + (1-r)\dot{q}_{fl,r}'' + \dot{m}_f'' h_{ng} - \dot{q}_{s,rr}'' - \dot{q}_{id,cond}'' - \dot{q}_{id,r}''. \tag{46}$$

The left-hand term represents the heat carried by fuel vapors away from the surface. The right-hand terms represent heat fluxes from the flame (convective and radiative

166

components), heat carried to the surface by the polymer in its non-volatile state, the outward surface re-radiation and the in-depth heat losses into the solid (namely conduction and radiation), where r represents the surface reflectivity. The term h_g is the effective heat of gasification commonly represented as the effective heat of vaporization. In the case of PMMA, the energy required to raise the temperature of a unit mass of polymer from ambient temperature to the final pyrolysis temperature (T_p) including melting, is given by $h_{ng} = h_m + \int_{T_\infty}^{T_p} c_p(T)dT$, where h_m is the heat of melting. Equation (46) slightly differs from that given by Orloff et al. [90], who disregarded melting, assuming that the polymer sublimes at a critical temperature and remains inert at temperature below this. As stated by Orloff et al. [90, 3] for steady burning of an infinitely thick slab, the heat carried to the surface by the solid exactly equals the conduction plus net radiation into the solid, yielding

$$\dot{m}_f'' h_{ng} = \dot{q}_{id,cond}'' + \dot{q}_{id,r}''. \tag{47}$$

Following Orloff's hypothesis and considering surface reflectivity to be zero, Equation (46) can be reduced to

$$\dot{m}_f'' h_g = \dot{q}_{fl,c}'' + \dot{q}_{fl,r}'' - \dot{q}_{s,rr}'', \tag{48}$$

which is of the same form as represented by Eqn. (44). This indicates that the

167

calculation of the steady burning rate does not require the estimation of heat losses into the solid interior. Figure 5.9 depicts a simplified model for the thermal pyrolysis of a solid fuel like PMMA.

For a boundary-layer diffusion flame, the convective heat flux can be further approximated as [8],

$$\dot{q}''_{fl,c} \approx h(T_{fl} - T_w) \approx \frac{k_f(T_{fl} - T_w)}{y_f} \tag{49}$$

where

$$h \approx \frac{k_f}{y_f}. \tag{50}$$

This crude approximation allows us to calculate the convective flux in boundary-layer diffusion flames by estimating the wall and flame temperatures at various streamwise locations along the pyrolysis zone together with knowledge of flame stand-off distances. k_f in the above equation is the thermal conductivity of the gas phase evaluated at a mean film temperature (preferably mean of the actual flame and wall temperatures). In order to calculate convective fluxes by using Eq. (49) above, it is very important that flame and wall temperatures must be accurately determined along with precise measurements of flame stand-off distances. Errors in estimating k_f, y_f, T_{fl} and T_w could lead to serious deviations in estimating convective heat fluxes by using Eq. (49) above. However, *using temperature gradients at the fuel surface is*

168

the most accurate way to evaluate the convective heat flux and will be compared to this crude approximation.

Re-radiation heat flux from the surface, $\dot{q}''_{s,rr}$ can be evaluated by knowledge of the wall and ambient temperatures, respectively. Utilizing the theoretical correlation in Eqn. (9), the net heat flux, $\dot{q}''_{net}$ ($\dot{q}''_{net}=\dot{m}''_f L_v$), can be estimated at various streamwise locations along the pyrolysis zone simply by the knowledge of local mass burning rates along the condensed fuel surface. The effective heat of gasification or vaporization was taken to be 1.2, 0.97 and 1.63 kJ/g for methanol, ethanol and PMMA, respectively [8]. $\dot{q}''_{fl,r}$ can then easily be computed by using Eqn. (45) above. The total heat flux incident to the surface, $\dot{q}''_{s,i}$, can be defined as the sum of the convective and radiative components of the flame heat flux. Figures 5.10 and 5.11 show the various components of flame heat flux in the pyrolysis zone of a methanol, ethanol and PMMA vertical wall flame, respectively.

Based on these results, the convective heat flux is relatively high and contributes approximately 85-90% of the total heat flux. Thus, convection is the dominant mode of heat transfer and radiative contributions are small. This is reasonable for the small, laminar flames studied here. The radiant component could increase downstream where the emissivity may increase if the soot volume fraction is high. The net heat feedback to the condensed fuel surface is the sum of the convective and

169

radiative components minus re-radiation from the surface.

$\dot{q}''_{s,i}$ Incident heat feedback from the flame (kW/m^2)

$\dot{q}''_{fl,r}$ Radiative heat feedback from the flame (kW/m^2)

$\dot{q}''_{fl,c}$ Convective heat feedback from the flame (kW/m^2)

$\dot{q}''_{s,rr}$ Re-radiation from the surface (kW/m^2)

$\dot{m}''_f$ Mass burning rate per unit area (kg/m^2-s)

y_f Flame stand-off distance (m)

δ_t Thermal boundary layer thickness (m)

g Gravity (m/s^2)
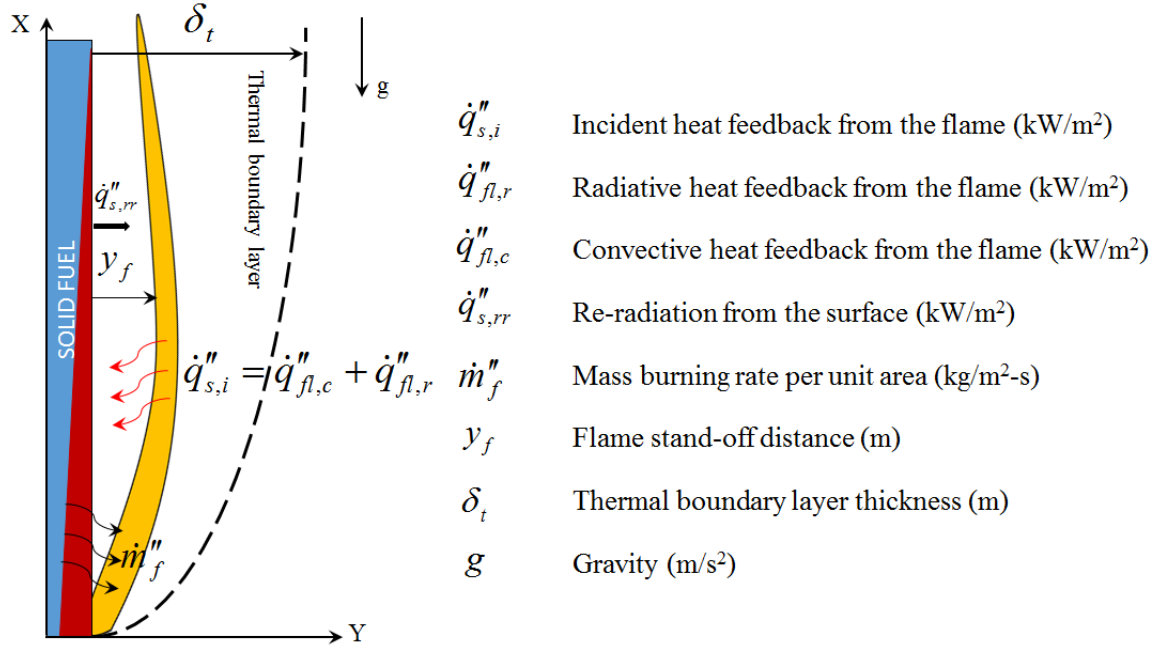
Figure 5.9: A simplified model depicting thermal pyrolysis of a solid fuel like PMMA.

For methanol and ethanol flames, all 3 components, namely $\dot{q}''_{s,i}$, $\dot{q}''_{net}$ and $\dot{q}''_{fl,c}$ follow a power law decay and were found to be almost proportional to $x^{-1/4}$, which in turn seems to follow the boundary-layer scaling rule. However, radiative heat feedback to the condensed fuel surface does not follow the boundary layer scaling rule. The re-radiation flux from the condensed fuel surfaces was found to be negligible for both methanol and ethanol diffusion flames. With the knowledge of local distributions of various components of heat flux, one can further compute the average value of the given components by using

$$\dot{q}''_{avg} = \left(\frac{1}{L}\right) \int\limits_0^L \dot{q}'' dx. \tag{51}$$

The total incident heat flux from the flame to the wall was estimated to be 21.9 and 19.9 kW/m² respectively for methanol and ethanol. The average convective heat flux from the flame to the wall was estimated to be 18.9 and 17 kW/m², for methanol and ethanol, respectively. The average radiative heat feedback from the flame was then calculated to be 3.0 and 2.9 kW/m², respectively for methanol and ethanol. Therefore, the radiative heat flux in the pyrolysis zone is only 13.7% and 14.7% of the total wall heat flux in case of methanol and ethanol, respectively. Thus, convection is the dominant mode of heat transfer in steady laminar boundary-layer diffusion flames and is primarily responsible for the pyrolysis of the fuel. Table 7 presents the various components of flame heat flux in kW/m² for free-convection boundary-layer diffusion flames.

For PMMA, all 3 components of heat flux, namely $\dot{q}''_{s,i}$, $\dot{q}''_{net}$ and $\dot{q}''_{fl,c}$ follow a power-law decay in x. The total incident flux on the surface was found to follow the laminar boundary-layer (LBL) scaling rule, however, the net and convective heat flux do not follow the LBL scaling rule. Since the net heat feedback to the solid does not follow this scaling, it follows that pyrolysis or the mass burning rate will not follow the LBL scaling rule either as outlined in section 5.4. Radiative heat feedback to the

solid was found to increase towards the trailing edge, most likely due to an increased volume of soot at the trailing edge.
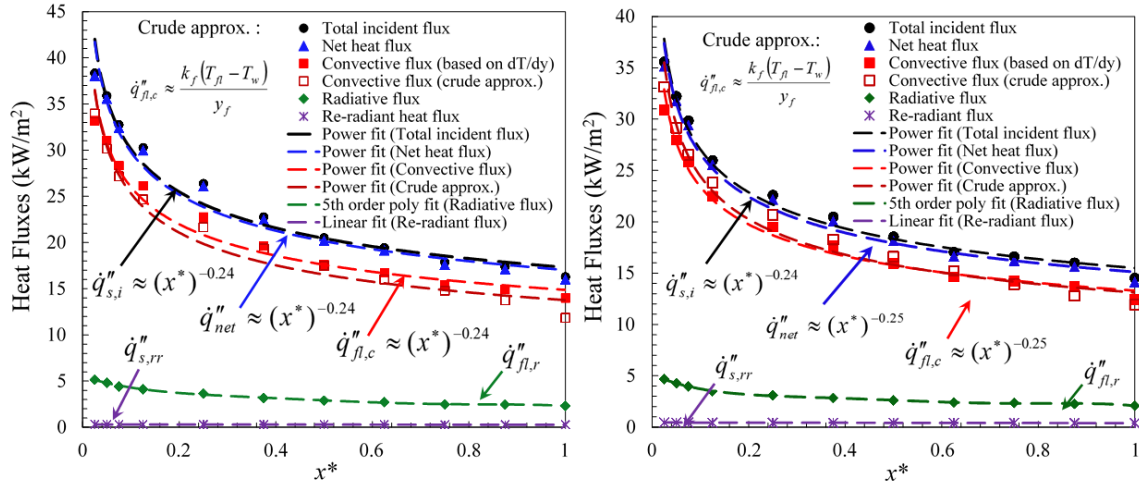
Figure 5.10: Distribution of various components of heat flux in the pyrolysis zone for a methanol and ethanol diffusion flame.

Re-radiation from the PMMA surface was found to be significant when compared to liquid fuels. This is primarily due to increased surface temperatures in the case of PMMA. The surface temperature for PMMA was found to be higher than in the case of liquid fuels (approximately twice that of liquid fuels). Recall that the average wall temperature for PMMA was measured to be 677 K. The total average incident heat flux to the wall was estimated to be 27.0 kW/m². The average convective heat feedback from the flame to the wall was estimated to be 22.9 kW/m². The average radiative heat flux from the flame to the wall was then calculated to be 4.1 kW/m².

172
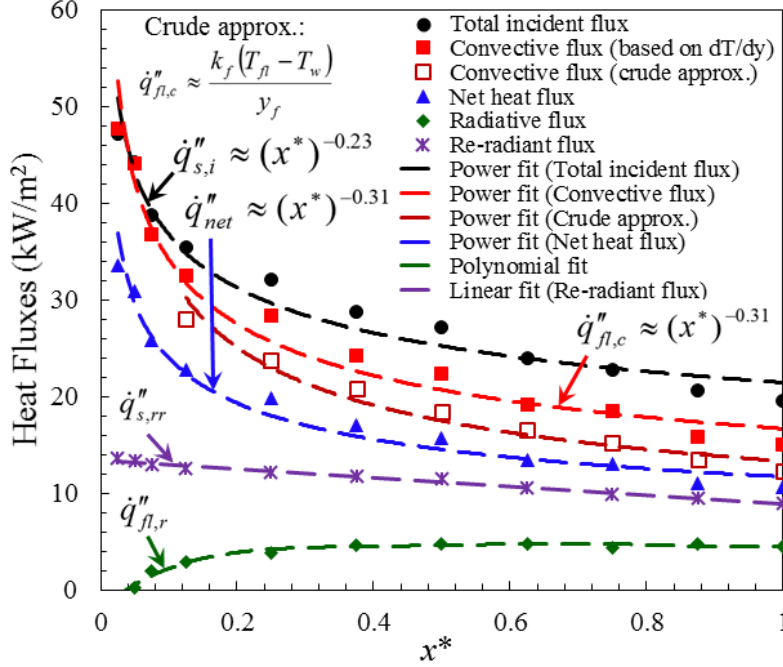
Figure 5.11: Distribution of various components of heat flux in the pyrolysis zone for a PMMA diffusion flame.

Therefore, the radiative heat flux is 15.3% of the total incident heat flux. The radiative heat flux component increases for solid PMMA because the flame is more sooty when compared to methanol and ethanol. However, the radiative component still does not exceed 20% of the total incident flux. This is because small laminar flames do not radiate out a significant portion of the heat released and because the convective heat flux is the dominant mode of heat transfer in such small flames. The average net heat flux that actually pyrolyzes the solid PMMA was estimated to be 16

173

kW/m². It is to be noted that in the case of PMMA, the average net heat flux which is basically the sum of the convective and radiative heat fluxes minus reradiation from the surface, was found to be quite lower than the total incident heat flux. This can be explained by the fact that a portion of the total incident flux is utilized in pyrolyzing the solid PMMA, whereas the rest is lost into the ambient surroundings through re-radiation from the solid wall. PMMA loses a considerable portion of total heat received by re-radiation compared to liquid fuels, owing to its higher surface temperatures.

Table 7: Various components of flame heat flux in kW/m² for free-convection boundary-layer diffusion flames.

Fuel	$\overline{\dot{q}''_{s,i}}$	$\overline{\dot{q}''_{fl,c}}$	$\overline{\dot{q}''_{fl,r}}$	$\overline{\dot{q}''_{s,rr}}$	$\overline{\dot{q}''_{net}}$	$\overline{\dot{q}''_{fl,c}}$ %
	kW/m²	kW/m²	kW/m²	kW/m²	kW/m²	
Methanol	21.92	18.92	3.00	0.25	21.67	86.28
Ethanol	19.89	16.97	2.93	0.32	19.58	85.28
PMMA	27.01	22.88	4.14	10.95	16.06	84.69

5.6. Convective Heat Transfer Coefficient

Convective heat transfer coefficients were also calculated for methanol, ethanol and PMMA wall flames. For a boundary-layer diffusion flame established over a

condensed fuel surface, convective heat transfer coefficients can be derived from the expression [13, 126],

$$h = \frac{k_w \left(\partial T / \partial y\right)_{y=0}}{T_{fl,ad} - T_{w,p}} = +\frac{k_w}{L}\left(\frac{\partial T^*}{\partial y^*}\right)_{y^*=0}. \tag{52}$$

The above expression comes from normalizing the boundary-layer equations by defining dimensionless independent variables [126]. Figure 5.12 shows the distribution of the convective heat transfer coefficient for a methanol, ethanol and PMMA wall flame, respectively. The theoretical results based on a thermal boundary-layer approximation [127] (outlined in Appendix A) and using this crude approximation from Eqn.(50) are also plotted for comparison. The expression for the boundary layer thickness (δ) for a free convection heat transfer on a vertical flat plate is given by [127],

$$\frac{\delta}{x} = 3.93 \mathrm{Pr}^{-1/2}(0.952 + \mathrm{Pr})^{1/4} \mathrm{Gr}_x^{-1/4}, \tag{53}$$

where Pr is the Prandtl number and Gr_x is the Grashof number. The convective heat transfer coefficient can then be derived as [127],

$$h = \frac{2k}{\delta} = \frac{2k}{3.93x Pr^{-1/2}(0.952 + \mathrm{Pr})^{1/4}\mathrm{Gr}_x^{-1/4}}. \tag{54}$$

In order to evaluate the above expression transport properties were evaluated
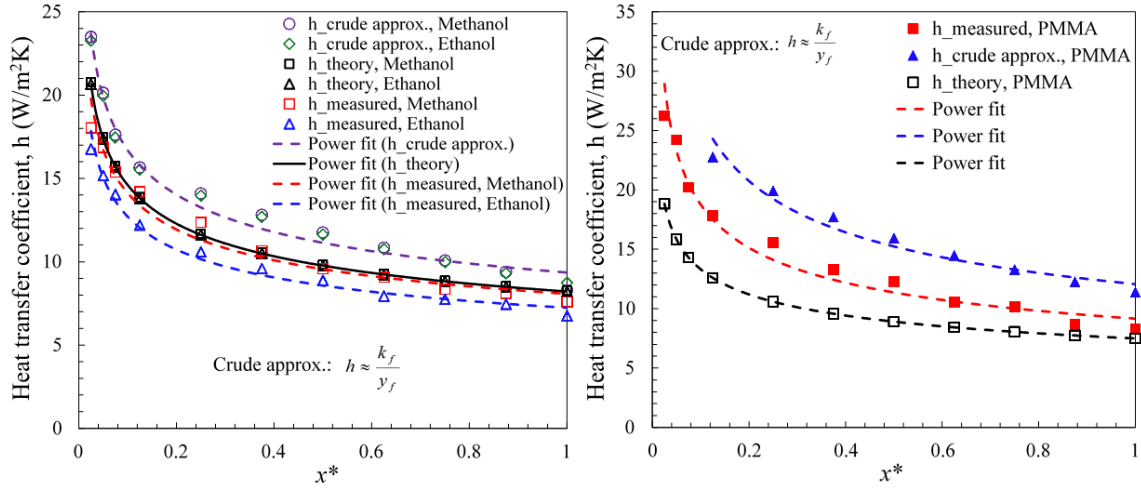
Figure 5.12: Variation of convective heat transfer coefficients in the pyrolysis zone for a methanol, ethanol and PMMA boundary-layer diffusion flame.

at an appropriate film temperature outlined in Appendix A. For both methanol and ethanol, the convective heat transfer coefficients evaluated through experiments follow a power-law decay in x consistent with the boundary-layer scaling rule. Experimentally determined heat transfer coefficients were found to be very similar to those predicted by theory for both the methanol and ethanol boundary-layer diffusion flames. However, for PMMA the heat transfer coefficients determined experimentally diverged from the values predicted theoretically. Theory seems to under-predict the convective heat transfer coefficients for PMMA, which may be due to the same reasons the local flame stand-off and temperature gradients diverge from the LBL theory, described earlier. However, the crude approximation using Eq. (50) slightly

176

over-predicts the heat transfer coefficient. The average value of the convective heat transfer coefficient was found to be 10.3 and 9.2 W/m²K for methanol and ethanol, respectively. For PMMA, the average value of the convective heat transfer coefficient was estimated to be 12.6 W/m²K.

5.7. Nusselt number

The Nusselt number was also calculated for methanol, ethanol and PMMA laminar boundary-layer diffusion flames. This parameter is equal to the dimensionless temperature gradient at the surface and provides a measure of the convective heat transfer occurring at the surface. The Nusselt number can be expressed as [126]

$$\mathrm{Nu} = \frac{hL}{k_w} = + \left(\frac{\partial T^*}{\partial y^*} \right)_{y^*=0}. \tag{55}$$

From the initial definition of T^*, it follows that for a prescribed geometry,

$$\mathrm{Nu} = f(x^*, \mathrm{Gr}, \mathrm{Pr}). \tag{56}$$

The Nusselt number is to the thermal boundary layer what the friction coefficient is to the velocity boundary layer. Eqn. (56) implies that for a given geometry, the Nusselt number must be some universal function of x^*, Gr and Pr. If this function were known, it could be used to compute the value of Nu for different fluids and for

different values of L and U (for forced flow).
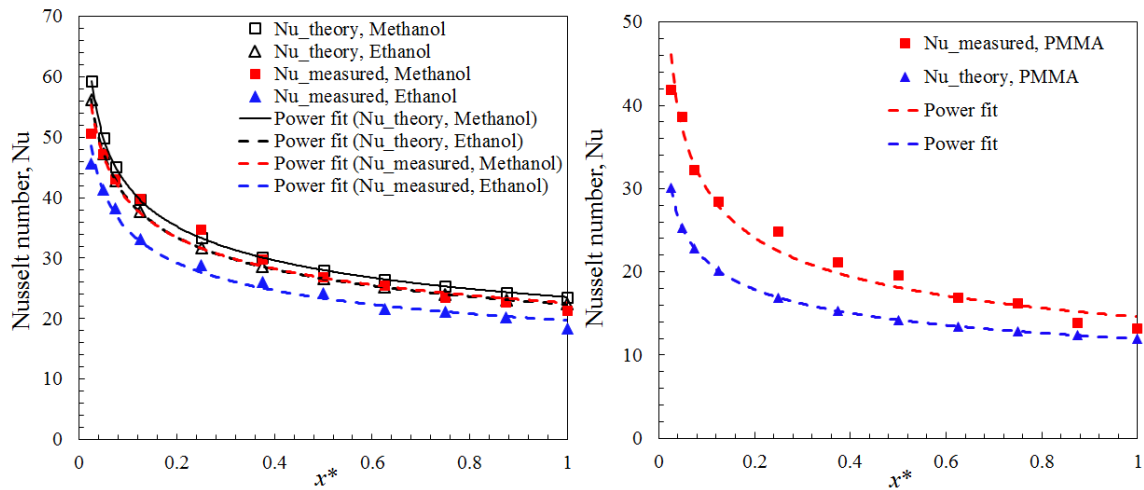
Figure 5.13: Variation of Nusselt number in the pyrolysis zone for a methanol, ethanol and PMMA boundary-layer diffusion flame.

From knowledge of Nu, the local convective heat transfer coefficient may be found and the local heat flux may then be computed using Eqn (49). Figure 5.13 shows the variation of Nu with non-dimensional distance downstream of the leading edge, x^* for a methanol, ethanol and PMMA wall flame. Theoretical results based on the thermal boundary layer approximation are also plotted for comparison [127]. Nu calculated by using Eqn. (55) versus Nu calculated by using the thermal boundary-layer approximation are very similar and provide good agreement for both methanol and ethanol. However, for PMMA the Nusselt number calculated from theory under predicts the measured value. This is expected because vertical burning of PMMA was

178

shown to not follow the LBL scaling rule. Correspondingly, the thermal boundary-layer approximation will not predict the Nu variation correctly.

Figure 5.14 shows the variation of local Nusselt number, $Nu_x = hx/k_w$, in the pyrolysis zone for a methanol, ethanol and PMMA boundary-layer diffusion flame. A closer look at the given figure reveals a good agreement between theoretical and
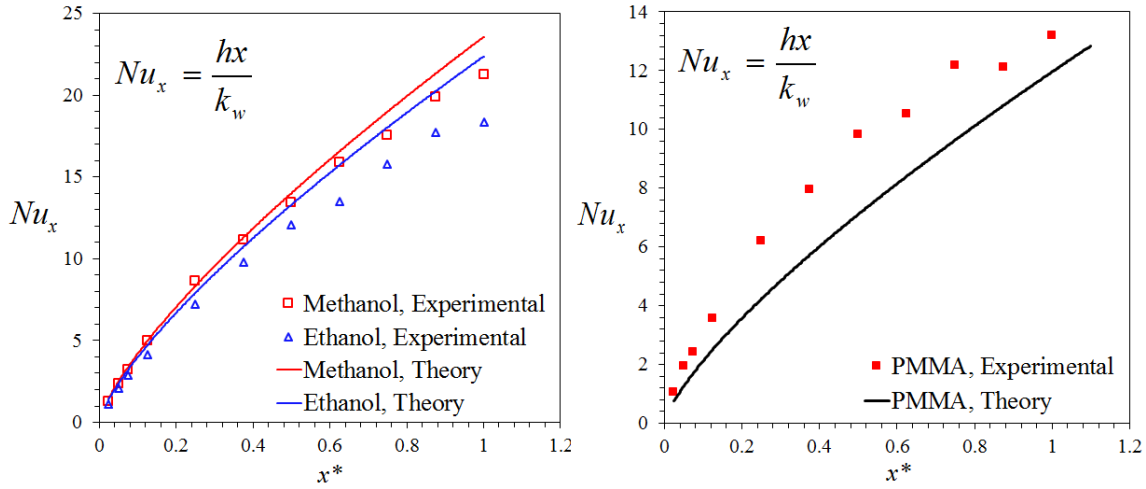
Figure 5.14: Variation of local Nusselt number, Nu_x in the pyrolysis zone for a methanol, ethanol (left) and PMMA (right) boundary-layer diffusion flame. The solid lines represent the theoretical results obtained for methanol, ethanol and PMMA boundary-layer diffusion flames.

experimental results for both methanol and ethanol boundary layer diffusion flames. In the case of methanol and ethanol, experimentally derived Nu_x was found to deviate from the theoretical results as we move downstream towards the trailing edge. In the case of PMMA, the experimentally derived Nu_x and theory showed a good agreement

near the leading edge. However, moving downstream towards the trailing edge, experimentally derived Nu_x was found to deviate from the theoretical results.

5.8. Plume Thermal Analysis

The fire and thermal plume both play important roles in flame spread, preheating unburnt fuel ahead of the flame front. The wall plume is also of fundamental interest as it differs from unconfined plumes, combining plume behavior and wall boundary-layer effects. The plume in this paper is defined as the region above (downstream) the pyrolysis front.

Detailed temperature measurements in a wall plume were carried out for methanol, ethanol and PMMA boundary-layer diffusion flames at several stream-wise locations downstream of the pyrolysis zone. The temperature profiles in the combusting and thermal plume were mapped at 7 steamwise locations, shown in Figure 5.15 and 5.16. The temperature measurements were compensated for radiation losses and represent the averages of at least five independent tests.

The maximum temperature in all cases decreases monotonically with increasing height along the wall. The reduction is not large in the pyrolysis zone, but the rate increases rapidly in the plume. The position of maximum temperature moves closer to the wall, in terms of y/x, as x increases. It is to be noted that peak temperatures in the thermal plume decrease significantly when compared to the combusting plume

180
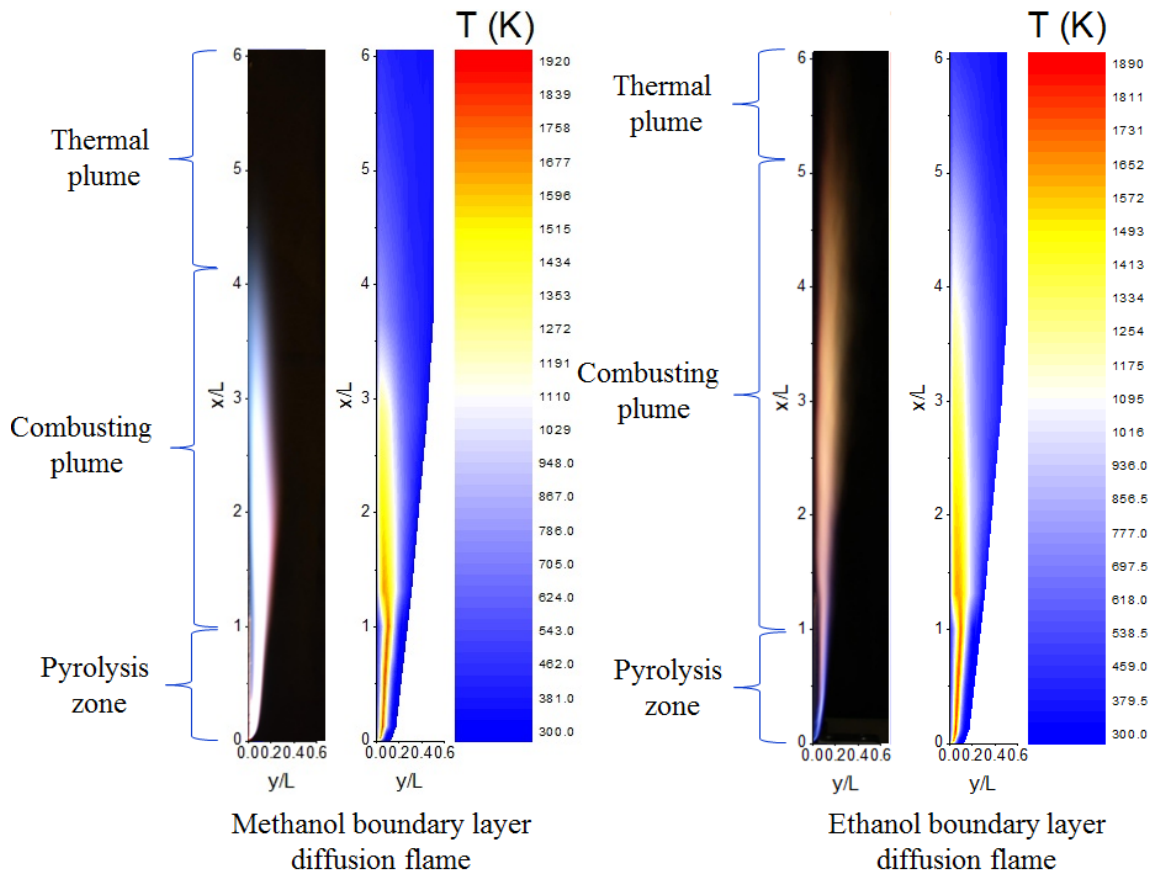
Figure 5.15: Flame and combusting plume photographs and temperature contours (experimental) for a (left) methanol and (right) ethanol boundary layer diffusion flame.

region. The plume grows in size (length) and thickness moving downstream. The temperature gradients in the combusting plume were found to be relatively constant (~ 450 K/mm) in both the methanol and ethanol wall-bounded flames. This behavior was typical for both flames until the tip of the flame was reached. Thereafter, temperature gradients decreased significantly downstream of the combusting plume.
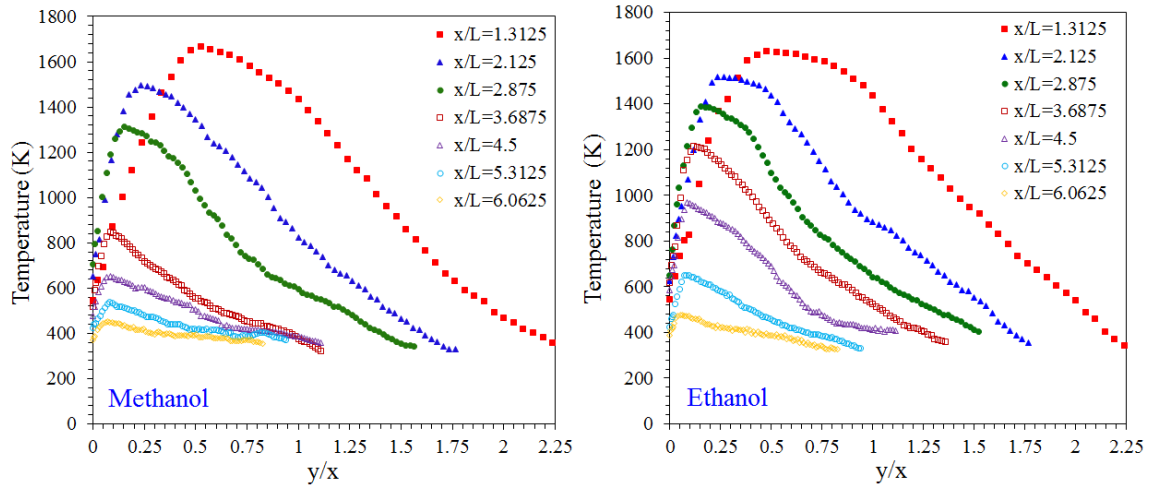
Figure 5.16: Temperature profiles in the combusting and thermal plume of a methanol and ethanol boundary layer diffusion flame.

Reduction in the flame stand-off distance and intermittent heating of the wall surface by direct flame contact in the combusting plume region caused temperature gradients and convective heat flux to increase at the wall, thereby contributing to higher incident fluxes (when compared to heat fluxes at the trailing edge of the condensed fuel surface) in the combusting plume region. The flame also comes back to the wall in the overfire region, heating up the wall surface to sufficiently high temperatures (on the order of 650 K in the combusting plume region). Thereafter, the wall temperature decreases significantly in the thermal plume region.

Figure 5.17 shows the temperature vs. time data in the combusting plume of a methanol diffusion flame at three different y-locations for $x/L = 1.31$. Temperature

fluctuations were found to be high on the air and fuel side of the flame and were found to be low at the location of the flame.
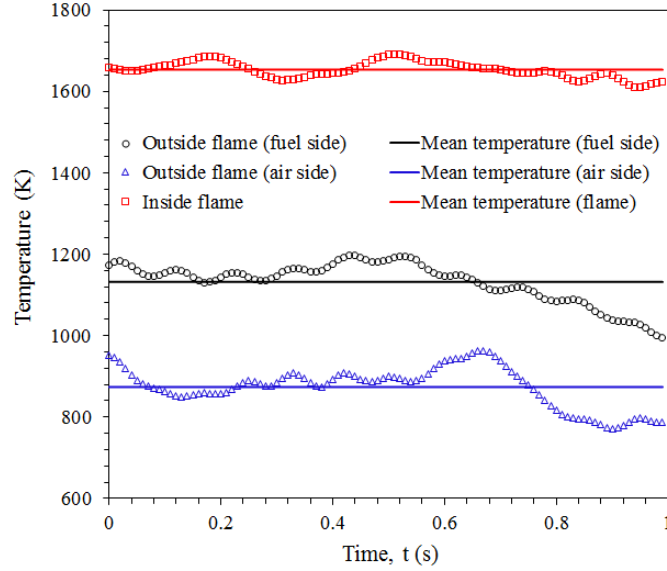
Figure 5.17: Variation of temperature with time in the combusting plume of a methanol boundary-layer diffusion flame.

5.9. Wall Heat Flux in the Plume or Overfire Region

The wall heat flux in the plume was measured at several stream-wise locations by a total heat flux gauge, a Medtherm model 64-10-20 mounted flush with the wall. The total heat flux measured by the heat flux gauge was de-convoluted into its convective and radiative components, shown in Figure 5.18. The convective flux was calculated by using the expression $k_w \left(dT/dy \right)_{y=0}$, where k_w was evaluated at the average plume-wall temperature. Also shown are convective heat fluxes resulting

from a crude approximation given by Eqn. (49). The only difference in the respective formula was to use the value of $T_{hfg,s}$ (~ 286 K) in place of T_w. It is to be noted that the surface of the heat flux gauge was kept at a constant temperature of 286 K using water-cooling and k_f was evaluated at the mean film temperature. Since the plume is characterized by large temperature variations, selection of transport properties at an appropriate temperature is essential. The transport properties were evaluated at a mean film temperature in the plume which was given by

$$T_f = \frac{T_{max} + T_\infty}{2}. \tag{57}$$

The selection of a mean film temperature is based on the work of Ahmad [34], where results, when correlated in this manner, agreed reasonably well with their theoretical model. The mean film temperature using this method was estimated to be ~ 1032 K for methanol and ~ 1007 K for ethanol.

No heating effects through surrounding insulation board were observed on readings from the total heat flux gauge. Radial heat transfer was also found to be negligible. Figure 5.18 shows a summary of the heat flux data obtained at various sensor positions in the plume. Values are provided for the total heat flux and its radiative and convective components. The flame also radiates heat flux to the ambient which was found to be generally larger than the radiant flux reaching the wall

[34]. This behavior has also been observed by Orloff et al. [90]. They attributed the effect to the absorption of radiation by the fuel and product-rich region near the wall. However, no attempt was made in this study to measure the radiant flux to the ambient, but these measurements can be found in literature elsewhere [128].

The heat flux to the wall increases just beyond the pyrolysis zone as the effect of blowing decays. However, the heat flux remains relatively constant throughout much of the combusting plume region. Therefore, the presence of the flame in the combusting plume provides an extended zone of high wall heat flux which heats the unignited combustibles during flame spread. It was observed that the heat flux increases from the trailing edge of the condensed fuel surface to a maximum and then decreases rapidly. The heat flux is low in the pyrolysis zone (towards the trailing edge of the condensed fuel surface), due to the blowing effect of fuel evaporating at the wall. In the overfire region, the heat flux increases, within one pyrolysis zone length, to a relatively constant value which is maintained until the tip of the flame is approached. Beyond the tip of the flame, the heat flux decreases rapidly once again.

The total heat flux reaching the HFG (Heat Flux Gauge) in the plume was estimated to be 16 kW/m^2 and 18.6 kW/m^2 for methanol and ethanol flames, respectively. The average convective heat flux for a methanol and ethanol flame was estimated to be 13.8 kW/m^2 and 15.6 kW/m^2, respectively in the overfire region.

The average radiative heat flux was then estimated to be 2.2 kW/m^2 and 3 kW/m^2 for methanol and ethanol flames respectively. The radiative heat flux to the wall was estimated to be 13.9% and 16% of the total wall heat flux for methanol and ethanol flames, respectively. It was observed that even in the plume region, the convective heat flux was the dominant mode of heat transfer to the wall. Even in the plume, radiation never accounts for more than 20% of the total wall heat flux for the present tests. The present low radiation levels are partly due to the fact that the fuels tested were relatively soot-free. Longer pyrolysis zone lengths would increase the contribution of radiation to the wall heat flux. Far above the fire in the thermal plume region, the radiant contribution is small and heat transfer rates are dominated by convection.
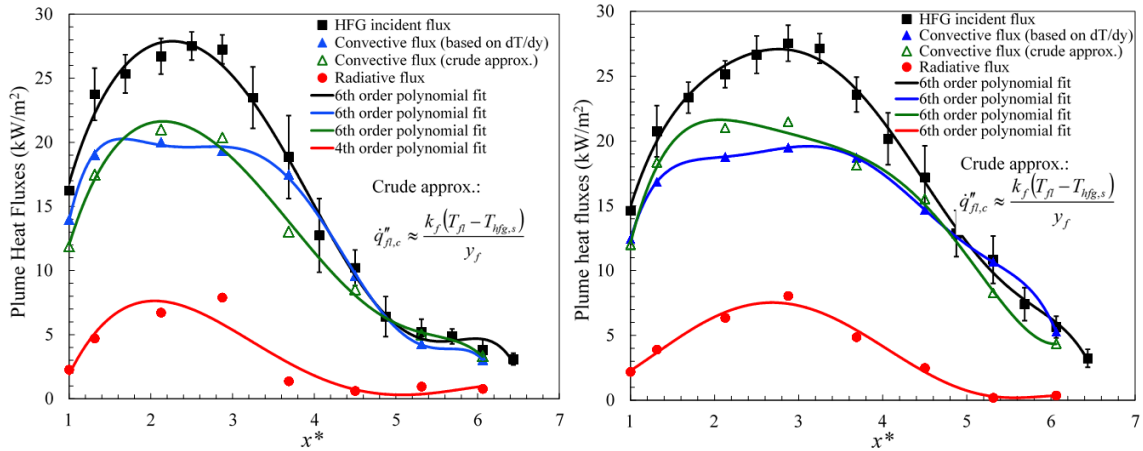
Figure 5.18: Plume heat fluxes at several stream-wise locations along the wall for (left) methanol and (right) ethanol boundary layer diffusion flames.

186

Although there have been numerous studies on boundary-layer diffusion flames established over condensed fuel surfaces, only Ahmad and Faeth [33] have evaluated the various components of wall heat flux in the laminar and turbulent fire plume with smaller burning samples. They estimated the radiative heat flux contribution to be small, never accounting for more than 20% of the total flame heat flux in both the laminar and turbulent fire plumes. This is in accordance with our observations of these laminar fire plumes.

Chapter 6: Forced Convection Boundary Layer Diffusion Flames

This chapter discusses the experimental results obtained from forced convection boundary layer diffusion flames. A laboratory-scale wind tunnel was designed and developed to conduct experiments under forced flow. An experimental set-up was designed and constructed to measure the burning rates and wall heat fluxes in forced convection boundary layer diffusion flames. The gas-phase temperature profiles across a laminar boundary-layer diffusion flame established over a methanol, ethanol and PMMA surface were measured for four different incoming flow velocities. Local mass burning rates, local temperature gradients, wall heat fluxes, flame stand-off distances, shear stress at the wall, local combustion and friction coefficients, local convective heat transfer coefficients, local Nu_x and profiles of mean temperatures were measured for methanol, ethanol and PMMA flames stabilized under forced flow (for a 10×10 cm condensed fuel surface). Regression rates and regression profiles for a PMMA surface were also measured at different burn-out times for 4 different free-stream conditions. Effects of free-stream conditions on local mass burning rates and heat flux profiles are also discussed. The theoretical correlation proposed in Eq.(9) was also validated for different free-stream conditions.

6. Forced Convection Boundary Layer Diffusion Flames

6.1. General Characteristics
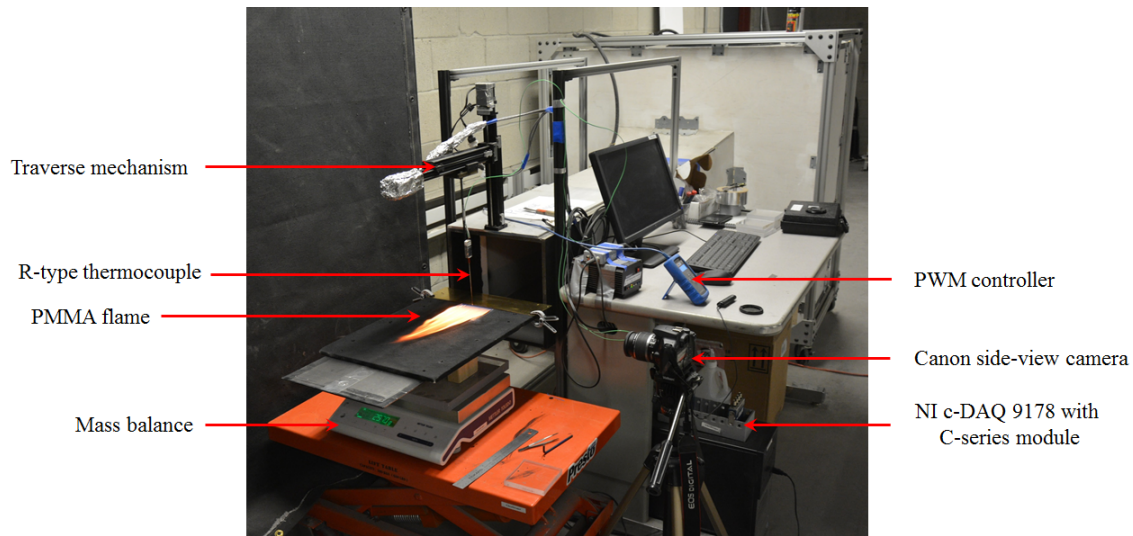
Figure 6.1: Experimental setup for investigating boundary layer diffusion flames under forced flow.

Figure 6.1 shows the forced flow experimental setup used for investigating boundary layer diffusion flames under forced flow. For an appropriate value of uniform air stream velocity U_∞, a stable, laminar two-dimensional diffusion flame could be established over a condensed fuel surface. When U_∞ was increased above the stability limit ($U_\infty > 2.2$ m/s), the leading flame edge became unstable and local quenching of the flame was observed at the leading edge of the fuel surface. Increasing the flow velocities further blew off the flame completely. These limits of stability were

previously investigated by Raghavan et al. [53] who used numerical simulations to determine the range of Reynolds numbers under which the Emmons solution is valid. Within this stable regime, the flame anchors near the leading edge of the condensed fuel surface and the combustion zone is confined beneath the hydrodynamic and thermal boundary layers. However, in the case of very low freestream velocities, the combustion zone is beyond the hydrodynamic boundary layer, and in cases of very high freestream velocities, the flame moves away from the leading edge and anchors at a location downstream, invalidating the Emmons solution in these regimes [53]. In the present work, freestream velocities were carefully chosen in the range where the Emmons solution is valid.

The flame stand-off distance was found to increase with the distance x from the leading edge. As U_∞ is increased, the flame approaches the condensed fuel surface and the flame anchoring distance was found to shift downstream. The luminosity of the blue flame zone decreased as x increased. PMMA flames were found to be more sooty when compared to methanol and ethanol flames. The averaged mass burning rates and flame lengths were observed to increase monotonically with an increase of U_∞. Figure 6.2 and 6.3 shows a comparison of averaged mass burning rates and flame lengths for methanol, ethanol and PMMA boundary-layer diffusion flames established under different free-stream velocities.
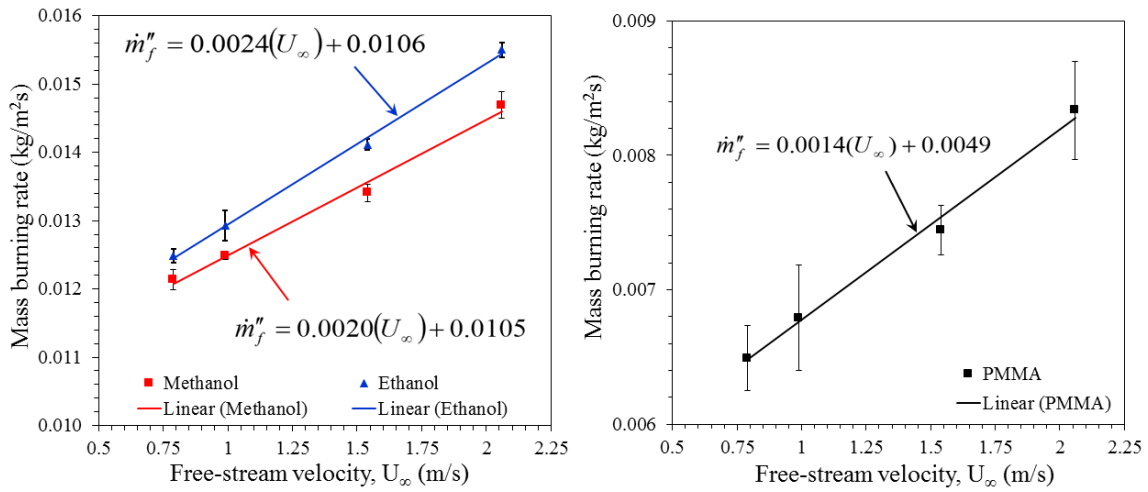
Figure 6.2: Averaged mass burning rates for (left) methanol/ethanol and (right) PMMA boundary-layer diffusion flames.
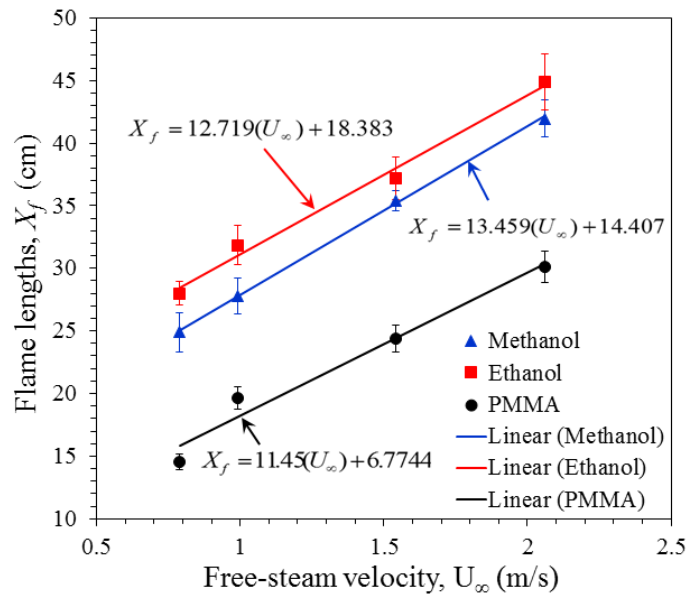
Figure 6.3: Average flame lengths for (left) methanol/ethanol and (right) PMMA boundary-layer diffusion flames.

Figure 6.4 shows side-view direct flame photographs of methanol, ethanol and PMMA boundary layer diffusion flames at free-stream velocities of 0.79 m/s and 2.06 m/s, respectively. It is clear from Figure 6.4 that for a low free-stream air velocity (U_∞=0.79 m/s), the flame has a first anchoring point just before the leading edge of the condensed fuel surface ($\sim$0.2 cm upstream of the leading edge) and another anchoring point downstream of the trailing edge ($\sim$2.1 cm downstream of the trailing edge) in the case of a methanol boundary layer diffusion flame. The same observations were made for an ethanol and PMMA boundary layer diffusion flame at a low free-stream velocity of (U_∞=0.79 m/s). However, the location of the second anchoring point for an ethanol flame occurred much further downstream of the trailing edge when compared against a methanol flame. In the case of an ethanol boundary layer diffusion flame, the first anchoring point was found to be at $\sim$0.15 cm upstream of the leading edge and the second anchoring point was found to be at $\sim$9 cm downstream of the trailing edge. In case of a PMMA flame, the first anchoring point was found to be at the leading edge and the second anchoring point was found to be at $\sim$3 cm downstream of the trailing edge. The second anchoring point in the case of a PMMA flame was found to occur intermittently and not permanently. It is clear that due to a buoyancy-induced recirculatory flow near the flame tip, a second flame anchoring point exists. Also, the flame is lifted upwards near the flame tip,

192
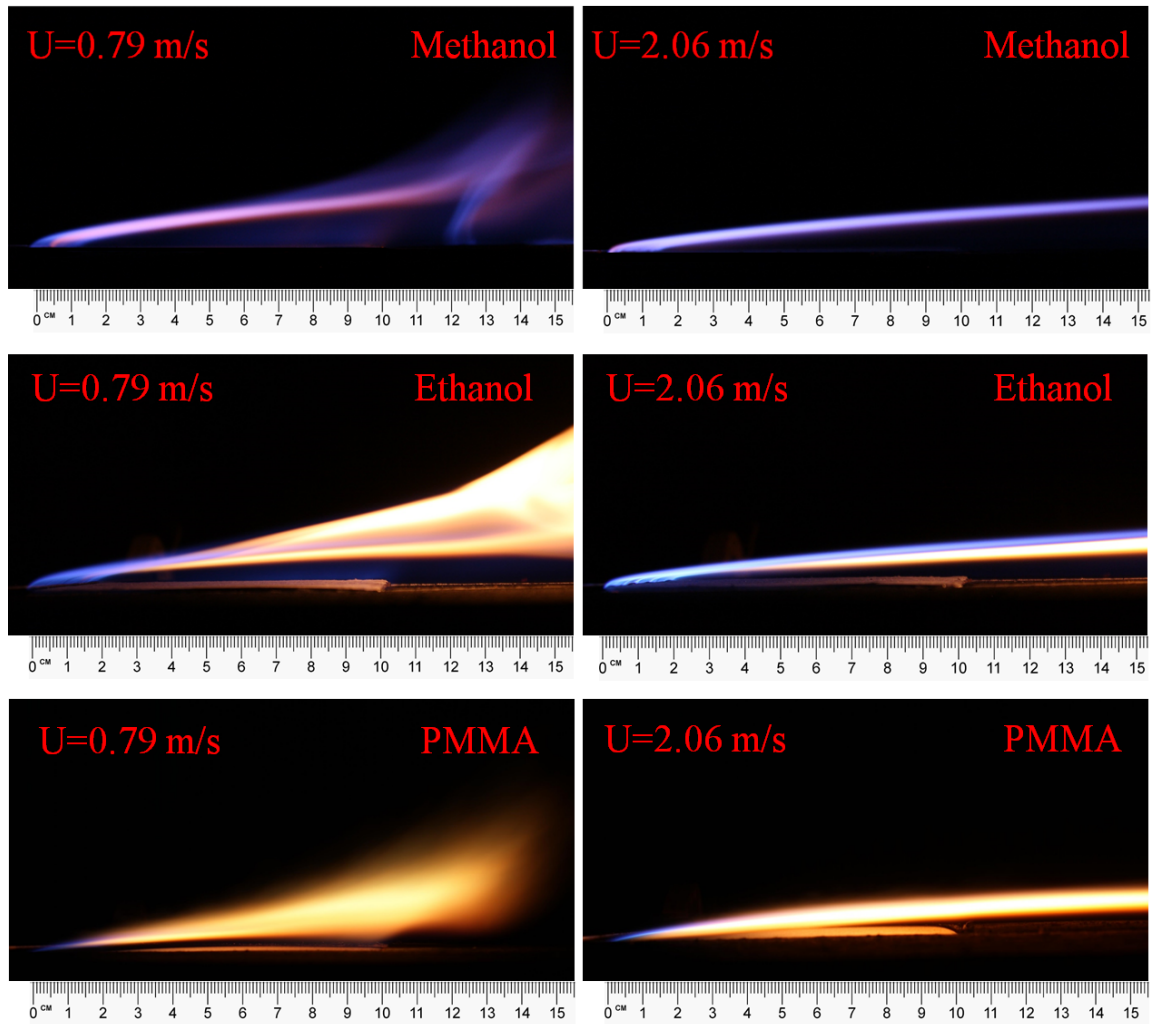
Figure 6.4: Side-view direct flame photographs of methanol (top), ethanol (middle) and PMMA (bottom) boundary layer diffusion flames at free-stream velocities of 0.79 m/s and 2.06 m/s, respectively. The second anchoring point is clearly visible for a methanol flame and intermittently for a PMMA flame at a free-stream velocity of 0.79 m/s. The second anchoring point for an ethanol flame is not visible as it occurs 9 cm downstream of the trailing edge.

changing its shape from convex to concave. For this case, the buoyancy induced flow

could entrain air from the exit, thereby pushing the flame up. This results in flame stretching in that region. However, as the free-stream air velocity increases, the second flame anchoring location shifts further downstream. At even higher velocities (greater than approximately 1.15 m/s for a methanol and ethanol flame), the flame does not re-anchor again downstream of the trailing edge. For instance, at a higher free-stream velocity of 1.54 and 2.06 m/s, the flame does not have a second anchoring point. For a PMMA flame, the flame does not have a second anchoring point for free-stream velocities greater than 0.95 m/s. Figure 6.4 clearly indicates that the buoyant forces are not sufficient to overcome the inertial forces of forced convection at higher freestream velocities (typically higher than 1.0 m/s) and the flame retains its typical boundary layer type shape throughout the flame length.

In order to estimate the relative strengths of inertial to buoyant forces, the Richardson number (Ri) is employed. For the range of free-stream velocities considered in this study, Ri is calculated as

$$\text{Ri} = \frac{\text{Gr}_L}{\text{Re}_L^2} = \frac{g\beta\Delta T L}{U_\infty^2}, \tag{58}$$

where Gr is the Grashof number, Re is the Reynolds number and L is the length of the fuel sample. In the above equation, the volumetric thermal expansion coefficient, β, was evaluated as an inverse of the average value of the flame and wall
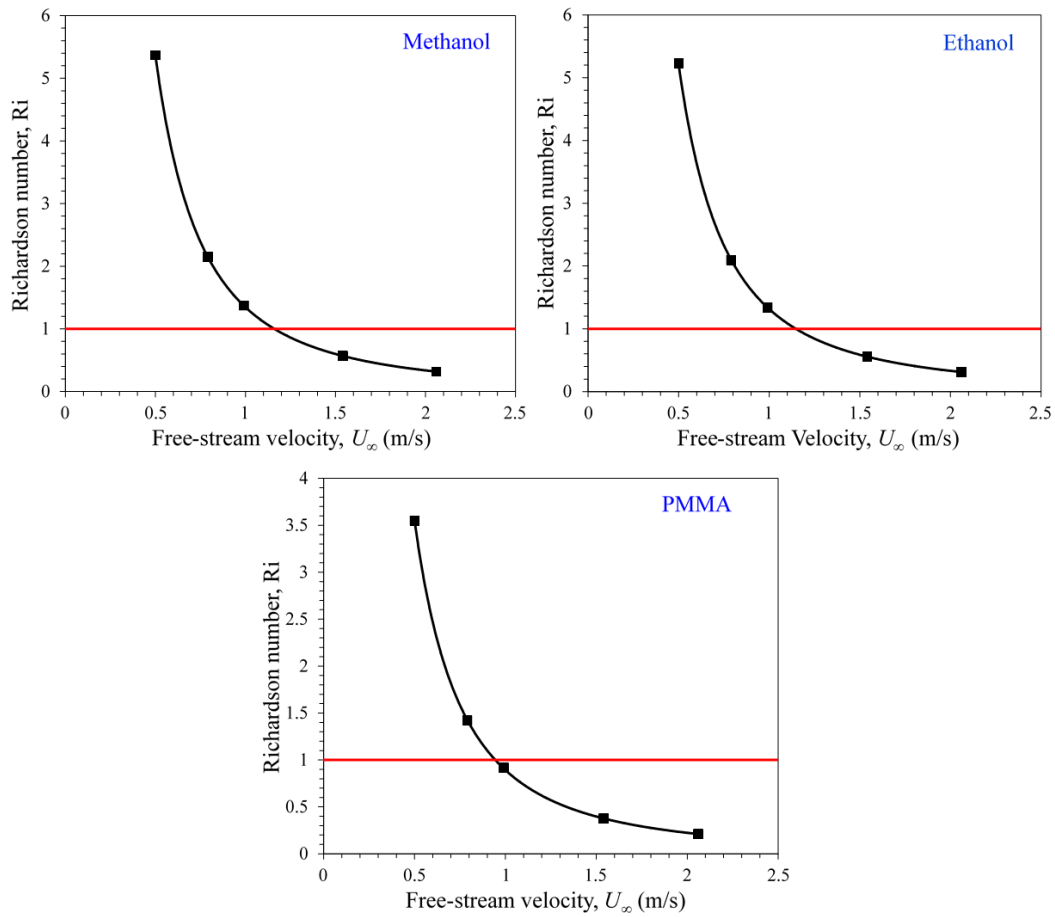
Figure 6.5: Variation of the Richardson number with free-stream air velocity for (top-left) methanol, (top-right) ethanol and (bottom) PMMA boundary layer diffusion flames.

temperatures for different free-stream air velocities and ΔT was taken as the temperature difference between the average flame and wall temperature for different free-stream air velocities. It was found that for a free-stream air velocity of 0.79 m/s, the Richardson number has a value of around 2.1, 2.0 and 1.42 for methanol,

ethanol and PMMA flames respectively, indicating that free-convective, buoyancy-induced flow effects would dominate. As the free-stream air velocity increases, Ri decreases as shown in Figure 6.5. The value of Ri reached a value below unity when the free-stream velocity just exceeded a critical value around 1.15 m/s for methanol and ethanol flames and 0.95 m/s for PMMA flames respectively. Therefore, when the free-stream velocity was less than 1.15 m/s for methanol and ethanol and less than 0.95 m/s for a PMMA flame (Ri value greater than 1.0), a second anchoring point was formed due to buoyancy-induced flow from the exit. The second anchoring point was then found to move away from the trailing edge as the free-stream air velocity further increased upto the critical velocity. Thereafter, the flame does not have a second anchoring point for free-stream velocities greater than critical velocity.

6.2. Gas-phase temperatures

Using the forced-flow experimental apparatus described in Chapter 3, measurements were taken for local temperature profiles along condensed fuel surfaces. Figures 6.6 and 6.7 show the temperature profiles at several stream-wise locations along the condensed fuel surface for methanol, ethanol and PMMA boundary-layer diffusion flames at free-stream velocities of 0.79 and 2.06 m/s respectively.

On the downstream side of the leading flame edge, T increases with y to a maximum flame temperature T_{fl} at the flame zone for methanol, ethanol and PMMA
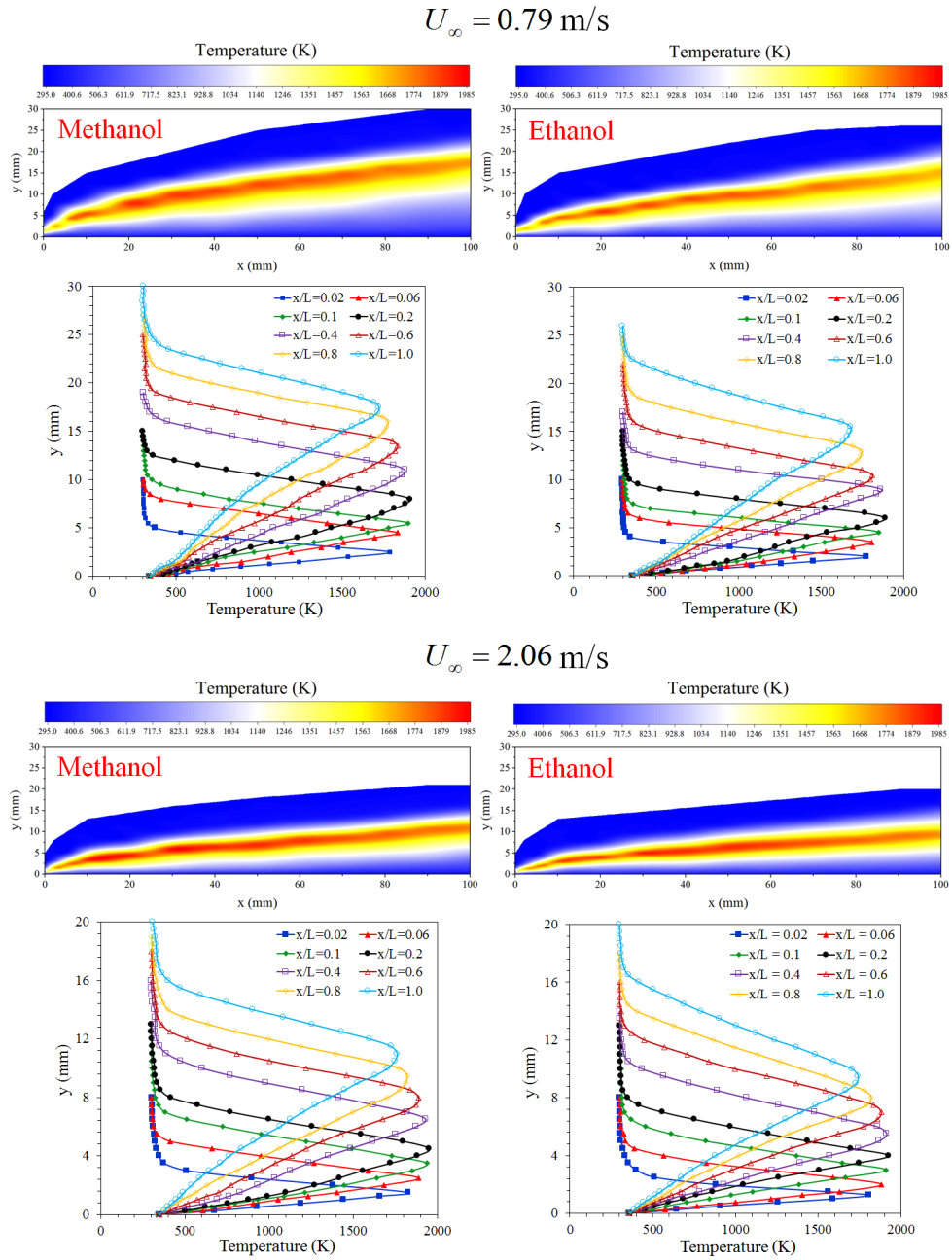
Figure 6.6: Temperature contours and profiles (experimental) at several stream-wise locations along the condensed fuel surface for methanol and ethanol boundary-layer diffusion flames at free-stream velocities of 0.79 (top) and 2.06 (bottom) m/s respectively.
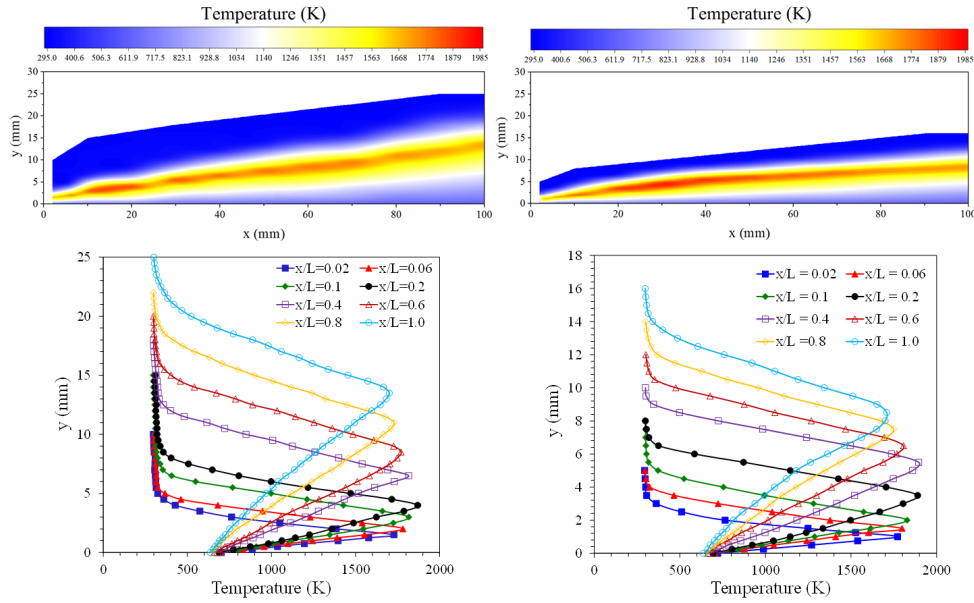
Figure 6.7: Temperature contours and profiles (experimental) at several stream-wise locations along the fuel surface for a PMMA boundary-layer diffusion flame at free-stream velocities of 0.79 (left) and 2.06 (right) m/s respectively.

boundary-layer diffusion flames. On the air-stream side of the flame zone, T decreases with y to ambient temperature at the thermal boundary layer edge. T_{fl} at a given streamwise location was found to increase slightly with an increase in U_∞. Within about 2-3 cm of the leading edge of the condensed fuel surface, T_{fl} increases in the x direction. Further downstream, T_{fl} decreases in the x direction. The same observations were made by Hirano and co-authors [26] when they studied ethanol and methanol diffusion flames in a forced convective environment. The peak flame temperatures were found to be 1906 K and 1980 K for a methanol flame at U_∞=0.79

and 2.06 m/s, respectively. The peak flame temperatures for an ethanol flame were found to be 1887 and 1958 K at U_∞=0.79 and 2.06 m/s, respectively. The peak flame temperatures for methanol, ethanol and PMMA flames at different free-stream velocity conditions are plotted in Figure 6.8. A closer look at the given figure suggests an increasing trend for the flame peak temperatures with incoming free-stream velocity. The increase in flame peak temperatures at higher free-stream velocities can be attributed to more complete combustion at higher free-stream velocities due to better transport of the combustion products downstream as well as increase in the local mass burning rate.

Average flame and wall temperatures for methanol, ethanol and PMMA boundary-layer diffusion flames was calculated by averaging the flame and wall temperatures at each streamwise location x along the condensed fuel surface for all the free-stream velocities considered in this study. The average flame temperature was then calculated to be 1844 K, 1825 K and 1799 K for methanol, ethanol and PMMA flames respectively. Similarly, the average wall temperature was then calculated to be 343 K, 358 K and 672 K for methanol, ethanol and PMMA flames, respectively. Thus, the temperature of the condensed fuel surface at different forced flow conditions was found to be approximately near the boiling points of the fuels studied here. Pyrolysis temperatures for fuels used in this study are listed in Table 6.

In the case of liquid fuels (methanol and ethanol) the temperature of the condensed fuel surface was found to decrease slightly with x. However, this change was very small and was found to be within the temperature uncertainty error of ± 14 K. In the case of a PMMA boundary layer diffusion flame, the difference between the molten layer temperatures at $x=$ 10 mm and $x=$ 100 mm was found to be larger than the temperature uncertainty error of ± 14 K. The PMMA molten layer temperature was measured precisely at several streamwise locations x by dipping the thermocouple probe directly into the molten layer during burning. Figure 6.9 shows the variation of the PMMA molten layer temperature with x for $U_\infty=$ 0.79 m/s. The temperature of the PMMA molten layer decreases with x more sharply than the surface temperatures of liquid fuels. The convective heat feedback to the surface was also found to decrease with x. The convective heat flux was estimated to be several times higher at the leading edge than in the trailing section, 25.4 kW/m^2 at $x = 10$ mm and 9.57 kW/m^2 at $x = 100$ mm for a PMMA flame at $U_\infty=$ 0.79 m/s. The convective heat flux was approximated here by measuring temperature gradients at the condensed fuel surface using the expression $k_w \left(\partial T/\partial y\right)_{y=0}$. Thus, both the heat feedback and the measured pyrolysis temperature decreased with x, but the pyrolysis temperature decreased more slowly. This is consistent with the results of Vovelle et al. [122] who reported that the pyrolysis temperature increases slightly with the
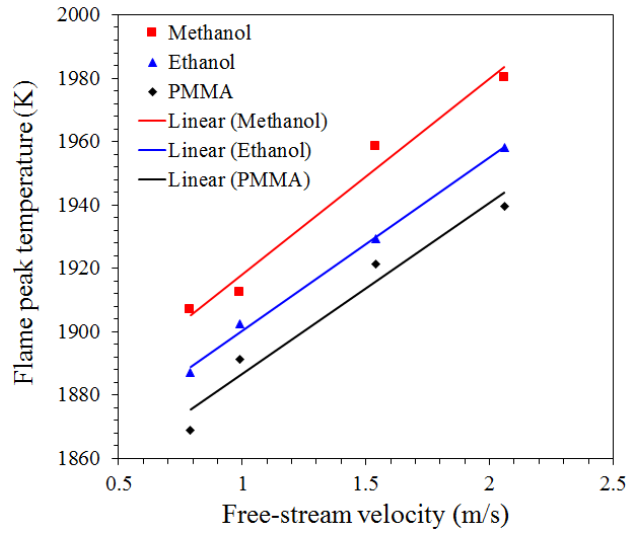
Figure 6.8: Flame peak temperatures for methanol, ethanol and PMMA boundary-layer diffusion flames under different free-stream conditions.
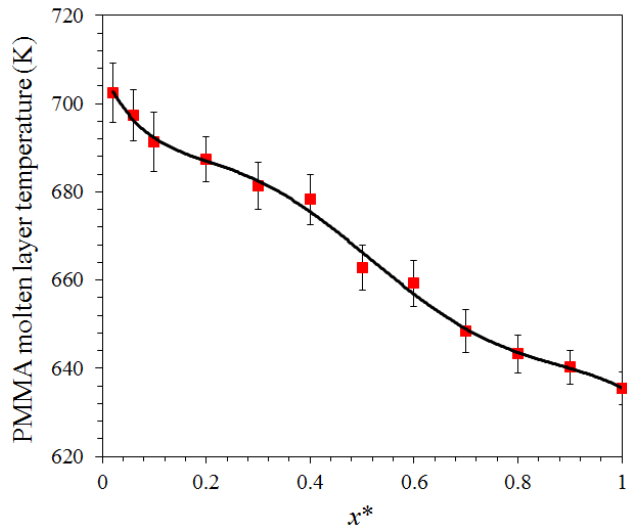
Figure 6.9: Variation of PMMA molten layer temperature with streamwise distance x for $U_\infty = 0.79$ m/s.

201

heat flux to the surface. They performed experiments in which thermocouples were embedded at various depths in the PMMA solid. The PMMA surface was irradiated at a constant rate ranging from 1.5 to 3.0 W/cm^2. They showed that the surface temperature approaches a steady state value, which increases slightly with heat flux ($\sim$ 600-650 K).

At the trailing edge of the sample for a methanol flame, the flame temperatures were found to drop by about 186 K and 218 K from peak temperatures at free-stream air velocities of 0.79 and 2.06 m/s, respectively. Similarly, for an ethanol flame the flame temperatures were found to drop by 209 K and 217 K from peak temperatures at free-stream air velocities of 0.79 and 2.06 m/s respectively. For a PMMA boundary-layer diffusion flame, the maximum peak flame temperature is about 1869 K for U_∞=0.79 m/s, which occurs about 20 mm from the leading edge. Thereafter, the value of the peak temperature decreases slowly, signaling the end of the heat release region and the beginning of the plume zone at the sample trailing edge. It dropped by about 168 K at the sample trailing edge. Similarly, for U_∞= 2.06 m/s the maximum peak flame temperature for a PMMA flame is about 1939 K which occurs about 30 mm from the leading edge. Thereafter, the value of the peak temperature decreases slowly and was found to drop by about 231 K at the sample trailing edge. This temperature decrease is primarily due to convective heat losses.

Observation of the temperature gradients normal to the fuel surface suggests that they are highest near the leading edge and decrease further downstream. The temperature gradient $(\partial T/\partial y)_0$ at $y = 0$ decreases in the x direction downstream of the leading edge. $(\partial T/\partial y)_0$ at a given streamwise location was found to increase with an increase in U_∞. This is consistent with known characteristics of boundary-layer diffusion flames, in that convective heat feedback decreases with x for a particular U_∞ and increases at a given streamwise location with an increase in U_∞. The local mass-loss rate from the fuel, driven by convective heat fluxes to the surface in these small, laminar flames, should similarly decrease with x. The flame usually becomes thicker when moving downstream of the leading edge and the flame stand-off distance increases with increasing x. It follows, therefore, that the local mass burning-rate should also decrease with x, discussed later.

6.3. Flame Stand-off Distance

The non-dimensional flame stand-off distance, $y_f^* = (y_f/L)$, at different locations along the fuel surface are plotted in Figure 6.10 for methanol, ethanol and PMMA boundary-layer diffusion flames established under free-stream air velocities of 0.79, 0.99, 1.54 and 2.06 m/s, respectively. The flame stand-off distance was measured in the direction normal to the condensed fuel surface and the location of peak temperature was taken as the location of the flame. The flame stand-off distance was
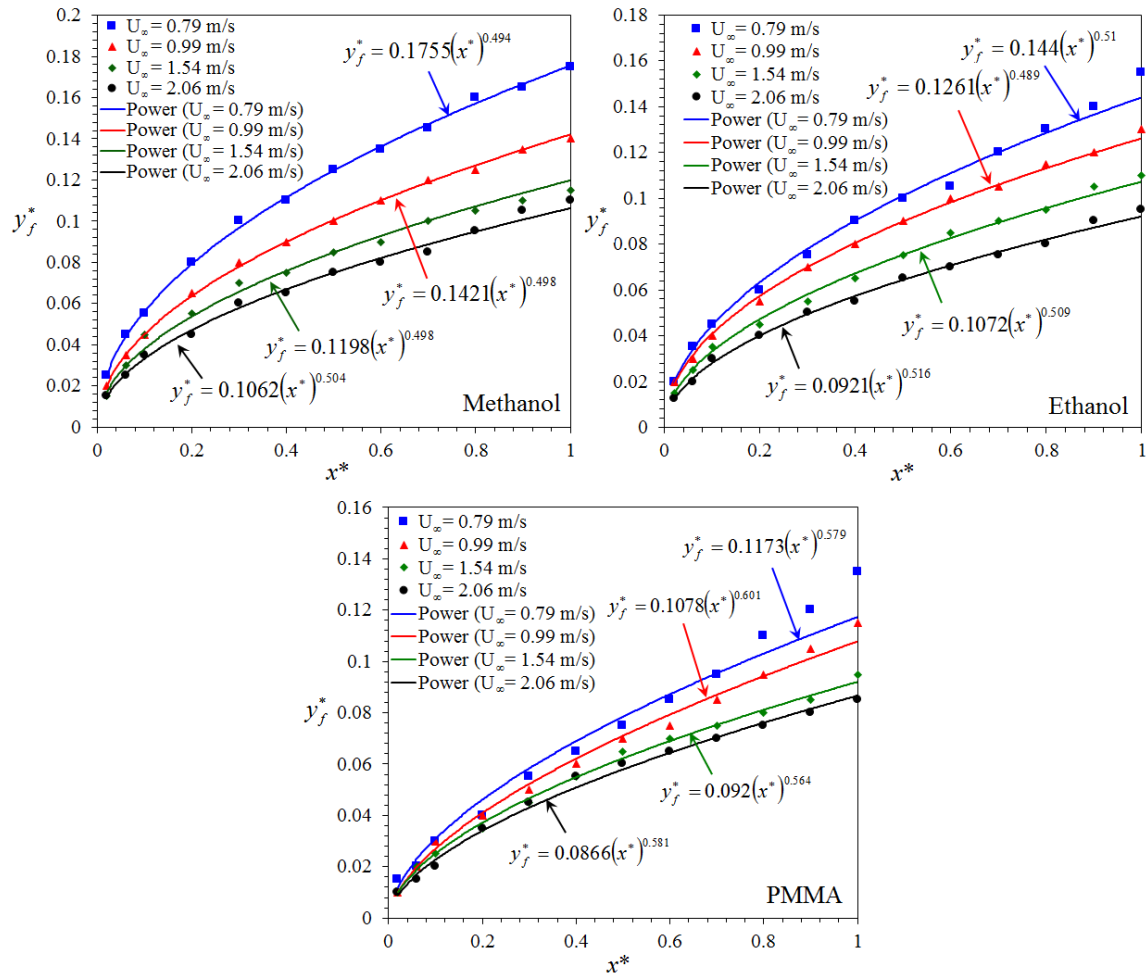
Figure 6.10: The flame stand-off distance at different locations along the fuel surface for (top-left) methanol, (top-right) ethanol and (bottom) PMMA boundary-layer diffusion flames established under free-stream velocities of 0.79, 0.99, 1.54 and 2.06 m/s, respectively.

also measured through side-view flame photographs. The flame stand-off distance calculated through side-view flame photographs and that measured through peak temperature location was found to be in relatively good agreement for methanol,

ethanol and PMMA flames. The results plotted in Figure 6.10 represent the flame stand-off distance measured by taking into account the location of peak temperatures.

For all flames, Figure 6.10 shows the flame stand-off distance is lower near the leading edge and increases further downstream up to the trailing edge. This leads to enhanced heat transfer to the fuel surface at the leading edge and hence higher evaporation rates of the fuel at this location. Accordingly, the local burning rate is highest at this location. The flame stand-off distance is higher for regions near the trailing edge and hence heat transfer rates at these locations are lower. Due to lower heat transfer rates at these locations, the local mass-burning rates are found to be lower at these locations. Also, the flame stand-off distance is almost proportional to $x^{0.5}$, confirming the similarity theory for a forced-convection boundary layer adjacent to a horizontal flat plate [6, 126]. As U_∞ is increased, the flame approaches the condensed fuel surface and the flame anchoring distance was found to shift downstream. Flame stand-off distance at a given streamwise location x decreases for higher free-stream velocities. This results in higher heat feedback to the condensed fuel surface at higher free-stream velocities.

6.4. Correlation Verification

Using the experimental set-up described in Chapter 3, average mass burning rates were calculated for methanol, ethanol and PMMA boundary layer diffusion flames by

using a load cell. Detailed temperature profiles for forced-convective flames enabled us to calculate the variation of the normal non-dimensional temperature gradients along the condensed fuel surface (described in section 6.5). Averaging the non-dimensional temperature gradient for the entire fuel surface from Figs. 6.12 and 6.13 for methanol, ethanol and PMMA flames and plotting them against the average mass burning rates obtained through load cell results in a linear correlation of the given data, similar to that proposed by Eq. (9). The slope of the linear curve was found to be 4.67 g/m^{2}s, 5.67 g/m^{2}s and 3.52 g/m^{2}s for methanol, ethanol and PMMA flames, respectively. Using the appropriate transport properties for methanol, ethanol and PMMA (given in Chapter 5, Table 6), Bk/c_pL for methanol, ethanol and PMMA was calculated to be 5.02 g/m^{2}s, 6.34 g/m^{2}s and 3.92 g/m^{2}s respectively.

The relatively close agreement in the two quantities [the slope and the proportionality constant in Eq. (9)] strongly suggests that a linear relationship exists between average mass burning rate and average non-dimensional temperature gradient at the condensed fuel surface, similar to that proposed by Eq. (9). Figure 6.11 shows the plot for average mass-burning rate per unit area vs. the average non-dimensional temperature gradient at the fuel surface for methanol, ethanol and PMMA boundary layer diffusion flames under different forced convective environments.
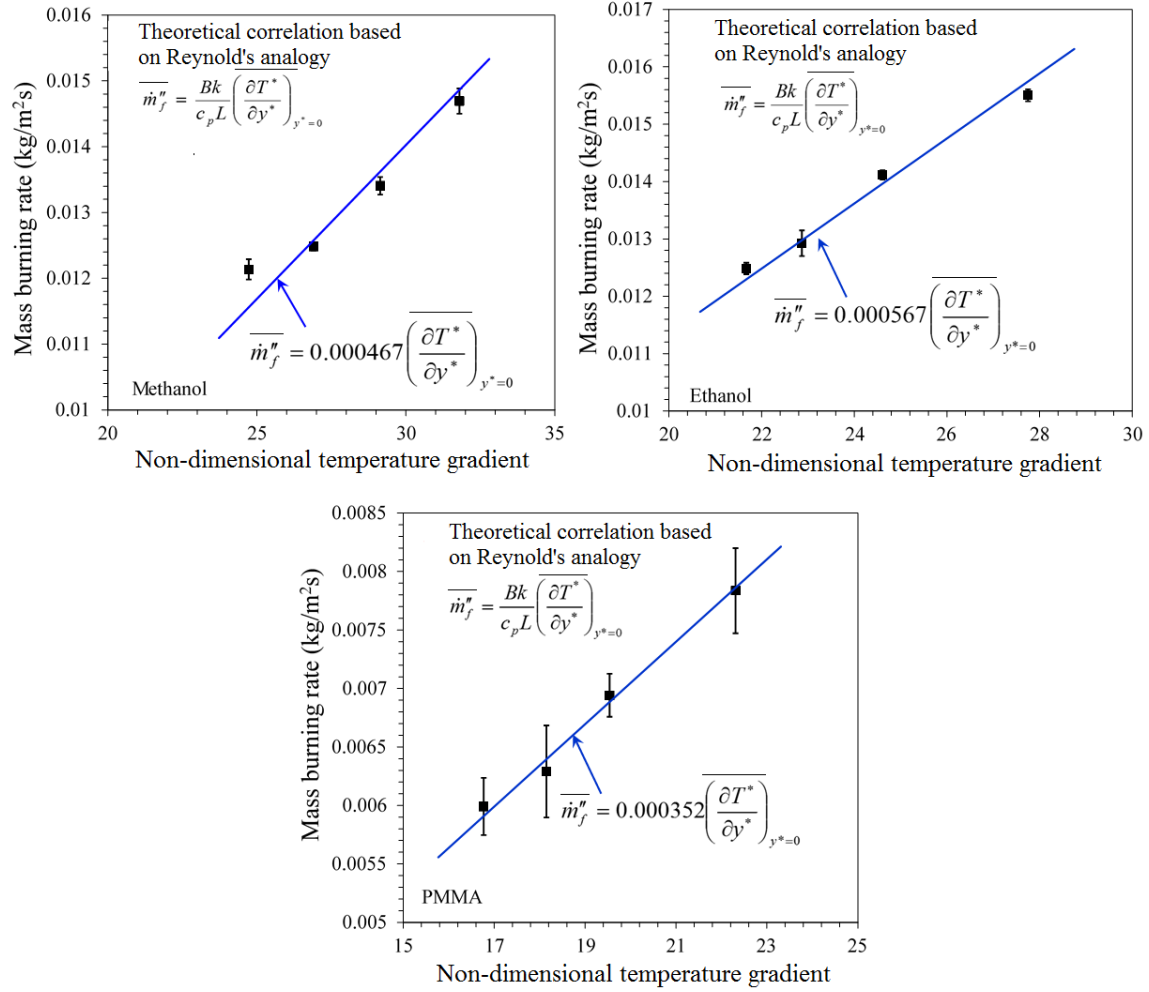
Figure 6.11: The average mass-burning rate per unit area $(\overline{\dot{m}''_f})$ versus the average non-dimensional temperature gradient $[\overline{(\partial T^*/\partial y^*)_{y^*=0}}]$ at the fuel surface for methanol, ethanol and PMMA boundary layer diffusion flames stabilized at $U_\infty = 0.79$, 0.99, 1.54 and 2.06 (m/s) over a fuel surface of length 10 cm. The blue straight line indicates the linear fit through experimental data points (indicated by black symbols). The given figure clearly indicates that a linear relationship exists between average mass burning rate and average non-dimensional temperature gradient at the fuel surface.

6.5. Non-dimensional Temperature Gradients

Figures 6.12 and 6.13 show the variation of the normal non-dimensional temperature gradients along the fuel surface extracted from experimental temperature data of methanol, ethanol and PMMA diffusion flames for U_∞=0.79 m/s and 2.06 m/s, respectively. The normal non-dimensional temperature gradients at the fuel surface, $(\partial T^*/\partial y^*)\,|_{y^*=0}$ were calculated from the slope at $y^* = 0$ of a fifth-order polynomial fit to the non-dimensional temperature distribution near the fuel surface. The temperature gradient normal to the fuel surface was found to be highest at the leading edge and lowest at the trailing edge ($x = 100$ mm). The local mass-burning rate should follow a similar trend, as is revealed by the calculated rates in Figures 6.17 and 6.18.

Averaging the non-dimensional temperature gradient for the entire fuel surface, the average mass-burning rate for a methanol flame is estimated to be 12.38 g/m²s, 13.47 g/m²s, 14.56 g/m²s and 15.96 g/m²s at U_∞=0.79, 0.99, 1.54 and 2.06 m/s, respectively, using Eq. (9). Similarly, for an ethanol flame, the average mass burning rate is estimated to be 13.75 g/m²s, 14.51 g/m²s, 15.61 g/m²s and 17.61 g/m²s at U_∞=0.79, 0.99, 1.54 and 2.06 m/s, respectively, using Eq. (9). Similarly, for a PMMA flame, the average mass burning rate is estimated to be 6.57 g/m²s, 7.11 g/m²s, 7.66 g/m²s and 8.74 g/m²s at U_∞=0.79, 0.99, 1.54 and 2.06 m/s, respectively.
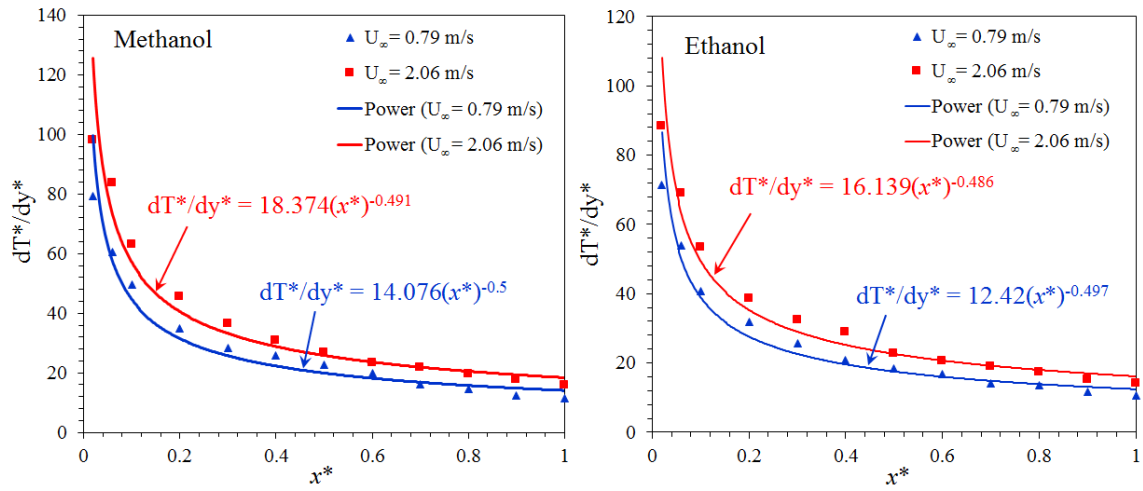
Figure 6.12: Variation of the normal non-dimensional temperature gradients along the fuel surface for (left) methanol and (right) ethanol boundary layer diffusion flames at U_∞=0.79 m/s and 2.06 m/s, respectively.
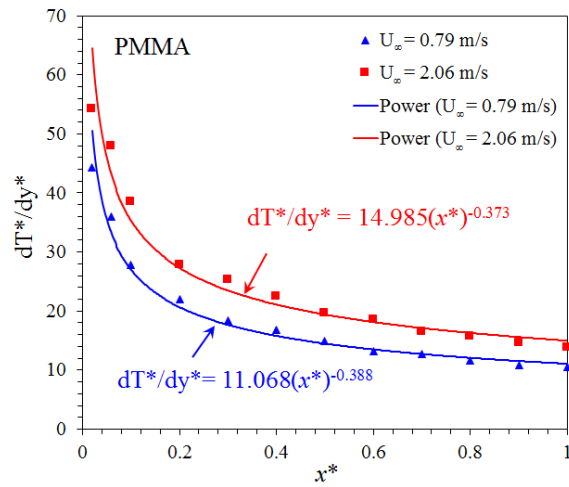
Figure 6.13: Variation of the normal non-dimensional temperature gradients along the fuel surface for a PMMA boundary layer diffusion flames at U_∞=0.79 m/s and 2.06 m/s, respectively.

Table 8: Measured (load cell) and predicted (using Eq. (9)) averaged mass burning rates.

Fuel and flow conditions	Measured $\overline{\dot{m}''_f}$ (g/m^2-s)	Correlation $\overline{\dot{m}''_f}$ (g/m^2-s)	Error (%)
Methanol (U_∞=0.79 m/s)	12.14	12.38	1.98%
Methanol (U_∞=0.99 m/s)	12.48	13.47	7.93%
Methanol (U_∞=1.54 m/s)	13.41	14.56	8.57%
Methanol (U_∞=2.06 m/s)	14.69	15.96	8.65%
Ethanol (U_∞=0.79 m/s)	12.49	13.75	10.08%
Ethanol (U_∞=0.99 m/s)	12.93	14.51	12.22%
Ethanol (U_∞=1.54 m/s)	14.12	15.61	10.55%
Ethanol (U_∞=2.06 m/s)	15.50	17.61	13.61%
PMMA (U_∞=0.79 m/s)	5.99	6.57	9.69%
PMMA (U_∞=0.99 m/s)	6.29	7.11	13.06%
PMMA (U_∞=1.54 m/s)	6.94	7.66	10.30%
PMMA (U_∞=2.06 m/s)	7.84	8.74	11.56%

Appropriate average values of transport properties were used to calculate the constant C in Eq. (9) and are given in Table 6 in Chapter 5. Table 8 shows the averaged mass burning rate results derived from the load cell data and by using

the semi-analytical expression in Eq. (9). The reasonably close agreement between the measured and predicted averaged mass-loss rates demonstrate that they can in theory be obtained from careful temperature measurements in the gas phase near the fuel surface.

6.6. PMMA Regression and Local Pyrolysis Rate

6.6.1. Local pyrolysis rate for PMMA

Figure 6.14 shows the time-averaged regression rate for a PMMA surface at various streamwise locations x. These tests were conducted with normal air at U_∞ = 0.79 and 2.06 m/s and test durations of 100, 150, 250, 550 and 850 s. In each case, the surface had regressed non-uniformly along x from its original flat profile. Significantly more regression took place in the leading section when compared with regions downstream, consistent with the non-uniform rate of heat feedback from the boundary layer flame to the PMMA surface. For $x > 0$, in all tests, the sample had receded significantly below the level of the original surface within 5 min. This resulted in the formation of a valley or a step in the leading section as shown in Fig. 6.14. Fig. 6.14 demonstrates that valley deepens with time and the position of the deepest point moves slightly downstream with time. A closer look at the regression profiles of a PMMA surface reveals that the surface remained almost flat near the

trailing edge within the burn-out time of 5 min and became increasingly curved as time progressed. Thus, nonuniform surface regression leads to the formation of a valley that deepens with time, which affects the local burning rate in the leading section.

It can be easily seen from Fig. 6.14 that the burned thickness is much larger upstream than downstream and also larger in the 850 s test than in the 100 s test. Therefore, one would expect the error in the burning rate measurements to be highest downstream at short times. In the leading section and/or at high velocities, where convection heat transfer rates are high, the error is smaller. For example, for $U_\infty = 0.79$ m/s and $x= 6$ mm, the error in the measured time-averaged regression rate is approximately 9.68% at $t = 100$ s. Downstream at $x= 100$ mm with $U_\infty = 0.79$ m/s, it is approximately 43% ($t = 100$ s), but with $U_\infty = 2.06$ m/s and $x= 100$ mm, the error is approximately 3.74 % ($t = 850$ s).

Figure 6.14 shows that the regression rate peaks near the leading edge and thereafter decreases sharply with x, consistent with the way heat feedback varies with x [12]. For $U_\infty = 0.79$ m/s , the peak regression rate is about 0.024 mm/s in the 100 s burn and decreases sharply with x thereafter. The rate of decrease with x is slower at longer burn times. The rate also decreases sharply from the peak towards $x = 0$, especially at burn times longer than 5 min.

Figure 6.14 also demonstrates that the regression rate decreases with time in the leading 6 mm of the sample. With $U_\infty = 0.79$ m/s, for example, in the 100, 150, 250, 550 and 850 s tests, the regression rates at $x = 2$ mm are 0.022, 0.019, 0.015, 0.008 and 0.007 mm/s, respectively. Furthermore, the peak regression rate decreased from 0.024 to 0.007 mm/s (a factor of 3.4) between the 100 and 850 s tests. Figure 6.14 also shows that as the surface regression rate decreased with time, the x position of the peak regression rate slightly shifted downstream with time. For example, in the 0.79 m/s and 2.06 m/s test the peak regression occurred at $x \sim 0$ mm in the 100 s test and $x \sim 6$ mm in the 850 s test, respectively.
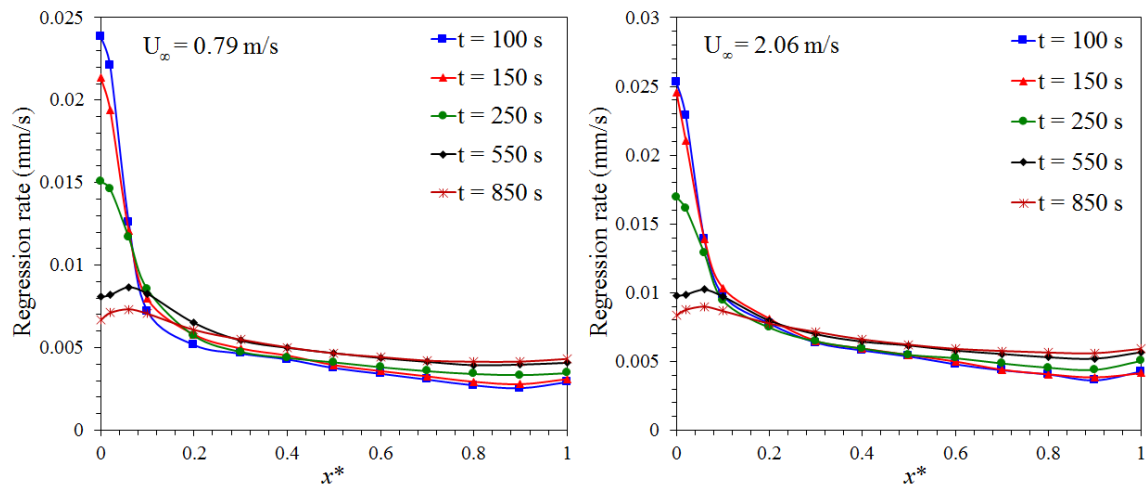
Figure 6.14: Surface regression rate at various streamwise locations in tests lasting 100, 150, 250, 550 and 850 s for $U_\infty = 0.79$ m/s (left) and 2.06 m/s (right).

It can be clearly seen in Figure 6.14 that the uneven surface regression and the

creation of a valley led to the transient surface regression rate in the leading section. In the mid and trailing section of the sample, where the heat feedback had decreased substantially, the degree of surface regression is small; hence, the effects of uneven moving boundary are expected to be very small. This is shown within $20 \leq x \leq 100$ mm in the 0.79 m/s test. Nonetheless, the local burning rate is time dependent although the trend is not easily discernible from Figure 6.14 because of scale. Indeed, the regression rate for the 850 s test is distinctly the largest at each x location near the trailing edge, and a closer look at the data reveals an increasing trend. For example, at $x = 80$ mm the regression rates after 100, 150, 250, 550 and 850 s are 0.0027, 0.0029, 0.0034, 0.0039 and 0.0042 mm/s, respectively for $U_\infty = 0.79$ m/s. Despite the large error associated with the data in this region at short times, the regression rate could be said to have doubled in 850 s. It is shown more clearly later that the regression rate definitely increases with time in the trailing section and that this is due to increased heat feedback with time and slow in-depth heat conduction in this section, where the heat feedback rate is small relative to that in the leading section.

6.6.2. Transient burning rate in the leading section

In the leading section of the solid, where heat feedback is very high, gas phase steady state is attained soon after uniform ignition, before a significant valley is

formed. In that period, approximately all the heat feedback is used to gasify the solid. Later, a valley is formed and the surface regression rate decreases with time as shown in Figure 6.14.

Experiments were performed to estimate the heat feedback to the sample surface in the leading section at various times. With one 50 μm wire-diameter R-type thermocouple, located at $x = 6$ mm, temperature profiles across the flame were measured 60, 300, 600, 900 and 1200 s into a test. At these times, the thermocouple was moved across the flame, and temperature measurements were made at 0.25 and 0.5 mm intervals until the thermocouple penetrated the molten layer, the temperature of which was ~ 669 K. Figure 6.15 shows the temperature profiles measured at different times. Here the objective is to measure the trend rather than the absolute values and so y_f and T are approximate. The flame stand-off distance y_f in each profile can be estimated as the height of the peak temperature above the surface. Figure 6.15 shows that y_f increases with time. For example, y_f increased from 2 mm in the first 300 s to about 4 mm in 1200 s. Also, within the same time peak temperature dropped from about 1782 K to about 1578 K. The profiles also show that the temperature gradients close to the surface decreases with time. For example, temperature gradients decreased from about 656 K/mm to about 317 K/mm in 60 and 1200 s tests, respectively. It should be noted that the flame stand-off distance increases by

a factor of 2 from the first 300 s to 1200 s. Subsequently, temperature gradients at the fuel surface were found to decrease by a factor of 2. Therefore, the convective heat feedback at this location will similarly be reduced to half as the burn-out time duration increases from 60 s to 1200 s. These data strongly suggest that the heat feedback to the curved sample surface is decreasing with time as the valley deepens. Generally, the flame moves down with the regressing PMMA surface. However, the current results indicate that as time progresses, the flame does not keep up with the regressing surface in the leading section. Therefore, the heat feedback to the surface decreases, resulting in the decrease of regression rate with time. It is, therefore, essential to measure the temperature gradients at the PMMA surface during initial stages of steady burning when the PMMA surface is relatively flat. A closer look at Figure 6.15 suggests that the temperature gradients do not change much between 60 and 300 s tests. The PMMA surface remains relatively flat up to 300 s. After 300 s, a valley begins to form in the leading section of the PMMA surface, thereby increasing the flame stand-off distance and decreasing the convective heat feedback to the PMMA surface. Figure 6.15 shows the temperature profiles at different burn-out times at $x = 6$ mm as the valley deepens in this location for $U_\infty = 0.79$ m/s.

It can be concluded that the change in surface curvature with time leads to the observed transient regression rate. It should be noted that the valley formation in

forced PMMA flames is driven by the rate of non-uniform heat feedback from the flame to the surface. The same observations were made by Ndubizu and co-authors when they burnt PMMA plates in a forced convective environment [46].
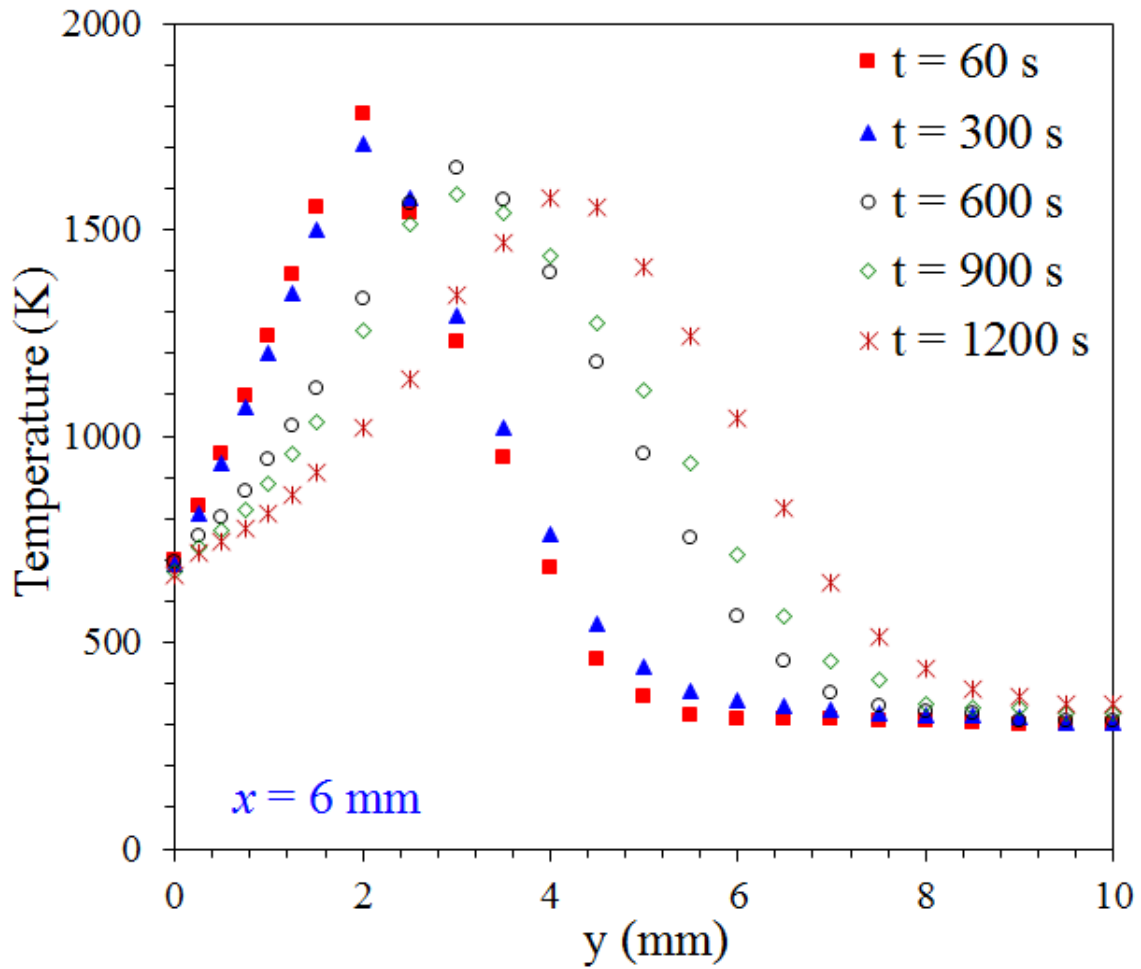
Figure 6.15: Temperature profiles at different burn-out times at $x = 6$ mm as the valley deepens in this location for U_∞=0.79 m/s.

6.6.3. Transient burning rate in the trailing section

The regression rate was found to increase slowly with time in the trailing section and can be easily seen in Figure 6.14. The transient burning downstream is due to transient heat feedback to the solid and solid-phase transient heating. During ignition, the entire surface is heated up at a very high rate so as to quickly obtain ignition and a stable boundary layer diffusion flame. Thereafter, the external heat is turned off and the surface pyrolysis rate entirely depends on the heat feedback from the flame to the surface. The heat feedback from flame to the surface is several times less than the rate from the ignition source in the trailing section. In the leading section, where the heat feedback to the surface is high, owing to smaller flame stand-off distances, pyrolysis of the PMMA surface continues at a high rate. However, in the trailing section where the heat feedback is now much lower, the surface that was pyrolyzing vigorously under the external source cools down and then slowly starts heating up. Hence, it takes significant time (order of minutes) for the trailing section to heat up enough to start pyrolyzing at a significant rate.

It was observed earlier that the flame moves down as the surface regresses in the trailing section. Since the surface regression is nonuniform along the length of the sample, the flame stand-off distance may be changing with time downstream. This would imply that the heat feedback to the surface in this region would be changing
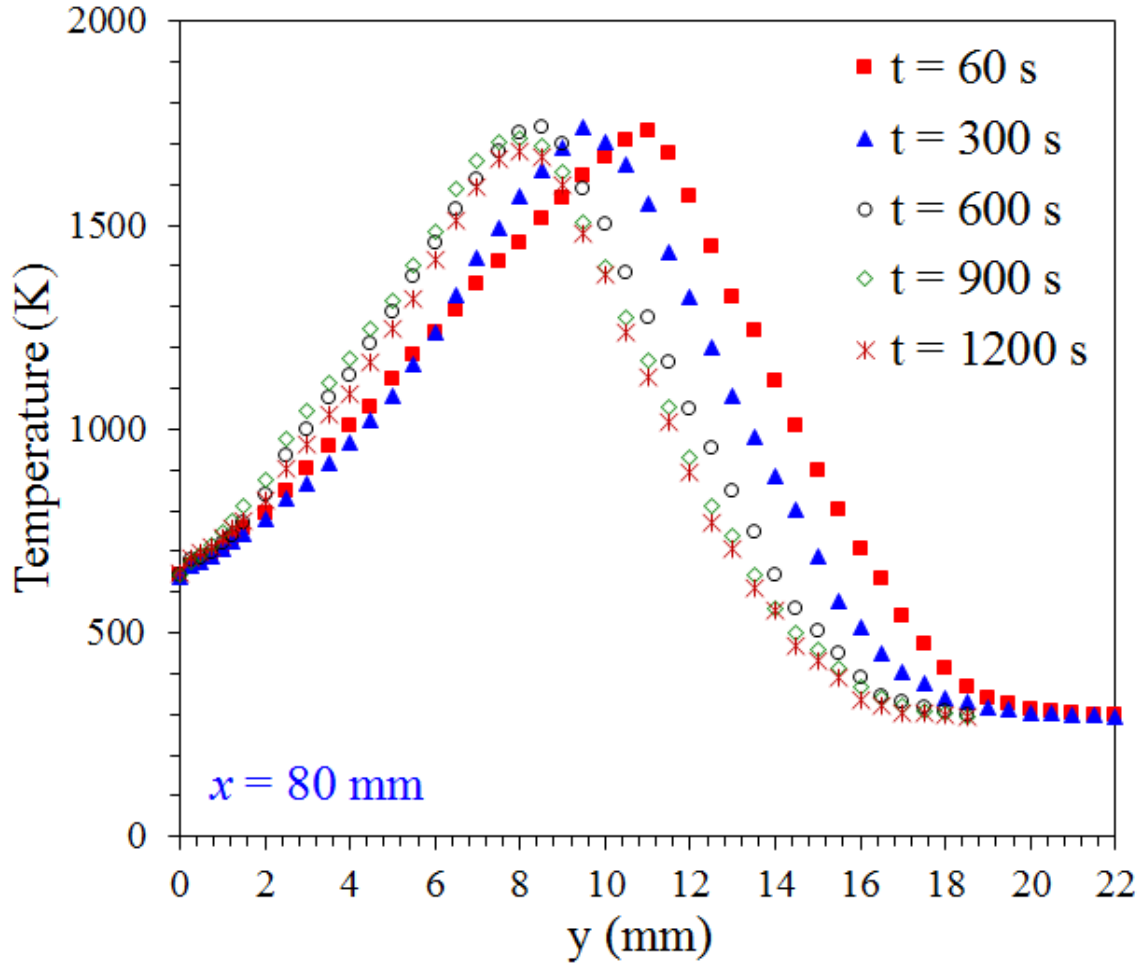
Figure 6.16: Temperature profiles at different burn-out times at $x = 80$ mm for U_∞=0.79 m/s.

with time. To test this, temperature profiles across the flame in the trailing section, $x = 80$ mm from the leading edge, were measured at various times during the test. Figure 6.16 shows the temperature profiles at various burn-out times at $x = 80$ mm from the leading edge for $U_\infty = 0.79$ m/s. Figure 6.16 shows that peak temperatures

remain relatively unchanged with time but the flame stand-off distance decreases significantly from about 11 mm at 60 s to 8 mm at 1200 s. Thus, it seems that in the trailing section flame moves closer to the surface with time which leads to an increase in the incident heat flux (convective and radiative) to the surface with time. This enhances the solid phase heating and leads to an increase in burning rate. As the solid warms up, evaporative flow increases, contributing to the burning rate approaching steady state. The transient burning rate in the trailing section would approach a steady state at long times, more quickly achieved with high convection rates. It is to be noted that although the flame stand-off distance decreases in the trailing section with time, the corresponding increase in temperature gradients and convective heat flux at the surface show only a marginal increase. For example, the temperature gradients at the surface only increase from 212 K/mm to 266 K/mm in the 60 and 1200 s tests. Therefore, an increase in surface incident heat flux due to a reduction in flame stand-off distance at the trailing section could be due to an increase in radiative heat flux with time in this section.

Table 9 summarizes the variation of the integrated burning rate (BR) over the entire sample, in the leading section ($0< x \leq 20$ mm), and over the rest of the sample ($20< x \leq 100$ mm), with time. Here the burning rate is obtained as $\sum R\rho_s \Delta xz$, where ρ_s is the PMMA solid density (1190 kg/m^3), R is the local regression rate, z

Table 9: Streamwise integrated burning rate (BR), total BR ($0 \leqslant x \leqslant 100$ mm), in the leading section ($0 < x \leqslant 20$ mm) and downstream ($x > 20$ mm) for free-stream velocities of 0.79 and 2.06 m/s.

Free-stream velocity (m/s)	Test time (s)	Total BR entire surface (g/min)	BR (g/min) $0 < x \leqslant 20$ mm	BR (g/min) $20 < x \leqslant 100$ mm	% of total BR $0 < x \leqslant 20$ mm	% of total BR $20 < x \leqslant 100$ mm
0.79	100	3.55	1.50	2.05	42.29	57.71
0.79	150	3.64	1.48	2.16	40.63	59.37
0.79	250	3.67	1.38	2.29	37.62	62.38
0.79	550	3.77	1.13	2.64	30.02	69.98
0.79	850	3.67	0.99	2.68	27.03	72.96
2.06	100	4.67	1.78	2.88	38.15	61.85
2.06	150	4.68	1.77	2.91	37.87	62.13
2.06	250	4.65	1.57	3.08	33.67	66.33
2.06	550	4.77	1.35	3.42	28.21	71.79
2.06	850	4.75	1.22	3.53	25.66	74.34

is the sample width (0.1 m), Δx is a small increment in x associated with R, and the summation is between the limits of x. Table 9 shows that the integrated burning rate decreases with time in the leading section (as expected), while it increases with time in the trailing section. Thus, the local regression rate downstream actually increased with time while it decreased with time in the leading section $0 < x \leqslant 20$ mm. Table 9 also indicates that the burning rate integrated over the entire plate does not vary

221

much with time. Thus, the decrease in burning rate in the leading section seems to be compensated by the increase in the burning rate in the trailing section, confirming the observations made by Ndubizu et. al. [46].

6.7. Local Mass Burning Rates

6.7.1. Liquid Fuels: Methanol and Ethanol

Figure 6.17 shows the variation of the local mass-burning rate for methanol and ethanol boundary layer diffusion flames, using the theoretical correlation from Eq. (9) and the non-dimensional temperature gradients at the condensed fuel surface. Due to the availability of fresh oxidizer, higher convective heat feedback, higher temperature gradients and lower stand-off distances near the leading edge, the local burning rate is highest here and subsequently decreases as we move downstream towards the trailing edge. The burning rate decreases, due to the lack of fresh oxidizer, lower convective heat feedback, lower temperature gradients and higher flame stand-off distances as we move downstream. Also, the local mass-burning rates for a methanol and ethanol boundary layer diffusion flame is almost proportional to $x^{-0.5}$, confirming the power-law relationship for laminar forced-convective burning on a horizontal surface [6]. The local mass-burning rate evaluated by using Eq. (9) was also compared against the theoretical mass-burning rate given by Emmons [6]. Emmons [6] carried out an

exact analysis for forced convection burning of a flat plate following the well-known

Blasius solution for incompressible flow. Glassman [129] presents a functional fit to

the Emmons solution as,

$$\frac{\dot{m}''_f c_p x}{k} = 0.385 \left(\frac{U_\infty x}{\nu_\infty} \right)^{1/2} \mathrm{Pr} \frac{ln(1+B)}{B^{0.15}}, \tag{59}$$

Figure 6.17: Variation of the local mass-burning rates for (left) methanol and (right) ethanol boundary layer diffusion flames at different free-stream conditions.

where k represents the thermal conductivity of the gas phase, c_p the specific heat of

the gas phase, Pr the Prandtl number, B the mass transfer number, U_∞ the free-

stream velocity, ν_∞ the kinematic viscosity of the gas phase and x the coordinate

parallel to the fuel surface. The transport properties in Eq. (59) are evaluated at free-

stream conditions [6]. The close agreement between the theoretical and experimental

local mass burning rates suggest that the proposed correlation works quite well in estimating the local mass burning rates for forced convective boundary layer diffusion flames as well.

6.7.2. Solid Fuel: PMMA

Figure 6.18 (a) shows the variation of the local mass-burning rates for PMMA boundary layer diffusion flames, using the theoretical correlation from Eq. (9) and the non-dimensional temperature gradients at the condensed fuel surface. The local mass-burning rate evaluated by using Eq. (9) was also compared against the theoretical mass-burning rate given by Emmons [6] and is shown in Figure 6.18 (a). The close agreement in estimating the local mass burning rates through Emmons theoretical solution and the solution given by Eq. (9) suggest that the proposed theoretical correlation (Eq. 9) works quite well for solid fuels as well.

Unlike liquid fuels, for PMMA the local mass-burning rate can also be approximated a posteriori by measuring the local surface regression over fixed intervals of time [124]. Once steady burning has been established the pyrolysis mass flow rate for PMMA is computed at each x location along the central symmetry axis using the first-order approximation given by Pizzo et al. [124], outlined in Chapter 5.

Using a PMMA density (ρ_s) of 1190 kg/m^3 and measuring regression from samples burned for fixed 50 s time intervals after ignition, the local mass-burning rate over

time can be assessed. A smaller time step would be desirable; however errors in measuring regression profiles become too apparent when the time step is less than 50 s. The regression data between burnout times of 100 and 150 s were used to evaluate the local mass-burning rate in Figure 6.18 (b) for PMMA. For comparison, the local mass burning rates obtained by using the theoretical correlation in Eq. (9) are also plotted in Figure 6.18 (b). It was observed that Eq. (9) calculated mass-burning rates followed a power law decay in x with exponents -0.39, -0.42, -0.42 and -0.38 for U_∞= 0.79, 0.99, 1.54 and 2.06 m/s, respectively. Similarly, regression-measured local pyrolysis rates followed a power law decay in x with exponents -0.41, -0.45, -0.53 and -0.43, respectively. It is to be noted that local mass burning rates obtained through regression profiles of a PMMA surface (using Pizzo's first order approximation) follow a power law decay in x with exponents quite close to -0.5 suggesting good agreement with the laminar boundary layer scaling rule. The agreement, however, was not very good for the data obtained through Eq. (9). As discussed in chapter 5, the departure from the $x^{-0.5}$ dependence predicted by the LBL theory could be due to a combination of the variations of flame and surface temperatures with x, which preclude the self-similar solution of boundary layer and that radiative heat feedback to the solid does not follow the boundary layer scaling rule, as discussed later in section 6.9. Jiang et al. [125] also observed that the

downstream flame, in the case of PMMA, deviated from the self-similar boundary layer scaling relation. They observed that the variation in flame stand-off distance and the fuel vapor blowing rate with x does not follow the self-similar boundary layer scaling relation. The close agreement, however, in estimating the local mass-burning rates by both the regression data and temperature gradients by using Eq. (9) suggest that the proposed theoretical correlation works well for both liquid and non-charring solid fuels, as the experimental mass burning rate was not used in any way to obtain the theoretical mass-burning rate.
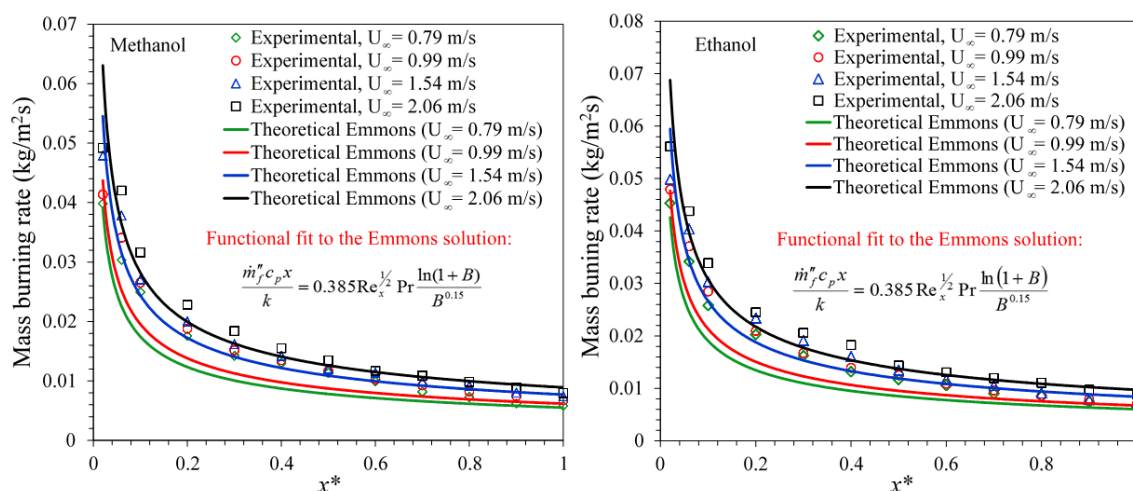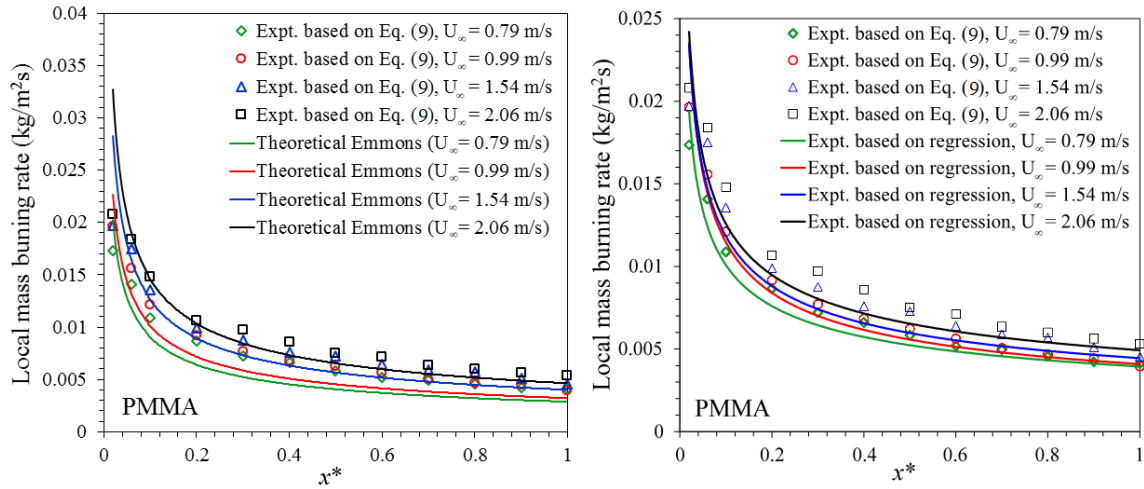

Figure 6.18: Variation of the local mass-burning rates for PMMA boundary layer diffusion flames at different free-stream conditions. (a) (left) Local mass burning rates obtained through Eq. (9) is compared against the classical Emmons solution. (b) (right) Local mass burning rates obtained through Eq. (9) is compared against the data obtained through Pizzo's approximation.

Figure 6.18 validates our theoretical correlation against datasets obtained by two different methods. The close agreement in estimating the local mass burning rates by all 3 methods suggest that the proposed theoretical correlation works quite well in estimating the local mass burning rates for non-charring solid fuels as well.

6.8. Shear Stress at the Fuel surface and Combustion and Friction Coefficients

6.8.1. Friction coefficient

Following the Reynolds Analogy, Emmons [6] hypothesized that the rate of fuel evaporation and hence the rate of burning either in the boundary layer or in the wake behind the body is related to the shear stress by

$$\dot{m}_f'' = B\frac{\tau_s}{U_\infty},\tag{60}$$

where, $\tau_s = \mu(\partial u/\partial y + \partial v/\partial x)_{y=0}$. With the knowledge of local mass burning rates using Eq. (9), the shear stress at the fuel surface can be estimated assuming Eq. (60) applies. Thus, the combustion rate in the boundary layer on a flat plate is simply related to the velocity gradient at the surface. Shear stress at the fuel surface follows the same power law dependence with streamwise distance x as that of the local mass burning rate and can be used to calculate the friction coefficient C_f, which can be

expressed as,

$$C_f = \frac{\tau_s}{\frac{1}{2}\rho_\infty U_\infty^2}. \tag{61}$$
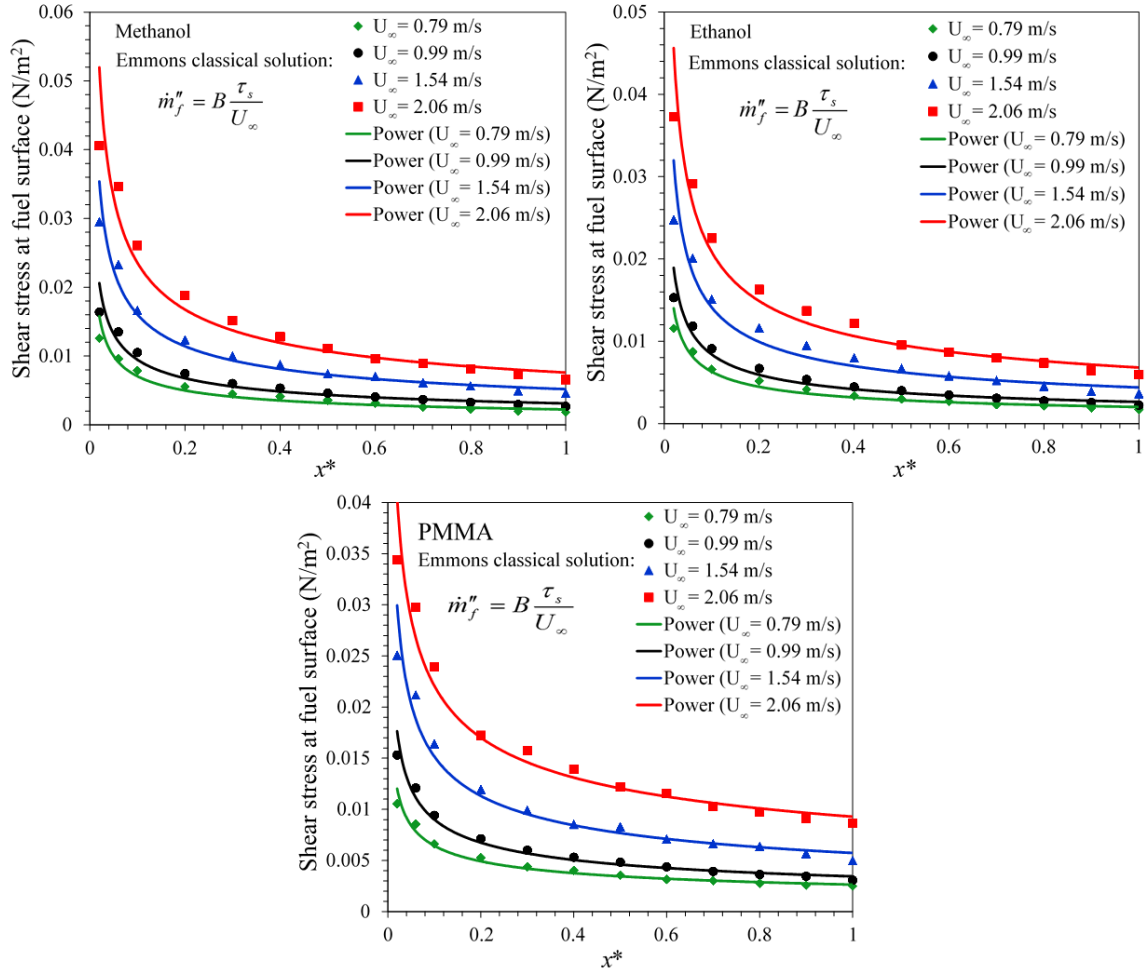
Figure 6.19: Variation of the local shear stress for (top-left) methanol, (top-right) ethanol and (bottom) PMMA boundary layer diffusion flames at different free-stream conditions.
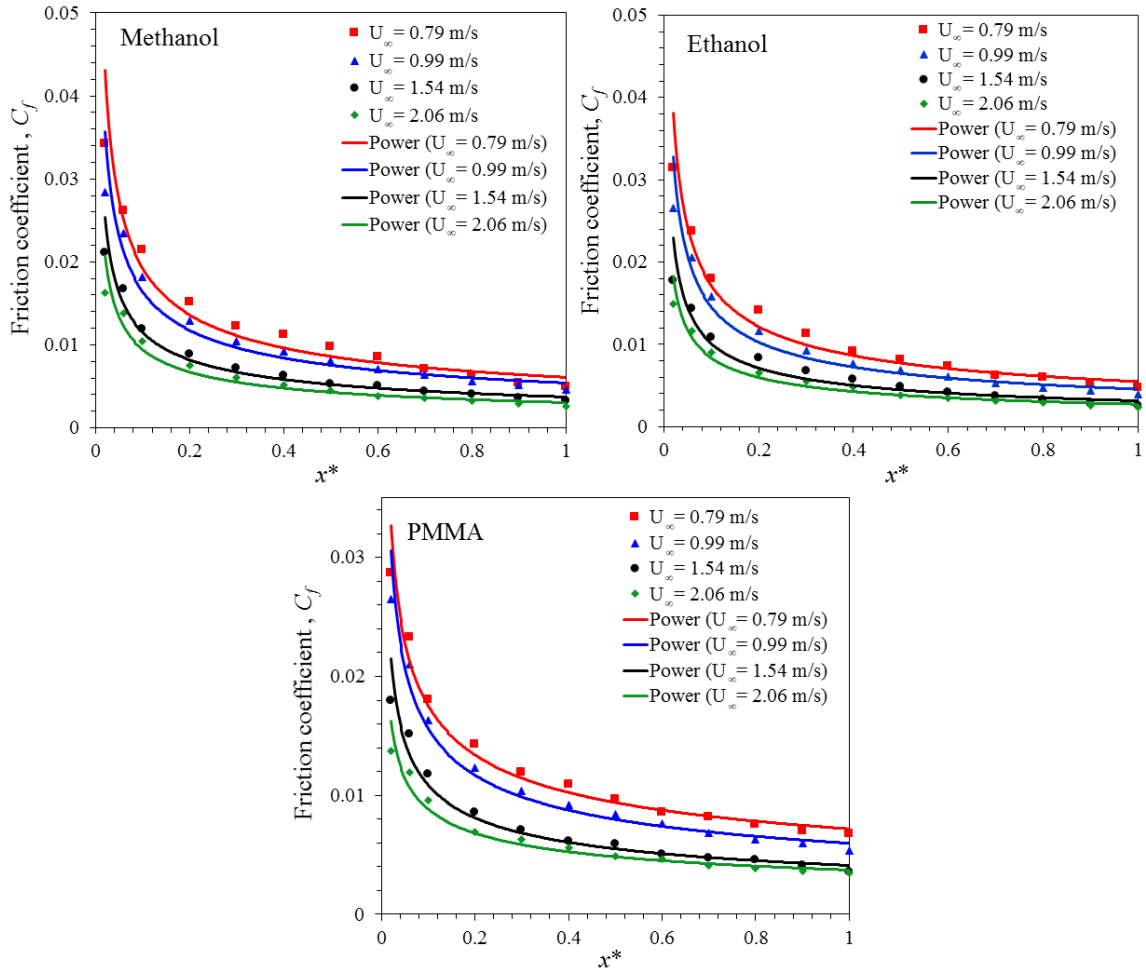
Figure 6.20: Variation of the local friction coefficient for (top-left) methanol, (top-right) ethanol and (bottom) PMMA boundary layer diffusion flames at different free-stream conditions.

Figure 6.19 shows the shear stress distribution at the fuel surface for methanol and ethanol boundary layer diffusion flames stabilized at $U_\infty = 0.79$, 0.99, 1.54 and 2.06 m/s, respectively. The average shear stress at the condensed fuel surface with a diffusion flame established over it is listed in Table 10 for different free-stream

229

air velocities. Figure 6.20 shows the variation of local friction coefficient at the fuel surface for methanol, ethanol and PMMA boundary layer diffusion flames stabilized at $U_\infty = $ 0.79, 0.99, 1.54 and 2.06 m/s, respectively.

6.8.2. Combustion coefficient

The combustion coefficient is a non-dimensional mass burning rate [6] and is defined by,

$$C_o = \frac{\dot{m}''_f}{\rho_\infty U_\infty}.$$ (62)

Hence, by Eq. (60), C_0 and C_f are related by

$$C_o = \frac{B}{2} C_f.$$ (63)

Thus, the combustion rate in the boundary layer over a flat plate is simply related to the velocity gradient at the surface [6, 13]. Figure 6.21 shows the variation of local combustion coefficient at the fuel surface for methanol, ethanol and PMMA boundary layer diffusion flames at $U_\infty = $ 0.79, 0.99, 1.54 and 2.06 m/s, respectively. The product of the average combustion coefficient value and the square root of the free steam Reynolds number should be a constant equal to 0.73 for methanol and 0.83 for ethanol according to Emmons [6]. In the range of free-stream velocities

between 0.79 m/s to 2.06 m/s, the average value of the above product is obtained as 0.85 for methanol and 0.93 for ethanol, close to what Emmons has reported [6]. Table 10 presents the friction and combustion coefficients for methanol, ethanol and PMMA boundary layer diffusion flames under forced flow.
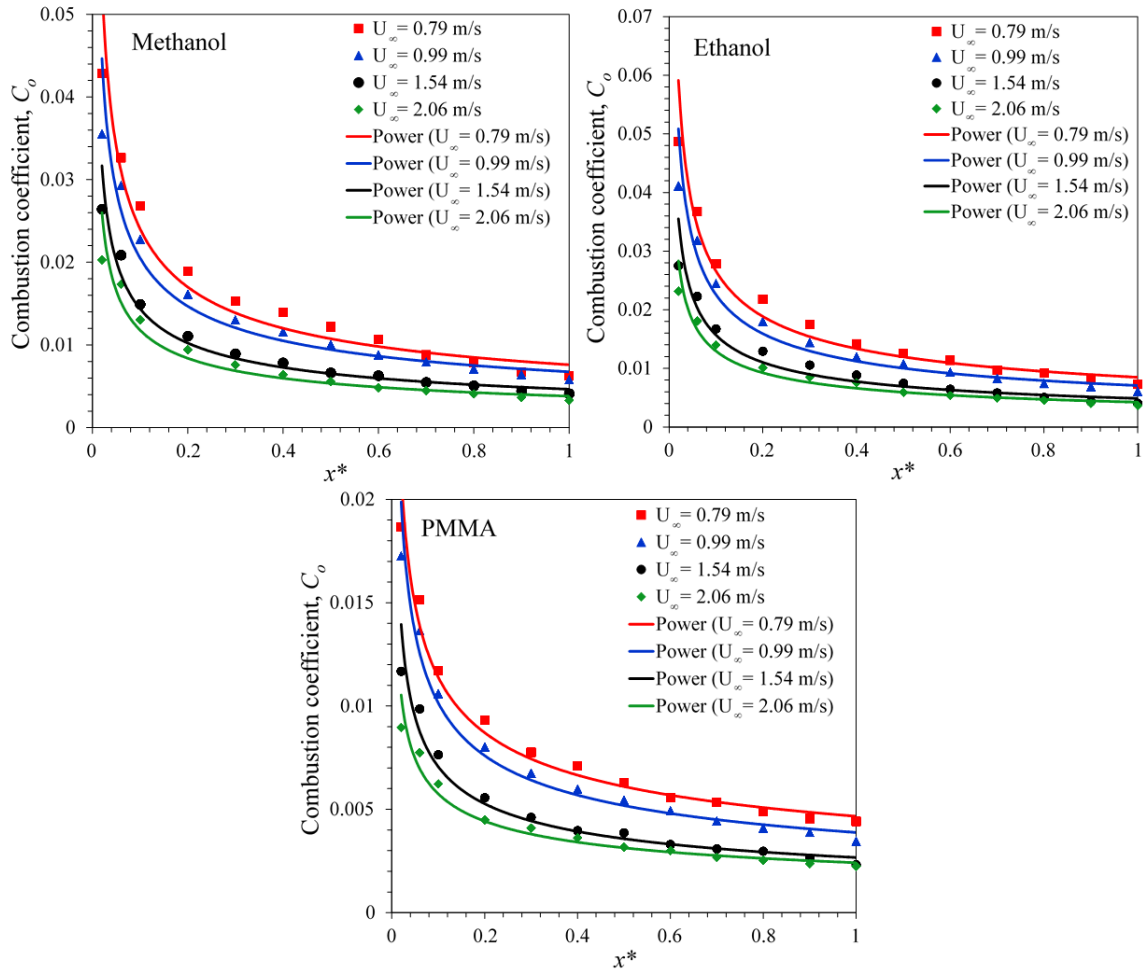
Figure 6.21: Variation of the local combustion coefficient for (top-left) methanol, (top-right) ethanol and (bottom) PMMA boundary layer diffusion flames at different free-stream conditions.

Table 10: Average shear stress at the condensed fuel surface along with combustion and friction coefficients for boundary-layer diffusion flames under forced flow.

Fuel and flow conditions	$\overline{\tau_s}$ (N/m^2)	$\overline{C_0}$	$\overline{C_0}Re^{1/2}$	$\overline{C_f}$	$\overline{C_f}Re^{1/2}$
Methanol (U_∞=0.79 m/s)	0.003855	0.013316	0.94	0.010688	0.76
Methanol (U_∞=0.99 m/s)	0.005309	0.011645	0.92	0.009248	0.73
Methanol (U_∞=1.54 m/s)	0.009001	0.007963	0.79	0.006405	0.63
Methanol (U_∞=2.06 m/s)	0.013156	0.006578	0.75	0.005193	0.59
Ethanol (U_∞=0.79 m/s)	0.003490	0.014833	1.05	0.009598	0.68
Ethanol (U_∞=0.99 m/s)	0.004587	0.012525	0.99	0.008115	0.64
Ethanol (U_∞=1.54 m/s)	0.007794	0.008679	0.86	0.005491	0.54
Ethanol (U_∞=2.06 m/s)	0.011692	0.007221	0.83	0.004642	0.53
PMMA (U_∞=0.79 m/s)	0.003940	0.007121	0.50	0.010909	0.77
PMMA (U_∞=0.99 m/s)	0.005349	0.006136	0.49	0.009440	0.75
PMMA (U_∞=1.54 m/s)	0.009026	0.004275	0.42	0.006492	0.64
PMMA (U_∞=2.06 m/s)	0.013884	0.003583	0.41	0.005524	0.63

6.9. Wall Heat Fluxes in the Pyrolysis Zone

Utilizing gas-phase temperature measurements and local mass-burning rates, heat fluxes were evaluated in the pyrolysis zone at various stream-wise locations along the condensed fuel surface. Reasonable approximations were made to simplify the heat balance analysis and are listed in section 5.5 of Chapter 5. The energy balance at the condensed fuel surface ($y = 0$) for steady burning of liquid and solid fuels becomes,

$$\dot{m}''_f L_v = \dot{q}''_{fl,c} + \dot{q}''_{fl,r} - \dot{q}''_{s,rr} \tag{64}$$

and

$$\dot{m}''_f L_v = k_w \left(\frac{dT}{dy}\right)_{y=0} + \dot{q}''_{fl,r} - \sigma \left(T_w^4 - T_\infty^4\right), \tag{65}$$

where $\dot{q}''_{fl,c}$, $\dot{q}''_{fl,r}$, $\dot{q}''_{s,rr}$ and L_v represents the convective heat flux, radiative heat flux, re-radiation heat flux from the surface and effective heat of gasification or vaporization, respectively. Here, the convective heat flux is measured by using the expression $k_w \left(\partial T/\partial y\right)_{y=0}$ which represents the gas phase convective heating. Convective heat fluxes in boundary-layer diffusion flames can also be evaluated by using the crude approximation outlined in Eq. (49).

Re-radiation heat flux from the surface, $\dot{q}''_{s,rr}$, can be evaluated by knowledge of the wall and ambient temperatures, respectively. Utilizing the theoretical correlation in Eqn. (9), the net heat flux, $\dot{q}''_{net}$ ($\dot{q}''_{net} = \dot{m}''_f L_v$), can be estimated at various

233

stream-wise locations along the pyrolysis zone simply by the knowledge of local mass burning rates along the condensed fuel surface. The effective heat of gasification or vaporization was taken to be 1.2, 0.97 and 1.63 kJ/g for methanol, ethanol and PMMA, respectively [8]. $\dot{q}''_{fl,r}$ can then easily be computed by using Eqn. (65) above. The total heat flux incident to the surface, $\dot{q}''_{s,i}$, can be defined as the sum of the convective and radiative components of the flame heat flux.

Based on these results, the convective heat flux is relatively high and contributes approximately 85-90% of the total heat flux for liquid fuels. Thus, convection is the dominant mode of heat transfer and radiative contributions are small. This is reasonable for the small, laminar flames studied here. The radiant component could increase downstream where the emissivity may increase if the soot volume fraction is high. The net heat feedback to the condensed fuel surface is the sum of the convective and radiative components minus re-radiation from the surface.

For methanol and ethanol flames, all 3 components, namely $\dot{q}''_{s,i}$, $\dot{q}''_{net}$ and $\dot{q}''_{fl,c}$ follow the power law decay and were found to be almost proportional to $x^{-1/2}$, which in turn seems to follow the boundary-layer scaling rule. However, radiative heat feedback to the condensed fuel surface does not follow the boundary layer scaling rule. The re-radiation heat flux from the condensed fuel surfaces was found to be negligible for both methanol and ethanol diffusion flames. With the knowledge of

234

local distribution of various components of heat flux one can further compute the average value of the given components by using

$$\dot{q}''_{avg} = \left(\frac{1}{L}\right) \int_0^L \dot{q}'' dx. \tag{66}$$

The average total incident heat flux from the flame to the wall was estimated to be 15.18 and 19.50 kW/m^2 at $U_\infty = 0.79$ and 2.06 m/s, respectively, for a methanol flame. The average convective heat flux from the flame to the wall was estimated to be 13.09 and 16.97 kW/m^2, at $U_\infty = 0.79$ and 2.06 m/s, respectively. The average radiative heat feedback from the flame was then calculated to be 2.09 and 2.53 kW/m^2, respectively for $U_\infty = 0.79$ and 2.06 m/s. Therefore, the radiative heat flux in the pyrolysis zone is only 13.77% and 12.97% of the total wall heat flux at $U_\infty = 0.79$ and 2.06 m/s respectively, for a methanol flame.

Similarly for ethanol, the average total incident heat flux from the flame to the wall was estimated to be 13.81 and 17.57 kW/m^2 for $U_\infty = 0.79$ and 2.06 m/s respectively. The average convective heat flux from the flame to the wall was estimated to be 12.13 and 15.54 kW/m^2, at $U_\infty = 0.79$ and 2.06 m/s, respectively, for an ethanol flame. The average radiative heat feedback from the flame was then calculated to be 1.68 and 2.03 kW/m^2, respectively for $U_\infty = 0.79$ and 2.06 m/s. Therefore, the radiative heat flux in the pyrolysis zone is only 12.16% and 11.55% of the total wall

235

heat flux at $U_\infty = 0.79$ and 2.06 m/s respectively, for an ethanol flame.

For PMMA, all 3 components of heat flux, namely $\dot{q}''_{s,i}$, $\dot{q}''_{net}$ and $\dot{q}''_{fl,c}$ follow a power-law decay in x, but none seems to follow the laminar boundary-layer (LBL) scaling rule. Since the net heat feedback to the solid does not follow this scaling, it follows that pyrolysis or the mass burning rate will not follow the LBL scaling rule either as outlined in section 6.7.2. Radiative heat feedback to the solid was found to increase towards the trailing edge, most likely due to an increased volume of soot fraction at the trailing edge.

Re-radiation from the PMMA surface was found to be significant when compared to liquid fuels. This is primarily due to increased surface temperatures in the case of PMMA. The surface temperature for PMMA was found to be higher than in the case of liquid fuels (approximately twice that of liquid fuels). The average wall temperature for PMMA was measured to be 669 K and 676 K at $U_\infty = 0.79$ and 2.06 m/s, respectively. The total average incident heat flux to the wall was estimated to be 21.35 kW/m^2 and 25.34 kW/m^2 for $U_\infty = 0.79$ and 2.06 m/s, respectively. The average convective heat feedback from the flame to the wall was estimated to be 15.31 kW/m^2 and 20.37 kW/m^2 for $U_\infty = 0.79$ and 2.06 m/s, respectively. The average radiative heat flux from the flame to the wall was then calculated to be 6.04 kW/m^2 ad 4.97 kW/m^2 respectively for $U_\infty = 0.79$ and 2.06 m/s. Therefore,

the radiative heat flux is 28.29% and 19.61% of the total incident heat flux for $U_\infty = 0.79$ and 2.06 m/s respectively. The radiative heat flux component increases for solid PMMA because the flame is more sooty when compared to methanol and ethanol. However, the radiative component still does not exceed 30% of the total incident flux. This is because small laminar flames do not radiate out a significant portion of the heat released and because the convective heat flux is the dominant mode of heat transfer in such small flames. The average net heat flux that actually pyrolyzes the solid PMMA was estimated to be 10.71 kW/m^2 and 14.25 kW/m^2, respectively for $U_\infty = 0.79$ and 2.06 m/s . It is to be noted that in the case of PMMA, the average net heat flux, which is basically the sum of the convective and radiative heat fluxes minus reradiation from the surface, was found to be quite lower than the total incident heat flux. This can be explained by the fact that a portion of the total incident flux is utilized in pyrolyzing the solid PMMA, whereas the rest is lost into the ambient surroundings through re-radiation from the solid wall. PMMA loses a considerable portion of total heat received by re-radiation compared to liquid fuels, owing to its higher surface temperatures.

The above results for methanol, ethanol and PMMA flames suggest that convection is the dominant mode of heat transfer in steady laminar boundary-layer diffusion flames and is primarily responsible for the pyrolysis of fuel. Also, convective

and total incident heat flux to the condensed fuel surface increases as the free-stream velocity increases. This results in higher burning rates at higher free-stream velocities. Figure 6.22 shows the various components of flame heat flux in the pyrolysis zone for methanol, ethanol and PMMA boundary-layer diffusion flames stabilized at U_∞= 0.79 and 2.06 m/s, respectively. Table 11 shows the various components of flame heat flux in kW/m^2 for forced-convection boundary-layer diffusion flames considered in this study. It can be clearly seen that for higher free-stream velocities the contribution of convective heat flux to the surface incident heat flux increases, thereby, decreasing the contribution of radiative heat flux. Though the change in contribution (represented as $\overline{\dot{q}''_{fl,c}}$ %) is slight for liquid fuels but is substantial for PMMA. For instance, the percentage contribution of convective heat flux increases from 71.71 % to 80.39 % for PMMA flames stabilized at U_∞=0.79 and 2.06 m/s, respectively. Subsequently, the radiative heat feedback contribution decreases from 28.29% to 19.61% for an increase of free-stream velocity from 0.79 m/s to 2.06 m/s.

Table 11: Various components of flame heat flux in kW/m^2 for forced-convection boundary-layer diffusion flames.

Fuel and flow conditions	$\overline{\dot{q}''_{s,i}}$	$\overline{\dot{q}''_{fl,c}}$	$\overline{\dot{q}''_{fl,r}}$	$\overline{\dot{q}''_{s,rr}}$	$\overline{\dot{q}''_{net}}$	$\overline{\dot{q}''_{fl,c}}$ %
	kW/m^2	kW/m^2	kW/m^2	kW/m^2	kW/m^2	
Methanol (U_∞=0.79 m/s)	15.18	13.09	2.08	0.32	14.86	86.28
Methanol (U_∞=0.99 m/s)	16.48	14.25	2.23	0.32	16.16	86.46
Methanol (U_∞=1.54 m/s)	17.79	15.42	2.37	0.31	17.48	86.68
Methanol (U_∞=2.06 m/s)	19.50	16.97	2.53	0.34	19.16	87.04
Ethanol (U_∞=0.79 m/s)	13.81	12.13	1.69	0.47	13.34	87.80
Ethanol (U_∞=0.99 m/s)	14.55	12.84	1.71	0.47	14.08	88.24
Ethanol (U_∞=1.54 m/s)	15.62	13.74	1.88	0.47	15.15	87.98
Ethanol (U_∞=2.06 m/s)	17.57	15.54	2.03	0.49	17.08	88.47
PMMA (U_∞=0.79 m/s)	21.35	15.31	6.04	10.64	10.71	71.71
PMMA (U_∞=0.99 m/s)	22.17	16.22	5.95	10.82	11.35	73.18
PMMA (U_∞=1.54 m/s)	23.46	17.84	5.62	10.98	12.48	76.06
PMMA (U_∞=2.06 m/s)	25.34	20.37	4.97	11.09	14.25	80.39
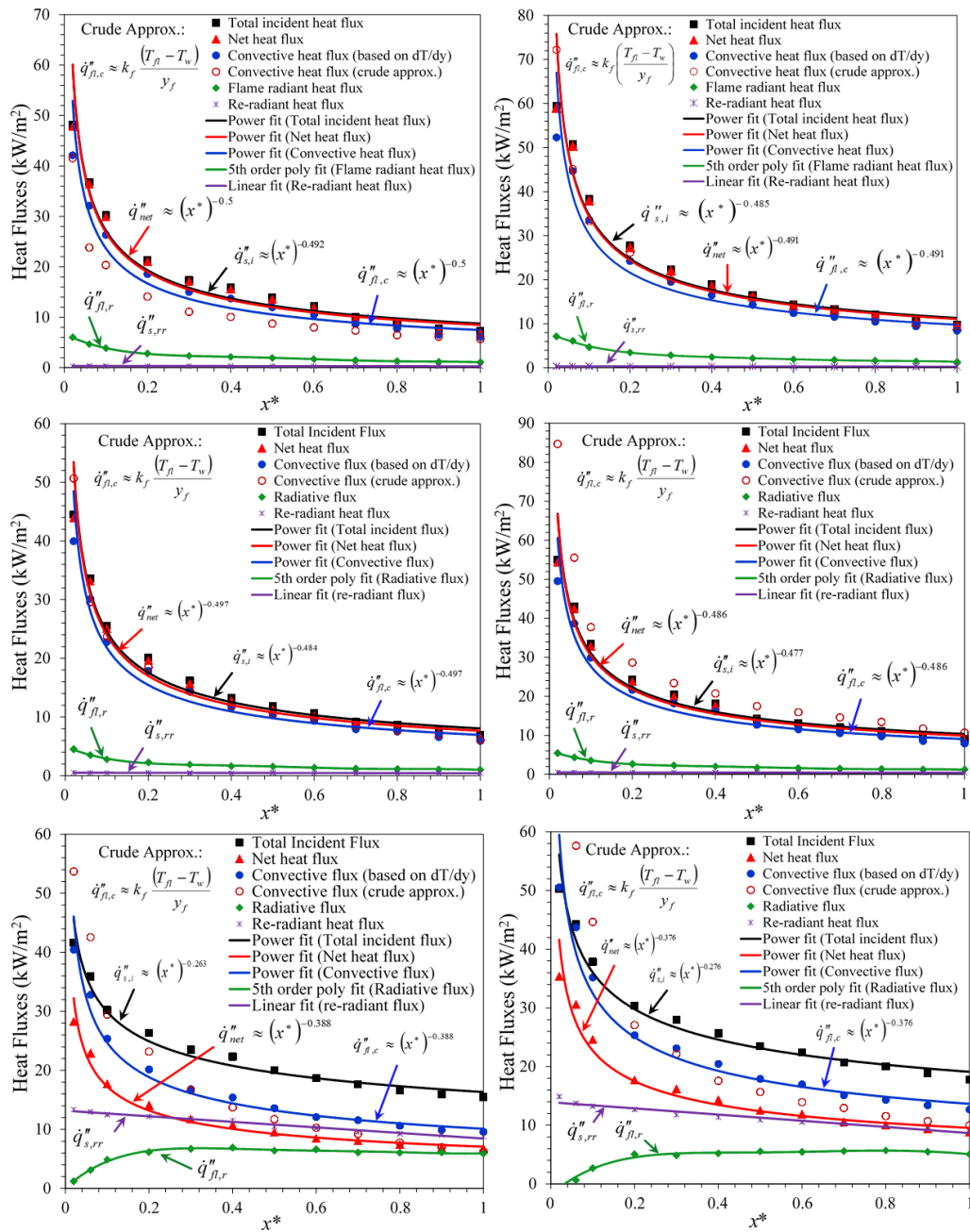
Figure 6.22: Distribution of various components of flame heat flux in the pyrolysis zone for (top) methanol,(middle) ethanol and (bottom) PMMA boundary layer diffusion flames at U_∞=0.79 (left) and 2.06 m/s (right).

240

6.10. Convective Heat Transfer Coefficient

Convective heat transfer coefficients were also calculated for methanol and ethanol flames. For a boundary-layer diffusion flame established over a condensed fuel surface, convective heat transfer coefficients can be derived from the expression [13, 126],

$$h = \frac{k_w \left(\partial T/\partial y\right)_{y=0}}{T_{fl,ad} - T_{w,p}} = +\frac{k_w}{L}\left(\frac{\partial T^*}{\partial y^*}\right)_{y^*=0}.$$
(67)

The above expression comes from normalizing the boundary-layer equations by defining dimensionless independent variables [126]. Figure 6.23 shows the distribution of the convective heat transfer coefficient for methanol, ethanol and PMMA flames using this method. The results using the crude approximation from Eq.(50) are also plotted for comparison. For both methanol and ethanol, the convective heat transfer coefficient evaluated through experiments follows a power-law decay in x consistent with the boundary-layer scaling rule. However, for PMMA the convective heat transfer coefficient do not follow the boundary-layer scaling rule. For methanol, the crude approximation using Eq. (50) slightly under and over-predicts the convective heat transfer coefficient for free stream air velocities of 0.79 and 2.06 m/s, respectively. However for both ethanol and PMMA flames, the crude approximation using Eq. (50) over-predicts the convective heat transfer coefficient for both the free-stream air velocities considered.

Table 12: Convective heat transfer coefficients for forced-convective boundary-layer diffusion flames.

Fuel and flow conditions	$\bar{h}_{measured}$ (W/m²-K)	$\bar{h}_{crude-approx.}$ (W/m²-K)
Methanol (U_∞=0.79 m/s)	7.21	7.21
Methanol (U_∞=0.99 m/s)	7.86	8.91
Methanol (U_∞=1.54 m/s)	8.52	10.64
Methanol (U_∞=2.06 m/s)	9.36	12.22
Ethanol (U_∞=0.79 m/s)	6.58	8.84
Ethanol (U_∞=0.99 m/s)	6.96	9.88
Ethanol (U_∞=1.54 m/s)	7.45	12.02
Ethanol (U_∞=2.06 m/s)	8.43	14.24
PMMA (U_∞=0.79 m/s)	8.38	13.11
PMMA (U_∞=0.99 m/s)	9.08	14.85
PMMA (U_∞=1.54 m/s)	9.77	16.49
PMMA (U_∞=2.06 m/s)	10.70	18.0

The average value of convective heat transfer coefficients for boundary-layer diffu-
sion flames established under different free-stream conditions are listed in Table 12.
Looking at the convective heat transfer coefficients, it is clear that average convective
heat transfer coefficient increases for increase in free-stream air velocity. This is
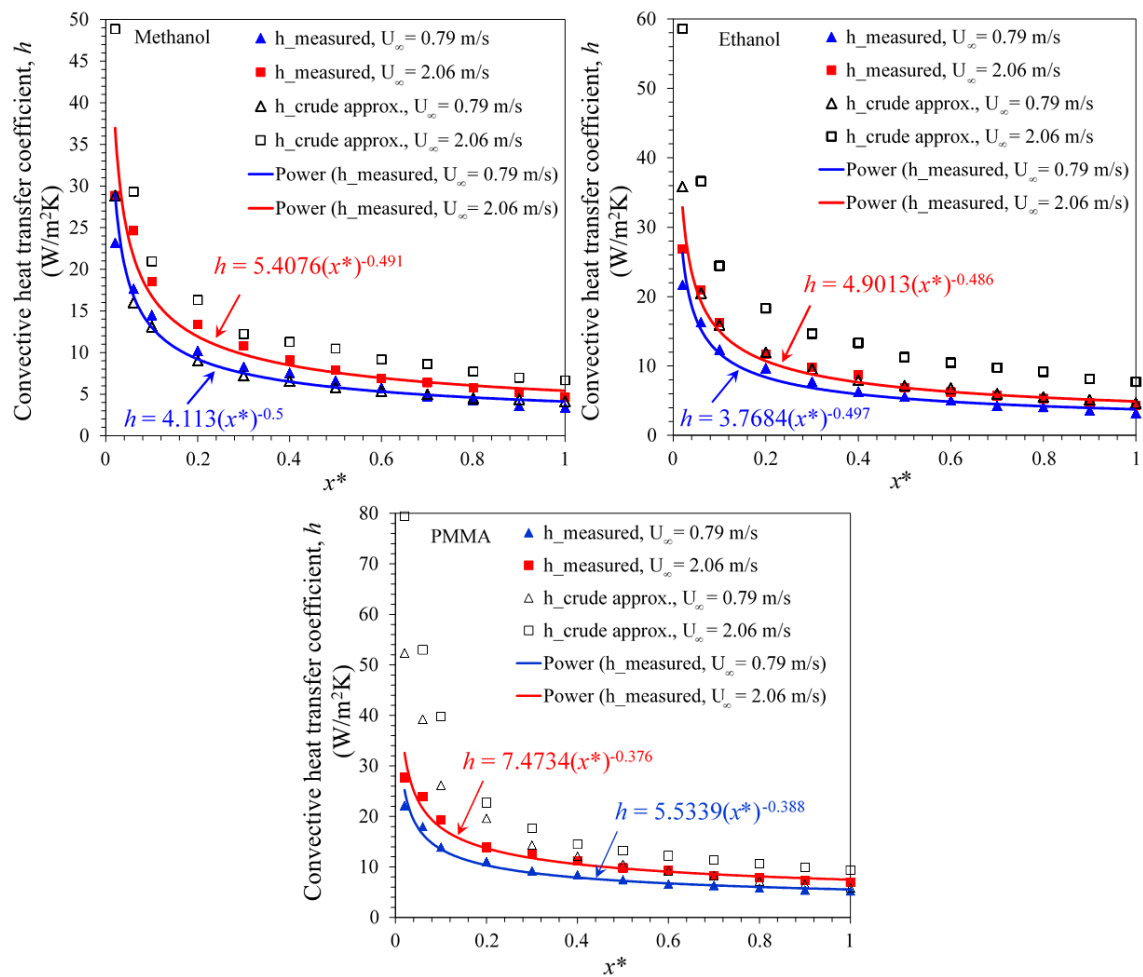
Figure 6.23: Variation of the convective heat transfer coefficients in the pyrolysis zone for (top-left) methanol, (top-right) ethanol and (bottom) PMMA boundary layer diffusion flames.

expected as convective heat transfer increases for higher free-stream velocities. Also, crude approximation of Eq. (50), seriously over-predicts the value of convective heat transfer coefficient.

6.11. Nusselt number

The Nusselt number was also calculated for methanol, ethanol and PMMA flames established under forced flow. This parameter is equal to the dimensionless temperature gradient at the surface and provides a measure of the convective heat transfer occurring at the surface. The Nusselt number can be expressed as [126]

$$\text{Nu} = \frac{hL}{k_w} = + \left(\frac{\partial T^*}{\partial y^*} \right)_{y^*=0}. \tag{68}$$

From the initial definition of T^*, it follows that for a prescribed geometry,

$$\text{Nu} = f(x^*, \text{Re}, \text{Pr}). \tag{69}$$

The Nusselt number is to the thermal boundary layer what the friction coefficient is to the velocity boundary layer. Eq. (69) implies that for a given geometry, the Nusselt number must be some universal function of x^*, Re and Pr. If this function were known, it could be used to compute the value of Nu for different fluids and for different values of L and U.

From knowledge of Nu, the local convection coefficient may be found and the local heat flux may then be computed using Eq. (49). Figure 6.24 shows the variation of Nu with non-dimensional distance downstream of the leading edge, x^* for methanol, ethanol and PMMA boundary layer diffusion flames, respectively.

244
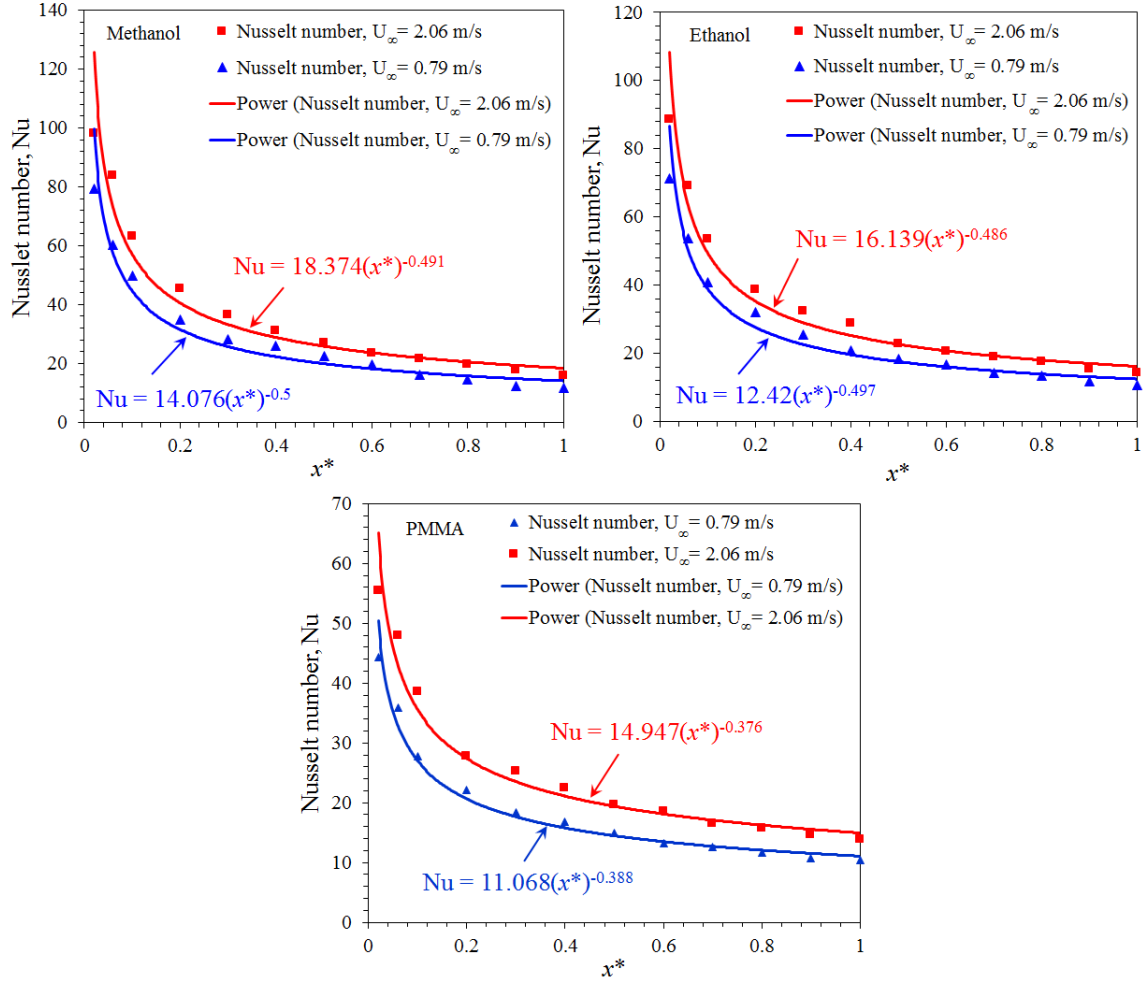
Figure 6.24: Variation of Nusselt number in the pyrolysis zone for (top-left) methanol, (top-right) ethanol and (bottom) PMMA boundary layer diffusion flames.

6.12. Functional form of the Nusselt number

In this section, the relationship between local Nu_x and Reynolds number, Re_x, is presented for methanol, ethanol and PMMA boundary layer diffusion flames. The

effects of time-dependent processes on the burning rate of a PMMA plate in terms of local Nu_x and Reynolds number, Re_x is also presented.

Emmons exact solution can be represented as

$$\dot{m}_f'' = \left(\frac{k}{c_p}\right)\left(\frac{\mathrm{Re}_x^{1/2}}{x\sqrt{2}}\right) - f(0) \tag{70}$$

or non-dimensionally expressed as,

$$\frac{\dot{m}_f'' x c_p}{k} = \left(\frac{\mathrm{Re}_x^{1/2}}{\sqrt{2}}\right) - f(0). \tag{71}$$

Assuming $\mathrm{Pr} = 1$, Eq. (71) can also be written as,

$$\frac{\dot{m}_f'' x}{\mu_\infty} = \left(\frac{\mathrm{Re}_x^{1/2}}{\sqrt{2}}\right) - f(0), \tag{72}$$

where $\mathrm{Re}_x = U_\infty x/\nu_\infty$ and ν_∞ is the kinematic viscosity at 300 K. $-f(0)$ is a function of the mass transfer number B and was approximated by Glassman as,

$$-f(0) = \frac{\ln(1+B)}{2.6B^{0.15}}. \tag{73}$$

The convective heat feedback to the fuel surface at any x location, $h\Delta T$, can be approximated as $k\Delta T/y_f$, where h is the convective heat transfer coefficient, k is the gas-phase thermal conductivity, ΔT is the difference between the flame temperature and the wall temperature, $\Delta T = T_{fl} - T_w$, and y_f is the flame standoff

distance. Therefore, the dimensionless Nusselt number can then be expressed in terms of normalized flame standoff distance (y_f/x) as,

$$\mathrm{Nu}_x = \frac{hx}{k} \approx \frac{x}{y_f}. \tag{74}$$

Local Nu_x at different streamwise locations along the condensed fuel surface can also be represented as,

$$\mathrm{Nu}_x = \frac{hx}{k_w} = \frac{h\Delta T x}{k_w \Delta T}. \tag{75}$$

Neglecting radiation effects for small steady laminar boundary layer diffusion flames and considering pure convective heating in such flames, $h\Delta T$ can be approximated as $\dot{m}_f'' L_v$.

$$\mathrm{Nu}_x = \frac{hx}{k_w} = \frac{h\Delta T x}{k_w \Delta T} \approx \frac{\dot{m}_f'' L_v x}{k_w \Delta T}, \tag{76}$$

Using Emmons' exact solution for $\dot{m}_f''$ in Eq. (76) above, Nu_x can be further approximated as,

$$\mathrm{Nu}_x = \frac{L_v x}{k_w \Delta T} \frac{\mu_\infty}{x} \left(\frac{\mathrm{Re}_x^{1/2}}{\sqrt{2}} \right) - f(0), \tag{77}$$

Using Glassman's approximation for $-f(0)$, Nu_x can finally be represented in a simplified form as,

$$\text{Nu}_x = \left(\frac{L_v \mu_\infty}{k_w \Delta T}\right) \left(\frac{\text{Re}_x^{1/2}}{\sqrt{2}}\right) \frac{\ln(1+B)}{2.6 B^{0.15}}. \tag{78}$$

Using appropriate values for methanol in Eq. (78), Nu_x can be expressed as

$$\text{Nu}_x = 0.1575\sqrt{\text{Re}_x}, \tag{79}$$

for an ethanol boundary-layer diffusion flame, as

$$\text{Nu}_x = 0.1371\sqrt{\text{Re}_x}, \tag{80}$$

and a PMMA boundary-layer diffusion flame, as

$$\text{Nu}_x = 0.1148\sqrt{\text{Re}_x}. \tag{81}$$

The transport properties used in the above expressions are given in Table 13. It is important to note that the average flame and wall temperature, obtained through experiments in different free-stream conditions, were used to calculate ΔT in Eq. (78). The normalized flame standoff distance, y_f/x can, therefore, be expressed as (from Eq. 74),

$$\frac{y_f}{x} = \frac{1}{\text{Nu}_x}. \tag{82}$$

248

Table 13: Physical properties for evaluating Nu_x from Eq. (78)

Properties	Methanol	Ethanol	PMMA
Mass transfer number, B	2.5 [8]	3.1 [8]	1.3 [46]
Thermal conductivity, k_w (W/m-K) evaluated at the pyrolyzing wall temperature	0.028 [123]	0.029 [123]	0.050 [123]
Effective heat of vaporization, L_v (kJ/g)	1.2 [8]	0.97 [8]	1.63 [8]
$T_{fl,avg}$ (K) (current work)	1844	1825	1799
$T_{w,avg}$ (K) (current work)	343	358	672
ΔT (K) (current work)	1501	1467	1127
Dynamic viscosity, μ_∞ ($\times 10^{-6}$ Ns/m^2)	18.57	18.57	18.57

6.12.1. Normalized flame stand-off distance

The normalized flame standoff distance, y_f/x can be expressed as the inverse of Nu_x for forced boundary-layer diffusion flames (see Eq. 82). Figures 6.25 and 6.26 show the normalized flame stand-off distance versus $\sqrt{Re_x}$ for methanol, ethanol and PMMA boundary-layer diffusion flames under forced flow using the location of peak

temperatures in such flames. The black line is Emmons' steady-state boundary layer solution and the symbols are the data points obtained experimentally.
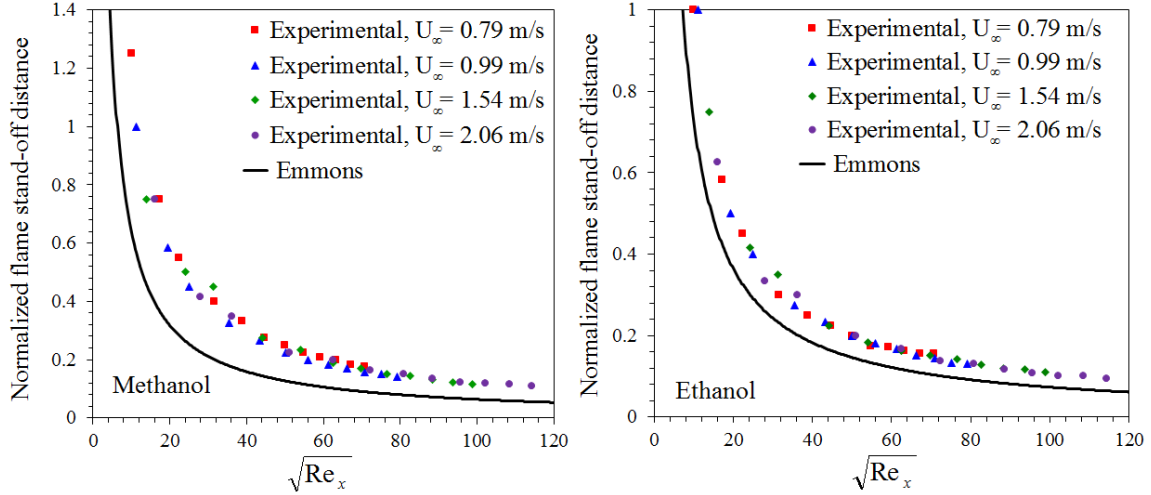
Figure 6.25: Normalized standoff distance versus $\sqrt{\text{Re}_x}$ for methanol (left) and ethanol (right) boundary-layer diffusion flames under forced flow .

The agreement of experimental data with the boundary layer predictions (Emmons solution represented by black line) is not bad considering the approximations involved in deriving Nu_x (normalized flame standoff distance, $y_f/x = 1/\text{Nu}_x$) from Eq. (78). The slight departure of the experimental data from the Emmons' steady state boundary layer solution could be due to the uncertainties involved in the measurement of the flame stand-off distance experimentally as well as due to the approximations involved in calculating Nu_x from Eq. (78). However, for PMMA flames under forced flow, the agreement between the experimental data and Emmons' steady-state

250

boundary layer solution is quite good, shown in Figure 6.26.
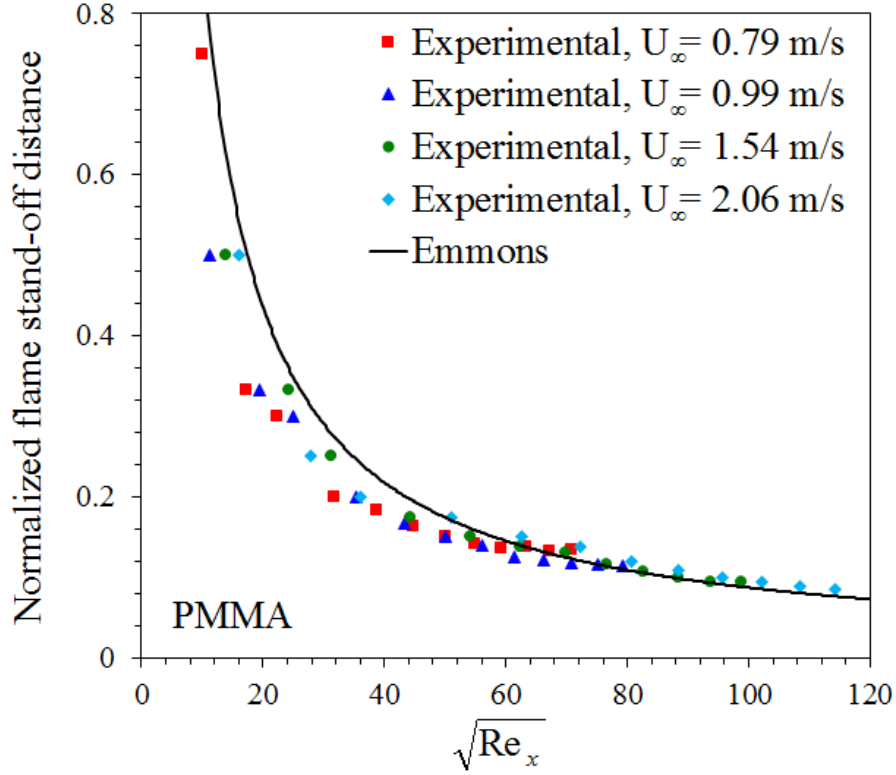
Figure 6.26: Normalized standoff distance versus $\sqrt{\text{Re}_x}$ for PMMA boundary-layer diffusion flames under forced flow.

6.12.2. Local Nusselt number, Nu_x

Figure 6.27 shows the variation of Nu_x with $\sqrt{\text{Re}_x}$ for methanol and ethanol boundary-layer diffusion flames for free-stream velocities of 0.79, 0.99, 1.54 and 2.06 m/s. Emmons' steady-state boundary layer solution for local Nusselt number (Nu_x) is obtained from Eqs. (79) and (80) for methanol and ethanol flames, respectively. It is

represented as a straight line in Figure 6.27. At low free-stream velocities, experimental data deviates slightly from the steady-state boundary layer solution. However, good agreement was observed between the experimental and theoretical data for higher free-stream velocities. The same observation was made for the PMMA case as shown in Figure 6.28.
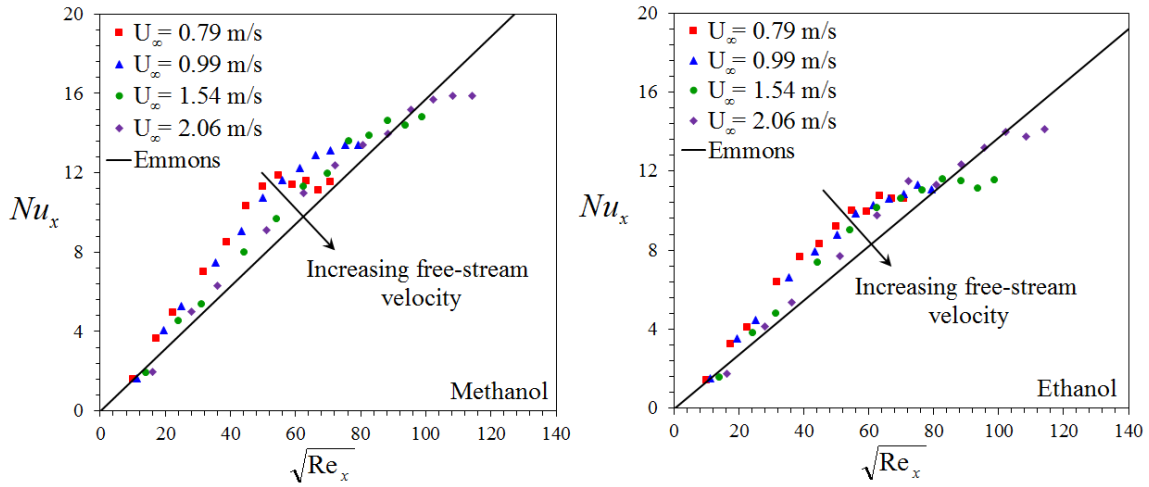
Figure 6.27: Local Nu_x versus $\sqrt{\mathrm{Re}_x}$ for methanol (left) and ethanol (right) boundary-layer diffusion flames.

For PMMA, Emmons' steady-state boundary layer solution for local Nusselt number was obtained from Eq. (81). At low $\sqrt{\mathrm{Re}_x}$ (the leading section), Figure 6.27 show that the measured Nu_x is less than Emmons' predictions in the leading 2 mm of the sample ($\sqrt{\mathrm{Re}_x} < 20$) for U_∞=0.99, 1.54 and 2.06 m/s for methanol and ethanol flames. For a PMMA flame,the measured Nu_x is also less than Emmons' predictions
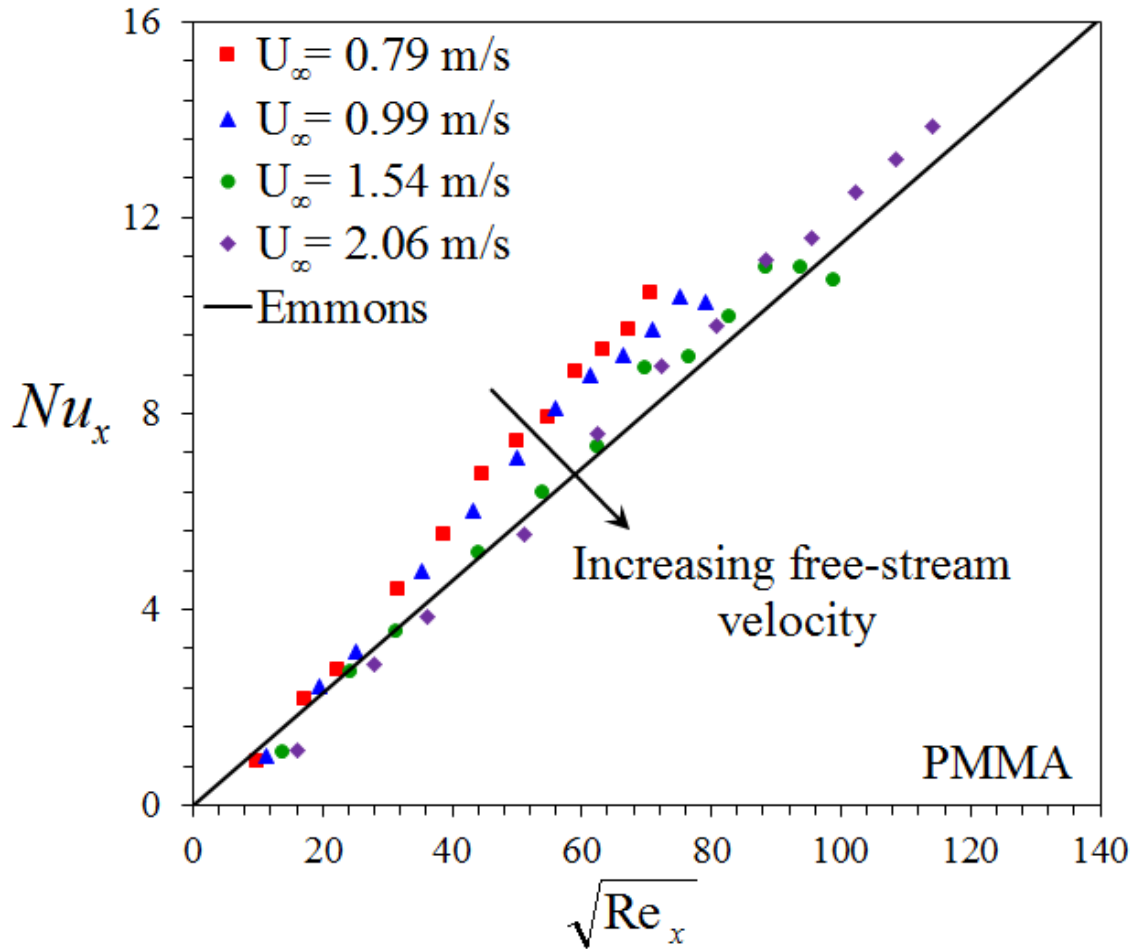
Figure 6.28: Local Nu_x versus $\sqrt{Re_x}$ for PMMA boundary-layer diffusion flames under forced flow.

in the leading 2 mm of the sample ($\sqrt{Re_x} < 20$) for all the free-stream velocities. For a PMMA flame stabilized at $U_\infty = 2.06$ m/s, the measured Nu_x is actually less than Emmons' predictions in the leading 20 mm of the sample ($\sqrt{Re_x} < 60$). For methanol and ethanol flames, the measured Nu_x again becomes less than Emmon's prediction near the trailing edge for higher free-stream velocities of 1.54 m/s and

253

2.06 m/s.

It is evident from Figures 6.27 and 6.28, that the measured Nu_x shows a relatively good agreement with Emmons' steady state solution for different free-stream conditions for both the solid and liquid fuels considered in this study. A close observation at the results suggest that the experimentally-derived Nu_x shows a good agreement with theory-derived Nu_x for higher free-stream velocities where effects due to buoyancy are small or negligible. However, at lower free-stream velocities experimental results were found to deviate from the theoretical results since buoyancy plays a huge role at lower free-stream velocities. Emmons steady state solution neglects buoyancy and hence shows good agreement with experimental results at higher free-stream velocities.

6.12.3. Transient local Nu_x for PMMA

For a PMMA burning surface, Nu_x can also be represented as [45],

$$Nu_x = \frac{hx}{k_w} = \frac{R\rho_s L_v x}{k_w \Delta T}, \tag{83}$$

where R is the local regression rate, ρ_s is the PMMA solid density (1190 kg/m^3), L_v is the effective heat of gasification or vaporization, k_w is the gas-phase thermal conductivity evaluated at the wall temperature and ΔT ($\Delta T = T_{fl,avg} - T_{w,avg}$) is the difference between the average flame and wall temperature given in Table 13.

254

Figures 6.29 and 6.30 shows the variation of Nu_x with $\sqrt{Re_x}$ for free-stream velocities of 0.79 and 2.06 m/s and test durations increasing from 100 to 850 s. The Emmons steady-state boundary layer solution for local Nusselt number is obtained as $Nu_x = 0.1148 \sqrt{Re_x}$ and is the straight line shown in Figures 6.29 and 6.30.

At low $\sqrt{Re_x}$ (the leading section), Figures 6.29 and 6.30 reveal that Nu_x decreases with time. This is seen in Figure 6.29 for $\sqrt{Re_x} < 20$ and in Figure 6.30 for $\sqrt{Re_x} < 30$. On the other hand, at large Re_x (downstream), the burning rate increases with time and transient effects are shown more clearly here than in Figure 6.14. This is observed in Figure 6.29 for $Re_x \geq 50$ and in Figure 6.30 for $Re_x \geq 62$. At an intermediate Re_x, burning rate is not transient and the data revealed a straight line trend (steady-state), which agrees well with the boundary layer solution.

Near the leading edge (small Re_x) a gas phase steady state is attained a short time after ignition, before a valley is formed. However, the burning rate soon starts decreasing as a valley forms because of nonuniform moving boundary effects due to surface regression. Thus, the burning rates in this section become smaller than the steady-state solution as time increases. Looking closely at Figure 6.29 for a free-stream velocity of 0.79 m/s, one can easily discern that for burn-out times of 100 and 150 s, the experimentally measured Nu_x conforms to Emmons' steady-state solution. At higher burn-out times ($t > 150$ s), the experimentally measured Nu_x is

large when compared to the steady-state boundary layer solution near the trailing edge ($\sqrt{Re_x} > 50$).
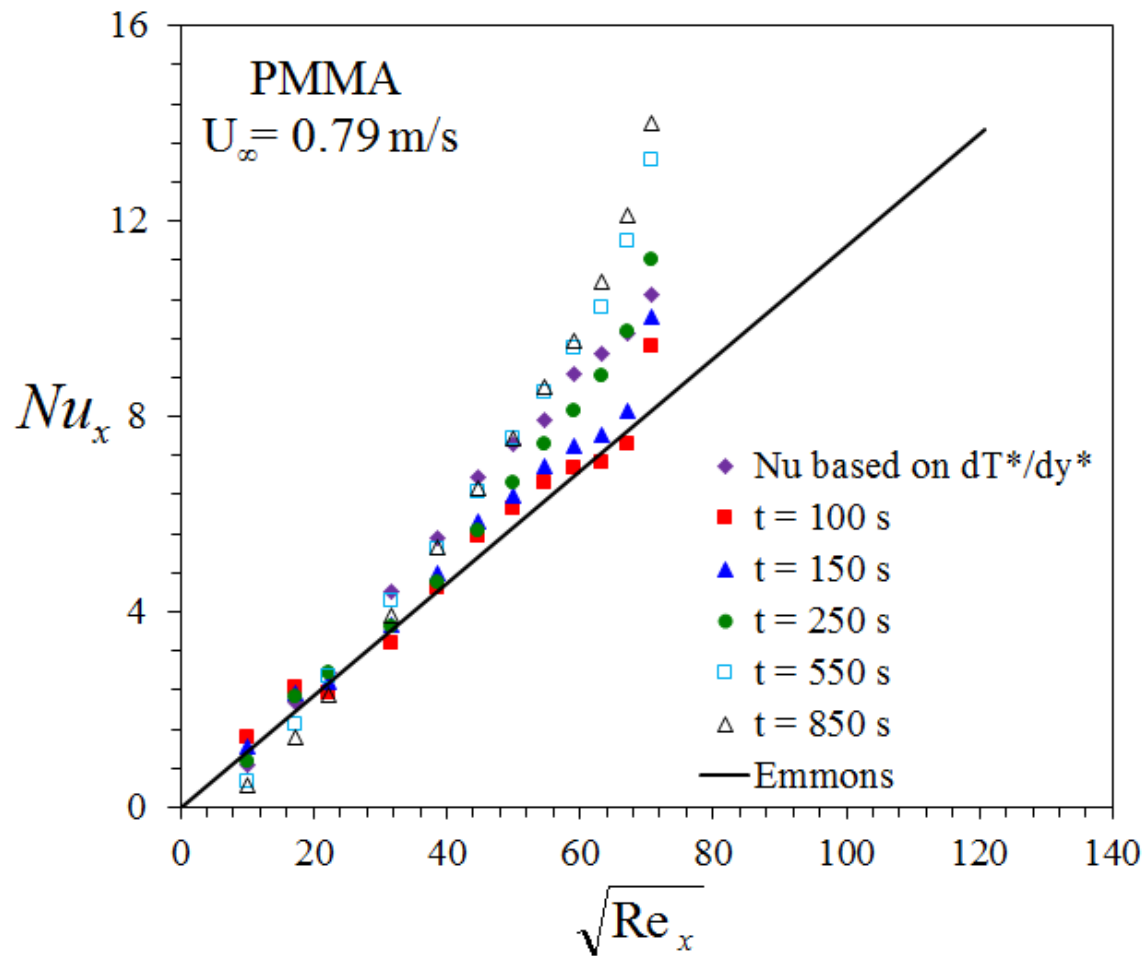
Figure 6.29: Transient Nu_x versus $\sqrt{Re_x}$ for a PMMA boundary-layer diffusion flame stabilized at $U_\infty = 0.79$ m/s.

This is because the gas phase attains a steady state soon after uniform ignition and remains steady during the initial stages of burning ($t < 150$ s) when the PMMA

surface is relatively flat. At later times, the heat feedback to the PMMA surface is not steady and this leads to transient gas-phase heating effects at later times. It is, therefore, essential to do the temperature mapping near the surface for the calculation of temperature gradients during the initial stages of burning. It is to be noted that for PMMA, both the temperature and mass loss rate measurements were carried out within the first 150 s (after the surface is uniformly ignited, but while the surface was still relatively flat). Similarly, for a higher free-stream velocity of 2.06 m/s, one can easily see that for burn-out times of 100 and 150 s, Emmons' steady-state solution slightly over-predicts the local Nu_x, as seen in Figure 6.30. However, the qualitative and quantitative agreement of experimentally-measured Nu_x with the steady-state boundary layer solution is not bad. At higher burn-out times ($t > 250$ s), the experimentally measured Nu_x is large when compared to the steady-state boundary layer solution near the trailing edge ($\sqrt{Re_x} > 80$).

At large Re_x (the trailing section) the heat feedback is small and it takes the sample considerable time to warm up and start pyrolyzing at a steady rate. Figures 6.29 and 6.30 show that at large U_∞, the warm up time is reduced and steady state is approached faster because of increased convection. For instance, looking at Figure 6.29, it can be clearly seen that at large Re_x (the trailing section), the experimentally measured Nu_x is large when compared to Emmon's steady-state solution for burn-out

times higher than 150 s. At higher free-stream inlet velocities, the difference between the experimentally measured Nu_x and Emmon's steady-state solution becomes less for higher burn-out times $(t > 150s)$.
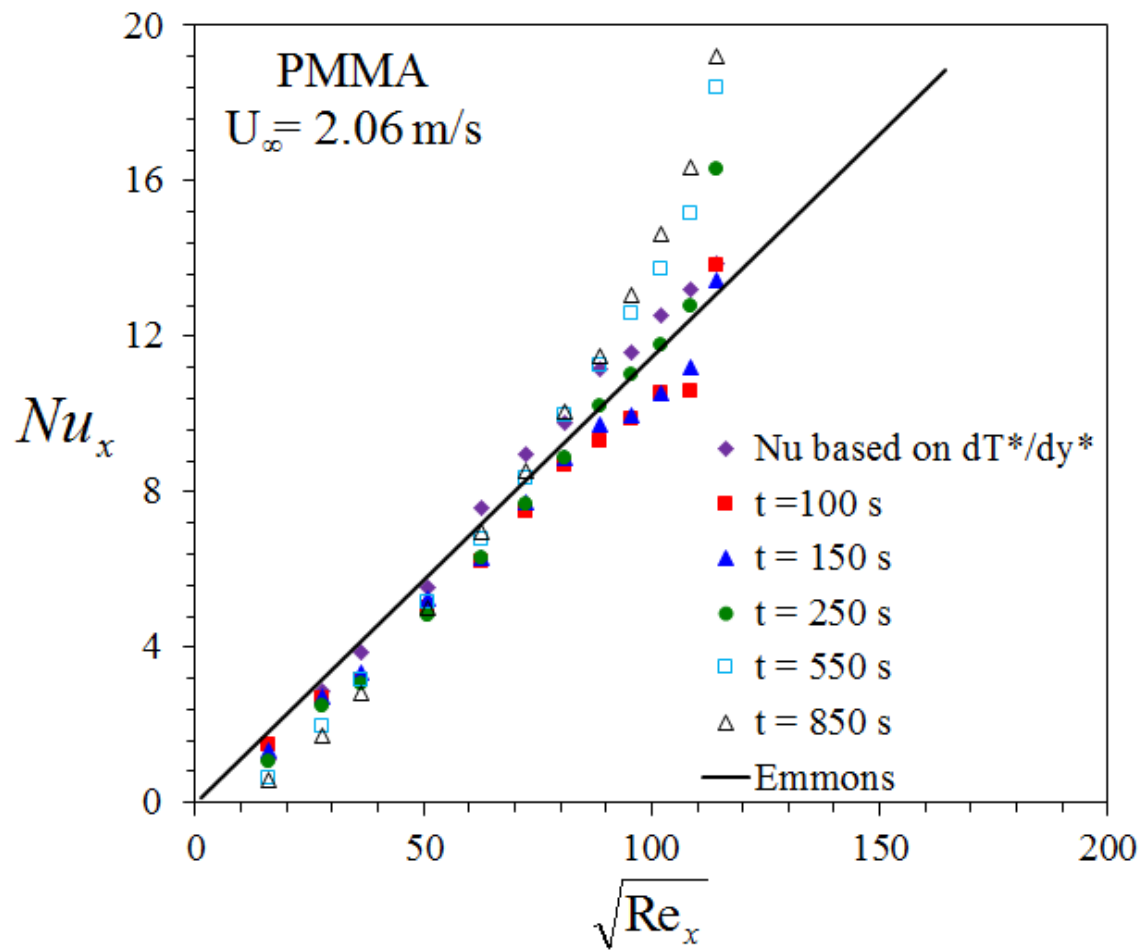
Figure 6.30: Transient Nu_x versus $\sqrt{\mathrm{Re}_x}$ for a PMMA boundary-layer diffusion flame stabilized at $U_\infty = 2.06$ m/s.

It is to be noted that since the non-dimensional mass burning rate is a function

of local Nu_x, PMMA mass burning rate is transient at longer burn-out times and is steady at shorter burn-out times. This can be clearly seen in Figures 6.29 and 6.30 where local Nu_x for PMMA shows a good agreement with Emmons' solution at shorter burn-out times. The local regression rate or burning rate of PMMA deviates from Emmons' steady state solution at longer burn-out times. Following above observations, the pyrolysis behavior of a clear cast PMMA can be understood in more depth. After uniform ignition, the PMMA surface starts to regress or pyrolyze at a steady rate at a given streamwise location. Although, the solid phase has not yet reached a steady state of burning, the gas phase achieves steady state behavior soon after ignition. This is because during short burn-out times, when the PMMA surface is relatively flat, approximately all the incident heat feedback is used to gasify the solid. However, as time progresses, the incident heat flux decreases at a given streamwise location due to the formation of a valley and inefficient combustion, which can be attributed to slow removal of combustion products due to formation of a valley in the leading section. Temperature gradients normal to the fuel surface decrease at a given streamwise location near the leading edge for longer burn-out times. The temperature gradients normal to the fuel surface remain relatively constant near the trailing edge and a closer look at the data reveals an increasing trend for longer burn-out times. For shorter burn-out times, temperature gradients normal to the

259

fuel surface remain relatively constant at a given streamwise location along the condensed fuel surface. Therefore, the convective heat flux, which is proportional to the normal temperature gradients at the fuel surface, follows a similar trend. For these small laminar flames, gas phase convective heating is the dominant mode of heat transfer to the fuel surface and helps in continuous pyrolysis of the PMMA surface. At shorter burn-out times, solid-phase pyrolysis can be assumed to be steady since it shows good agreement with Emmons' steady state solution both qualitatively and quantitatively. However, for longer burn-out times, the gas phase becomes highly transient due to formation of a valley in the leading section and therefore local pyrolysis rates for PMMA at a given streamwise location becomes transient. However, the solid phase now behaves in the exact opposite way, achieving steady state at longer burn-out times. For burning PMMA, any gas-phase measurements made at a later stage will not correspond to Emmons steady state boundary layer solution due to transient effects of the gas phase. Figures 6.29 and 6.30 support the above observations for the burning of a clear cast PMMA in a forced convective environment.

Chapter 7: Conclusions and Scope for Future Work

7. Conclusions and Scope for Future Work

The major accomplishments from this work along with major conclusions is reported in this chapter. The scope for future work is also discussed here.

7.1. Summary

The general purpose of this investigation was to develop a new methodology for the estimation of local mass burning rates for both liquid and solid fuels under a variety of flow-field conditions. The study considered two cases: a) free convection boundary layer diffusion flames and b) forced convection boundary layer diffusion flames established under different free-stream conditions, using both liquid and solid fuels. Based on the experimental and numerical results, it was confirmed that there is indeed a unique correlation between the local mass burning rates and the temperature gradients at the fuel surface. The correlating factor depends on the Spalding mass transfer number and works in the prediction of both integrated as well as local variations of the mass burning rate as a function of non-dimensional temperature gradient. The given methodology was also used to deconvolute the various compo-

nents of flame heat flux in both free and forced convection boundary layer diffusion flames.

7.1.1. Free Convection Boundary Layer Diffusion Flames

An experimental set-up was constructed to measure the burning rates and wall heat fluxes in free convection boundary layer diffusion flames. Local mass burning rates, local temperature gradients, flame stand-off distances, local wall heat fluxes, local convective heat transfer coefficients and profiles of mean temperatures were measured for methanol, ethanol and PMMA wall flames (for a 8×8 cm condensed fuel surface). Regression rates and regression profiles for a PMMA surface were also measured at different burn-out times.

The burning rate was obtained by measuring the rate of mass loss of the condensed fuel surface. Measurements of local temperature gradients at the fuel surface ensured the calculation of local mass burning rates in such flames. The knowledge of local mass burning rates and temperature distributions along a condensed fuel surface were then utilized to deconvolute the convective and radiative components of total flame heat flux in the pyrolysis region. Additionally, a total heat flux gauge was used in the plume together with high spatial resolution temperature measurements to deconvolute the convective and radiative components of total flame heat flux incident on the heat flux gauge.

7.1.2. Forced Convection Boundary Layer Diffusion Flames

A laboratory-scale wind tunnel was designed and developed to conduct experiments in forced flow. An experimental set-up was designed and constructed to measure the burning rates and wall heat fluxes in forced convection boundary layer diffusion flames. Local mass burning rates, local temperature gradients, wall heat fluxes, flame stand-off distances, shear stress at the wall, local combustion and friction coefficients, local convective heat transfer coefficients, local Nu_x and profiles of mean temperatures were measured for methanol, ethanol and PMMA flames stabilized under forced flow (for a 10×10 cm condensed fuel surface). Regression rates and regression profiles for a PMMA surface were also measured at different burn-out times for 4 different free-stream conditions.

The mass burning rate was obtained by measuring the rate of mass loss of the condensed fuel surface. The gas-phase temperature profiles across a laminar boundary layer diffusion flame established over a methanol and ethanol condensed fuel surface were measured for 4 different incoming flow velocities. The knowledge of local mass burning rates and temperature distributions along a condensed fuel surfaces were then utilized to deconvolute the convective and radiative components of total flame heat flux in such flames. With the knowledge of local mass burning rates, shear stresses and hence the strain rates at the condensed fuel surface were easily obtained

for forced convection boundary layer diffusion flames.

7.2. Conclusions

From the present study, the results suggest that local mass burning rates can be obtained in steady laminar boundary layer diffusion flames by using a mass burning rate correlation that is based on the Reynolds analogy. The results from the present study show there is indeed a unique correlation between the local mass burning rate and the local temperature gradient at the condensed fuel surface. The correlating factor depends upon the Spalding transfer number and gas-phase thermo-physical properties and works in the prediction of both integrated as well as local variations of local mass burning rate. Numerical and experimental results closely support the given theoretical correlation. The burning rate correlation performs well irrespective of flow conditions and can be used in both free and forced convective environments and is capable of giving accurate estimates of local mass burning rates and heat fluxes in such flames. The theoretical correlation agrees with experimental methanol, ethanol and PMMA burning data within 15% accuracy and works well in predicting both the average and local mass burning rates.

A new methodology is also proposed for the estimation of local heat fluxes in steady laminar boundary layer diffusion flames. The methodology used here is novel in the sense that it allows determination of various components of flame heat flux

accurately, both in the pyrolysis and plume regions, by knowledge of local temperature gradients along the condensed fuel surface. The work presented here also discusses the selection of transport properties at appropriate temperatures that allows researchers to calculate convective fluxes by using a crude approximation.

Based on Emmons solution, a functional form of the Nusselt number was also derived for forced convective boundary later diffusion flames.

7.3. Scope for Future Work

The proposed burning rate correlation is based upon laminar assumptions, however, it is hypothesized that this technique should follow a similar form for turbulent burning of a fuel surface. Further research must be undertaken to study the effects of grid generated turbulence on the proposed burning rate correlation.

The theory upon which the burning rate correlation is based neglects radiation. The theory is very oversimplified leading to uncertainty in its predictive capabilities in circumstances that are not covered by the present work. For instance, the given methodology may not work for high sooting flames where the heat flux to the surface is largely radiative. For large turbulent wall flames, where radiative heat flux to the condensed fuel surface is high, the proposed burning rate correlation may or may not work. Inclusion of radiation effects in the proposed correlation is, thus, desirable and further research must be undertaken in order to determine this functional

relationship. This area requires improvements in the model if confident prediction methods are to be achieved for such flames.

Having said that, looking back at Ahmad's work [33], it was found that the theory upon which his burning rate correlation was based neglected radiation too, yet the experimental data where the heat flux to the surface was largely radiative, quantitative agreement was observed between the theory and experiments. Ahmad and co-authors could not explain this happy circumstance and proposed that further research must be undertaken in order to explain why radiation-dominated cases correlate according to a convective scheme. If this is true, the proposed burning rate correlation may give good results in such cases as well, without the need of including the radiation effects in the proposed correlation. Further research must be undertaken in order to determine this.

List of Publications from the Present Work

Articles in Refereed Journals

1. Singh, A.V. and Gollner, M.J., "Local Burning Rates and Heat Flux for Forced Flow Boundary Layer Diffusion Flames," AIAA Journal (2015) (*Accepted*).

2. Singh, A.V. and Gollner, M.J., "A Methodology for Estimation of Local Heat Fluxes in Steady Laminar Boundary Layer Diffusion Flames," Combustion and Flame (2015), Vol. 162, No. 5, pp. 2214-2230.

3. Singh, A.V. and Gollner, M.J., "Estimation of local mass burning rates for steady laminar boundary layer diffusion flames," Proceedings of the Combustion Institute (2015), Volume 35, No. 3, pp. 2527-2534. **(Selected as the Distinguished Paper in the Fire Research colloquium of the 35th International Symposium on Combustion)**

Refereed Conference Proceedings

1. Singh, A.V. and Gollner, M.J., "Boundary Layer Combustion Under Forced Flow," 9th U.S. National Combustion Meeting of the Central States Section of the Combustion Institute, May 17-20, 2015, Cincinnati, Ohio, USA.

2. Singh, A.V. and Gollner, M.J., "Local Burning Rates and Heat Flux for Boundary Layer Diffusion Flames under Forced Flow," AIAA-2015-1386, 53rd AIAA Aerospace Sciences Meeting, Jan. 5-9, 2015, Kissimmee, Florida, USA.

3. Singh, A.V. and Gollner, M.J., "Estimation of Local Mass Burning Rates for Steady Laminar Boundary Layer Diffusion Flames," 35th International Symposium on Combustion, Aug. 3-8, 2014, San Francisco, CA, USA.

4. Singh, A.V. and Gollner, M.J., "Thermal and Burning Rate Characteristics of Laminar Boundary Layer Diffusion Flames," Fall Technical Meeting of the Eastern States Section of the Combustion Institute, Oct. 13-16, 2013, Clemson University, Clemson, SC, USA.

Appendices

Appendix A.

A. Theoretical Predictions of Convective Heat Transfer Coefficients

The expression for the boundary layer thickness for a free convection heat transfer on a vertical flat plate is given by [127],

$$\frac{\delta}{x} = 3.93 Pr^{-1/2}(0.952 + Pr)^{1/4} Gr_x^{-1/4} \qquad \text{(A.1)}$$

where Pr is the Prandtl number and Gr_x is the Grashof number. Convective heat transfer coefficient can then be derived as [127],

$$h = \frac{2k}{\delta} \qquad \text{(A.2)}$$

The physical and transport properties are evaluated at the mean film temperature, $T_f = (T_w + T_\infty)/2$. For a boundary layer diffusion flame, this might be approximated as $T_f = (T_w + T_{fl})/2$ where T_{fl} is the average flame temperature for the given fuel and T_w is the average wall temperature (taken as the pyrolysis temperature of the given fuel). Similarly, Grashof number takes the form,

$$Gr_x = \frac{g\beta(T_{fl} - T_w)x^3}{\nu^2}, \beta = \frac{1}{T_f} \tag{A.3}$$

Using the above equations, convective heat transfer coefficient can be calculated theoretically. Based on the convective heat transfer coefficient Nu can be calculated correspondingly.

Appendix B.

A. Description of the Numerical Model

A.1. Numerical Model

A detailed user-defined function was written in Fluent to model the steady burning of liquid pools in both free and forced convective environments. The numerical model described here is the one used for forced convective environment. The numerical model for free and forced convective environment is almost the same except for the changes in the orientation of condensed fuel wick and the change in axes with respect to the wick. In order to simplify the complexity in the problem under study, the following assumptions were made:

1. The flow was assumed to be two-dimensional and laminar.

2. Ideal gas mixture formulation was used to account for density variations with temperature and concentration. As the flow velocity is small, the incompressible flow solution methodology has been adopted to derive the pressure field. This makes the model capable of taking into account changes in density due to temperature variations in the domain.

271

3. Gas-phase alone has been modeled in a decoupled manner with appropriate interfacial conditions. No slip boundary condition was assumed for tangential velocity (x-direction velocity) and no liquid-phase heating effect was considered.

4. Detailed reaction mechanisms for methanol [120] and ethanol oxidation [119] were used to get proper values of flame temperature.

5. The partial pressure of vapor adjacent to the pool surface was assumed to be equal to the vapor pressure of the fuel at the interface temperature, which is valid in low to moderate pressure environments.

6. The liquid fuel pool was considered to be thin and its level was maintained constant by supplying fuel at a rate at which it was being consumed. A user-defined function was used to create a mass source at the interface that was based on an energy balance at the surface of the fuel film. This allows for the liquid film to be maintained at the interface at all times. The user-defined function is described in Chapter 4 section 4.1.2.

7. Heat addition through thermal radiation to the liquid fuel pool was considered negligible when compared to the conductive addition.

In a heterogeneous combustion problem of this type, gas-phase combustion occurs following evaporation from the liquid fuel surface. The present numerical model

272

includes a detailed Discrete Ordinates radiation model [130] to describe the radiative heat transfer.

A.2. Governing Equations

The governing equations for mass, momentum, species and energy conservation in the gas-phase for forced flow boundary layer diffusion flames are given below:

Continuity equation:

$$\frac{\partial(\rho u)}{\partial x} + \frac{\partial(\rho v)}{\partial y} = 0 \tag{B.1}$$

x-momentum equation:

$$\frac{\partial(\rho u)}{\partial t} + \frac{\partial(\rho u u)}{\partial x} + \frac{\partial(\rho u v)}{\partial y} = \frac{\partial(\sigma_{xx})}{\partial x} + \frac{\partial(\tau_{yx})}{\partial y} \tag{B.2}$$

y-momentum equation:

$$\frac{\partial(\rho v)}{\partial t} + \frac{\partial(\rho u v)}{\partial x} + \frac{\partial(\rho v v)}{\partial y} = \frac{\partial(\tau_{xy})}{\partial x} + \frac{\partial(\sigma_{yy})}{\partial y} + (\rho_\infty - \rho)g \tag{B.3}$$

The stress terms in the above equations can be written as:

$$\sigma_{xx} = -p + 2\mu\frac{\partial u}{\partial x}, \sigma_{yy} = -p + 2\mu\frac{\partial v}{\partial y}, \tau_{xy} = \tau_{yx} = \mu\left(\frac{\partial u}{\partial y} + \frac{\partial v}{\partial x}\right) \tag{B.4}$$

Species conservation equation:

For a particular species 'i', the species conservation equation is of the form,

$$\frac{\partial(\rho Y_i)}{\partial t} + \frac{\partial(\rho u Y_i)}{\partial x} + \frac{\partial(\rho v Y_i)}{\partial y} = \frac{\partial}{\partial x}\left(\rho D_{i,m}\frac{\partial Y_i}{\partial x}\right) + \frac{\partial}{\partial y}\left(\rho D_{i,m}\frac{\partial Y_i}{\partial y}\right) + \dot{\omega}_i \tag{B.5}$$

Energy equation:

The energy conservation equation, which includes enthalpy transport by species and radiative heat flux, is given by

$$\frac{\partial(\rho c_p T)}{\partial t} + \frac{\partial(\rho u c_p T)}{\partial x} + \frac{\partial(\rho v c_p T)}{\partial y} = \frac{\partial}{\partial x}\left(k\frac{\partial T}{\partial x}\right) + \frac{\partial}{\partial y}\left(k\frac{\partial T}{\partial y}\right) - \sum_{i=1}^{n}\dot{\omega}_i \Delta h_{f,i} + \dot{q}_R'''$$

$$+ \sum_{i=1}^{n}\left[\frac{\partial}{\partial x}\left(\rho D_{i,m}C_{p,i}T\frac{\partial Y_i}{\partial x}\right) + \frac{\partial}{\partial y}\left(\rho D_{i,m}C_{p,i}T\frac{\partial Y_i}{\partial y}\right)\right] \quad \text{(B.6)}$$

where $h_{f,i}$ is the enthalpy of formation for ith species. For the low ambient temperature considered in this study, the radiative heat transfer is determined using the Discrete Ordinates radiation model. The reader is referred to Fluent technical guide for the given information [130].

A.3. Initial and Boundary Conditions

The initial flow field within the computational domain is assumed to be stationary ($u=v=0$) and only air ($Y_{O_2} = 0.23$ and $Y_{N_2} = 0.77$) is present at the ambient temperature of 300 K. The overall dimensions of the computational domain is 13.5 cm in the x-direction and 9.8 cm in the y-direction.

The following conditions exist at the boundaries (see Figure 4.2):

1. **Inlet boundary**: Atmospheric air with uniform velocity U_∞ and temperature T_∞ enters the domain. The mass fractions of oxygen and nitrogen correspond

to those of normal air. Hence, at inlet, $u = U_\infty$, $v = 0$, $Y_{O_2} = 0.23$, $Y_{N_2} = 0.77$, and $T = T_\infty$.

2. **Wall boundary**: In a test section of wind tunnel, typically wall boundary conditions are prescribed before and after the fuel pool at the bottom as well as at the top boundaries. At the walls, no slip and impermeability boundary conditions are prescribed for velocities, while temperature and mass fractions are prescribed zero diffusive flux values.

3. **Pressure outlet boundary or pressure specified boundary (in case of free convection flames)**: A pressure outlet condition, which drives the flow with respect to the local pressure gradient, has been chosen at this boundary. Due to combustion reactions occurring in the vicinity of the fuel pool surface, the outgoing fluxes of species (at the outlet boundary) will not be equal to the net incoming fluxes entering the computational domain. However, in case of reversed flow at the exit boundary, the boundary variables are set to ambient conditions. These conditions are given below:

$$\frac{\partial \varphi}{\partial n} = 0, \varphi = u, v, T, Y_i; u, v > 0 \tag{B.7}$$

$$T = T_\infty, p = p_\infty, Y_{O_2} = 0.23, Y_{N_2} = 0.77; u, v < 0 \tag{B.8}$$

4. **Fuel pool interface conditions**: Liquid fuel combustion is dominated by the

mass transfer rate, especially for volatile fuels such as alcohols and gasoline. Methanol has high volatility as well as low boiling point (337 K). Accordingly, even at an ambient temperature of 300 K, sufficient amount of vapor is present on top of the liquid pool. The liquid fuel surface is initially assumed to be 5 K below the normal boiling point of the liquid fuel. A detailed User-defined function (UDF) was written in Fluent to define the interface boundary conditions. A mass source is created at the interface to take care of the regression of the pool surface and is described in Chapter 4 section 4.1.2. The interface temperature is derived by solving the heat balance equation at the interface using interior gas-phase temperatures and evaporation mass flux ($\rho_s v_s$). Heat balance at the interface can be written as,

$$k \left(\frac{\partial T}{\partial y} \right)_s = \rho_s v_s h_{fg} \tag{B.9}$$

For evaluation of the interface temperature as well as the evaporation mass flux, Stephen mass transfer velocity at the interface (normal velocity component at the liquid surface, v_s) should be known. The total fuel mass flow rate at the interface is equal to the sum of the fuel mass flow rates due to convection and diffusion. Assuming the liquid-phase to be constituted only by the liquid fuel, the local evaporation velocity (v_s) can be evaluated as:

$$\rho_s v_s = \rho_s v_s Y_{F_s} + \left[-\rho_s D_s \left(\frac{\partial Y_F}{\partial y} \right)_s \right] \tag{B.10}$$

$$v_s = \frac{-D_s \left(\frac{\partial Y_F}{\partial y} \right)_s}{1 - Y_{F_s}} \tag{B.11}$$

The mass fraction of fuel vapor, which is required in Eq. (B.11) is given as,

$$Y_{F,s} = X_{F,s} \frac{MW_F}{MW_{mix}} \tag{B.12}$$

where MW denotes the molecular weight. To calculate the mole fraction of the fuel vapor, local thermodynamic equilibrium between vapor and liquid is assumed at the interface. The partial pressure of the fuel vapor at the interface is obtained as a function of the surface temperature using the Clausius-Clayperon equation given below:

$$X_{F,s} = \frac{p_{sat}}{p_{atm}} = exp \left[-\frac{h_{fg} MW_F}{R_u} \left(\frac{1}{T_s} - \frac{1}{T_b} \right) \right] \tag{B.13}$$

where p_{sat} is the saturation pressure at the interface temperature T_s and p_{atm} is the atmospheric pressure. T_b is the boiling temperature of the given liquid fuel. It should be noted here that due to non-linearity of Eq. (B.13), the interface conditions given by Eqs. (B.9-B.13) are solved for few iterations to arrive at the converged values of quantities such as temperature, fuel vapor mass fraction and evaporating velocity at the interface. Once the evaporating

velocity at the interface is known (v_s), local mass burning rate $(\dot{m}''_f)$ at each streamwise location along the condensed fuel surface can be calculated from the expression, $\rho_s v_s$.

Variable thermo-physical properties in the gas phase are calculated as follows. Density (ρ) is calculated using the ideal gas equation of state and mixture molecular weight. Viscosity (μ) and thermal conductivity (k) are evaluated as a function of temperature and molecular weight using kinetic theory. In order to evaluate the specific heat of each species, piece-wise polynomials in temperature have been employed from CHEMKIN thermodynamic database. Mass diffusivity for any species diffusing into the mixture has been calculated using a multi-component diffusion approach.

A.4. Solution Procedure

A Finite Volume Method (FVM) based discretization approach and SIMPLE algorithm for pressure velocity coupling are employed for solving the governing transport equations. Explicit time marching scheme with a time step of 1×10^{-5} s has been employed for solving the governing equations. A laminar species transport model is used along with finite rate chemistry. More details on the combustion model can be found in the literature elsewhere [130]. Full multi-component diffusion along with a diffusion energy source is used to model the species diffusion. Initially, a certain

number of iterations were carried out for flow solution alone without solving the reaction rate equation. After obtaining the cold flow solution, high temperature air is passed into the domain for a short duration to achieve ignition. Subsequently, the transient time marching procedure is carried out. Mass fraction conservation equations and the energy equation are solved using a smaller time step value $(1{\times}10^{-6})$ for a certain number of inner iterations due to the non-linear source terms present in them. The reaction chemistry is solved for each cell, to obtain the net reaction rate of each species at the updated temperature values. All the thermo-physical properties are updated using appropriate temperature dependent equations. The transient time marching procedure is carried out until either a steady state or a time independent oscillatory solution is obtained.

References

[1] V. Babrauskas and R. D. Peacock, "Heat release rate: the single most important variable in fire hazard," *Fire safety journal*, vol. 18, no. 3, pp. 255–272, 1992.

[2] P. Pagni and T. Shih, "Excess pyrolyzate," *Proceedings of the Combustion Institute*, vol. 16, no. 1, pp. 1329–1343, 1977.

[3] L. Orloff, A. T. Modak, and R. Alpert, "Burning of large-scale vertical surfaces," *Proceedings of the Combustion Institute*, vol. 16, no. 1, pp. 1345–1354, 1977.

[4] T. H. Chilton and A. P. Colburn, "Mass transfer (absorption) coefficients prediction from data on heat transfer and fluid friction," *Industrial & engineering chemistry*, vol. 26, no. 11, pp. 1183–1187, 1934.

[5] R. Silver, "Application of the reynolds analogy to combustion of solid fuels," *Nature*, vol. 165, pp. 725–726, 1950.

[6] H. Emmons, "The film combustion of liquid fuel," *ZAMM-Journal of Applied Mathematics and Mechanics/Zeitschrift für Angewandte Mathematik und Mechanik*, vol. 36, no. 1-2, pp. 60–71, 1956.

[7] S. M. Ali, V. Raghavan, and A. S. Rangwala, "A numerical study of quasi-steady burning characteristics of a condensed fuel: effect of angular orientation of fuel surface," *Combustion Theory and Modelling*, vol. 14, no. 4, pp. 495–518, 2010.

[8] J. G. Quintiere, *Fundamentals of fire phenomena*. John Wiley and Sons, England, 2006.

[9] D. Spalding, "Combustion of liquid fuel in gas stream," *Fuel*, vol. 29, no. 1, pp. 2–7, 1950.

[10] J. L. Torero, T. Vietoris, G. Legros, and P. Joulain, "Estimation of a total mass transfer number from the standoff distance of a spreading flame," *Combustion science and technology*, vol. 174, no. 11-12, pp. 187–203, 2002.

[11] F. Jiang, H. Qi, J. L. de Ris, and M. M. Khan, "Radiation enhanced b-number," *Combustion and Flame*, vol. 160, no. 8, pp. 1510–1518, 2013.

[12] A. V. Singh and M. J. Gollner, "A methodology for estimation of local heat fluxes in steady laminar boundary layer diffusion flames," *Combustion and Flame*, vol. 162, no. 5, pp. 2214–2230, 2015.

[13] A. V. Singh and M. J. Gollner, "Estimation of local mass burning rates for

steady laminar boundary layer diffusion flames," *Proceedings of the Combustion Institute*, vol. 35, no. 3, pp. 2527 – 2534, 2015.

[14] S. Burke and T. Schumann, "Diffusion flames," *Proceedings of the Combustion Institute*, vol. 1, pp. 2–11, 1948.

[15] D. B. Spalding, "The combustion of liquid fuels," *Proceedings of the Combustion Institute*, vol. 4, pp. 847–864, 1953.

[16] F. J. Kosdon, F. A. Williams, and C. Buman, "Combustion of vertical cellulosic cylinders," *Proceedings of the Combustion Institute*, vol. 12, pp. 253–64, 1969.

[17] J. Kim, J. de Ris, and F. Kroesser, "Laminar free-convective burning of fuel surfaces," *Proceedings of the Combustion Institute*, vol. 13, pp. 949–961, 1971.

[18] K. Annamalai and M. Sibulkin, "Flame spread over combustible surfaces for laminar flow systems part i: Excess fuel and heat flux," *Combustion Science and Technology*, vol. 19, no. 5-6, pp. 167–183, 1979.

[19] P. J. Pagni, "Diffusion flame analyses," *Fire Safety Journal*, vol. 3, no. 4, pp. 273–285, 1981.

[20] W. Sirignano, "Theory of flame spread above solids," *Acta Astronautica*, vol. 1, no. 9, pp. 1285–1299, 1974.

[21] F. Williams, "Mechanisms of fire spread," in *Symposium (International) on Combustion*, vol. 16, pp. 1281–1294, Elsevier, 1977.

[22] D. Spalding, "A theory of the extinction of diffusion flames," *Fuel*, vol. 33, no. 3, pp. 255–273, 1954.

[23] M. Sibulkin and J. Kim, "The dependence of flame propagation on surface heat transfer ii. upward burning," *Combustion Science and Technology*, vol. 17, no. 1-2, pp. 39–49, 1977.

[24] Y. Nakagawa, N. Nishiwaki, and M. Hirata, "Effect of combustion on a laminar boundary layer," in *Symposium (International) on Combustion*, vol. 13, pp. 813–819, Elsevier, 1971.

[25] K. Shinzo and Y. Katsuhiro, "Theoretical investigation on laminar boundary layer with combustion on a flat plate," *International Journal of Heat and Mass Transfer*, vol. 16, no. 6, pp. 1215–1229, 1973.

[26] T. Hirano, K. Iwai, and Y. Kanno, "Measurement of velocity distribvution in boundary-layer over a flat plate with a diffusion flame," *Astronautica Acta*, vol. 17, no. 4-5, p. 811, 1972.

[27] T. Hirano and Y. Kanno, "Aerodynamic and thermal structures of the lami-

narboundary layer over a flat plate with a diffusion flame," *Proceedings of the Combustion Institute*, vol. 14, no. 1, pp. 391–398, 1973.

[28] T. Hirano and M. Kinoshita, "Gas velocity and temperature profiles of a diffusion flame stabilized in the stream over liquid fuel," *Proceedings of the Combustion Institute*, vol. 15, no. 1, pp. 379–387, 1975.

[29] P. Andreussi and L. Petarca, "Film combustion of ethyl alcohol in a parallel air stream," *Proceedings of the Combustion Institute*, vol. 18, no. 1, pp. 1861–1869, 1981.

[30] P. Andreussi, "Modelling of laminar diffusion flames over a horizontal plate," *Combustion and Flame*, vol. 45, pp. 1–6, 1982.

[31] S. Andreotti, P. Andreussi, and L. Petarca, "Boundary layer burning of fuel surfaces: thermal and aerodynamic structure of the flame," *Combustion Science and Technology*, vol. 40, no. 5-6, pp. 279–291, 1984.

[32] M. Lavid and A. Berlad, "Gravitational effects on chemically reacting laminar boundary layer flows over a horizontal flat plate," in *Symposium (International) on Combustion*, vol. 16, pp. 1557–1568, Elsevier, 1977.

[33] T. Ahmad and G. M. Faeth, "Turbulent wall fires," *Proceedings of the Combustion Institute*, vol. 17, pp. 1149–1160, 1978.

[34] T. Ahmad, *Investigation of the combustion region of fire-induced plumes along upright surfaces.* Ph.D. Thesis, Pennsylvania State University, 1978.

[35] T. Ueda, M. Mizomoto, S. Ikai, and T. Kobayashi, "Velocity and temperature fluctuations in a flat plate boundary layer diffusion flame," *Combustion Science and Technology*, vol. 27, no. 3-4, pp. 133–142, 1982.

[36] A. Ramachandra and B. Raghunadan, "On the velocity overshoot in a laminar boundary layer diffusion flame," *Combustion Science and Technology*, vol. 33, no. 5-6, pp. 309–313, 1983.

[37] J. S. Ha, S. H. Shim, and H. D. Shin, "Boundary layer diffusion flame over a flat plate in the presence and absence of flow separation," *Combustion science and technology*, vol. 75, no. 4-6, pp. 241–260, 1991.

[38] J. Torero, L. Bonneau, J. Most, and P. Joulain, "The effect of gravity on a laminar diffusion flame established over a horizontal flat plate," in *Symposium (International) on Combustion*, vol. 25, pp. 1701–1709, Elsevier, 1994.

[39] L. Krishnamurty and F. Williams, "Laminar combustion of polymethyl methacrylate in o2/n2 mixtures," in *14th Symposium (International) on combustion, The combustion Institute*, pp. 1151–1164.

[40] K. Mekki, A. Atreya, S. Agrawal, and I. Wichman, "Wind-aided flame spread over charring and non-charrring solids: An experimental investigation," in *Symposium (International) on Combustion*, vol. 23, pp. 1701–1707, Elsevier, 1991.

[41] L. Zhou and A. Fernandez-Pello, "Turbulent, concurrent, ceiling flame spread: The effect of buoyancy," *Combustion and flame*, vol. 92, no. 1, pp. 45–59, 1993.

[42] S. Agrawal and A. Atreya, "Wind-aided flame spread over an unsteadily vaporizing solid," in *Symposium (International) on Combustion*, vol. 24, pp. 1685–1693, Elsevier, 1992.

[43] S. Agrawal, "Determination of surface heat flux in the burning zone during wind-aided flame spread using burned pmma samples," *Combustion science and technology*, vol. 91, no. 1-3, pp. 187–190, 1993.

[44] T. Vietoris, P. Joulain, and J. L. Torero, "Experimental observations on the geometry and stability of a laminar diffusion flame in micro-gravity," in *Sixth International Symposium on Fire Safety Science*, pp. 5–9, 1999.

[45] R. Ananth, C. C. Ndubizu, and P. Tatem, "Burning rate distributions for boundary layer flow combustion of a pmma plate in forced flow," *Combustion and flame*, vol. 135, no. 1, pp. 35–55, 2003.

[46] C. Ndubizu, R. Ananth, and P. Tatem, "Transient burning rate of a noncharring plate under a forced flow boundary layer flame," *Combustion and flame*, vol. 141, no. 1, pp. 131–148, 2005.

[47] A. S. Rangwala, S. G. Buckley, and J. L. Torero, "Upward flame spread on a vertically oriented fuel surface: The effect of finite width," *Proceedings of the Combustion Institute*, vol. 31, no. 2, pp. 2607–2615, 2007.

[48] A. S. Rangwala, S. G. Buckley, and J. L. Torero, "Analysis of the constant b number assumption while modeling flame spread," *Combustion and Flame*, vol. 152, no. 3, pp. 401–414, 2008.

[49] A. Ramachandra and B. Raghunandan, "An analysis of a boundary layer diffusion flame over a porous flat plate in a confined flow," *Combustion Science and Technology*, vol. 38, no. 1-2, pp. 59–73, 1984.

[50] C.-H. Chen and J. S. T'IEN, "Diffusion flame stabilization at the leading edge of a fuel plate," *Combustion Science and Technology*, vol. 50, no. 4-6, pp. 283–306, 1986.

[51] H. Kodama, K. Miyasaka, and A. Fernandez-Pello, "Extinction and stabilization of a diffusion flame on a flat combustible surface with emphasis on thermal

controlling mechanisms," *Combustion science and technology*, vol. 54, no. 1-6, pp. 37–50, 1987.

[52] S. Rouvreau, J. Torero, and P. Joulain, "Numerical evaluation of boundary layer assumptions for laminar diffusion flames in microgravity," *Combustion Theory and Modelling*, vol. 9, no. 1, pp. 137–158, 2005.

[53] V. Raghavan, A. Rangwala, and J. Torero, "Laminar flame propagation on a horizontal fuel surface: Verification of classical emmons solution," *Combustion Theory and Modelling*, vol. 13, no. 1, pp. 121–141, 2009.

[54] S. M. Ali, V. Raghavan, and S. Tiwari, "A study of steady laminar diffusion flame over methanol pool surface," *International Journal of Heat and Mass Transfer*, vol. 53, no. 21, pp. 4696–4706, 2010.

[55] S. M. Ali, V. Raghavan, and A. S. Rangwala, "Numerical analysis of flame heating on arbitrarily oriented condensed fuel surfaces," *Fire Safety Journal*, vol. 49, pp. 67–78, 2012.

[56] J. de Ris, "Spread of a laminar diffusion flame," *Proceedings of the Combustion Institute*, vol. 12, no. 1, pp. 241–252, 1969.

[57] C. Fernandez-Pello and C.-P. Mao, "A unified analysis of concurrent modes of

flame spread," *Combustion Science and Technology*, vol. 26, no. 3-4, pp. 147–155, 1981.

[58] T. Suzuki and T. Hirano, "Flame propagation across a liquid fuel in an air stream," in *Symposium (International) on Combustion*, vol. 19, pp. 877–884, Elsevier, 1982.

[59] A. Fernandez-Pello and T. Hirano, "Controlling mechanisms of flame spread," *Combustion Science and Technology*, vol. 32, no. 1-4, pp. 1–31, 1983.

[60] A. FernandezPello, "Flame spread modeling," *Combustion science and technology*, vol. 39, no. 1-6, pp. 119–134, 1984.

[61] K. Saito, J. Quintiere, and F. Williams, "Upward turbulent flame spread," in *Fire Safety Science-Proceedings of the First International Symposium*, pp. 75–86, 1986.

[62] K. Saito, F. Williams, I. Wichman, and J. Quintiere, "Upward turbulent flame spread on wood under external radiation," *Journal of Heat Transfer*, vol. 111, no. 2, pp. 438–445, 1989.

[63] Y. Hasemi, M. Yoshida, A. Nohara, and T. Nakabayashi, "Unsteady-state upward flame spreading velocity along vertical combustible solid and influence of

external radiation on the flame spread," in *Proceedings of the Third International Symposium*, pp. 197–206, 1991.

[64] D. Schiller, H. Ross, and W. Sirignano, "Computational analysis of flame spread across alcohol pools," *Combustion science and technology*, vol. 118, no. 4-6, pp. 203–255, 1996.

[65] D. Schiller and W. Sirignano, "Opposed-flow flame spread across n-propanol pools," in *Symposium (International) on Combustion*, vol. 26, pp. 1319–1325, Elsevier, 1996.

[66] I. Kim, D. Schiller, and W. Sirignano, "Axisymmetric flame spread across propanol pools in normal and zero gravities," *Combustion Science and Technology*, vol. 139, no. 1, pp. 249–275, 1998.

[67] H. D. Ross and F. J. Miller, "Flame spread across liquid pools with very low-speed opposed or concurrent airflow," in *Symposium (International) on Combustion*, vol. 27, pp. 2723–2729, Elsevier, 1998.

[68] J. Cai, F. Liu, and W. A. Sirignano, "Three-dimensional flame propagation above liquid fuel pools," *Combustion science and technology*, vol. 174, no. 5-6, pp. 5–34, 2002.

[69] R. A. Borgeson and J. S. T'ien, "Modelling the fuel temperature effect on flame spread limits in opposed flow," *Combustion Science and Technology*, vol. 32, no. 1-4, pp. 125–136, 1983.

[70] A. E. Frey and J. S. Tien, "Near-limit flame spread over paper samples," *Combustion and Flame*, vol. 26, pp. 257–267, 1976.

[71] I. Wichman, F. Williams, and I. Glassman, "Theoretical aspects of flame spread in an opposed flow over flat surfaces of solid fuels," in *Symposium (International) on Combustion*, vol. 19, pp. 835–845, Elsevier, 1982.

[72] C. Di Blasi, G. Continillo, S. Crescitelli, and G. Russo, "Numerical simulation of opposed flow flame spread over a thermally thick solid fuel," *Combustion science and technology*, vol. 54, no. 1-6, pp. 25–36, 1987.

[73] C. Di Blasi, S. Crescitelli, G. Russo, and A. Fernandez-Pello, "Predictions of the dependence on the opposed flow characteristics of the flame spread rate over thick solid fuel," in *Second International Symposium on Fire Safety Science, Tokyo, Japan*, 1988.

[74] C. Di Blasi, S. Crescitelli, and G. Russo, "Numerical modelling of flow assisted flame spread," *Computer methods in applied mechanics and engineering*, vol. 75, no. 1, pp. 481–492, 1989.

[75] A. Kumar, H. Y. Shih, and S. James, "A comparison of extinction limits and spreading rates in opposed and concurrent spreading flames over thin solids," *Combustion and flame*, vol. 132, no. 4, pp. 667–677, 2003.

[76] C. Kumar and A. Kumar, "A computational study on opposed flow flame spread over thin solid fuels with side-edge burning," *Combustion Science and Technology*, vol. 182, no. 9, pp. 1321–1340, 2010.

[77] T. Hirano and K. Saito, "Fire spread phenomena: The role of observation in experiment," *Progress in energy and combustion science*, vol. 20, no. 6, pp. 461–485, 1994.

[78] S. L. Olson and U. Hegde, "Imposed radiation effects on flame spread over black pmma in low gravity," 1994.

[79] J. V. Creeden Jr and M. Sibulkin, "The effect of an uninhibited edge on downward flame propagation," *Combustion Science and Technology*, vol. 14, no. 1-3, pp. 123–124, 1976.

[80] W. Mell and T. Kashiwagi, "Effects of finite sample width on transition and flame spread in microgravity," *Proceedings of the Combustion Institute*, vol. 28, no. 2, pp. 2785–2792, 2000.

[81] W. Mell, S. Olson, and T. Kashiwagi, "Flame spread along free edges of thermally thin samples in microgravity," *Proceedings of the Combustion Institute*, vol. 28, no. 2, pp. 2843–2849, 2000.

[82] M. Sibulkin, W. Ketelhut, and S. Feldman, "Effect of orientation and external flow velocity on flame spreading over thermally thin paper strips," *Combustion Science and Technology*, vol. 9, no. 1-2, pp. 75–77, 1974.

[83] A. Fernandez-Pello and F. Williams, "Laminar flame spread over pmma surfaces," in *Symposium (International) on Combustion*, vol. 15, pp. 217–231, Elsevier, 1975.

[84] T. Kashiwagi and D. L. Newman, "Flame spread over an inclined thin fuel surface," *Combustion and Flame*, vol. 26, pp. 163–177, 1976.

[85] A. Ito and T. Kashiwagi, "Characterization of flame spread over pmma using holographic interferometry sample orientation effects," *Combustion and Flame*, vol. 71, no. 2, pp. 189–204, 1988.

[86] D. Drysdale and A. Macmillan, "Flame spread on inclined surfaces," *Fire Safety Journal*, vol. 18, no. 3, pp. 245–254, 1992.

[87] J. G. Quintiere, "The effects of angular orientation on flame spread over thin materials," *Fire Safety Journal*, vol. 36, no. 3, pp. 291–312, 2001.

[88] M. Gollner, X. Huang, J. Cobian, A. Rangwala, and F. Williams, "Experimental study of upward flame spread of an inclined fuel surface," *Proceedings of the Combustion Institute*, vol. 34, no. 2, pp. 2531–2538, 2013.

[89] Y. Zhang, M. J. Bustamante, M. J. Gollner, P. B. Sunderland, and J. G. Quintiere, "Burning on flat wicks at various orientations," *Journal of Fire Sciences*, pp. 52–71, 2013.

[90] L. Orloff, J. De Ris, and G. Markstein, "Upward turbulent fire spread and burning of fuel surface," *Proceedings of the Combustion Institute*, vol. 15, no. 1, pp. 183–192, 1975.

[91] J. Quintiere, M. Harkleroad, and Y. Hasemi, "Wall flames and implications for upward flame spread," *Combustion Science and Technology*, vol. 48, no. 3-4, pp. 191–222, 1986.

[92] A. Kulkarni and C. Kim, "Heat loss to the interior of a free burning vertical wall and its influence on estimation of effective heat of gasification," *Combustion Science and Technology*, vol. 73, no. 4-6, pp. 493–504, 1990.

[93] E. G. Brehob and A. K. Kulkarni, "Experimental measurements of upward flame spread on a vertical wall with external radiation," *Fire Safety Journal*, vol. 31, no. 3, pp. 181–200, 1998.

[94] P. Wu, L. Orloff, and A. Tewarson, "Assessment of material flammability with the fsg propagation model and laboratory test methods," 1997.

[95] P. A. Beaulieu and N. A. Dembsey, "Effect of oxygen on flame heat flux in horizontal and vertical orientations," *Fire Safety Journal*, vol. 43, no. 6, pp. 410–428, 2008.

[96] K. Tsai and F. Wan, "Upward flame spread: the width effect," *Fire Safety Science*, vol. 8, pp. 409–419, 2005.

[97] K.-C. Tsai, "Influence of sidewalls on width effects of upward flame spread," *Fire Safety Journal*, vol. 46, no. 5, pp. 294–304, 2011.

[98] Y. Pizzo, C. Lallemand, A. Kacem, A. Kaiss, J. Gerardin, Z. Acem, P. Boulet, and B. Porterie, "Steady and transient pyrolysis of thick clear pmma slabs," *Combustion and Flame*, vol. 162, no. 1, pp. 226–236, 2015.

[99] D. Collis and M. Williams, "Two-dimensional convection from heated wires at low reynolds numbers," *Journal of Fluid Mechanics*, vol. 6, no. 03, pp. 357–384, 1959.

[100] D. Pollock, "Thermocouples in high-temperature reactive atmospheres," *Combustion Science and Technology*, vol. 42, no. 1-2, pp. 111–113, 1984.

[101] J. Madson and E. Theby, "Sio2 coated thermocouples," *Combustion Science and Technology*, vol. 36, no. 3-4, pp. 205–209, 1984.

[102] K. C. Smyth, J. H. Miller, R. C. Dorfman, W. G. Mallard, and R. J. Santoro, "Soot inception in a methane/air diffusion flame as characterized by detailed species profiles," *Combustion and Flame*, vol. 62, no. 2, pp. 157–181, 1985.

[103] F. Lockwood and A. Odidi, "Measurement of mean and fluctuating temperature and of ion concentration in round free-jet turbulent diffusion and premixed flames," in *Symposium (International) on Combustion*, vol. 15, pp. 561–571, Elsevier, 1975.

[104] A. Ballantyne and J. Moss, "Fine wire thermocouple measurements of fluctuating temperature," *Combustion Science and Technology*, vol. 17, no. 1-2, pp. 63–72, 1977.

[105] P. Miles and F. Gouldin, "Determination of the time constant of fine-wire thermocouples for compensated temperature measurements in premixed turbulent flames," *Combustion science and technology*, vol. 89, no. 1-4, pp. 181–199, 1993.

[106] A. Yule, D. Taylor, and N. Chigier, "Thermocouple signal processing and on-line digital compensation," *Journal of Energy*, vol. 2, no. 4, pp. 223–231, 1978.

[107] A. V. Singh, M. Yu, A. K. Gupta, and K. M. Bryden, "Thermo-acoustic behavior of a swirl stabilized diffusion flame with heterogeneous sensors," *Applied Energy*, vol. 106, pp. 1–16, 2013.

[108] A. V. Singh, A. Eshaghi, M. Yu, A. K. Gupta, and K. M. Bryden, "Simultaneous time-resolved fluctuating temperature and acoustic pressure field measurements in a premixed swirl flame," *Applied Energy*, vol. 115, pp. 116–127, 2014.

[109] C. R. Shaddix, "Correcting thermocouple measurements for radiation loss-a critical review," in *1999 National Heat Transfer Conference, 33 rd, Albuquerque, NM*, 1999.

[110] L. M. Jakob, *Heat Transfer: Vol. 1*. Wiley, 1967.

[111] C. D. Hodgman, R. C. Weast, and S. M. Selby, *Handbook of chemistry and physics: a ready-reference book of chemical and physical data*. Chemical Rubber Publishing Company, 1961.

[112] G. Gubareff, J. Janssen, and R. Torborg, "Thermal radiation properties survey, 1960," *Minneapolis-Honeywell Regulator Company, Honeywell Research Center, Minneapolis*.

[113] D. Bradley and K. Matthews, "Measurement of high gas temperatures with fine wire thermocouples," *Journal of Mechanical Engineering Science*, vol. 10, no. 4, pp. 299–305, 1968.

[114] C. Petit, P. Gajan, J.-C. Lecordier, and P. Paranthoen, "Frequency response of fine wire thermocouple," *Journal of Physics E: Scientific Instruments*, vol. 15, no. 7, p. 760, 1982.

[115] M. du Plessis, R. Wang, and R. Kahawita, "Investigation of the near-region of a square jet," *Journal of Fluids Engineering*, vol. 96, no. 3, pp. 246–251, 1974.

[116] A. Sfeir, "The velocity and temperature fields of rectangular jets," *International Journal of Heat and Mass Transfer*, vol. 19, no. 11, pp. 1289–1297, 1976.

[117] P. Sforza, M. Steiger, and N. Trentacoste, "Studies on three-dimensional viscous jets.," *AIAA journal*, vol. 4, no. 5, pp. 800–806, 1966.

[118] X. Wang, T. Suzuki, Y. Ochiai, and S. Ohyagi, "Numerical studies of reacting flows over flat walls with fuel injection.(part 1, velocity anomaly and hydrodynamic instability).," *JSME International Journal Series B Fluids and Thermal Engineering*, vol. 41, no. 1, pp. 19–27, 1998.

[119] J.-Y. Chen, "Reduced reaction mechanisms for methanol-air diffusion flames," *Combustion Science and Technology*, vol. 78, no. 1-3, pp. 127–145, 1991.

[120] F. Vaz, "Vaz, f., a., de bortoli, a., l.,(2010).development of reduced reaction mechanism for ethylene and ethanol diffusion flames," *Mecánica Computacional*, vol. 29, pp. 2655–2661.

[121] D. Spalding, "Combustion of a single droplet and of a fuel spray," *Aeronatical Appl*, p. 340, 1954.

[122] C. Vovelle, R. Akrich, J.-L. Delfau, and S. Gresillaud, "Influence of the thickness on the thermal degradation of pmma," *Fire Safety Science*, vol. 1, p. 473, 1986.

[123] S. Turns, *An introduction to combustion*, vol. 287. McGraw-Hill New York, 1996.

[124] Y. Pizzo, J. Consalvi, P. Querre, M. Coutin, L. Audouin, B. Porterie, and J. Torero, "Experimental observations on the steady-state burning rate of a vertically oriented pmma slab," *Combustion and Flame*, vol. 152, no. 3, pp. 451–460, 2008.

[125] C.-B. Jiang, J. S. Tien, and H.-Y. Shih, "Model calculation of steady upward

flame spread over a thin solid in reduced gravity," *Proceedings of the Combustion Institute*, vol. 26, no. 1, pp. 1353–1360, 1996.

[126] F. P. Incropera, *Fundamentals of heat and mass transfer*. John Wiley & Sons, 2011.

[127] J. Holman, *Heat transfer, 1986*. McGraw-Hill, 1986.

[128] G. Parent, Z. Acem, A. Collin, R. Berfroi, P. Boulet, Y. Pizzo, P. Mindykowski, A. Kaiss, and B. Porterie, "Radiative flux emitted by a burning pmma slab," in *6th European Thermal Sciences Conference (Eurotherm 2012)*, vol. 395, p. 012153, 2012.

[129] I. Glassman, *Combustion*. Academic press, 1997.

[130] I. Fluent, "Fluent 6.3 users guide," *Fluent documentation*, 2006.